Thermoelectric Transport Phenomena in Magnetic Nanowires and Topological Micro-Ribbons

Dissertation

zur Erlangung des Doktorgrades
an der Fakultät für Mathematik, Informatik und Naturwissenschaften
Fachbereich Physik
der Universität Hamburg

vorgelegt von
Anna Corinna Niemann

Hamburg

2019

Gutachter der Dissertation:	Prof. Dr. Kornelius Nielsch
	Prof. Dr. Michael Rübhausen
Zusammensetzung der Prüfungskommission:	Prof. Dr. Kornelius Nielsch
	Prof. Dr. Michael Rübhausen
	Prof. Dr. Robert Blick
	Dr. Elena Vedmedenko
	Prof. Dr. Wolfgang Hansen
Vorsitzender der Prüfungskommision:	Prof. Dr. Wolfgang Hansen
Datum der Dissertation:	13.01.2020
Vorsitzender Fach-Promotionsausschuss Physik:	Prof. Dr. Michael Potthoff
Leiter des Fachbereichs Physik:	Prof. Dr. Wolfgang Hansen
Dekan der MIN Fakultät:	Prof. Dr. Heinrich Graener

Abstract

Since its discovery, thermoelectricity has been developed and advanced as an energy conversion method. At the same time, thermoelectric measurements have also evolved as a method to investigate transport phenomena in condensed matter physics. In this thesis, studies on magnetic nanostructures as well as topological microstructures are presented, contributing to current research in the fields of spincaloritronics and topological materials by using thermoelectric characterization. The presented studies show how thermoelectric measurements can be used to investigate transport phenomena in systems with multiple, parallel transport channels, namely the spin up and the spin down channel in ferromagnetic systems and topological and non-topological transport channels in topological insulators and semimetals.

For magnetic CoNi alloy and CoNi/Cu multilayered nanowires a classical, magneto-thermoelectric characterization has been conducted, revealing that thermoelectric power generation from waste heat at the nanoscale is a competitive scenario compared to conventional thermoelectric materials, because the thermoelectric power factors can compete with the power factors of conventional thermoelectric Bi–Sb–Se–Te based bulk materials. Utilizing magnetoresistance and magnetothermopower measurements on CoNi/Cu multilayered nanowires, we developed a simple model based on the Mott formula to distinguish between the absolute thermopower contribution of the magnetic nanowires and the non-magnetic, electrical leads. Our model is a virtual tool to determine the absolute thermopower contributions in an electrical measurement circuit. We further investigated the magnetic switching behavior of CoNi and NiFe alloy nanowires under the influence of a temperature gradient. We found that a temperature gradient can counteract the thermally assisted switching process in the magnetic nanowires, which reveals an engineering challenge in future heat-assisted magnetic recording devices to carefully distinguish between elevated temperatures and temperature gradients.

In our magneto-transport study on $HfTe_5$, which is a promising low-temperature thermoelectric material and has a topologically non-trivial band structure, we found that the application of a magnetic field enhances the thermoelectric power output between 150 K and 300 K, this being the temperature range relevant to thermoelectric applications of $HfTe_5$, by up to 40 % compared to the power output at zero magnetic field. Furthermore, we observed an almost complete suppression of the magneto-thermoelectric transport for temperatures below 100 K and we introduced different possible transport mechanisms for this observation. In a bulk sample of the Weyl semimetal NbP, we investigated the band structure by magnetometry measurements and identified multiple non-topological transport channels as well as one transport channel hosting Weyl fermions. This verification of the existence of Weyl fermions at the Fermi energy of NbP set the basis for our transport studies on NbP. In a micro-structured NbP sample, we achieved a separation of the W2 Weyl cones in momentum space by a slight shift of the Fermi energy compared to the bulk sample and measured the breakdown of the chiral symmetry in the W2 Weyl cones by applying collinear magnetic and electric fields. Finally, the mixed, axial-gravitational anomaly, a breakdown of the chiral symmetry due to collinear magnetic fields and temperature gradients has been observed in NbP. Thereby, we were able to realize an experiment that remains elusive in high-energy physics.

Kurzfassung

Seit ihrer Entdeckung wird Thermoelektrizität hauptsächlich als Methode der elektrischen Energieerzeugung weiterentwickelt. Gleichzeitig haben sich thermoelektrische Messungen auch als Untersuchungsmethode für Transportphänomene in der Festkörperphysik etabliert. In dieser Arbeit werden Untersuchungen an magnetische Nanostrukturen und topologischen Mikrostrukturen vorgestellt, die zu aktuellen Fragestellungen aus der Spinkaloritronik als auch aus dem Bereich der topologischen Materialien beitragen. Die Studien in dieser Arbeit zeigen wie thermoelektrische Messungen zur Untersuchung von Systeme mit mehreren, parallelen Transportkanälen, gegeben durch den Spin-Up- und den Spin-Down-Kanal in ferromagnetischen Materialien sowie topologische und nicht-topologische Kanäle in topologischen Isolatoren und Halbmetallen, beitragen können.
CoNi-Alloy- and CoNi/Cu-Multischichtnanodrähte wurden magneto-thermoelektrische charakterisiert. Wir konnten zeigen, dass unser Nanostrukturen für die thermoelektrische Energiegewinnung durch die Nutzung von Abwärme auf der Nanoskala konkurrenzfähig zur konventionellen thermoelektrischen Materialien ist, da die thermoelektrischen Powerfaktoren der Nanodrähte in der gleichen Größenordnung liegen wie die von konventionellen Bi–Sb–Se–Te-basierten Materialien. Mit Hilfe von Magnetowiderstands- und Magneto-Seebeckmessungen an CoNi/Cu-Multischichtnanodrähten wurde ein einfaches, auf der Mott Formel basierendes Model aufgestellt um zwischen den absoluten Seebeck-Koeffizienten zwischen den magnetischen Nanodrähten und der nicht-magnetischen, elektrischen Kontaktstruktur zu unterscheiden. Schließlich wurde noch das magnetische Schaltverhalten von CoNi und FeNi Nanodrähten unter dem Einfluss von Temperaturgradienten untersucht mit dem Ergebnis, dass die Temperaturgradienten dem thermisch unterstützen, magnetischen Schalten der Nanodrähte entgegenwirken kann. Es zeigt sich somit, dass bei der Konstruktion von Bauteilen zur wärmeunterstützten Magnetaufzeichnung (HAMR) sorgfältig zwischen Temperaturgradienten und erhöhten Umgebungstemperaturen unterschieden werden muss.
$HfTe_5$ ist ein vielversprechendes Material für thermoelektrische Tieftemperaturanwendungen zwischen 150 K und 300 K und hat eine topologisch nicht-triviale Bandstruktur. In unseren Magneto-Transportmessungen an $HfTe_5$ konnten wir zum einen zeigen, dass zwischen 150 K und 300 K der thermoelektrische Power Faktor durch das Anlegen eines magnetischen Feldes um 40 % im Vergleich zum Nullfeldwert gesteigert werden kann. Zum Anderen wurde der magneto-thermoelektrische Transport für Temperaturen unter 100 K fast komplett unterdrückt. Mögliche Transportmechanismen für diese Beobachtung werden vorgestellt. In einem Bulk-Kristall des Weyl Halbmetalls NbP wurden in Magnetometrie-Messungen verschieden nicht-topologische Leitungsbänder sowie ein Weyl Band identifiziert. Der Nachweis von Weyl-Fermionen an der Fermi-Energie legt die Grundlage für unsere Transportstudien an NbP. In einer mikrostrukturierten NbP-Probe, konnten wir durch eine kleine Verschiebung des Fermi Niveaus die W2 Weyl Bänder an der Fermi-Energie separieren und den Zusammenbruch der chiralen Symmetrie in den W2 Weyl-Bändern in parallel-verlaufenden, magnetischen und elektrischen Feldern nachweisen. Schlussendlich haben wir die gemischte, axial-gravitative Anomalie, welches ein Zusammenbruch der chiralen Symmetrie in parallel-verlaufenden magnetischen Feldern und Temperaturgradienten ist, ebenfalls in einer mikrostrukturierten NbP Probe nachweisen können. Wir konnten somit ein Experiment aus der Hochenergiephysik realisieren, zu dem bisher kein experimenteller Zugang bestand.

List of Publications

This cumulative thesis is based on seven original publications [I]-[VII] and one overview article [VIII], summarizing the results from publication [VI] and [VII].

	original research paper
I	**Thermoelectric Power Factor Enhancement by Spin-Polarized Currents – A Nanowire Case Study**, Anna C. Niemann, Tim Böhnert, Ann-Kathrin Michel, Svenja Bäßler, Bernd Gotsmann, Katalin Neuróhr, Bence Tóth, László Péter, Imre Bakonyi, Victor Vega, Victor M. Prida, Johannes Gooth, and Kornelius Nielsch *Advanced Electronic Materials* **2**, 9 (2016)
II	**Magnetothermopower and magnetoresistance of single Co-Ni/Cu multilayered nanowires**, Tim Böhnert, Anna C. Niemann, Ann-Kathrin Michel, Svenja Bäßler, Johannes Gooth, Bence G. Tóth, Katalin Neuróhr, László Péter, Imre Bakonyi, Victor Vega, Victor M. Prida, and Kornelius Nielsch, *Physical Review B* **90**, 165416 (2014)
III	**Temperature gradient-induced magnetization reversal of single ferromagnetic nanowires**, Ann-Kathrin Michel, Anna C. Niemann, Tim Böhnert, Stephan Martens, Josep M Montero Moreno, Detlef Görlitz, Robert Zierold, Heiko Reith, Victor Vega, Victor M Prida, Andy Thomas, Johannes Gooth & Kornelius Nielsch, *Journal of Physics D: Applied Physics* **50**, 494007 (2017)
IV	**Magneto-thermoelectric characterization of a HfTe$_5$ micro-ribbon**, Anna Corinna Niemann, Johannes Gooth, Yan Sun, Felix Thiel, Andy Thomas, Chandra Shekhar, Vicky Süß, Claudia Felser, and Kornelius Nielsch, *Applied Physics Letters* **115**, 072109 (2019)
V	**Berry phase and band structure analysis of the Weyl semimetal NbP**, Philip Sergelius, Johannes Gooth, Svenja Bäßler, Robert Zierold, Christoph Wiegand, Anna C. Niemann, Heiko Reith, Chandra Shekhar, Claudia Felser, Binghai Yan & Kornelius Nielsch, *Scientific Reports* **6**, 33859 (2016)
VI	**Chiral magnetoresistance in the Weyl semimetal NbP**, Anna C. Niemann, Johannes Gooth, Shu-Chun Wu, Svenja Bäßler, Philip Sergelius, Ruben Hühne, Bernd Rellinghaus, Chandra Shekhar, Vicky Süß, Marcus Schmidt, Claudia Felser, Binghai Yan & Kornelius Nielsch, *Scientific Reports* **7**, 43394 (2017)
VII	**Experimental signatures of the mixed axial-gravitational anomaly in the Weyl semimetal NbP**, Johannes Gooth, Anna C. Niemann, Tobias Meng, Adolfo G. Grushin, Karl Landsteiner, Bernd Gotsmann, Fabian Menges, Marcus Schmidt, Chandra Shekhar, Vicky Süß, Ruben Hühne, Bernd Rellinghaus, Claudia Felser, Binghai Yan & Kornelius Nielsch, *Nature* **547**, 7663 (2017)
	overview paper
VIII	**Universum im Kristall**, Anna C. Niemann, Johannes Gooth, Claudia Felser & Kornelius Nielsch, *Physik in unserer Zeit* **49**, 4 (2018)

Author's Contributions

	original research paper
I	The author Anna Corinna Niemann fabricated and measured the multilayered nanowire microdevice. The author had a major part in analyzing the data. The author wrote the manuscript.
II	The author fabricated the nanodevices and performed the electric and thermoelectric measurements as well as the SEM study. The author had a major role in interpreting the data and made a minor contribution to the manuscript preparation.
III	The author contributed to the analysis of the data. The author wrote the manuscript.
IV	The author fabricated the micro-device and performed the electrical and thermoelectric transport measurements. The author had a major role in interpreting the data. The author wrote the manuscript.
V	The author assisted with the data evaluation and made a minor contribution to the preparation of the manuscript.
VI	The author drafted the micro-ribbon geometry, fabricated the microdevice and performed the electrical measurements. The author analyzed the transport data and wrote the manuscript together with Johannes Gooth, who contributed equally to this work.
VII	The author fabricated the microdevice and assisted in the transport measurements. The author assisted in interpreting the data and made a minor contribution to the manuscript preparation.
	overview paper
VIII	The author had a major part in writing the manuscript.

Abbreviations and Acronyms

AAO	anodized alumina oxide
AC	alternating current
ALD	atomic layer deposition
AMR	anisotropic magnetoresistance
ARPES	angle-resolved photoemission spectroscopy
DC	direct current
dHvA	de Haas-van Alphen
DSI	discrete scale invariance
EDS	energy dispersive X-ray spectroscopy
FIB	focused ion beam
GMR	giant magnetoresistance
HAADF	high-angle annular dark field
HAMR	heat-assisted magnetic recording
MOKE	magneto-optical Kerr microscope/microscopy
MR	magnetoresistance
NMR	negative magnetoresistance
SAED	selected area electron diffraction
SdH	Shubnikov-de Haas
SEM	scanning electron microscope/microscopy
SOC	spin-orbit coupling
TEM	transmission electron microscope/microscopy
TMR	tunneling magnetoresistance
VSM	vibrating sample magnetometer/magnetometry
XRD	X-ray diffraction

Contents

1 Introduction **1**

2 Theoretical Background **3**
- 2.1 Thermoelectricity 3
- 2.2 Ferromagnetic Materials 6
- 2.3 Spincaloritronic Transport 8
- 2.4 Topologically Insulators and Semimetals 13
- 2.5 Signatures of Dirac and Weyl Fermions in Transport and Magnetometry Experiments . 16

3 Experimental Methods **21**
- 3.1 Growth, Compositional and Structural Analysis 21
- 3.2 Definition of the Electrical Contact Structure 25
- 3.3 Measurement Techniques 26

4 Selected Results and Discussion **29**
- 4.1 Thermoelectric Characterization of Ferromagnetic Nanowires 30
  - 4.1.1 [I] Thermoelectric Power Factor Enhancement by Spin-Polarized Currents – A Nanowire Case Study 30
  - 4.1.2 [II] Magnetothermopower and Magnetoresistance of Single Co-Ni/Cu Multilayered Nanowires 32
  - 4.1.3 [III] Temperature Gradient-Induced Magnetization Reversal of Single Ferromagnetic Nanowires 34
- 4.2 Thermoelectric characterization of topologically protected materials 36
  - 4.2.1 [IV] Thermoelectric characterization of a $HfTe_5$ micro-ribbon 36
  - 4.2.2 [V] Berry Phase and Band Structure Analysis of the Weyl Semimetal NbP 39
  - 4.2.3 [VI] Chiral Magnetoresistance in the Weyl Semimetal NbP 41
  - 4.2.4 [VII] Experimental Signatures of the Mixed Axial-Gravitational Anomaly in the Weyl Semimetal NbP 43

5 Conclusion and Outlook **47**

Experimental Details **50**

Fundamental Constants **52**

Bibliography **53**

1 Introduction

Thermoelectricity presents a method for power generation by directly converting heat into electrical power without mechanically moving parts.[1] The most efficient, near-room temperature thermoelectric materials are nowadays Bi–Se–Te–Sb based.[2] Nevertheless, the efficiencies of these materials are still not sufficient to be competitive with other means of industrial power generation.[3] However, thermoelectric measurement techniques also evolved to be a versatile tool to explore the influence of a temperature gradient on the transport of different kinds of charge carriers in condensed matter systems.

For example, the research field of spincaloritronics,[4] dealing with the fundamental understanding of the interplay of charge, spin and heat currents, uses thermoelectric measurements as one of its main characterization methods. In spincaloritronics, the generation of pure spin currents due to a temperature gradient, the spin Seebeck effect[5,6] as well as spin-polarized currents due to a temperature gradient, the spin-dependent Seebeck effect,[7–9] are investigated. Due to the continuous down-scaling of micro-electronic and spintronic devices, spincaloritronic and especially thermoelectric effects have moved into the focus of current research. On the one hand, there are approaches to build nanostructured, thermoelectric energy converters with the aim to reuse the energy that is wasted by heat losses.[10] On the other hand, due to the miniaturization of electronic devices, Peltier heating can become dominant over Joule heating[11] and large temperature gradients can change currents in a device through the Thompson effect.[12] Another closely related technology, in which temperature hot spots are used to alter the local magnetization is the heat-assisted magnetic recording (HAMR) that is exploited to maximize memory capacities in magnetic memory devices.[13,14]

Furthermore, there is a close connection between the research area of thermoelectricity and the field of topological non-trivial materials, which is mainly given by the large pool of common, investigated materials. For highly efficient thermoelectric materials, a small band gap and a high spin orbit coupling caused by heavy elements are beneficial because they promote high thermoelectric power factors and a low thermal conductivity, respectively. A small band gap and high spin orbit coupling is also a precondition for the band inversion that is needed to form a topological insulator.[15–17] Therefore, topological insulators are quite often also good bulk thermoelectric materials and by the miniaturization of thermoelectric materials to the nanoscale, the topological character of these materials becomes observable in transport measurements.[15,18–20] With the realization of 3D-Dirac[21,22] and Weyl[23,24] fermions in topological semimetals, there is an opportunity to investigate a whole new class of relativistic bulk fermions in condensed matter systems. Thermoelectric measurements give the opportunity to observe the influence of temperature gradients on these relativistic charge carriers.[25]

The aim of this thesis is to contribute to the investigation of the influence of temperature gradients on different condensed matter systems, including magnetic materials as well as topological Dirac and Weyl systems. More specifically, the investigated materials are alloy and multilayered magnetic nanowires as well as micro-ribbons of the topological non-trivial material $HfTe_5$ and the Weyl semimetal NbP. These materials were mainly investigated by electrical and thermoelectric transport measurements but also magnetometry were utilized combined with a structural and compositional analysis of the materials.

In the field of spincaloritronics, we investigated the thermoelectric power output of magnetic CoNi alloy as well as CoNi/Cu multilayered nanowires and found that their thermoelectric power factor can compete with standard Bi–Se–Te–Sb thermoelectric materials. Furthermore, we showed that the thermoelectric power factor can be described in the framework of the two-current model for magnetoresistive systems. Utilizing magnetoresistance and magneto-thermopower measurements on CoNi/Cu multilayered nanowires, a simple model was developed to distinguish between the absolute thermopower of the magnetic nanowires and the electric leads. We thereby established a versatile tool to distinguish different thermopower contributions of a thermoelectric measurement circuit, with one ferromagnetic component, without relying on superconducting leads or the Thompson effect.[26,27] Finally, we investigated the influence of temperature gradients on the coercive fields of magnetic CoNi and FeNi alloy nanowires and showed that for magnetic materials with a high magneto-elastic anisotropy the temperature gradient counteracts the thermally-assisted switching process, so that a careful distinction between elevated base temperatures and temperature gradients has to be made in future HAMR devices.

In the field of topologically insulators and semimetals, we conducted magnetoresistance and magneto-thermopower measurements on $HfTe_5$, which hosts 2D/3D Dirac fermions.[28–30] For one, we found that the thermoelectric power factor of $HfTe_5$ can be enhanced by the application of a magnetic field for temperatures between 150 K and 300 K, which is the temperature range that is relevant for thermoelectric applications of $HfTe_5$.[31] Furthermore, we observe an almost complete suppression of the thermoelectric transport in $HfTe_5$ for temperatures below 100 K when a sufficiently strong magnetic field is applied. By comparing the magneto-thermoelectric measurements to the corresponding magnetoresistance measurement, we propose different transport mechanisms that might be responsible for the vanishing magneto-thermoelectric transport at low temperatures. Moreover, we investigated the band structure of the bulk and micro-sized Weyl semimetal NbP by de Haas-van Alphen and Shubnikov-de Haas measurements, respectively. For the bulk NbP sample, we identified several non-topological transport channels as well as one Weyl band and for the micro-sized NbP, we found that the Fermi-level is located sufficiently close to the Weyl points, for Weyl physics to be observed in transport experiments. Accordingly, we observed signatures of the chiral anomaly, which is the breakdown of the chiral symmetry[32] in one set of Weyl points in collinear magnetic and electric fields, in electric transport experiments. In thermoelectric measurements, we found signatures of the mixed axial-gravitational anomaly, this being the breakdown of the chiral symmetry in collinear magnetic fields and temperature gradients and we were able to draw a conclusion from our transport experiment in a condensed matter system on a current question of high-energy physics.

This thesis is organized as follows: In chapter 2, the theoretical background needed for the presented studies is introduced, including the basics of thermoelectricity, magnetic and topological materials and their transport characteristics. Chapter 3 gives an overview of the experimental methods, which include the sample growth, the compositional and structural analysis of the samples and the utilized measurement techniques. In chapter 4, the main results of the studies that constitute this cumulative thesis, including three publications about thermoelectric effects on magnetic nanostructures and four publications on topological materials. In chapter 5, a general conclusion and outlook is given.

2 Theoretical Background

In this thesis, transport phenomena in magnetic nanowires and topological micro-ribbons are investigated, with a focus on thermoelectric transport phenomena. Therefore, this chapter begins with a brief introduction of thermoelectricity. Subsequently, the investigated materials – ferromagnetic materials and topological materials – as well as relevant transport characteristics of these systems are introduced.

2.1 Thermoelectricity

Thermoelectric materials directly convert heat into electrical power.[33] The first observation of thermoelectricity was made by T. J. Seebeck in 1820, when he reported on a compass needle that was deflected when one junction of two dissimilar conductors in a closed circuit was heated.[34] While Seebeck believed to observe a thermo-magnetic effect, it was later revealed that the temperature difference ΔT caused an electric field that is proportional to ΔT – $E = S \cdot \Delta T$ – with the proportionality factor S being the Seebeck coefficient or thermopower. Within the closed circuit of Seebeck's experiment, E caused an electric current which then resulted in a magnetic field. In 1834, J. Peltier saw the reversed effect of Seebeck's observation, when he reported on an electric current j through two dissimilar conductors that caused a heat flux Q between the junctions, which can be described by $Q = \Pi \cdot j$, with the Peltier coefficient Π as the proportionality factor.[35] As a final fundamental effect Thomson (Lord Kelvin) described the reversible change of heat $\dot{Q}$ along a current carrying conductor in which a temperature gradient is also present.[36] The Thomson effect is given by $\dot{Q} = \frac{j}{\sigma} - \mu j \Delta T$, with the electrical conductivity σ and the Thomson coefficient μ. It was also Thomson who found the relation between the three thermoelectric coefficients S, Π and μ to be $\mu = T\frac{\mathrm{d}S}{\mathrm{d}T}$ and $\Pi = T \cdot S$, today known as the Thomson relations.[37]

A simple picture that captures the Seebeck effect is that the charge carriers on the hot side of a material have more thermal energy than the charge carriers on the cold side of the material. The system minimizes its energy by the diffusion of charge carriers from the hot side to the cold side of the sample. An electric field builds up and the resulting potential difference is referred to as the thermovoltage $U_{\mathrm{thermo}} = S \cdot \Delta T$. Note that S is an intrinsic material property and not caused by an interface effect. A positive/negative sign of S refers to holes/electrons that diffuse from the hot side to the cold side of a sample. Normally, electron conductors have a negative S and hole conductors possess a positive S. Nevertheless, some electron conductors have a positive S. This is the case if the enhanced temperature at one end of the sample leads to a strong reduction of the mean free path of the hot electrons. The electrons then diffuse on average from the cold side of the sample to the hot side of the sample and a positive S is measured.[1]

In general, one distinguishes between the diffusive thermopower, when charge carriers predominantly scatter on impurities and lattice defects and non-diffusive contributions to the thermopower, when other scattering mechanisms dominate. The diffusive part of the thermopower can be described by the Mott formula, as described in more detail in section 2.3. One example of a non-diffusive thermopower contribution is the so-called phonon drag thermopower, when at low T – commonly between 5 K and 50 K – and for sufficiently pure metals phonon-electron collisions are the dominant scattering process.[33,38,39] In these collisions, phonons transfer heat and momentum to the electrons and due to the Umklapp scattering the momentums of the electrons reverse and the electrons are predominantly dragged to the hot side of the sample. The diffusive thermopower $S_{\text{diffusive}}$ and the phonon-drag thermopower $S_{\text{p-e}}$ are independent and can be simply added up.[33] It is: $S = S_{\text{diffusive}} + S_{\text{p-e}}$.

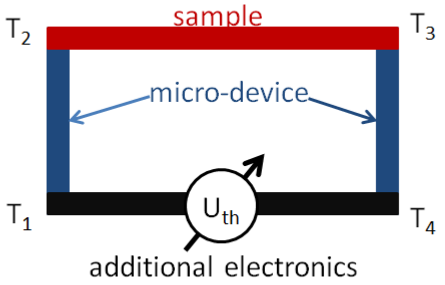

Figure 2.1: Thermoelectric measurement circuit, consisting of 3 different materials – the sample (red), the micro-device (blue), and additional electronics (black)– with different temperatures T_1 - T_4 at the interfaces.

The thermopower of a sample is always measured with respect to a contact material – the sample and the contact materials form a so-called thermocouple.[1] A schematic measurement setup is given in **Fig.2.1**, consisting of a sample along which a temperature gradient ($\Delta T = T_2 - T_3$) is applied one part of the electrical contacts (in this thesis the micro-device) that is also subject to ΔT and additional electronics that is kept at one temperature. In this measurement circuit, the different thermovoltages add up: $U_{\text{th}} = S_{\text{md}}(T_1 - T_2) + S_{\text{sample}}(T_2 - T_3) + S_{\text{md}}(T_3 - T_4) + S_{\text{ae}}(T_4 - T_1)$, with the thermopower of the micro-device, the sample, and the additional electronics S_{md}, S_{sample}, and S_{ae}, respectively. For $T_4 = T_1$, it directly follows:

$$U_{\text{thermo}} = (S_{\text{sample}} - S_{\text{md}}) \cdot \Delta T, \tag{2.1}$$

which shows that the measured U_{thermo} will always give S of the sample as well as the part of the contact material, which is subject to the temperature gradient. Normally Pt is chosen as a contact material. Absolute thermopower values Pt are known and were determined by using superconducting leads at low T and the Thomson effect at higher temperatures.[26,27] If it is not possible to have $T_1 = T_4$ within an experimental setup, normally an offset-voltage is measured while keeping $T_2 = T_3$, which can be subtracted after the actual thermopower measurement.

Thermoelectric devices are built from thermocouples that consist of one n-type and one p-type semiconductor leg, connected thermally in parallel but electrically in series, see **Fig.2.2**.[1,2] Within a thermoelectric generator, ΔT is used to run an electric current through an external load (**Fig.2.2 a**) and within a thermoelectric cooler (also called Peltier cooler), ΔT is generated by running an electrical current through the thermocouple. As a result, one side is cooled while at the other side heat is dissipated (**Fig. 2.2 b**).

The power generation efficiency of a thermoelectric device is given by:[1]

$$\eta = \frac{T_{\text{hot}} - T_{\text{cold}}}{T_{\text{cold}}} \cdot \frac{\sqrt{1 + Z\bar{T}} - 1}{\sqrt{1 + Z\bar{T}} + \frac{T_{\text{cold}}}{T_{\text{hot}}}} \quad \text{with} \quad Z\bar{T} = \frac{\sigma S^2}{\kappa_{\text{el}} + \kappa_{\text{el}}} \cdot \bar{T}. \tag{2.2}$$

$Z\bar{T}$ is the dimensionless, thermoelectric figure of merit, σ is the electrical conductivity, κ_{el} and κ_{ph} are the electronic and phonon part of the thermal conductivity, respectively, and $\bar{T} = \frac{T_{\text{hot}} - T_{\text{cold}}}{2}$ is the average temperature of the hot end and the cold end of the device, T_{hot} and T_{cold}. The thermoelectric power factor PF, given by $\text{PF} = \sigma \cdot S^2$, is a measure for the thermoelectric power output of a material. The highest energy conversion efficiency can be reached for $Z\bar{T} = \infty$, becoming equivalent with the Carnot efficiency. To reach a high $Z\bar{T}$ within a material, one needs a large S, a large σ and a low κ.[2] For metals and degenerated semiconductors, the relation between σ and S is given by $S \sim \sigma^{-\frac{2}{3}}$. Materials with a high σ normally have a low S and vice versa.[2] A relation between σ and κ_{el} is given by the Wiedemann-Franz law: $\kappa_{\text{el}} = L \cdot T \cdot \sigma$, with the Lorenz number L, showing that for a high σ also a high κ_{el} follows.[40,41]

In general, thermoelectric material optimization is complex and there are several quantities that can be optimized. Highly doped semiconductors with a carrier concentration between $10^{19}$and$10^{21}\,\frac{1}{cm^3}$ are considered to be good thermoelectric materials. Further, charge carrier mobilities and the effective mass have to be optimized for a thermoelectric material.[2] Often the expression "phonon glass-electron crystal" is used to describe to describe a new material engineering approach to design high-efficient thermoelectric materials with a high σ and a low κ_{ph}.[42] For near-room temperature applications, the Bi–Se–Te–Sb materials such as Bi_2Te_3 with a maximum $Z\bar{T}$ around 1 are used.[2] This corresponds to a heat conversion efficiency around 10 %, which is still far off from the power conversion efficiencies of conventional power generation between 30 % and 50 %.[3] Nevertheless, thermoelectricity is used for example in outer space missions, because no mechanically moving parts are needed for thermoelectric power generation, which makes for a very robust and long-living technology.[43] Furthermore, there is a recent trend to apply thermoelectricity to waste heat recovery.[44]

In the beginning of the 1990s, there was the idea to minimize thermoelectric materials for higher thermoelectric efficiency. On the one hand, researchers made use of the classical size effect, which describes a reduction of κ_{ph} due to an enhanced scattering on sample boundaries or grain boundaries when minimizing the sample geometry or introducing superlattices.[3] On the other hand, there is the quantum size effect, described by Hicks and Dresselhaus,[45,46] who discovered an enlarged thermoelectric PF for quantum wells and quantum wires with one or two sample dimensions a smaller than the de Broglie wave length λ_{dB} ($a < \lambda_{\mathrm{dB}}$), respectively. They predicted an increased PF due to a change in the energy-dependence of the density of states for reduced dimensions. Nevertheless, numerous transport experiments on thermoelectric nanowires could not observe the predicted increase in PF, which was later explained by the topological nature of many thermoelectric materials like Bi_2Te_3. In topological insulator materials with a high surface-to-volume ratio, the highly conductive surface channel forms a parallel circuit with the (thermoelectric) bulk channel and has a measurable impact on the transport properties, which significantly decreases the thermoelectric performance of the sample.[47] Although the anticipated enhancement of the thermoelectric efficiency could not be achieved by minimizing thermoelectric materials, much of what was learned in transport experiments on low-dimensional thermoelectric materials turned out to be useful in the newly-established research field of topological insulators.[15]

Thermoelectric measurements are nowadays employed in other material systems as well. For example, in the research field of spincaloritronics,[4] in which the correlation between electrical current, spin and heat transport is investigated, thermoelectric measurements are applied to magnetic and magnetoresistive materials to observe the influence of a temperature gradient on these systems. Here, one distinguishes between the spin-dependent Seebeck coefficient[7–9] – or: spin-dependent thermopower – that describes the flow of a electrical current due to a temperature gradient in a spin-polarized system, and the spin-Seebeck effect[5,6] that deals with the flow of a pure spin current (without a charge current) due to a thermal gradient.

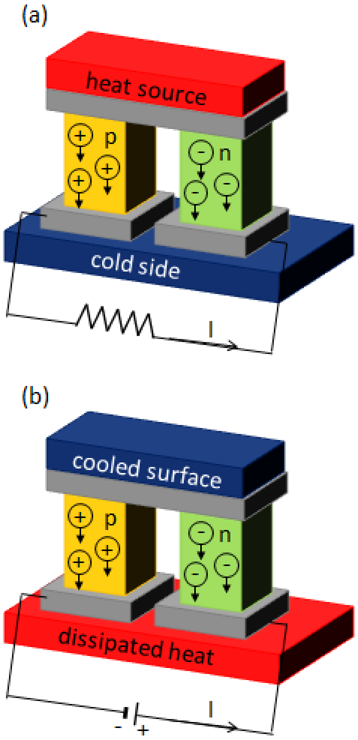

Figure 2.2: Thermoelectric devices can be divided into (a) thermoelectric generators, in which a temperature gradient is used to generate an electrical current and (b) thermoelectric coolers, in which an electrical current is used to generate a temperature difference and therefore cool one side of the device.

2.2 Ferromagnetic Materials

The first part of this cumulative thesis deals with the investigation of ferromagnetic nanowires. In this section, first the Stoner model of band magnetism is introduced, which is needed to understand the occurrence of negative magnetoresistance in the ferromagnetic systems being investigated in Ref. [I] and Ref. [II]. Further, different magnetic anisotropies are presented, which are studied on magnetic CoNi and FeNi nanowires in Ref. [III]. Finally, the magnetic hysteresis is shortly introduced, in order to interpret the hysteresis curves obtained in the magneto-optical Kerr measurements in Ref. [III]. Signatures of a magnetic hysteresis can be also seen in the magnetoresistance and magneto-thermopower measurements in Ref. [I] and Ref. [II].

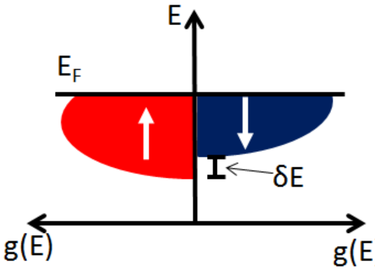

Figure 2.3: For ferromagnetic materials below the Curie temperature, the density of states shows a spontaneous spin splitting of the energy bands without the application of an external magnetic field.

Ferromagnetic materials are characterized by a spontaneous magnetization even in the absence of an external magnetic field. This spontaneous magnetization $\vec{M}$ evolves due to the parallel alignment of individual magnetic moments of the free electron gas in a ferromagnetic material. Given that there is a certain number of majority (↑) and minority (↓) electrons, $n_\uparrow$ and $n_\downarrow$respectively, $\vec{M}$ is given by $\vec{M} = \mu_B(n_\uparrow - n_\downarrow)$, with the Bohr magneton μ_B. An explanation of the occurrence of a ferromagnetic order is given by the Stoner model of band magnetism[48, 49] that is based on the spontaneous spin splitting of the population of the majority and minority spin bands that causes a reduction of the total energy of the system. The amount of electrons that is shifted in the process of the band splitting from the minority band to the majority is given by $g(E_F)(\delta E)/2$, with the density of states g and the energy difference δE, compare **Fig. 2.3**. The total amount of gained, kinetic energy is given by $\Delta E_{\text{kin}} = g(E_F)(\delta E)^2/2$. Simultaneously, there is a decrease of the potential energy ΔE_{pot} because for an unequal population of the majority band and the minority band, the mean free distance between two electrons increases due to the Pauli principle. The decrease of ΔE_{pot} is given by $\Delta E_{\text{pot}} = -\frac{1}{2}U(g(E_F)\delta E)^2$, while U is a constant from the exchange interaction and gives a measure for the Coulomb interaction. The total energy E_{tot} of the system is then given by:

$$E_{\text{tot}} = \Delta E_{\text{kin}} + \Delta E_{\text{pot}} = -\frac{1}{2}g(E_F)(\delta E)^2(1 - U \cdot g(E_F)) \tag{2.3}$$

A spontaneous magnetization occurs when the total energy can be minimized:

$$E_{\text{tot}} < 0 \Longleftrightarrow 1 < U \cdot g(E_F) \tag{2.4}$$

Eq. 2.4 is called the Stoner criterium for a ferromagnetic order and is fulfilled for the elements Fe, Co and Ni.

The total energy E of a ferromagnetic material can be divided into different contributions $E = E_{\text{ex}} + E_{\text{Zee}} + E_{\text{shape}} + E_{\text{mc}} + E_{\text{me}}$, with the exchange energy E_{ex}, the Zeeman energy E_{Zee} and energy contributions that can arise from magnetic anisotropies, namely from the shape anisotropy E_{shape}, from the magneto-crystalline anisotropy E_{mc} and from the magneto-elastic anisotropy E_{me}.[48, 49]
In the Heisenberg model, the exchange energy between two atoms i and j with the spins S_i and S_j, respectively, is given by:

$$E_{\text{ex}} = -\sum_{i,j} J_{i,j}\vec{S}_i\vec{S}_j. \tag{2.5}$$

The exchange integral $J_{\mathrm{i,j}}$ describes the overlap of the charge distribution of the two atoms i and j and has a quantum mechanical origin. For positive $J_{\mathrm{i,j}}$, there is a parallel spin alignment and E_{ex} is minimized. A ferromagnetic spin order occurs.

A Zeeman interaction occurs in a ferromagnetic material that is placed into an external magnetic field. In a homogenous magnetic field $\vec{H}_{\mathrm{ex}}$, the Zeeman energy is given by:

$$E_{\mathrm{Zee}} = -\vec{M} \cdot \vec{H}_{\mathrm{ex}}. \tag{2.6}$$

E_{Zee} is minimized when $\vec{M}$ is aligned parallel to $\vec{H}_{\mathrm{ex}}$.

For the orientation of the magnetization in a ferromagnetic material, certain directions can be preferred over others. These axes are called easy and hard axes, respectively. Different magnetic anisotropies give rise to the occurrence of easy and hard axes in a ferromagnetic materials.

The magneto-crystalline anisotropy is caused by an anisotropic overlap of the charge distributions of neighboring atoms, which is dependent on the crystal axes and can be caused by lattice constants that differ for different crystal axes and atomic charge distributions that are not spherical due to spin orbit coupling. As a result of this anisotropic overlap of the charge distributions, the exchange energy contribution depends on the crystal axis.[50] The magneto-crystalline anisotropy is given as a function of the angle Φ between the magnetization and and a specific crystal axis, and additionally depends on the anisotropy constants (K_1, K_2, ...) with respect to the crystal axis. For example, the magneto-crystalline anisotropy energy of Co is given by:

$$E_{\mathrm{mc}} = K_1 \sin^2(\Phi) + K_2 \sin^4(\Phi) + \mathcal{O}(\sin^6(\Phi)) \tag{2.7}$$

Even though the magneto-crystalline anisotropy is a result of the crystal structure of ferromagnetic materials, this anisotropy is also measurable in poly- and nano-crystalline samples.[51] For Co, Ni and Co-Ni alloys, the magneto-crystalline anisotropy constant[52,53] varies between $2\,\mathrm{kJm^{-3}}$ and $5\,\mathrm{kJm^{-3}}$ and the magneto-crystalline anisotropy constant[54] of $\mathrm{Fe_{15}Ni_{85}}$ is $7.5\,\mathrm{kJm^{-3}}$.

The shape anisotropy results from the stray field outside of a magnetic sample and is small for small stray fields. The demagnetization energy E_{d}, which is equivalent to the stray field energy, is given by:

$$E_{\mathrm{d}} = -\frac{1}{2}\vec{M}\vec{H}_{\mathrm{d}}, \tag{2.8}$$

with the demagnetization field H_{d}. For ferromagnetic samples with high aspect ratios, like ferromagnetic nanowires, the stray field becomes dominant and the magnetization aligns with the longest axis of the sample. For nanowires that are approximated as an infinite long wire, the shape anisotropy constant can be calculated as:[55]

$$K_{\mathrm{shape}} = \frac{1}{4}\mu_0 M_{\mathrm{S}}^2, \tag{2.9}$$

with the vacuum permeability μ_0 and the saturation magnetization M_{S}.

The magneto-elastic anisotropy describes the effect of stress on the magneto-crystalline anisotropy. The corresponding energy E_{me} is given by:[56]

$$E_{\mathrm{me}} = \frac{3}{2}\lambda_{\mathrm{m}}\sigma cos^2(\Phi), \tag{2.10}$$

with the magnetostriction coefficient λ_{m}, the axial stress σ and the angle Φ between the magnetization and the stress direction. The elastic and magnetic properties of ferromagnetic materials are connected by the effect of magnetostriction,[57] which describes the change in the magnetization when mechanical stress is applied and vice versa. Mechanical stress can be induced in a ferromagnetic system by applying a temperature gradient among other sources. In this case, σ is given by:[58] $\sigma = \alpha_{\mathrm{Co/Ni/Fe}} Y \Delta T$, with the thermal expansion coefficient α, the Young's modulus Y and the temperature gradient ΔT.

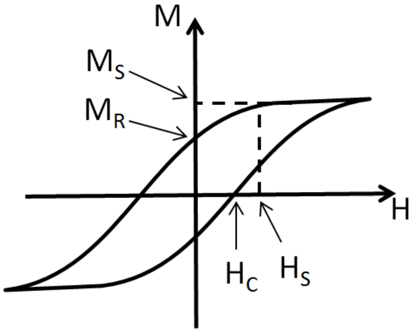

Figure 2.4: Sketch of the hysteresis curve of a ferromagnetic material, showing the magnetization M as a function of the external magnetic field H. The saturation magnetization M_S, the remanence magnetization M_R, the coercive field H_C and the saturation field H_S are indicated.

The formation of magnetic domains is one process to minimize the total magnetic energy of a ferromagnetic material. Inside a magnetic domain, the magnetic moments are homogeneously aligned in one direction. The regions between magnetic domains, which have an inhomogeneous magnetization distribution, are called domain walls.

Magnetic hysteresis curves show M of a ferromagnetic material as a function of the applied magnetic field H and give information how M is influenced by the magnetic history of the sample.[48,49] In order to have a defined magnetization alignment within the sample, the saturation field H_s is applied for measuring maximum hysteresis loops. The saturation magnetization M_S is reached when all magnetic moments are aligned along H. Upon approaching a magnetic field of zero, ferromagnetic samples retain a remanence magnetization M_r. The applied magnetic field necessary to achieve a magnetization of zero within the sample is called coercive field H_c.

2.3 Spincaloritronic Transport

In the first part of this thesis (Ref. [I] –[III]), magnetic nanowires exhibiting giant magnetoresistance and anisotropic magnetoresistance are investigated. By performing thermoelectric measurements on these nanowires, we added a spincaloritronic component to our studies. In this section, magnetoresistive effects of ferromagnetic systems, the relation between thermopower and the resistivity as well as the magnetic field-dependence of the thermopower of ferromagnetic materials are introduced.

Magnetoresistance

The magnetoresistance MR[48] is defined as the change of the resistance of a material when a magnetic field is applied:

$$\mathrm{MR} = \frac{R(H) - R(0)}{R(0)}, \tag{2.11}$$

with the resistance $R(0)$ in the absence of an applied magnetic field and the resistance $R(H)$ within an applied magnetic field. In general, one distinguishes between the longitudinal MR, when the magnetic field is applied parallel to the current direction, and the transversal MR, when the magnetic field is applied perpendicular to the current direction.

All electrically conducting materials possess a so-called ordinary or positive MR that is proportional the H^2. This positive MR is caused by the Lorentz force, which forces the charge carriers onto spiral trajectories when a magnetic field is applied. Therefore, the mean free path between two scattering events is reduced and the resistance increases for increasing magnetic fields.

In ferromagnetic materials below the Curie temperature T_C, the positive MR is normally superimposed with a much stronger negative MR caused by the magnetization M of the material. The negative MR therefore depends only implicitly on the applied magnetic field. The negative MR is proportional to $-H^2$ as long as there is a non-vanishing angle between M and H, and reaches a saturation value as soon as M is fully aligned to H.

The negative MR[48] can be explained within the framework of the Stoner band model. Ferromagnetic materials have an s-band with a low density of states (DOS) at the Fermi energy E_F and a low DOS at E_F. Below T_C, there is a band splitting of the d-bands: The majority spin state (↑) is more populated that the minority spin state (↓), as shown in **Fig. 2.5**. In general, the electric current is carried by the s-electrons due to their low effective mass. For a non-vanishing spin orbit coupling (SOC), s-d scattering is allowed. S-electrons that scatter into empty d-states can no longer contribute to the electric current and a higher resistivity is measured. As the exchange splitting between majority and minority electrons increases, the DOS of the d-bands at E_F decreases. There is less s-d scattering and therefore an increasing conductance/decreasing resistance.

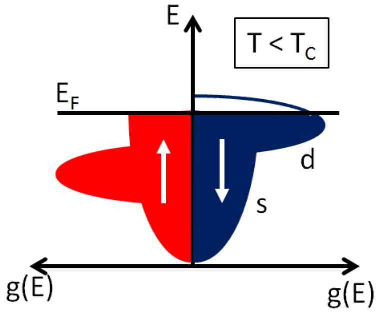

Figure 2.5: The Stoner band model for a ferromagnetic material below the Curie temperature T_C shows a splitting of the majority (↑) and minority (↓) d-bands, resulting a different density of states $g(E)$ for ↑ and ↓ electrons at the Fermi energy E_F.

A rather descriptive picture of the negative MR is given by Mott's two-current model,[48,59–61] that shows the two different spin channels in a parallel circuit, see **Fig. 2.6**. The total resistance of the ferromagnetic system is than given by:

$$R_\mathrm{total} = \frac{R_\downarrow \cdot R_\uparrow}{R_\downarrow + R_\uparrow}, \tag{2.12}$$

Two kinds of negative MR, namely the anisotropic MR and the giant MR are relevant for this thesis and will be discussed in more detail.

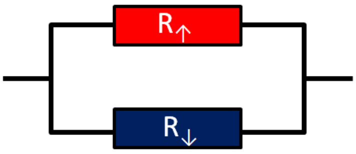

Figure 2.6: In Mott's two current model the majority and minority spins, ↑ and ↓, form a parallel circuit.

The **anisotropic MR (AMR)** is defined as the change of resistivity of a ferromagnetic material or a material system having ferromagnetic compounds depending on the angle between the electrical current and the magnetization.[48,62] Due to the orbital anisotropy of the empty d-states, the scattering cross section of the s-d scattering depends on the angle between the magnetization and the electrical current. Therefore, the resistivity is also angle-dependent, and can be expressed as:

$$\rho(\alpha) = \rho_0 (1 + \frac{\rho_\mathrm{sd}}{\rho_0} \cdot \cos^2(\alpha)), \tag{2.13}$$

with the angle α between the magnetization and the electrical current, the resistivity ρ_0 without an applied magnetic field, and the resistivity ρ_sd due to the s-d scattering. In ferromagnetic bulk materials, the magnetization of the different domains is assumed to be randomly distributed in zero magnetic field and the resistivity ρ_0 is given as:

$$\rho_0 = \frac{1}{3}\rho_\| + \frac{2}{3}\rho_\perp, \tag{2.14}$$

with the longitudinal resistivity $\rho_\|$ and the transverse resistivity $\rho_\perp$. This expression can be easily understood when considering $M \| H$ along one spatial direction and $M \perp H$ along the other two spatial directions. In bulk materials, the AMR is commonly defined as:

$$\mathrm{AMR_{bulk}} = \frac{\rho_\| - \rho_\perp}{\rho_0}, \tag{2.15}$$

In contrast to bulk materials, ferromagnetic nanowires normally have a strong shape anisotropy, which aligns the magnetization of the nanowire parallel to the nanowire axis. Therefore $\rho_0 \approx \rho_{\|}$ and the AMR can be expressed as:

$$\mathrm{AMR}_{\mathrm{nw}} = \frac{\rho_{\|} - \rho_{\perp}}{\rho_0} \approx \frac{\rho_{\|} - \rho_{\perp}}{\rho_{\|}} \approx \frac{\rho_0 - \rho_{\perp}}{\rho_0}, \tag{2.16}$$

Moreover, the AMR of ferromagnetic nanowires with M fully aligned along the nanowires axis in zero magnetic field can be distinguished from bulk AMR by showing a sharp resistivity jump when M is reversed due to an applied magnetic field, compare for example Ref. [III] Fig. 2. The AMR effect size is on the order of a few percent in bulk as well as in nanostructured materials.

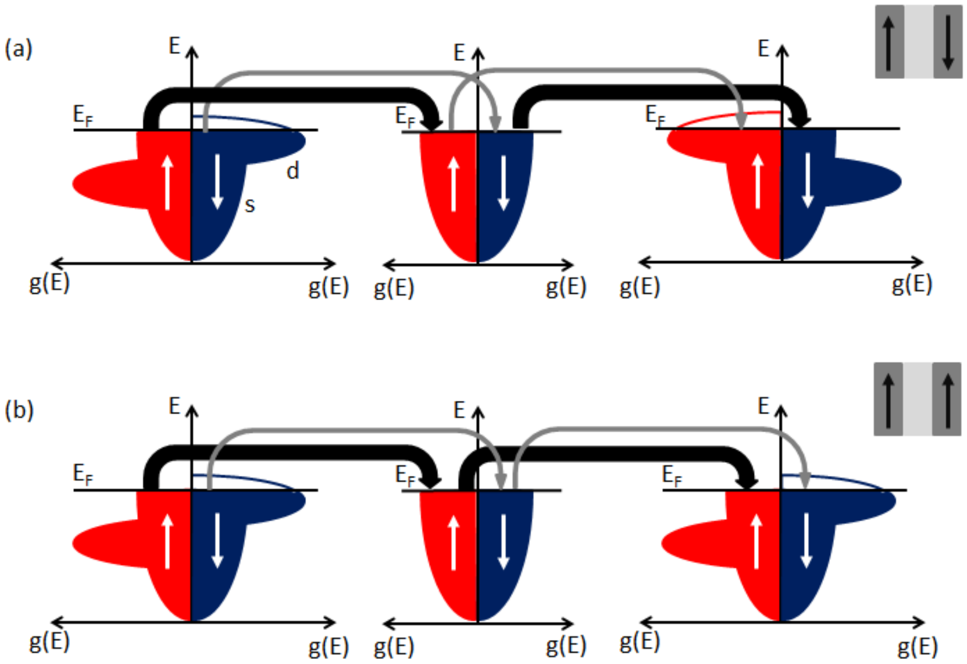

Figure 2.7: The Stoner band model for two ferromagnetic layers that are separated by a non-magnetic spacer layer for (a) an antiparallel magnetization alignment and (b) a parallel magnetization alignment. The bold and thin arrows indicate a high conductance and low conductance within a spin channel, respectively.

Another negative MR effect is the **giant MR (GMR)**, which occurs in layered systems, in which at least two magnetic layers are separated by one non-magnetic metal or antiferromagnetic layer. In these systems, the GMR is defined as:

$$\mathrm{MR} = \frac{R(B) - R(0)}{R(0)}, \tag{2.17}$$

and was first observed by Baibich *et al.*[63] and Binasch *et al.*[64] on Fe/Cr multilayers and Fe/Cr/Fe trilayers, respectively. The GMR effect size[65,66] can be on the order of 100 % and is therefore much larger than the AMR effect. In layered systems that show a GMR effect, there is a general distinction between the electrical current in plane (CIP) and the current perpendicular to plane (CPP) geometry. In this thesis, the CPP geometry is used.

Without an applied magnetic field, the magnetizations of neighboring magnetic segments are aligned antiparallel due to the dipole interaction. To achieve maximum GMR effect sizes, a complete antiparallel alignment of M of neighboring magnetic layers is crucial. Therefore, sputtered samples with smooth and parallel aligned surfaces have higher GMR effect sizes than for example electrodeposited samples, which nevertheless can reach GMR effect sizes up to 35 %.[67] In sputtered thin films with very smooth layers, an interlayer exchange coupling (RKKY- interaction)[68] that shows an oscillating coupling strength depending on the interlayer thickness is observed. Nevertheless, this effect has never been observed in electrodeposited material systems, likely due to the higher surface roughness of the single layers. Within the magnetic saturation field, the magnetizations of all magnetic layers are aligned in parallel. **Fig 3.1** shows the density of states for two magnetic layers and a non-magnetic spacer layer for **(a)** the antiparallel alignment of the magnetizations and **(b)** for the parallel alignment of the magnetizations. As described above, a spin channel has a high conductance (low resistance) if there is only little s-d scattering due to a small DOS of the d-band at E_F. Contrarily, there is a low conductance (high resistance) if there is a large s-d scattering cross section at E_F. In Mott's two current model (**Fig 2.8**), the resistance from the two parallel spin channels can be summarized as follows. For an antiparallel of the magnetizations of the two magnetic layers, there is a total resistance of :

$$R_\mathrm{ap} = \frac{R_{\uparrow\uparrow} + R_{\uparrow\downarrow}}{2}, \tag{2.18}$$

and for a parallel magnetization alignment, there is a total resistance of:

$$R_\mathrm{p} = 2\frac{R_{\uparrow\uparrow} \cdot R_{\uparrow\downarrow}}{R_{\uparrow\uparrow} + R_{\uparrow\downarrow}}, \tag{2.19}$$

where $R_{\uparrow\uparrow}$ and $R_{\uparrow\downarrow}$ give the parallel and antiparallel alignment of the spin to the magnetization, respectively. From **Fig. 2.7** it can be directly seen that $R_{\uparrow\uparrow} < R_{\uparrow\downarrow}$ and from eq. 2.18 and eq. 2.19 $R_\mathrm{ap} > R_\mathrm{p}$ directly follows, which is equivalent to a negative MR in these layered systems.

To maximize the GMR effect, magnetic materials with a high spin-polarization are normally chosen. Common spin-polarizations are for example 40 % for Fe[69] and 44 % measured in Ni-nanowires.[70] A second approach maximizing the GMR effect is to aim for a large spin diffusion length in the normal metal spacer layer. The spin-diffusion length gives the length scale over which the spin polarization is kept in a paramagnetic metal layer. It decays exponentially in a normal metal.[71] In Cu, the spin-diffusion length can be up to 400 nm at room temperature.[71]

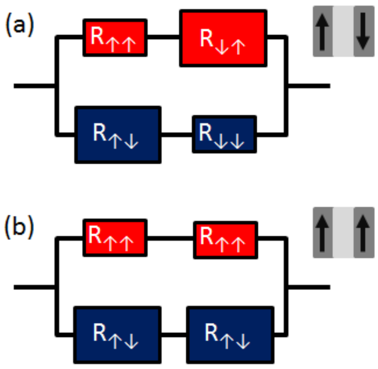

Figure 2.8: Mott's two current model for two ferromagnetic layers separated by a non-magnetic layer for (a) a antiparallel magnetization alignment and (b) a parallel magnetization alignment. The index of the resistance R is given as $R_\mathrm{M,\ spin}$.

The final type of magnetoresistance that is relevant for the ferromagnetic nanostructures investigated in this thesis is the **magnon-induced MR (MMR)**, which occurs when conduction electrons are scattered on magnons.[72] This effect can occur even within the magnetic saturation field. For decaying temperatures as well as increasing magnetic fields, the magnons are less exited and finally start to freeze out. The electron-magnon scattering decreases and the conductivity increases. Accordingly, for the MMR, the resistivity is proportional to $-|H|$.

Mott Relation

The Mott formula describes the relation between the thermopower S and the resistivity ρ within the free electron model and is given by:[73]

$$S = -\frac{\pi^2}{3}\frac{k_\mathrm{B}^2 T}{q}\frac{1}{\rho}\left(\frac{d\rho(E)}{dE}\right)_{E=E_\mathrm{F}}, \tag{2.20}$$

with the carrier charge q and the energy of the charge carriers E. The Mott relation is a first-order approximation of the Boltzmann transport equation in $k_\mathrm{B}T/E_\mathrm{F}$. Deviations are expected for high temperatures from approx. 1000 K on.[73] The Mott formula describes only the diffusive part of the thermopower with predominat scattering of the charge carriers on impurities, grain boundaries and lattice defects. Non-diffusive parts of the thermopower like the phonon-drag[38,39] are not covered by the Mott relation.

The resistivity as well as the thermopower depend on an externally applied magnetic field. A linear relation $S(\rho(H)) \sim \frac{1}{\rho(H)}$ is commonly observed in magnetoresistive material systems like magnetic-non-magnetic multilayers, spin valves and granular alloys.[7,8,74–82] Inserting this linear relation into eq. 2.20 shows that $\left(\frac{d\rho(E)}{dE}\right)_{E_\mathrm{F}}$ is independent of the applied magnetic field. It follows:

$$S(H) = -\frac{\pi^2}{3}\frac{k_\mathrm{B}^2 T}{q}\frac{1}{\rho(H)}\left(\frac{d\rho(E)}{dE}\right)_{E=E_\mathrm{F}}. \tag{2.21}$$

Magneto-Thermopower

The thermopower S – like the resistivity – of a ferromagnetic material depends on the external magnetic field as given in eq. 2.21. The change of S within an applied magnetic field can be quantized by the magneto-thermoelectric power (MTEP):

$$\mathrm{MTEP} = \frac{S(H) - S(0)}{S(H)}, \tag{2.22}$$

with S being the measured thermopower $S = S^\mathrm{abs}_\mathrm{sample} + S^\mathrm{abs}_\mathrm{contact}$. Inserting this relation into eq. 2.22 one can derive:

$$\mathrm{MTEP} = \frac{S^\mathrm{abs}_\mathrm{sample}(H) - S^\mathrm{abs}_\mathrm{sample}(0)}{S^\mathrm{abs}_\mathrm{sample}(0) + S^\mathrm{abs}_\mathrm{contact}(0)}. \tag{2.23}$$

In contrast to the MR – given the MR was measured in a four-point geometry – the MTEP does not only describe the sample properties but the sample and the contact material. S^abs is available for common electrical contact materials,[26,27] like Pt, Au, and Cu but these values are sensitive to size effects[39,83] and impurities.[84] Also, the MTEP can reach infinite values for $S^\mathrm{abs}_\mathrm{sample} \approx -S^\mathrm{abs}_\mathrm{contact}$. A more precise but also harder to obtain in an experiment definition of the magneto-thermopower was given by Gravier *et al.*[75] as:

$$\mathrm{MTP} = \frac{S^\mathrm{abs}_\mathrm{sample}(H) - S^\mathrm{abs}_\mathrm{sample}(0)}{S^\mathrm{abs}_\mathrm{sample}(0)} = \frac{S(H) - S(0)}{S(H) - S^\mathrm{abs}_\mathrm{contact}(0)}. \tag{2.24}$$

The change of the thermopower within an applied magnetic field can be illustrated in an analogous picture to Mott's two current model with the minority and majority spin carriers in a parallel circuit. In such a parallel circuit, the thermopower is given by:[85,86]

$$S_\mathrm{total} = \frac{\sigma_\uparrow S_\uparrow + \sigma_\downarrow S_\downarrow}{\sigma_\uparrow + \sigma_\downarrow}, \tag{2.25}$$

with the conductivity/thermopower of the majority spin channel $\sigma_\uparrow/S_\uparrow$ and the minority spin channel $\sigma_\downarrow/S_\downarrow$, respectively.

2.4 Topologically Insulators and Semimetals

Recently, topological insulators and semimetals have attracted great attention in the condensed matter research community. In this thesis, the topologically non-trivial materials $HfTe_5$ and NbP are investigated. Different studies see $HfTe_5$ either at the phase transition between a weak and a strong topological insulator[28,29] or as a 3D Dirac semimetal.[30] In contrast, NbP is a Weyl semimetal.[87,88] In this section, the basic principles of 3D topological insulators and Dirac and Weyl semimetals are introduced.

Topological Insulators

3D topological insulators are a new state of quantum matter in which the 2D topological surface band structure has different properties compared to the bulk band structure.[16,89] This leads to different transport properties of the bulk and the surface channels of topological insulator samples. More specifically, the bulk channel represents a small-gap semiconductor, while the band structure of the surface channel is characterized by a gapless, linear band structure, the so-called Dirac cone, as sketched in **Fig. 2.9**.

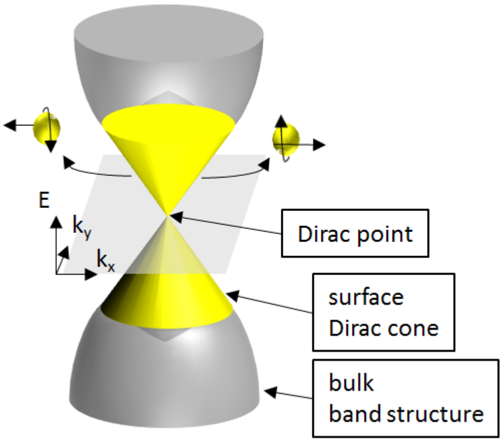

Figure 2.9: The band structure of topological insulators is given by parabolic bulk bands with an band inversion and a linear surface band structure that forms a 2D Dirac cone hosting spin-momentum locked fermions.

The gapless surface states occur in materials that have a small band gap in the bulk band structure combined with a strong SOC.[16] These materials exhibit a band inversion in their bulk band structure. On the surface of the topological insulator, a continuous transition of the inverted bulk conduction and valence band of the topological insulator to the conduction and valence band of the surrounding matter is required.[89] If the surrounding material is non-topological (e.g. vacuum) the linear, gapless surface states occur. This gapless and linear band structure – the Dirac-cone – of the surface states can be described by the the relativistic Dirac equation. Fermions that are hosted by the Dirac cone – the Dirac fermions – are massless because $m_{\text{eff}} \sim \delta^2 E/\delta k^2$.[40] Due to the strong SOC, the spin of the Dirac fermions is locked to the momentum vector at a right angle, which is referred to as protection by time-reversal symmetry.[90] This protection by time-reversal symmetry results in a suppressed back-scattering of the Dirac fermions because in this case a spin-flip would also be required. In conclusion, a topological insulator can be described by a semiconductor bulk band structure and surface states that host massless Dirac fermions that form a spin-polarized current with a high mobility that is protected from back-scattering by time-reversal symmetry.

In recent years, a number of materials has been identified as 3D topological insulators, among them $Bi_{1-x}Sb_x$, Sb_2Te_3, Bi_2Te_3, Bi_2Se_3, and $(Bi_{1-x}Sb_x)_2Te_3$.[16,17,91] It becomes apparent that there is a broad overlap between topological insulator materials and highly efficient bulk thermoelectric materials. While topological insulator materials have a small band gap and high SOC, due to heavy elements, high-efficient thermoelectric materials need the same preconditions to exhibit a high thermoelectric

power factor and a low thermal conductivity, respectively.[15]
3D topological insulators were first predicted by Teo *et al.*[91] and realized and observed in ARPES measurements by Hsieh *et al.*[92] in 2008. In ARPES measurements, the surface and bulk band structure can be directly mapped.[93] Therefore, ARPES can be used as measurement technique to directly identify topological insulators by resolving the Dirac cone of the surface band structure and the gapped bulk band structure. Furthermore, spin-resolved ARPES allows for measuring the spin-distribution of the Fermi surface.[89] Thereby, one can estimate the Berry phase which is a geometric phase that arises when the electron wave function travels a closed trajectory in momentum space. The spin of the surface Dirac electrons of a 3D topological insulator rotates by 2π when the Dirac fermions move around the Dirac cone. The Dirac fermions pick up an additional phase of π, which is referred to as the π-Berry phase.[89]
A second important investigation method for 3D topological insulators are electrical transport measurements, which can only give indirect evidence of the topological surface states. To observe the signatures of topological surface states in the electrical transport, such as for example quantum oscillations or weak antilocalization, a thin film or nanowire geometry is required because a high surface to volume ratio is needed to measure transport contributions from the surface conduction channel.[18–20, 94]

Dirac Semimetals

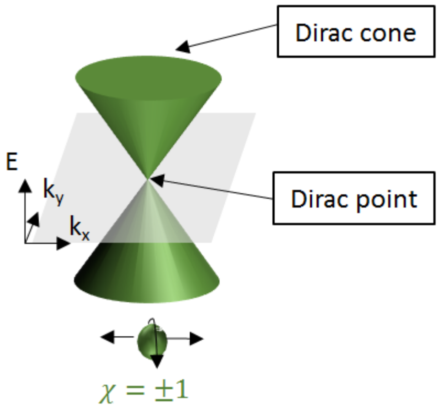

Figure 2.10: The band structure of 3D Dirac semimetals characterized by the Dirac cone that is formed by linear valence and conduction bands that touch near the Fermi energy and are degenerate with respect to the chirality.

Unlike topological insulators, 3D Dirac semimetals host relativistic and massless fermions not only in two, but in all three dimensions. Therefore, the bulk band structure of 3D Dirac semimetals consists of a Dirac cone with linearly dispersing bands along all three momentum axes hosting relativistic and massless Dirac fermions, as shown in **Fig. 2.10**.[95] Each state on the Dirac cone can host up to two Dirac fermions of different chirality ($\chi = \pm 1$), which gives the fermion spin direction relative to its linear momentum.[95] Interestingly, Dirac semimetals are named after Paul Dirac, who solved the Schrödinger equation for relativistic fermions and not after Herman Weyl who found a solution of the Schrödinger equation for relativistic and massless fermions, which might at first glace be a more fitting description. The chosen naming of Dirac semimetals gives tribute to the fact that the Weyl equation falls into two decoupled equations for the two different chiralities,[96] which does not find any representation in the band structure of Dirac semimetals but which is represented by the two separated Weyl cones in momentum space in Weyl semimetals, as introduced in the next section.
For 3D Dirac semimetals, materials on the phase boundary between normal insulators and topological insulators are considered,[95] in which inversion symmetry as well as time reversal symmetry is kept.[21]
3D Dirac fermions as quasi-particles in solid state physics were first predicted by Young *et al.*[21] in 2012 and first observed by Borisenko *et al.*[22] in Cd_3As_2 in 2014 via the imaging of a bulk Dirac cone in ARPES experiments. $NaBi_3$ is another well investigated 3D Dirac semimetal but also other material like $ZrTe_5$ and $HfTe_5$ are considered to host 3D Dirac fermions.[30, 97, 98]
In the presence of an external magnetic field, the Dirac cone of a 3D Dirac semimetal splits into two Weyl cones,[97] which are discussed in more detail in the next section. Therefore, 3D Dirac semimetals posed the first opportunity since their realization in 2014 to investigate so-called Weyl physics such as transport effects related to topological surface Fermi arcs[99] or quantum anomalies,[32] which are

discussed in more detail in the next sections.

Weyl Semimetals

Weyl semimetals are a newly realized quantum matter, in which massless and relativistic fermions – Weyl fermions – exist in the bulk band structure.[95] The band structure of Weyl semimetals consists of pairs of so-called Weyl cones that host the Weyl fermions and are spatially separated in momentum space, as depicted in **Fig. 2.11**. For the Weyl fermions, the chirality is given by the spin direction relative to its linear momentum. They are left-handed Weyl fermions when the spin is aligned antiparallel to the linear momentum and right-handed Weyl fermions when the fermion spin is aligned parallel to the linear momentum. One of the Weyl cones is populated by left-handed fermions while the other Weyl cone is exclusively populated by right-handed fermions, compare **Fig. 2.11**. For Weyl fermions, the chirality is normally a strictly conserved quantum number.[32, 95]

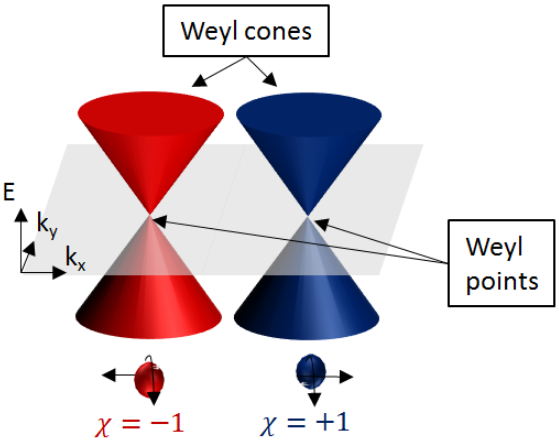

Figure 2.11: The band structure of Weyl semimetals consist of two spatially separated Weyl cones in momentum space, that each host relativistic Weyl fermions of one chirality, either $\chi = -1$ or $\chi = +1$ depicted in red and blue, respectively.

Compared to Dirac semimetals, in Weyl semimetals either inversion symmetry or time-reversal symmetry is broken.[23, 88, 100] Inversion-breaking Weyl semimetals are given by the four members TaAs, TaP, NbAs, NbP, which are summarized as the TaAs family.[24, 101–104] Furthermore, WTe_2 and $MoTe_2$ and their alloys $Mo_xWe_{1-x}Te_2$ belong to the inversion breaking Weyl semimetals, but differ from the TaAs family by belonging to the so-called type II Weyl semimetals, which possess tilted Weyl cones.[105–109] The first proposed time-reversal breaking Weyl semimetals are magnetic pyrochlores ($X_2Ir_2O_7$ with X = Y, Eu, Nd, Sm and Pr);[23] further examples are Mn_3Sn and Mn_3Ge.[110] In general, all 3D-Dirac semimetals behave like Weyl semimetals in sufficiently strong external magnetic fields, because in an external magnetic field the Dirac cone splits into two Weyl cones.[97]
Historically, Weyl fermions were first thought of by Hermann Weyl in 1929, who solved the Dirac equation for massless particles and found two independent solutions for left-handed and right-handed, chiral fermions – the so-called Weyl fermions.[96] For some time it was assumed that neutrinos might be these massless and relativistic fermions predicted by Hermann Weyl, but since it was finally revealed that neutrinos possess a mass, there are no fundamental particles believed to be Weyl fermions.[95] Renewed interest in Weyl fermions arose when Weyl fermions were proposed as quasi-particles the in pyrochlore iridates by Wan *et al.* in 2011.[23] Weyl fermions were experimentally realized and observed by ARPES in TaAs in 2015.[24, 101] For one, in these ARPES experiments the Weyl cones in the bulk band structure of the Weyl semimetals can be observed. Also, topological Fermi arc surface states arise at the 2D surface band structure of the Weyl semimetals, given by the bulk boundary correspondence of the topological 3D Weyl semimetals. These Fermi surface states connect two Weyl points of different chirality in the surface Brillouin zone and are a second characteristic signature of Weyl semimetals in ARPES experiments.
Transport experiments give the opportunity to investigate the massless, relativistic and spin-polarized Weyl electrons under the influence of electric and magnetic fields as well as temperature gradients.

Weyl fermions give rise to new phenomena like the chiral anomaly that is detected by a negative MR (positive magnetoconductance) in parallel electric and magnetic fields due to the breakdown of the chiral symmetry in the system when E||B.[32,95] In a similar configuration, when $\Delta T||B$, which for massless Weyl fermions can be used as a proxy for $\Delta g||B$, with the gravitational field Δg, also a breakdown of the chiral symmetry occurs.[111,112] This so-called mixed axial-gravitational anomaly can be experimentally verified by positive magneto-thermoelectric conductance for $\Delta T||B$. Additionally, Weyl semimetals can also show transport signatures that do not originate from bulk transport, but is rather mediated by the Fermi arc surface states. Here, Fermi arc oscillations in thin Weyl fermion samples can be detected for example in WTe_2 and Cd_2As_3.[99,106]

2.5 Signatures of Dirac and Weyl Fermions in Transport and Magnetometry Experiments

In this thesis, the topological materials $HfTe_5$ and NbP are investigated using electric and thermoelectric transport (Ref. [IV], [VI], and [VII]) as well as magnetometry (Ref. [V]) measurements. To evaluate the obtained data, we conducted an analysis of the Shubnikov-de Haas (SdH) and the de Haas-van Alphen (dHvA) effect, signatures that result from transport within the quantum limit as well as quantum anomalies, namely the chiral anomaly and the mixed, axial-gravitational anomaly. A theoretical introduction to theses transport phenomena is given in this section.

Shubnikov-de Haas Effect

In solid state materials, charge carriers condense into quantized energy levels perpendicular to a sufficiently strong magnetic field at sufficiently low temperatures, as shown in **Fig. 2.12**. This process is called Landau quantization.[113] As the externally applied magnetic field is increased, the distance between the Landau levels increases and the Landau levels are continuously shifted through the Fermi energy. When a Landau level lies within the Fermi energy, charge carriers can be scattered to free states within the Landau level and a high resistance is measured. When the Fermi energy lies between two Landau levels there are no free states into which the charge carriers can be scattered (except for a small number of states provided by the edge channels). As a result, a high conductance (low resistance) is measured. These oscillations of the resistance depending on the position of the Fermi energy with respect to the Landau levels is referred to as the Shubnikov-de-Haas effect. The SdH oscillations are periodic in the inverse magnetic field with an oscillation period of:

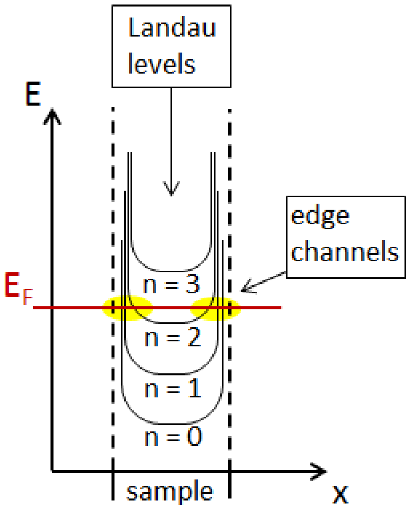

Figure 2.12: Quantized energy levels – the Landau levels – in an electron gas when an external magnetic field is applied.

$$\Delta\left(\frac{1}{B}\right) = \frac{2\pi e}{\hbar S_F} \tag{2.26}$$

with S_F being the cross section of the Fermi surface perpendicular to the magnetic field.
SdH oscillations are normally analyzed regarding their oscillation frequency in $1/B$ and their oscillation amplitude as a function of the temperature. From eq. 2.26 and the geometry of S_F, the Fermi vector k_F can be derived. The oscillation amplitude ΔR of the SdH-oscillations depending on the temperature

and the external magnetic field is described by the Lifshitz-Kosevich-Schoenberg-theory:[113–115]

$$\Delta R(T,B) \propto B^{\frac{1}{2}} \cdot e^{-\chi T_{\mathrm{D}} B} \cdot \frac{\chi T/B}{\sinh(\chi T/B)} \tag{2.27}$$

With the parameter $\chi = 4\pi^3 k_{\mathrm{B}} m_{\mathrm{eff}}$ and the Dingle temperature $T_{\mathrm{D}} = \frac{h}{4\pi^2 k_{\mathrm{B}} \tau}$ the effective mass m_{eff} and the mean carrier life time τ can be calculated. The mobility of the charge carriers is given by $\mu = \frac{e\tau}{m_{\mathrm{eff}}}$.[40] From the conservation of momentum, $\hbar \cdot k_{\mathrm{F}} = v_{\mathrm{F}} \cdot m_{\mathrm{eff}}$, the Fermi velocity v_{F} can be derived and the Fermi energy E_{F} is calculated by using the corresponding dispersion relation, e.g. $E_{\mathrm{F}} = \hbar \cdot k_{\mathrm{F}} \cdot v_{\mathrm{F}}$ for Dirac fermions.[89] Additionally the position of the SdH oscillation minima and maxima as a function of the inverse magnetic field can be used to calculate the Berry phase and therefore give information about the topological nature of the transport channels.[18,89,115]

In general, SdH oscillations can occur for 2D as well as 3D electronic systems. Since the SdH effect only arises for a perpendicular magnetic field with respect to the cross section of the Fermi surface, 2D electronic systems do not show SdH oscillations when the magnetic field is applied parallel to the current direction. 3D electronic systems exhibit SdH oscillations for any configuration of the magnetic field and electric current direction. Angle-dependent SdH oscillation measurements can therefore be a convenient tool to distinguish between 2D and 3D electronic systems in transport measurements.[116]

De Haas-van Alphen Effect

The de Haas-van Alphen (dHvA) effect – like the SdH effect – is caused by the Landau quantization (**Fig. 2.12**) that takes place when an electron gas is placed into a sufficiently strong magnetic field at sufficiently low temperatures.[113] For increasing magnetic fields, the distance between the Landau levels increases. As a consequence, the Landau levels are shifted through the Fermi energy and the density of states at E_{F} oscillates for continuously increasing magnetic fields. The magnetic susceptibility is directly related to the density of states at the Fermi energy and determines the magnetic moment. The oscillation of the magnetic moment caused by the Landau quantization in an increasing magnetic field is described by the dHvA effect.[113] The dHvA effect shows the same periodicity in $1/B$ as the SdH effect (compare eq. 2.26), and the amplitude of the magnetization oscillation Δm depending on T and B can equally be described by the Lifshitz-Kosevich-Shoenberg theory (eq. 2.26).[113–115] Accordingly, analyzing the dHvA effect yields the same parameters as analyzing the SdH effect, which are k_{F}, m_{eff}, τ, μ, v_{F} and E_{F}. Moreover, information about the Berry phase and therefore about the topological nature of the transport channels can be gained from the position of the magnetization minima and maxima as a function of the inverse magnetic field equally to analyzing the Berry phase of the SdH oscillations.[18,89,115]

Quantum Limit

As previously discussed, the SdH effect and the dHvA effect are a consequence of the Landau quantization of an electron gas that is placed into an increasingly strong magnetic field. A closer look at **Fig. 2.12** shows that in the case of Landau quantization, there are not only the discrete Landau levels ($n = 0, 1, 2, ...$), but so-called edge channels also evolve. These conducting edge channels emerge at the Fermi energy, because the Landau levels are bent upward at the geometric edges of the sample due to the edge potential. As the Landau quantization increases in increasing magnetic fields, less Landau levels are energetically below the Fermi energy and the number of conducting edge channels decreases.[113] When the electric transport only takes place in the lowest Landau level, the so-called quantum limit is reached. According to Abrikosov,[117] the preconditions for the transport in the lowest

Landau level are given by:

$$n_\mathrm{e} \ll \left(\frac{eB}{\mu\hbar c}\right)^{\frac{3}{2}} \qquad \text{and} \qquad T \ll \frac{eB\hbar}{\mu m_\mathrm{eff} c} \tag{2.28}$$

with the carrier concentration n_e, the mobility μ and the effective mass m_eff. The first equation describes the condition that is needed for the condensation of all charge carriers within the lowest Landau level. The second equation describes a thermal broadening that is smaller than the band splitting between two Landau levels. According to these equations, a low carrier concentration and low effective masses are beneficial for reaching the quantum limit at moderate magnetic fields. Consequently, for Dirac and Weyl fermions with relatively low effective masses, the quantum limit can be reached by applying relatively small magnetic fields, readily reached in today's transport setups, such as 8 T for Bi and 9 T for TaAs and 0.2 T for ZrTe5.[118–120]

In transport measurements, entering the quantum limit is accompanied by a number of experimental observations. Firstly, when there is a transition from multi-Landau level transport to transport only in the lowest Landau level, a transition from parabolic magnetoresistance to a linear magnetoresistance – sometimes also called quantum linear magnetoresistance – is observed.[117] Secondly, the thermoelectric transport vanishes within the quantum limit because of $S \sim \frac{dD}{dE}$ with the constant density of states D as soon as the quantum limit is reached.[25] Additionally, the SdH and dHvA oscillations that can be observed below the quantum limit vanish as soon as the quantum limit is reached.

Several transport phenomena are predicted to appear within the quantum limit, like, for example, the fractional quantum Hall effect.[118,121] Moreover, recently, discrete scale invariant quantum oscillations were predicted to emerge when Dirac fermions are confined in an attractive Coulomb potential.[122–126] These $\log(B)$-periodic oscillations in the density of states as well as in transport properties like ρ and S can generally also appear below the quantum limit, but are predicted to be clearly identified only in 3D Dirac systems within the quantum limit, because there is only a single scaling factor of the oscillations when the transport takes place entirely in the lowest Landau level.[124]

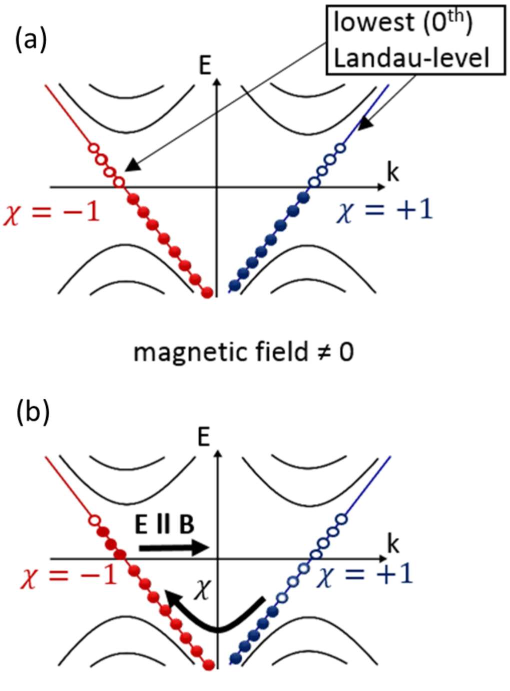

Figure 2.13: (a) Within a magnetic field, there is a Landau quantization of the band structure of a Weyl semimetal. (b) For parallel electric and magnetic fields ($E \parallel B$), a breakdown of the chiral symmetry occurs expressed by a particle flow between the two Weyl cones.

Chiral Anomaly

For Dirac and Weyl fermions, the chirality is defined as the spin direction with respect to the linear momentum. There are left-handed fermions that have an antiparallel alignment of the spin and the linear momentum ($\chi = -1$) and there are right-handed fermions that have a parallel alignment of the spin and the linear momentum ($\chi = +1$).[32,97] In general, the chirality is a strictly conserved quantum number.[32,97] Until recently, the only breakdown of the chiral symmetry was thought of by Adler as well as Bell and Jackiw who independently explained the observed decay of the neutral pion into two photons by this chiral anomaly.[127,128] Recently, the breakdown of the chiral symmetry was also observed in solid state physics as the occurrence of a negative magnetoresistance in Weyl semimetals in electromagnetic fields with parallel electric and magnetic field components.[129] In Weyl semimetals, there are pairs of two Weyl cones of different chirality, which are separated in momentum space. The chiral symmetry within the Weyl band structure is represented by the two equally filled Weyl cones. When only an electric field is applied, the chiral electrons which are hosted by the Weyl cones cannot take part into the electrical transport, because this would violate the chiral symmetry – or in the band structure picture: because this would cause an uneven population of the Weyl cones. When a magnetic field is applied to a Weyl semimetal, there occurs a Landau quantization of the band structure as depicted in **Fig. 2.13 a**. In this scenario, only the lowest Landau level still hosts chiral fermions. When an additional electric field is applied, parallel to the magnetic field, a breakdown of the chiral symmetry occurs (**Fig. 2.13 b**).[32,97] There is an additional axial current with a flow rate proportional to $E \cdot B$.[130] In electrical transport measurements, therefore, a positive magnetoconductance (a negative magnetoresistance) can be observed in $E \parallel B$ due to the chiral anomaly.[129] Recently, transport signatures of the chiral anomaly have been detected in 3D Dirac and Weyl semimetals like Cd_3As_2, Na_3Bi, TaAs, NbAs, Zn-doped NbP and WTe_2.[88,97,131–135]

Mixed Axial-Gravitational Anomaly

Chiral fermions are also predicted to exhibit the so-called mixed axial-gravitational anomaly, which describes the breakdown of the chiral symmetry in collinear magnetic and gravitational fields ($B \parallel \bigtriangledown g$).[136,137] In curved space time, the mixed axial-gravitational anomaly contributes to the violation of the covariant conservation laws of the axial current, which are relevant to the chiral anomaly and to the conservation law of the energy-momentum tensor. Therefore, the mixed axial-gravitational anomaly has been suggested as relevant for the chiral vortical effect in the context of a quark-gluon plasma and the hydrodynamic description of neutron stars.[111,138]

In flat space time, the mixed axial-gravitational anomaly can be derived from different approaches such as Boltzmann equations, Kubo formalism and relativistic field theory by considering conservation laws as well as the topological character of Weyl nodes.[111,112,139–142] The main idea is that for relativistic and massless Weyl fermions, a temperature gradient $\bigtriangledown T$ can be seen as a proxy for a gravitational field $\bigtriangledown g$.[143] This way, an elusive experiment from high energy physics – which needs sufficiently strong gravitational fields – can be simulated in solid state physics by performing thermoelectric measurements in collinear magnetic fields and temperature gradients ($B \parallel \bigtriangledown T$) on Weyl semimetals.[112,139–142] In contrast to the chiral anomaly, where the chiral symmetry is broken by a flow of particles between the two Weyl cones of different chirality for $B \parallel E$, for the mixed axial-gravitational anomaly, there is a flow of particles and energy between the two Weyl cones for $B \parallel \bigtriangledown T$, as shown in **Fig. 2.14**. In 3D Dirac semimetals as well as Weyl semimetals, the mixed axial-gravitational anomaly can be measured as a positive magneto-thermoelectric conductance in collinear temperature gradients and magnetic fields below the quantum limit. This positive magneto-thermoelectric conductance is caused by an additional axial current that flows when the chiral symmetry between the two Weyl cones is broken. At high magnetic fields and low temperatures, when the quantum limit is reached, a suppression of the thermoelectric transport – and therefore a negative

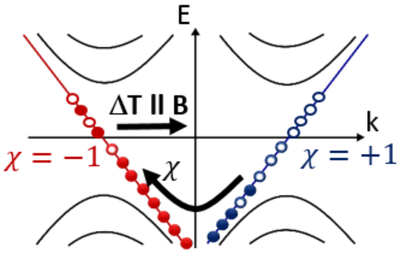

Figure 2.14: For a magnetic field parallel to a temperature gradient ($B \parallel \bigtriangledown T$), a breakdown of the chiral symmetry occurs expressed by a flow of particles and energy between the two Weyl cones.

magneto-thermoelectric conductance – is expected.[25] The reason for this phenomenon is that the thermoelectric conductance G_{T} is proportional to the derivative of the density of states D with respect to the temperature ($G_{\mathrm{T}} \propto \frac{\delta D}{\delta T}$). Within the quantum limit, D is constant and therefore independent of the temperature, which leads to a suppression to the thermoelectric transport within the quantum limit.

3 Experimental Methods

In this chapter, the sample fabrication as well as the methods for the compositional and structural analysis of the samples are described. Furthermore, the definition of the electrical contact structures and the utilized electric, thermoelectric, magnetometry and magneto-optical measurement techniques are introduced.

3.1 Growth, Compositional and Structural Analysis

Magnetic nanowires

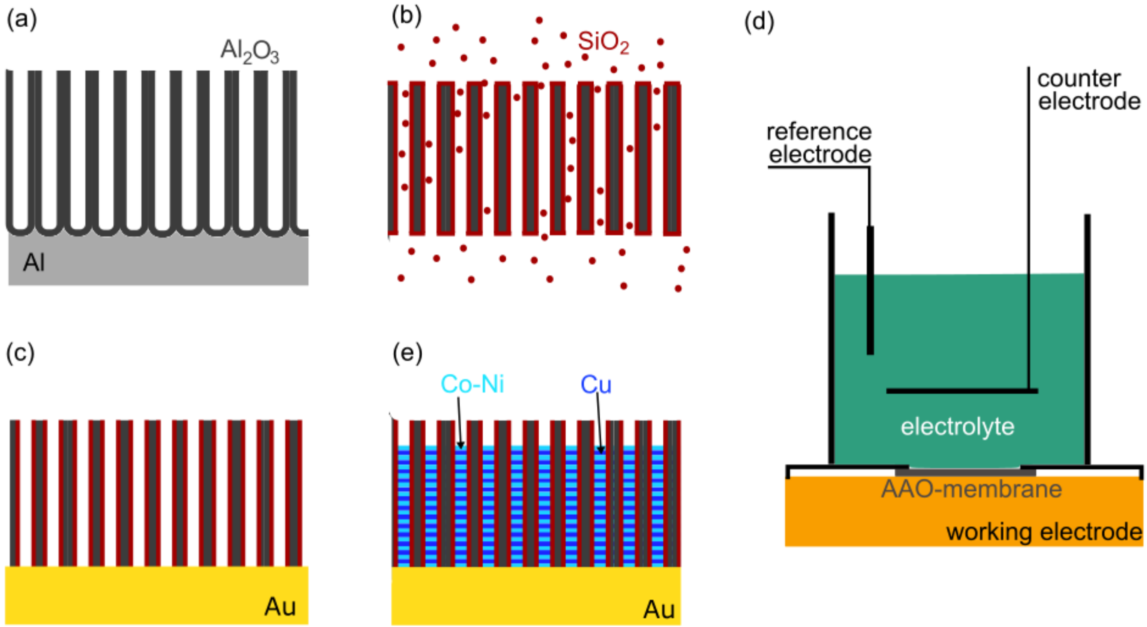

Figure 3.1: Sketch of the nanowire fabrication process. (a) The AAO membrane is synthesized by a two-step anodization process. (b) In an ALD process, the AAO membrane is covered by an protective SiO_2 layer. (c) To the backside of the AAO membrane, an Au layer is applied by sputtering and subsequent electrodeposition. (d) The electrodeposition cell, equipped with a three electrode setup. (e) Multilayered nanowires inside the AAO membrane after the electrodeposition process.

The magnetic nanowires were synthesized by electrodeposition into self-ordered, hard-anodized alumina oxide (AAO) membranes with a pore diameter between 120 nm and 270 nm. We partly used commercial AAO membranes provided by *SmartMembranes*, while another part of the anodization process was carried out in-house. The self-made AAO-membranes were fabricated by firstly pre-anodizing cleaned and electropolished high-purity aluminum foils (Al 99.999 %) under mild anodization conditions ($U = 80\,\mathrm{V}$, $t = 10\,\mathrm{min}$) in a 0.03 mol oxalic aqueous solution containing 5 % of ethanol. Subsequently, the applied voltage was increased to for the hard-anodization process to 140 V with a rate of $0.08\,\mathrm{Vs}^{-1}$. The hard anodization process was performed for 1.5 h at a temperature of 0 °C $< T <$ 3 °C. After the anodization process, we used chemical wet etching in $CuCl_2$/HCl aqueous solution to remove the Al backside of the membranes. The alumina bottom layer as well as the protective mild anodized top layer were opened exposing the membrane to a 5 wt % H_3PO_4 solution for 2.5 h at $T = 30$ °C.[51] We used atomic layer deposition (ALD) to cover the inner walls of the pores of the AAO membranes by a 5 nm – 10 nm protective SiO_2-layer.[144,145] By reactive ion etching, we removed the SiO_2-layer at the bottom and the top side of the AAO membrane. To the backside of the AAO membrane, a gold electrode was applied by first sputtering and subsequent electrodeposition of a gold layer.

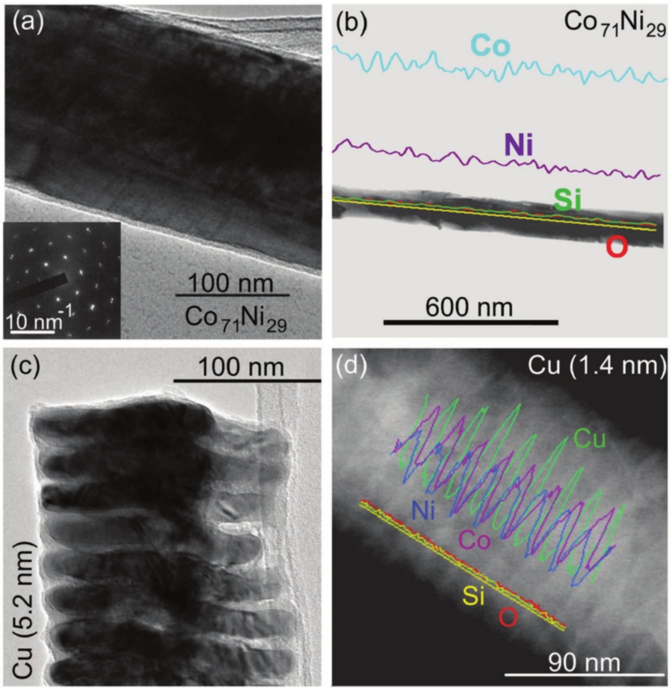

Figure 3.2: Structural, morphological, and compositional characterization of the magnetic nanowires: a) TEM image of sample $Co_{71}Ni_{29}$. The inset shows the SAED pattern of the nanowire, which reveals the [0001] zone axis of an hcp lattice. b) A broader TEM image of sample $Co_{71}Ni_{29}$ combined with superimposed TEM-EDS data obtained from a line scan along the nanowire length shows a fairly homogeneous Co:Ni ratio along the wire axis. c) TEM image of sample Cu (5.2 nm) revealing the multilayered structure of the nanowire. d) TEM image of the multilayered nanowire Cu (1.4 nm) with superimposed TEM-EDS data obtained from a line scan measured along the nanowire axis. Figure taken from Ref. [I]

The electrodeposition process of the magnetic nanowires was performed in a three-electrode setup. The gold layer at the backside of the AAO membrane serves as a working electrode. We used a platinum mesh as the counter electrode and a Ag/AgCl(3M)KCl reference electrode. The CoNi alloy nanowires were electrodeposited at 35 ° under potentiostatic conditions (-0.8 V $< U <$ -1 V vs. reference electrode) from a Watts-type electrolyte containing different amounts of Co^{2+} and Ni^{2+} ions as reported by Vega *et al.*.[51] The FeNi alloy nanowire was synthesized as described by Salem *et al.*.[146] The CoNi/Cu multilayered nanowires were grown from a single bath with an applied voltage of -1.5 V and -0.58 V for the CoNi and Cu layers, respectively. We controlled the CoNi and Cu layer thickness by adjusting the electrodeposited charge equivalent.[147] After the electrodeposition process, the Au backside was removed by using (0.6 M)KI(0.1M)I_2 aqueous solution. The AAO membrane was dissolved in chromic-phosphoric acid (1.8 wt % CrO_3, 6 wt % H_3PO_4) for ≈ 48 h at 45 °C. The released, individual nanowires were filtrated and stored in ethanol. The CoNi alloy nanowires studied in Ref. [I] and Ref. [III] were synthesized by Victor Vega and Tim Böhnert at the University of Hamburg. The CoNi/Cu multilayered nanowires investigated in Ref. [I] and Ref. [II] were fabricated by Svenja Bäßler and Ann-Kathrin Michel in the group of Imre Bakonyi at the Wigner Research Center for Physics in Budapest.

The crystal structure of the CoNi alloy nanowires inside the AAO membrane was investigated by XRD (X'Pert PRO-PANalytical) in a $\Theta - 2\Theta$ setup using CuK-α1 radiation ($\lambda = 1.54056\,\mathring{A}$).[51] The crystal structure of individual CoNi alloy nanowires was investigated by TEM-SAED (**Fig. 3.2 a**).[74] We found an fcc crystal structure for the Ni-rich CoNi nanowires and an hcp crystal structure for the Co-richest sample ($Co_{71}Ni_{29}$). The crystallite size of the CoNi nanowires was determined from XRD analysis to be between 5 ± 2 nm and 9 ± 2 nm.[51] The composition of the Co-Ni alloy nanowires was determined by TEM EDS line scans as shown in **Fig. 3.2 b**. Next to Co and Ni, Si and O_2 from the

SiO_2-shell of the nanowires were also detected.

Individual CoNi/Cu nanowires were investigated by TEM to visualize the layered structure of the nanowires and measure the bilayer thickness (**Fig. 3.2 c**) and by TEM-EDS to analyze the atomic composition (**Fig. 3.2 d**). Combining this data, the Cu and CoNi layer thickness was calculated. We investigated six different samples with varying Cu layer thicknesses of 0.2 nm, 0.8 nm, 0.9 nm, 1.4 nm, 3.5 nm, and 5.2 nm. We aimed for a constant CoNi layer thickness of approx. 20 nm (for more information see Ref. [II]). The Co:Ni composition within magnetic layer ranged from 50:50 to 30:70. Due to an unavoidable co-deposition of Cu during the electrodeposition process, a Cu-content of approx. 2 % is estimated in the magnetic layer.[148]
The length and the diameter of all magnetic nanowires was investigated by SEM (Refs. [I] – [III]).

NbP Micro-Ribbons

From niobium (Chempur 99.9 %) and red phosphorus (Hereaus 99.999 %) polycrystalline NbP powder was synthesized by a direct reaction in an evacuated fused silica tube at 800 °C for 800 h. High-quality single crystals of NbP were grown from the multicrystalline NbP powder via a chemical vapor transport reaction. The utilized temperature gradient increased from 850 °C (source) to 950 °C (sink). Iodine (Alfa Aesar 99.998 %) with a concentration of 13.5 $\mathrm{mgcm^{-3}}$ was used as a transport agent.[149] The NbP bulk crystal utilized in (Refs. [V] - [VII]) was synthesized by Vicky Süß, Marcus Schmidt and Chandra Shekhar at the Max Planck Institute for Chemical Physics of Solids in Dresden.

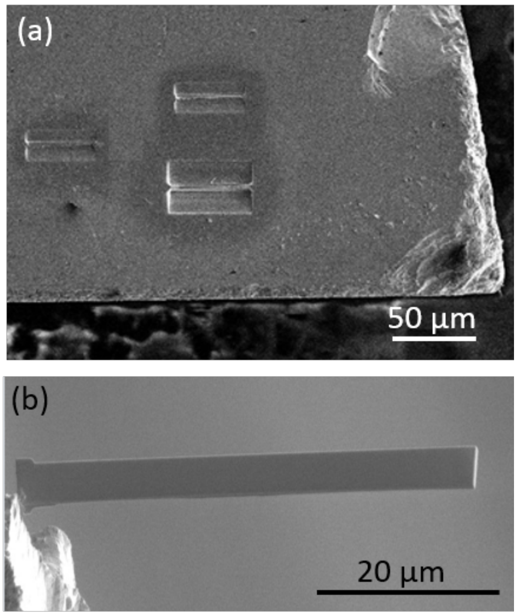

Figure 3.3: Definition of the NbP micro-ribbon by Ga-FIB. (a) The NbP bulk sample with 3 trenches defined by FIB to extract one NbP micro-ribbon per trench. (b) A free-standing NbP micro-ribbon.

To identify the crystal axes of the NbP bulk crystal, we performed XRD measurements in a Panalytical X'Pert four-circle diffractometer using Cu-K_α radiation. NbP-micro-ribbons were cut from the NbP bulk sample by using 30 keV Ga^+ions ($I = 65\,\mathrm{nA} - 80\,\mathrm{pA}$) in a FIB system (FEI Helios 600i). To achieve defined crystal axes along the outer edges of the micro-ribbons, the FIB cut was carried out along the bulk crystal axes. In **Fig. 3.3 a**, the NbP bulk crystal with three open trenches can be seen. From each trench, a micro-ribbon (**Fig. 3.3 a**) was removed. To avoid electrostatic repulsion, the as-cut NbP micro-ribbons were picked up ex-situ with a glass needle and transferred to a glass substrate for the electrical contacting process.

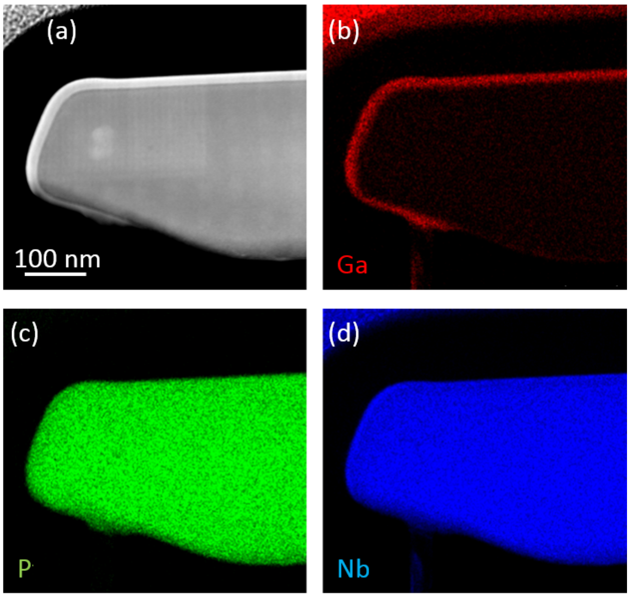

Figure 3.4: Qualitative analysis of the cross section of a NbP micro-ribbon. (a) HR-TEM image of the cross section of the NbP micro-ribbon. On the same NbP micro-ribbon cross section the Ga- (b), P- (c), and Nb- (d) concentration was mapped.

The atomic composition of the surface of the NbP micro-ribbon was analyzed by SEM-EDX using a 15 keV electron beam. We measured an atomic composition of 53 % Nb, 45 % P, and 2 % Ga. A cross section of the NbP micro-ribbon (**Fig. 3.4 a**) was defined to investigate the amorphous layer on the surface of the NbP micro-ribbon due to the Ga-FIB process. The measured thickness of the amorphous layer is $\sim$ 20 nm. Using TEM-EDS (FEI TALOS F200X), we qualitatively analyzed the Nb-P-Ga composition of the cross section of the micro-ribbon (**Fig. 3.4 b-d**). The Ga-concentration in the outer amorphous shell is significantly increased compared to the inner part of the NbP micro-ribbon (**Fig. 3.4 b**). We note that also in the inner part of the NbP micro-ribbon, a certain amount of Ga is present because the cross section of the NbP micro-ribbon was also defined by Ga-FIB. In general, an exponential decay of Ga-ions from the micro-ribbon surface towards the center of the FIB-defined micro-ribbon is assumed.[99] In contrast, the Nb and P is homogeneously distributed across the whole NbP micro-ribbon cross section (**Fig. 3.4 c & d**).

$HfTe_5$ Micro-Ribbons

$HfTe_5$ single crystals were synthesized by Vicky Süß and Chandra Shekhar at the Max Planck Institute for Chemical Physics of Solids by using the vapor transport method with Te as a self-flux. For the fabrication process, an atomic ratio of 0.0025 % Hf and 99.9975 % Te were transferred into a crucible under argon atmosphere. The crucible was then heated to 900 °C under vacuum inside a quartz tube for 24 h. Subsequently, there was a rapid cooling to 580 °C followed by a further temperature decrease of 0.5 Kh^{-1} until a temperature of 470 °C was reached.[150]
The crystal structure of the $HfTe_5$ crystals was investigated by single-crystal x-ray diffraction (SXRD) with Mo-Kα radiation. To determine the elementary composition, energy-dispersive x-ray spectroscopy (EDS) inside a scanning electron microscope was utilized.[151]

Due to the layered structure of $HfTe_5$,[152] we were able to mechanically extract $HfTe_5$ micro-ribbons from the bulk crystal using a micro-manipulator. The orientation of the crystal axes with respect to the micro-ribbon geometry was determined with electron back scattering diffraction (EBSD) equipped with a TSL DigiView detector inside a scanning electron microscope (FEI Helios 600i).

3.2 Definition of the Electrical Contact Structure

To define the electrical contact structure on our nanowires and micro-ribbons, we used laser lithography combined with a Ti/Pt metallization process as sketched in Fig.**3.5**. A solution of dispersed magnetic nanowires in ethanol was dropped onto glass substrates (thickness 150 μm) and the ethanol was evaporated using a hot-air gun. The NbP and HfTe$_5$ micro-ribbons were transferred mechanically to the glass substrates using a micro-manipulator. Subsequently, the substrates were spin coated with a double layer of LOR-3B lift-off resist followed by a maP-1205 photoresist. This double layer of resist enabled us to obtain an undercut structure during the photoresist development process, which facilitates the lift-off after the metallization process. The electrical contact structures were exposed using a laser lithography system (Heidelberg Instruments μpG 101). This system is equipped with an optical camera and movable sample stage to align the electrical contact structure layout with the nano- or micro-structures before the exposure. After the exposure, the photoresist was developed using maD-331 until the undercut structure could be observed. Subsequently, in-situ Ar-ion etching inside the Ti/Pt sputtering machine (Torr international, CRC-600) was used to remove the SiO$_2$-shell of the magnetic nanowires and any native oxides of the NbP and HfTe$_5$ micro-ribbons in order to ensure ohmic contacts. Afterward, a Ti adhersion layer and the Pt contacts were applied by sputter deposition. The thickness of the Pt-layer was chosen to be in the range of the thickness of the sample ($\sim$150 nm –500 nm). For the deposition onto the thicker micro-ribbons, the substrates were rotated by

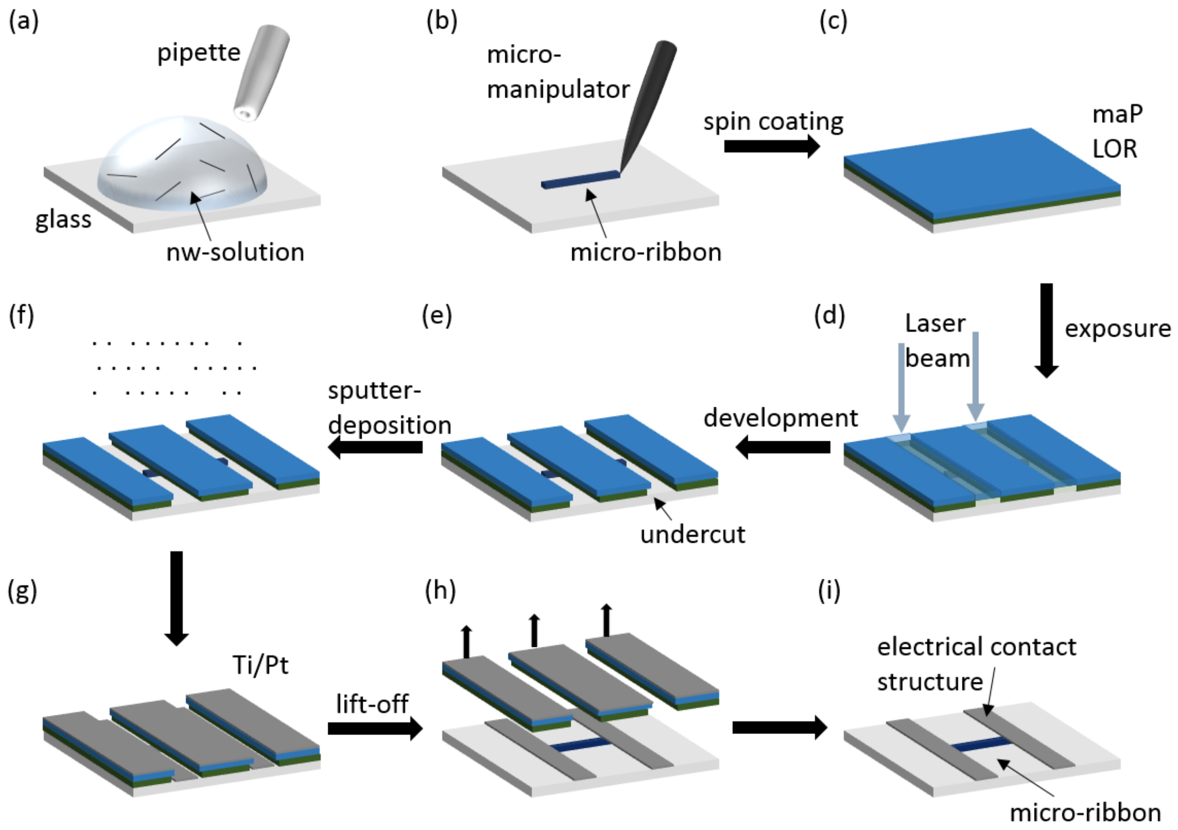

Figure 3.5: Sketch of the microdevice fabrication process. (a) Magnetic nanowires dispersed in an ethanol solution are applied to the glass substrate. (b) The NbP and HfTe$_5$ micro-ribbons are mechanically transferred to the glass substrate using a micro-manipulator. (c) The glass substrates are coated with an double layer of LOR-3B lift-off resist and maP-1205 photoresist. (d) Via laser lithography, the electrical contact structures are exposed. (e) The exposed resist is developed and an undercut structure evolves. (f) and (g) Inside the sputtering machine, the contact areas are cleaned from SiO$_2$ or native oxides and then a Ti/Pt bilayer is applied by sputter deposition. (h) In a lift-off process, residual metal parts are removed. (i) The final micro-device.

180 ° after half of the Pt deposition time to avoid shadowing effects. After the sputter deposition, the residual metal layer was removed in a lift-off process. Detailed process parameters for the definition of the electrical contact structures are given in **Tab. 5.1** and **Tab. 5.2**.

3.3 Measurement Techniques

In the following, the utilized measurement techniques to characterize the magnetic nanostructures and topological microstructures are introduced, with a focus on the electrical and thermoelectric characterization methods. These measurements were performed in a DynaCool PPMS (by QuantumDesign) at a low pressure at the order of 10^{-3} mbar. A typical micro-device for measuring the electrical as well as thermoelectric characterization is shown in **Fig. 3.6 a and b**, respectively. Vibrating sample magnetometry (VSM) and magneto-optical Kerr effect (MOKE) measurements are introduced briefly.

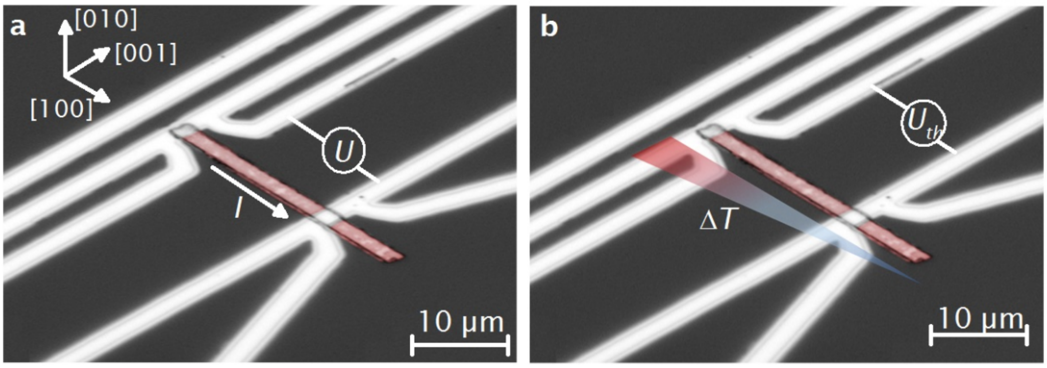

Figure 3.6: A typical micro-device – shown here with an embedded $HfTe_5$ micro-ribbon – to measure the electrical resistivity (a) as well as the thermopower (b). The crystal orientation of the $HfTe_5$ micro-ribbon is given in (a).

Electrical Measurements

We determined the resistance of our samples by two-terminal measurements using a low frequency ($f \leq$ 200 Hz) lock-in technique, as sketched in **Fig. 3.7**. Additionally, we performed 4-point measurements on our samples and found that contact resistances of our samples were typically below 2 %. Magnetoresistance measurements were performed in an external magnetic field up to ± 14 T. A rotary sample holder allowed for a parallel and perpendicular alignment of the magnetic field B with the current I direction as well as intermediate angles between B and I.

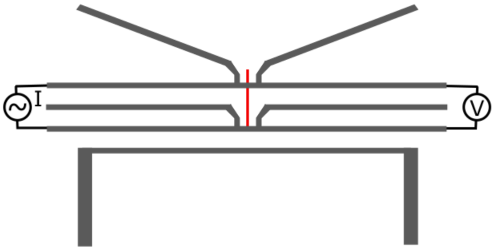

Figure 3.7: Experimental configuration of the resistivity measurements on the joint resistivity/thermopower measurement device.

Thermoelectric Measurements

The micro-device that was utilized for the thermopower measurements (**Fig. 3.6 b**) consists of three different parts – one resistive heater line and two resistive thermometers. The resistive heater is connected to a DC current source (Agilent E3644A) and generates a 1D temperature gradient along the sample. Typically, heater powers of up to 5 mW were applied and temperature differences ΔT along the sample of up to 10 K were achieved. ΔT was measured by the two resistive thermometers. The

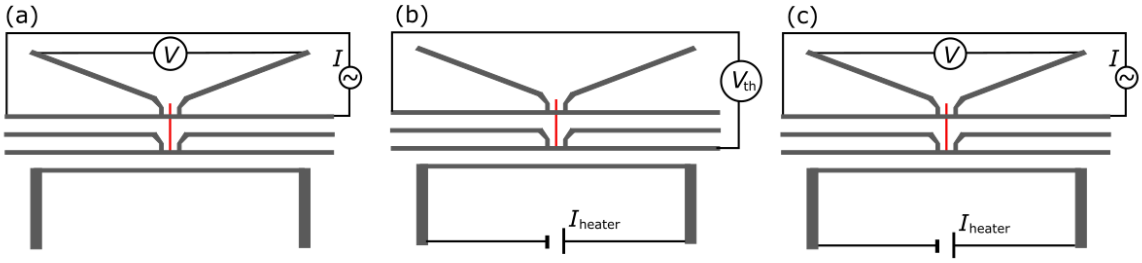

Figure 3.8: Measurement procedure to determine the thermovoltage S of individual micro- and nanostructures. (a) Calibration of the resistive thermometers: The resistance of both thermometers R_{Th1} and R_{Th2} is measured as a function of the cryostat base temperature. There is no temperature gradient applied. (b) Thermovoltage measurement: A current I_{heater} is applied to the resistive heater line and the thermovoltage V_{th} along the sample is measured. (c) Measurement of the temperature gradient along the sample: I_{heater} is applied to the resistive heater line and R_{Th1} and R_{Th2} are measured.

resistance of the thermometers was measured by standard low frequency lock-in technique ($f \leq 200\,\mathrm{Hz}$) provided by the DynaCool PPMS. Additionally, the resistive thermometers are in electrical contact with the sample and are therefore used as leads for the thermopower measurement via a DC multimeter (Keithley 2182A). Overall, the determination of the thermopower can be divided into three different steps. Firstly, the resistive thermometers were calibrated by measuring their resistance as a function of the base temperature of the cryostat without applying a temperature gradient (**Fig 3.8 a**). Secondly, we applied a temperature gradient via the resistive heater and measured the thermovoltage (**Fig 3.8 b**). In a third step, the resistance of the thermometers was measured when applying a temperature gradient (**Fig 3.8 c**) and the temperatures of both resistive thermometers T_{Th1} and T_{Th2} were calculated using the calibration lines from the first measurement step. Subsequently, the temperature difference along the sample $\Delta T = T_{\mathrm{Th1}} - T_{\mathrm{Th2}}$ and the thermopower $S = V_{\mathrm{th}}/\Delta T$ was determined. The obtained thermopower is always given with respect to the Ti/Pt leads. At room temperature, S(Ti/Pt) is estimated to be -5 μV/K.[26]

Magnetization Measurements

VSM measurements were performed in a DynaCool system by Quantum Design with magnetic fields of up to ±9 T. In each measurement one crystal axis of the NbP bulk crystal was aligned parallel along the magnetic field. Magnetization measurements in a temperature range from 2.5 K to 60 K were conducted. The VSM measurements on NbP which are studied in Ref. [V] were performed by Philip Sergelius at the University of Hamburg.

Magneto-Optical Measurements

The MOKE measurements on the magnetic nanowires were performed with a NanoMOKE$^{\mathrm{TM}}$2 by *Durham Magneto Optics*. The device is equipped with a 45° incidence continuous wave-laser with a power output of 1.9 mW and an in-plane focused spot size of approx. 3 μm. Within the setup, magnetic fields of up to ±0.08 T can be applied with a quadrupole magnet in the plane of the incidental beam of light and therefore parallel to the nanowire axis. The estimated heating of the nanowire due to the laser light is less than 1 K and the recorded hysteresis loops show no difference between the laser beam directed at the center and at the ends of the nanowire. The coercive fields of the nanowires were measured via the longitudinal MOKE.[153] The MOKE measurements studied in Ref. [III] were performed by Ann-Kathrin Michel and Stephan Martens at the University of Hamburg.

4 Selected Results and Discussion

In this chapter, the key results of this dissertation are presented, which are given in detail in the end of this thesis as seven peer-reviewed publications (Refs. [I] – [VII]) as well as one overview-article (Ref. [VIII]). The publications are divided into two different sections.

The first section (4.1) deals with thermoelectric transport in single ferromagnetic CoNi/Cu multilayered as well as CoNi alloy nanowires (Refs. [I], [II]) and the temperature- and temperature gradient-dependent magnetic switching of $Co_{39}Ni_{61}$ and $Fe_{15}Ni_{85}$ magnetic nanowires (Ref. [III]). The nanowires were characterized using resistivity ρ and thermopower S measurements as well as magneto-optical Kerr effect measurements. It is shown that the magnetic nanowires have thermoelectric power factors PF ($\mathrm{PF} = S/\rho^2$) ranging between $0.3\,\mathrm{mWK^{-2}m^{-1}}$ and $3.6\,\mathrm{mWK^{-2}m^{-1}}$, which is in the same order of magnitude as standard thermoelectric materials like Bi_2Te_3 ($\mathrm{PF(Bi_2Te_3)}$=$1.9\,\mathrm{mWK^{-2}m^{-1}}$).[154] Additionally, in the magnetic nanowires, the possibility of further tuning the thermoelectric power output of up to 50 % is given when a magnetic field is applied (Ref. [I]). Using the Mott formula, we found that one can distinguish between the absolute thermopower of the magnetic nanowires and the platinum leads (Ref. [II]). Finally, we found that the thermally-assisted magnetization reversal process of individual $Co_{39}Ni_{61}$ nanowires is significantly altered because applied temperature gradients lead to an increase of the magneto-elastic anisotropy constant (Ref. [III]).

In the second section of this chapter (4.2), the topological materials $HfTe_5$ and NbP are studied, using magnetometry, magnetoresistance and magneto-thermopower measurements. First, the magnetoresistance and magnetothermopower of $HfTe_5$ are investigated (Ref. [IV]). We report on an increase of the thermopower at sufficiently strong magnetic fields for temperatures between 150 K and 300 K which is the temperature range that is relevant to thermoelectric applications and we observed on a vanishing magneto-thermoelectric transport for temperatures below 100 K. To properly understand the transport phenomena in Weyl semimetals, a precise understanding of the band structure and the position of the Fermi level is required. Therefore, dHvA-oscillations on bulk NbP are obtained (Ref. [V]) in VSM measurements and SdH oscillations in NbP micro-ribbons are analyzed (Ref. [VI]). Subsequently, the chiral anomaly in collinear magnetic and electric fields (Ref. [VI]) and the mixed, axial-gravitational anomaly in collinear magnetic fields and temperature gradients (Ref. [VII]) are investigated. The results of the quantum anomaly studies on NbP (Ref. [VI], [VII]) were also summarized in a comprehensive overview article (Ref. [VIII]).

4.1 Thermoelectric Characterization of Ferromagnetic Nanowires

4.1.1 [I] Thermoelectric Power Factor Enhancement by Spin-Polarized Currents – A Nanowire Case Study

In the past few years, an increasing integration density of microelectronic devices has brought thermoelectric effects back to the focus of current research.[10–12] When it comes to nanostructures, thermoelectric effects can be either beneficial or hindering. An example where local temperature hot spots are essential is heat-assisted magnetic recording (HAMR).[13,14] Thermoelectric effects can be hindering when due to miniaturization Peltier heating becomes dominant over Joule heating. It was shown that by neglecting the Peltier heating of nanodevices, one may fail to predict magnetic switching properties by more than 40 %.[12] An interesting class of integrated circuit elements is based on MR effects, which are nowadays used in reading heads for magnetic hard disks, magnetic sensors and magnetoresistive random access memories (MRAMs).[155] These devices are based on the AMR,[53,62,156] GMR[63,64] and TMR[157] effect. Driven by the need to constantly increase data storage densities, tremendous progress in the miniaturization of MR devices has been made,[158] which makes thermoelectric effects in these devices an interesting research topic.

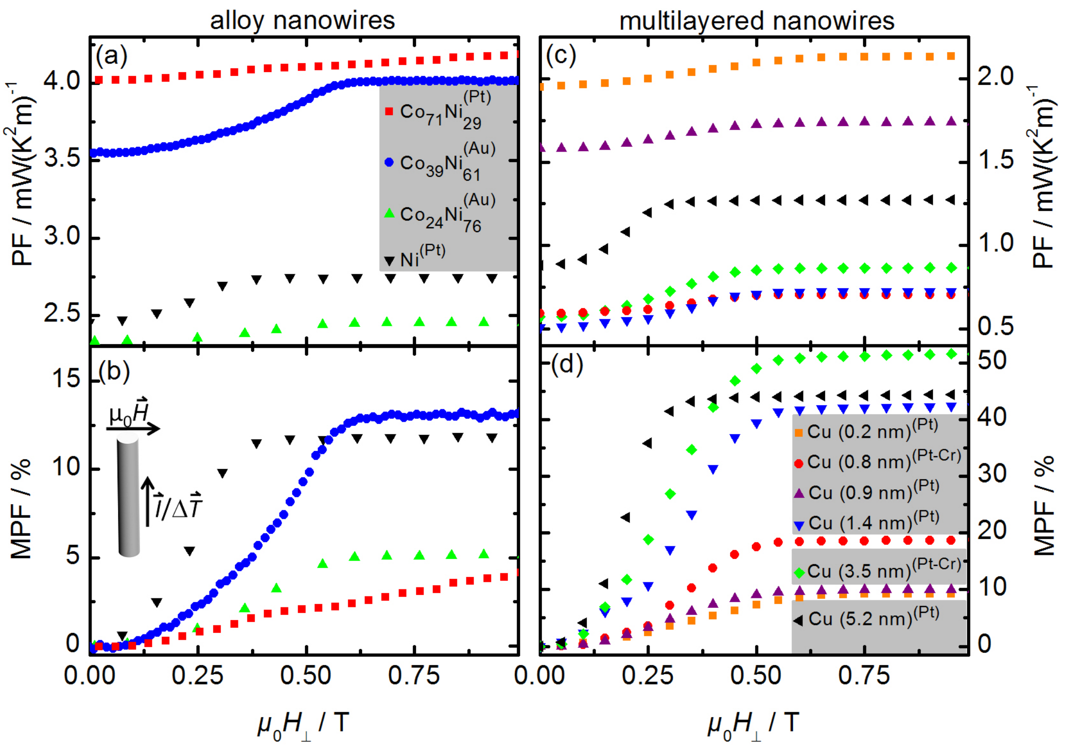

Figure 4.1: a) Thermoelectric power factor, PF, and b) magneto-power factor, MPF (MPF = $(\mathrm{PF}_H - \mathrm{PF}_0)/\mathrm{PF}_0$) as a function of the external magnetic field, $\mu_0 H_\perp$, applied perpendicular to the single Ni and Co–Ni alloy nanowire axis. Corresponding PF and MPF values for the Co–Ni/Cu multilayered nanowires are shown in (c) and (d), respectively. The base temperature was set to 300 K. Heating powers of 4.1 mW for the alloy samples and 2 mW for the multilayered samples were applied, which resulted in quite different mean temperatures $\bar{T}$($\bar{T} = (T_{\mathrm{hot}} - T_{\mathrm{cold}})/2$) of the nanowires [$\mathrm{Co_{71}Ni_{29}}$: 320 K, $\mathrm{Co_{39}Ni_{61}}$: 314 K, $\mathrm{Co_{24}Ni_{76}}$: 342 K, Ni: 362 K, Cu (0.2 nm): 307 K, Cu (0.8 nm): 315 K, Cu (0.9 nm): 314 K, Cu (1.4 nm): 310 K, Cu (3.5 nm): 311 K, Cu (5.2 nm): 305 K] depending on the type of material and the thickness of the microdevice. Figure taken from Ref. [I]

In the presented study, we investigate the thermoelectric power output of an AMR model system and a current-perpendicular-to-plane GMR model system, given by Co-Ni alloy nanowires and CoNi/Cu multilayered nanowires, respectively. The magnetic nanowires were synthesized by electrodeposition into self-ordered, nanoporous AAO membranes according to procedures from Vega *el al.*[51] and Tóth *et al.*.[148] Before the electrodeposition process, the membranes were coated with SiO_2 using ALD, in order to give the future nanowires a passivation layer.[144,145] After electrodeposition, the AAO membranes were dissolved using chromic-phosphoric acid. In total, we investigated one Ni nanowire and 3 Co-Ni alloy nanowires with a Co-content ranging from 24 % up to 71 % and additionally, six CoNi/Cu multilayered nanowires with a varying Cu-layer thickness between 0.2 nm and 5.2 nm. The structural and compositional analysis was performed by transmission electron microscopy (TEM) and TEM-energy dispersive x-ray spectroscopy.[74,147] For more information see Ref. [I].

The individual nanowires were electrically contacted by laser lithography followed by a Ti/Pt metallization process. The electrical contact structure is designed to measure S and ρ in one device.[74,159] For the alloy, AMR nanowires, we measured maximum values for the MR of up to 6 %, for S of up to 26.5 μV/K and for magneto-thermoelectric power MTEP (MTEP $= \frac{S(H)-S(0)}{S(0)}$, see section 2.3) of up to 8 %. As expected, multilayered, GMR nanowires showed a higher maximum MR of up to 14 % and also a higher maximum MTEP of up to 30 %, but a slightly lower S of only up to 24.5 μV/K. Using the Thompson relation $\Pi = S \cdot \bar{T}$, we calculated the Peltier coefficients of the nanowires as well as the Peltier heat flow $\dot{Q} = \Pi \cdot I$ at room temperature. For the $Co_{71}Ni_{29}$ nanowires, we derived $\Pi = 7.95\,\mathrm{mV}$ and $\dot{Q} = 80\,\mathrm{nW}$, which exceeds the heat generation by Joule heating by a factor of 8 when using $R(Co_{71}Ni_{29}) = 100\,\Omega$ and $I = 10\,\mu\mathrm{A}$, which are typical values for the nanowire resistance and measurement current in our experiments. Peltier heating in the magnetic nanowires should therefore not be neglected.

At room temperature and zero magnetic field, we calculated a thermoelectric power factor PF (PF $= \rho S^2$, see section 2.1 for more information) of up to 3.6 mW/K^{2}m for the alloy nanowires and a thermoelectric PF of up to 2.0 mW/K^{2}m for the multilayered nanowires, which is of the same order of magnitude as standard thermoelectric materials like bulk Bi_2Te_3 (PF(Bi_2Te_3)=1.9 mWK^{-2}m^{-1}),[154] and exceeds the thermoelectric PF of Bi_2Te_3 nanowires by a factor of 5.[160] The investigated magnetic materials might therefore be interesting candidates for thermoelectric power generation under specific conditions like waste heat recovery as well as heat management in electronic materials at the nano- and micro-scale. Applying an external magnetic field at room temperature increased the PF by up to 13 % for the alloy nanowires and by up to 52 % for the multilayered nanowires within the magnetic saturation field, see **Fig. 4.1**, to maximum thermoelectric PF values of 2.1 mW/K^{2}m and 4.2 mW/K^{2}m, respectively.

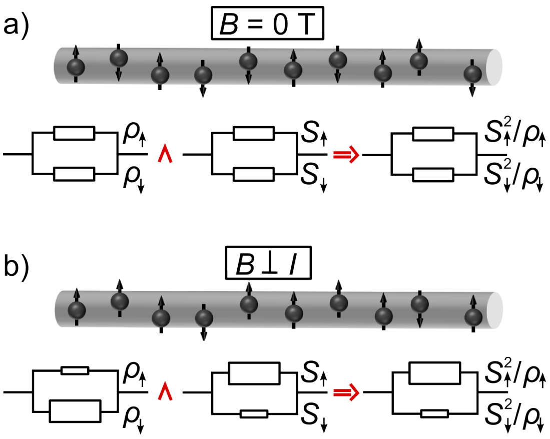

Figure 4.2: The two-current model for the resistivity as well as the thermopower S and the resulting thermoelectric power factor S^2/ρ. a) Without an external magnetic field, the majority and minority spin channel, ↑ and ↓, exhibit equal $\rho_\uparrow$ and $\rho_\downarrow$, as well as equal $S_\uparrow$ and $S_\downarrow$, resulting in equal S^2/ρ for both spin channels. b) With an externally applied magnetic field, ↑ exhibits lower ρ than ↓, and according to our observation, $S_\uparrow$ is increased compared to $S_\downarrow$, which results in an increase of $S_\uparrow^2/\rho_\uparrow$ and, finally, in an increase of the thermoelectric power factor of the whole system. Figure taken from Ref. [I]

For the alloy and multilayered nanowires, the increased thermoelectric performance in increasing magnetic fields can be understood in the framework of Mott's two current model.[161] The two current model is given by two conducting channels by majority electrons ↑ and minority electrons ↓ in a parallel circuit, see **Fig. 4.2**. The total resistivity of the magnetoresistive system is given by $\rho_{\mathrm{tot}} = (1/\rho_\uparrow + 1/\rho_\downarrow)^{-1}$, with the resistivity of the majority and minority channel $\rho_\uparrow$ and $\rho_\downarrow$, respectively. Due to different s-d scattering cross sections for minority and majority electrons (see section 2.3), one spin channel has a higher resistivity than the other spin channel. We assume $\rho_\uparrow << \rho_\downarrow$, so that in the limit of full spin-polarization $\rho_{\text{tot}}(H > H_{\text{sat}}) \rightarrow \rho_\uparrow < \rho_{\text{tot}}(H = 0\,\text{T})$. The total thermopower of the two parallel conducting spin channels is given by $S_{\text{tot}} = (S_\uparrow/\rho_\uparrow + S_\downarrow/\rho_\downarrow)\,/\,(1/\rho\uparrow + 1/\rho\downarrow)$ with the thermopower of the majority and minority spin channel $S_\uparrow$ and $S_\downarrow$, respectively, and with $\min[S_\uparrow, S_\downarrow] < S_{\text{tot}} < \max[S_\uparrow, S_\downarrow]$. In large applied magnetic fields, $S_{\text{tot}} \approx (S_\uparrow/\rho_\uparrow)/(1/\rho_\uparrow) = S_\uparrow$ follows directly from $\rho\uparrow << \rho\downarrow$. Since in our experiments, S increases with increasing H, $S_{\text{tot}} = \max[S_\uparrow, S_\downarrow]$ and $S\uparrow >> S\downarrow$ follows, see **Fig. 4.2 b**. Consequently, the thermoelectric PF of the AMR and GMR systems benefits from the fact that for a high degree of spin polarization, the prevailing low resistivity majority channel also exhibits the higher thermopower compared to the minority spin channel.

4.1.2 [II] Magnetothermopower and Magnetoresistance of Single Co-Ni/Cu Multilayered Nanowires

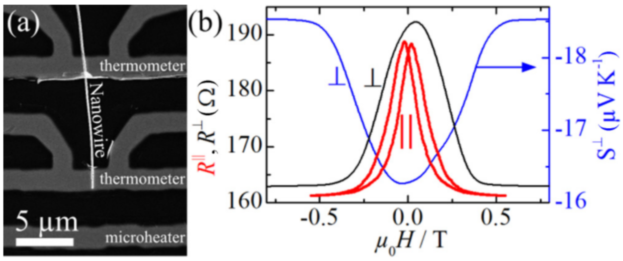

Figure 4.3: (a) Scanning electron microscope image of a nanowire and the electrical contact structure. (b) Parallel (probe station setup) and perpendicular (cryostat) resistance measurements at RT and a Seebeck coefficient measurement (cryostat) in a magnetic field for the 3.5-nm Cu sample. Figure taken from Ref. [II]

For thermoelectric measurements, the distinction between the absolute Seebeck coefficient of the sample and the leads, $S^{\text{abs}}_{\text{sample}}$ and $S^{\text{abs}}_{\text{leads}}$, respectively, is difficult, because the measured thermopower S_{m} always gives the sum of these two contributions. It is: $S_{\text{m}} = S^{\text{abs}}_{\text{sample}} + S^{\text{abs}}_{\text{leads}}$ as derived in section 2.1. To perform thermopower measurements without the influence of the contact material at low T, one usually chooses superconducting leads with no thermoelectric voltage drop. At higher T, S^{abs} can be determined using the Thompson effect.[27,162] As a standardized lead material for which S^{abs} is well known, platinum is usually used in thermoelectric measurements.[26,27] Nevertheless, there can be deviations from the literature values because S is very sensitive to impurities[84] and there can be size effects.[39,83] Within the presented study of the magnetoresistance and magnetothermopower of multilayered nanowires, we utilized the Mott formula to establish an easy model that distinguishes between the absolute thermopower contributions of the magnetic nanowires $S^{\text{abs}}_{\text{nw}}$ and the non-magnetic leads $S^{\text{abs}}_{\text{leads}}$. Our model can be applied to ferromagnetic samples in which non-diffusive parts of the thermopower can be neglected, that means electron scattering on grain boundaries and impurities is the dominant scattering mechanism.

Multilayered $Co_{50}Ni_{50}/Cu$ nanowires were synthesized by electrodeposition into self-ordered AAO membranes. In order to passivate the surface of the nanowires, the pores of the AAO template were coated by ALD with 5 nm of SiO_2 previous to the electrodeposition process.[144,145] The multilayered Co-Ni/Cu nanowires were prepared by two-pulse plating from a single Watts bath.[148] After electrodeposition, the nanowires were released from the AAO membrane by chemical wet etching. Within the electrodeposition process, we aimed for a 50/50 – Co/Ni composition and for a fixed CoNi layer thickness but varying Cu layer thicknesses among the different samples. The layer thicknesses as well as the Co : Ni : Cu composition was tested by high-resolution TEM and TEM-EDS (compare Ref. [II]), respectively. In total, we investigated six different samples with a Cu layer thickness between 0.2 nm and 5.2 nm. Individual nanowires were electrically contacted using laser lithography followed by a Ti/Pt metallization process.[74,159] The utilized electrical contact structure (**Fig. 4.3 a**) is designed to measure the resistivity ρ of the nanowires as well as S within the same device. Therefore, the contact structure consists of one heater line to generate a temperature gradient ΔT along the nanowire as well as two resistive thermometers to detect ΔT along the nanowire and to measure the thermovoltage U_{th}.

The MR of the multilayered nanowires in a magnetic field B perpendicular to the nanowire axis (see for example **Fig. 4.3 b**) varies between 3 % and 14 % at room temperature. Utilizing additional MR measurements with B applied parallel to the nanowire axis and calculating the AMR (AMR $= \frac{R_\perp - R_\parallel}{R_\parallel}$), we can distinguish between two different MR regimes within our nanowires. For samples with very thin Cu spacer layers (Cu (0.2 nm) and Cu (0.9 nm)), pinholes in the non-magnetic spacer layer can be assumed, which lead to a direct exchange coupling and therefore a parallel alignment of the magnetization of neighboring magnetic segments even within zero magnetic field. This results in low MR values around 3 %. Samples with thicker Cu layers show higher MR values up to 14 %, indicating closed Cu spacer layers and therefore an antiparallel magnetization alignment of neighboring magnetic layers in zero magnetic field can be assumed. Samples with the unclosed Cu-layers showed a magneto-thermoelectric power MTEP (see Eq. 2.22 in section 2.3) between 2.7 % and 4.1 %. Nanowires with closed Cu-layers showed slightly a higher MTEP than MR with MTEP values between 14 % and 30 % at room temperature.

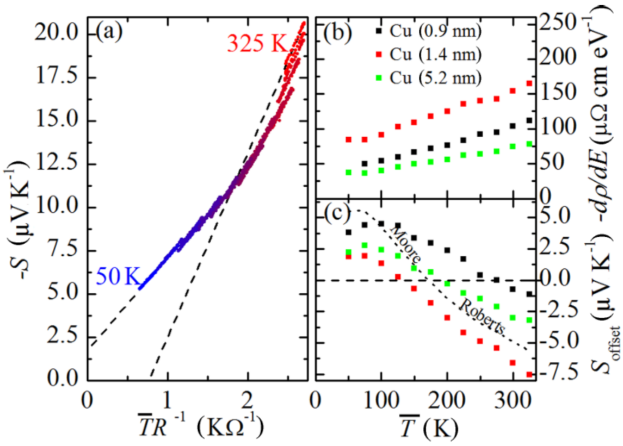

Figure 4.4: (a) Seebeck coefficient versus average temperature times the conductance of the 1.4-nm Cu sample in 25-K steps from 50 to 325 K with the applied magnetic field as an implicit variable. For simplicity, only data for $U_{\mathrm{heater}} = 5\,V$ are shown, which correspond to ΔT of 3 K at 25 K to 2 K at 325 K. (b) Energy derivative of the resistivity at the Fermi energy derived from Eq. **??** against the temperature. (c) Offset from Eq. **??** and the absolute literature values[26, 27] of Pt. Figure taken from Ref. [II]

To evaluate the relation between ρ and S under the influence of B, we divide S_{m} into one part that describes the absolute thermopower of the nanowire $S_{\mathrm{nw}}^{\mathrm{abs}}$, which can be substituted by the Mott formula, and one offset part S_{offset}. It is:

$$S_{\mathrm{m}}(H) = S_{\mathrm{nw}}^{\mathrm{abs}}(H) + S_{\mathrm{offset}} = -\frac{\pi^2 k_{\mathrm{B}}}{3q} T \left(\frac{\delta\rho}{\delta E}\right)_{E=E_{\mathrm{F}}} \rho_{\mathrm{nw}}(H)^{-1} + S_{\mathrm{offset}}, \tag{4.1}$$

with the electron charge q and the Boltzmann constant k_{B}. The Mott formula describes only the diffusive part of $S_{\mathrm{nw}}^{\mathrm{abs}}$, any non-diffusive parts $S_{\mathrm{nw}}^{\text{non-dif.}}$ like the phonon drag[163] as well as the absolute thermopower of the contact material $S_{\mathrm{leads}}^{\mathrm{abs}}$ are summarized by S_{offset} as $S_{\mathrm{offset}} = S_{\mathrm{nw}}^{\text{non-dif.}} + S_{\mathrm{leads}}^{\mathrm{abs}}$. Nevertheless, we assume that $S_{\mathrm{nw}}^{\text{non-dif.}}$ can be neglected because the polycrystalline nature of the electrodeposited nanowires makes electron scattering on grain boundaries and impurities the most likely scattering mechanism. Note that we assume a magnetic field-independent $\left(\frac{\delta\rho}{\delta E}\right)_{E=E_{\mathrm{F}}}$, which can be justified by the linear dependence of $S(\rho(H)^{-1})$ that is commonly described for magnetic samples in literature.[7, 8, 74–82]

Eq. **??** gives a linear relation between S and $\overline{T}\rho_{\mathrm{nw}}^{-1}$, which is plotted for all base temperatures T_{base} between 50 K and 325 K in **Fig. 4.4 a**. For each T_{base}, this linear relation is observed, whereas H is an implicit variable. At each $\overline{T}$, a different slope and a different offset value can be extracted. A representation of the slope is given as $\left(\frac{\delta\rho}{\delta E}\right)_{E=E_{\mathrm{F}}}$ in **Fig. 4.4 b** and the offset value S_{offset} is given in **Fig. 4.4 c** together with the absolute thermopower of platinum $S_{\mathrm{Pt}}^{\mathrm{abs}}$ which is given as a dotted line. For $S_{\mathrm{Pt}}^{\mathrm{abs}}$ as well as S_{offset}, a thermopower maximum that is caused by the phonon-drag can be observed between 50 K and 100 K. One can see that $S_{\mathrm{Pt}}^{\mathrm{abs}}$ and S_{offset} have a common trend. Deviation between $S_{\mathrm{Pt}}^{\mathrm{abs}}$ and S_{offset} can arise due to impurities within the Pt leads[84] as well as size effects that reduce the phonon-drag peak.[39]

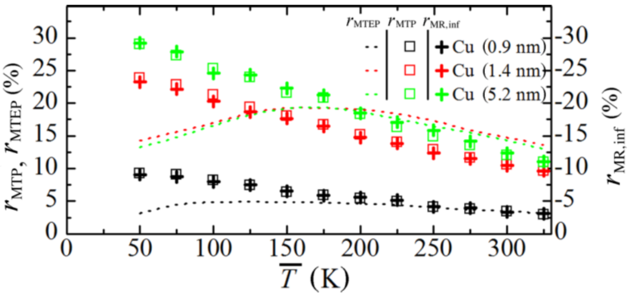

Figure 4.5: (Temperature dependence of $r_{\mathrm{MR,inf}}$, r_{MTEP}, and r_{MTP} values, which are corrected under the assumption of $S_{\mathrm{contact}} = S_{\mathrm{offset}}$. The expected relation between r_{MTP} and $r_{\mathrm{MR,inf}}$ according to Eq. 4.2 is observed. Figure taken from Ref. [II]

To quantify the changes of S within an applied magnetic field, the MTEP and the MTP (compare Eq. 2.22 and Eq. 2.23 in section 2.3) can be used. MTEP has thermopower contributions from the sample and from the leads. We use $S_{\mathrm{offset}} = S_{\mathrm{leads}}^{\mathrm{abs}}$ to calculate MTP, which only describes the thermopower change of the magnetic nanowire without any contributions from the leads. Using MTP together with the Mott formula, one can derive:

$$\mathrm{MTP} = \frac{S_{\mathrm{m}}(H) - S_{\mathrm{m}}(0)}{S_{\mathrm{m}}(0) - S_{\mathrm{leads}}(0)} = \frac{S_{\mathrm{nw}}^{\mathrm{abs}}(H) - S_{\mathrm{nw}}^{\mathrm{abs}}(0)}{S_{\mathrm{nw}}^{\mathrm{abs}}(0)} = -\left[\frac{R(H) - R(0)}{R(H)}\right] = MR_{\mathrm{inf}}, \tag{4.2}$$

with $\mathrm{MR}_{\mathrm{inf}}$ as the "inflated" MR, an alternative MR definition. In **Fig. 4.5** MTEP, MTP and $\mathrm{MR}_{\mathrm{inf}}$ are plotted as a function of T. While MTEP shows deviations from the other two curves, MTP and $\mathrm{MR}_{\mathrm{inf}}$ give identical values, underscoring our hypothesis that $S_{\mathrm{Pt}}^{\mathrm{abs}} = S_{\mathrm{offset}}$.

4.1.3 [III] Temperature Gradient-Induced Magnetization Reversal of Single Ferromagnetic Nanowires

In magnetic memory devices, continuous down-scaling of the geometrical single magnetic bit unit sizes is required to achieve increasing magnetic memory densities. One widely-discussed approach to realizing these high memory capacities is the heat-assisted magnetic recording (HAMR).[13,14] Following this concept, shape and crystal anisotropy enhance the magnetic switching fields H_{SW} (as well as the coercive field H_{C}) and therefore suppress the superparamagnetic limit. To allow for the magnetic bit writing process, a heating laser is used to reduce H_{C} for a short period of time. In the presented study in Ref. [III], we show that for the writing process within the HAMR technique, and depending on the magnetic material, a careful distinction between elevated temperatures and temperatures gradients has to be made. We find that for magnetic materials with a high positive magneto-elastic anisotropy, H_{C} is actually increased and not decreased when applying a temperature gradient.

Two types of soft magnetic alloy nanowires – $\mathrm{Co_{39}Ni_{61}}$ and $\mathrm{Fe_{15}Ni_{85}}$ – were synthesized by electrodeposition.[51,146] After releasing the nanowires from the AAO membranes, single, cylindrical nanowires with an average diameter of 150 nm and a length of 30 μm were acquired. To investigate the temperature gradient-dependent H_{C} of the nanowires, measurement devices as shown in **Fig. 4.6 a** were fabricated. In these devices, the nanowire is enclosed but not electrically contacted by two resistive thermometers, one of which is simultaneously used as a resistive heater. The coercive fields of the nanowires were measured via the longitudinal magneto-optical Kerr effect.[153] We used a NanoMOKE$^{\mathrm{TM}}$2 by *Durham Magneto Optics*, which was equipped with a 45° incidence continuous wave laser light with a power output of 1.9 mW and an in-plane focused spot size of approximately 3 μm. In this setup, an external magnetic field of up to ± 0.08 T could be applied. A second micro-device (see Fig. 2a in Ref. [III]) was used to measure coercive fields of the $\mathrm{Co_{39}Ni_{61}}$ and $\mathrm{Fe_{15}Ni_{85}}$ nanowires at different temperatures, but under isothermal conditions via anisotropic magnetoresistance measurements inside a PPMS system.

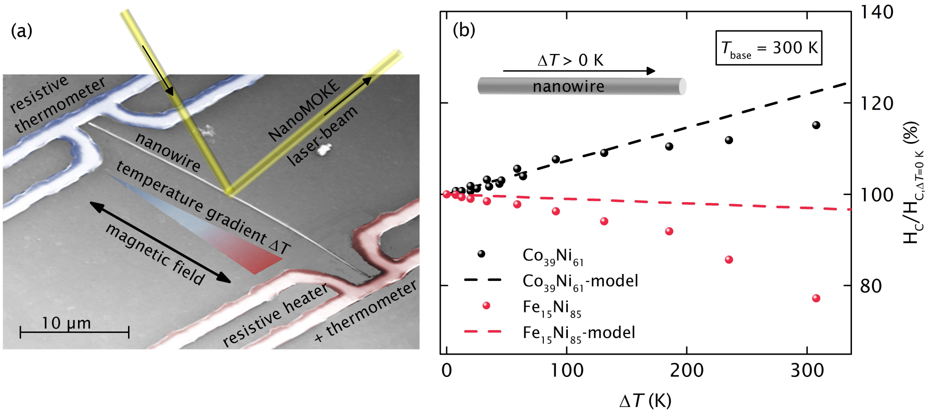

Figure 4.6: (a) Nanowire device used for magneto-optical Kerr effect (MOKE) measurements. (b) Normalized coercive fields $H_\mathrm{C}/H_{\mathrm{C},\,\Delta\mathrm{T}=0\,\mathrm{K}}$ for $\mathrm{Co_{39}Ni_{61}}$ and $\mathrm{Fe_{15}Ni_{85}}$ nanowires as a function of the temperature gradient ΔT. Increasing H_C with increasing ΔT for $\mathrm{Co_{39}Ni_{61}}$ nanowires contradicts the basic concept of heat assisted magnetization reversal (HAMR).

As expected, we observed decreasing H_C for increasing T for both $\mathrm{Co_{39}Ni_{61}}$ and $\mathrm{Fe_{15}Ni_{85}}$ nanowires under isothermal conditions, due to the thermally assisted switching process (see Fig. 3a in Ref. [III]). We further see a decreasing H_C for increasing ΔT for $\mathrm{Fe_{15}Ni_{85}}$ nanowires, but we surprisingly observed increasing H_C for increasing ΔT of 17 % for $\Delta T = 300\,\mathrm{K}$ for $\mathrm{Co_{39}Ni_{61}}$ nanowires (**Fig. 4.6 b**).
To explain the unexpected $H_\mathrm{C}(\Delta T)$ dependence of the $\mathrm{Co_{39}Ni_{61}}$ nanowire, we derived an simple model in which the enhancement of H_C is related to axial stress due to an increasing ΔT along the nanowire. We start with:[164]

$$H_\mathrm{C} = \frac{2K_\mathrm{eff}}{\mu_0 M_\mathrm{S}} \left| cos(\Theta) \right| , \tag{4.3}$$

with the vacuum permeability μ_0, the saturation magnetization M_S, the angle Θ between the external magnetic field and the magnetization vector and the effective anisotropy constant K_eff of the nanowires, which is given by $K_\mathrm{eff} = K_\mathrm{shape} + K_\mathrm{me}$. Here, K_shape is the shape anisotropy and K_me is the magneto-elastic anisotropy. We neglect the magneto-crystalline anisotropy because of its small values.[52,54] K_shape is given by eq. 2.3 in section 2.2 and can be calculated to be $K_\mathrm{shape}(\mathrm{Co_{39}Ni_{61}}) = 350\,\mathrm{kJm^{-3}}$ and $K_\mathrm{shape}(\mathrm{Fe_{15}Ni_{85}}) = 200\,\mathrm{kJm^{-3}}$ using M_S values[55,165] of $M_\mathrm{S}(\mathrm{Co_{50}Ni_{50}}) = 1060\,\mathrm{kJm^{-3}}$ and $M_\mathrm{S}(\mathrm{Fe_{20}Ni_{80}}) = 795\,\mathrm{kJm^{-3}}$. The magneto-elastic anisotropy constant is given by eq. 2.4 in section 2.2 and shows a ΔT-dependence. While we use the averaged values $\alpha_\mathrm{Co/Ni/Fe} = 12.7 \cdot 10^{-6}\,\mathrm{K^{-1}}$ as the thermal expansion coefficient[166] and $Y_\mathrm{Co/Ni/Fe} \approx 209\,\mathrm{GJm^{-3}}$ gives the Young's modulus for both $\mathrm{Co_{39}Ni_{61}}$ and $\mathrm{Fe_{15}Ni_{85}}$ nanowires, λ_me differs by one order of magnitude for both magnetic alloys.[167,168] With $\lambda_\mathrm{me}(\mathrm{Co_{39}Ni_{61}}) = 65 \cdot 10^{-6}$ and $\lambda_\mathrm{me}(\mathrm{Fe_{15}Ni_{85}}) = -5 \cdot 10^{-6}$, we calculated the magneto-elastic anisotropy constants to be $K_\mathrm{me}(\mathrm{Co_{39}Ni_{61}}) = 78\,\mathrm{kJm^{-3}}$ and $K_\mathrm{me}(\mathrm{Fe_{15}Ni_{85}}) = -6\,\mathrm{kJm^{-3}}$. Under the assumption that M_S is not changing significantly between 300 K and 600 K, we calculated the normalized coercive fields of the $\mathrm{Co_{39}Ni_{61}}$ nanowires at $\Delta T = 300\,\mathrm{K}$ to be

$$\frac{H_\mathrm{C}(\Delta T = 300\,\mathrm{K})}{H_\mathrm{C}(\Delta T = 0\,\mathrm{K})} = \frac{K_\mathrm{shape} + K_\mathrm{me}}{K_\mathrm{shape}} = 1.22$$

In contrast, the normalized coercive field of the $\mathrm{Fe_{15}Ni_{85}}$ nanowires at $\Delta T = 300\,\mathrm{K}$ is given by:

$$\frac{H_\mathrm{C}(\Delta T = 300\,\mathrm{K})}{H_\mathrm{C}(\Delta T = 0\,\mathrm{K})} = \frac{K_\mathrm{shape} + K_\mathrm{me}}{K_\mathrm{shape}} = 0.97$$

Plotting these normalized coercive field trend lines together with the measured data (**Fig. 4.6 b**), we find very good agreement between our estimation and the measured data for $\Delta T < 200\,\mathrm{K}$. At higher

ΔT , the experimental $\frac{H_\mathrm{C}(\Delta T = 300\,\mathrm{K})}{H_\mathrm{C}(\Delta T = 0\,\mathrm{K})}$ are lower than predicted my our model, which we attribute to the heat-assisted magnetization reversal process due to the elevated average temperature of the nanowire because of the high applied ΔT.

In this study, other possible origins of the altered $H_\mathrm{C}(\Delta T)$-dependence of the $\mathrm{Co_{39}Ni_{61}}$ nanowires are also briefly discussed, but excluded in the end. Firstly, we excluded radial stress as a cause for the increasing H_C for increasing ΔT for the $\mathrm{Co_{39}Ni_{61}}$ nanowires because radial stress due to the $\mathrm{SiO_2}$-shell of the nanowires would also appear for an increasing base temperature of the nanowires, where we observed decreasing H_C for increasing T_base. Another mechanism that could influence the magnetic switching mechanism of the nanowires is the longitudinal spin-Seebeck (SSE) effect.[5,6] In that case, a pure spin current could have a stabilizing or destabilizing effect on the magnetization of the nanowires and could therefore increase or decrease H_C. Even if there were a possible influence of the SSE, we think that our model fits the measurement data in so well that additional major influences can be excluded.

4.2 Thermoelectric characterization of topologically protected materials

4.2.1 [IV] Thermoelectric characterization of a $\mathrm{HfTe_5}$ micro-ribbon

In recent years, there has been renewed interest in well-established thermoelectric materials due to new theoretical and experimental band structure investigations. For example, thermoelectric Bi-Te-Sb-Se based materials have proven to be topological insulators.[16] In Dirac[21,22] and Weyl[23,24] semimetals, new transport phenomena like the chiral anomaly caused by the breakdown of chiral symmetry between the Weyl nodes[131,133] or the anomalous Hall effect (AHE) that arises due to a Berry curvature associated with the Weyl nodes[169] are commonly investigated by electrical transport measurements. Nevertheless, thermoelectric transport has also been investigated in Dirac and Weyl semimetals such as the thermoelectric response to the breakdown of chiral symmetry[25,170] and the anomalous Nernst effect,[171] this being the thermoelectric equivalent to the AHE.

$\mathrm{HfTe_5}$ and $\mathrm{ZrTe_5}$ have an orthorhombic crystal structure[152] with the space group *Cmcm* and have been investigated since the 1980s. They were first studied for their resistivity anomaly,[172,173] and their thermoelectric transport.[174] $\mathrm{HfTe_5}$ and $\mathrm{ZrTe_5}$ possess a higher thermoelectric power factor (PF) than $\mathrm{Bi_2Te_3}$ between 150 K and 300 K[31] and are therefore interesting materials for thermoelectric low-T applications. To further enhance the PF of $\mathrm{HfTe_5}$ and $\mathrm{ZrTe_5}$, the effect of doping was intensively studied[31,175,176] and in $\mathrm{HfTe_5}$:Nd a PF of up to $6\,\mathrm{mWK^{-2}m^{-1}}$ was achieved for 300 K. Recently, the band structure of $\mathrm{HfTe_5}$ and $\mathrm{ZrTe_5}$ has

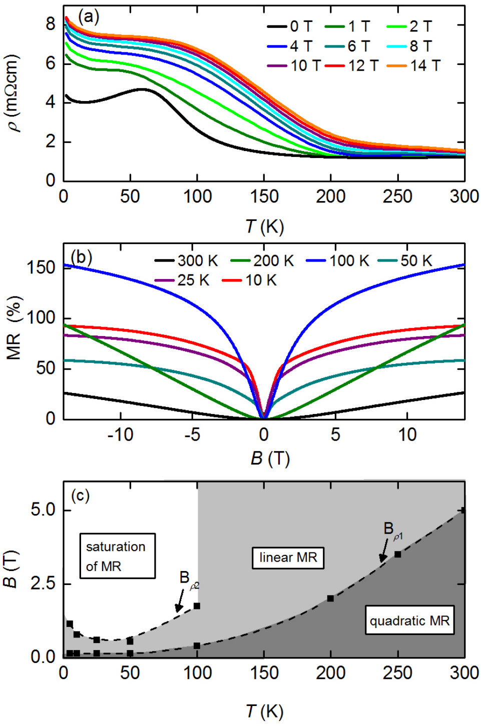

Figure 4.7: (a) Resistivity ρ as a function of temperature T for different applied magnetic fields B up to 14 T. (b) MR (MR=$(\rho_B - \rho_0)/\rho_0$) as a function of B at different T. (c) The three different regimes of the MR (quadratic, linear, and saturating) depending on T and B. The transition magnetic fields from quadratic to linear and from linear to saturating MR are labeled as $B_{\rho 1}$ and $B_{\rho 2}$, respectively. Figure taken from Ref. [IV]

been intensively investigated in theoretical and experimental studies.[28–30,98] Ab-inito band simulations[28] as well as angle-resolved photoemission spectroscopy investigations[29] concluded that $HfTe_5$ and $ZrTe_5$ are located at a phase transition between a weak and a strong topological insulator. The existence of 3D-Dirac bands is supported by the reported chiral anomaly[30,98] in $HfTe_5$ and $ZrTe_5$. Additionally, the resistivity anomaly in $HfTe_5$ and $ZrTe_5$ was reported to be caused by a temperature-induced Lifshitz transition, in which the Fermi level is shifted across the Dirac point as the temperature increases.[29,177]

Here, we report on magneto-transport measurements on a single-crystalline $HfTe_5$ micro-ribbon. The micro-ribbon ($20\,\mu m \times 2.1\,\mu m \times 0.7\,\mu m$) was mechanically extracted from the bulk crystal and electrically contacted using laser lithography followed by a Ti/Pt metallization process. The utilized micro-device for the transport measurements consists of one resistive heater line and two resistive thermometers and is designed to measure the resistivity ρ and the thermopower S in one sample.[159] The electric current ($I = 100\,nA$) for the resistivity measurements as well as the temperature gradient ($\Delta T = 0{,}29\,K$) for the thermopower measurements were applied along the [100]-axis of the $HfTe_5$ micro-ribbon and the external magnetic field B was applied perpendicular to the current direction along the [010]-axis.

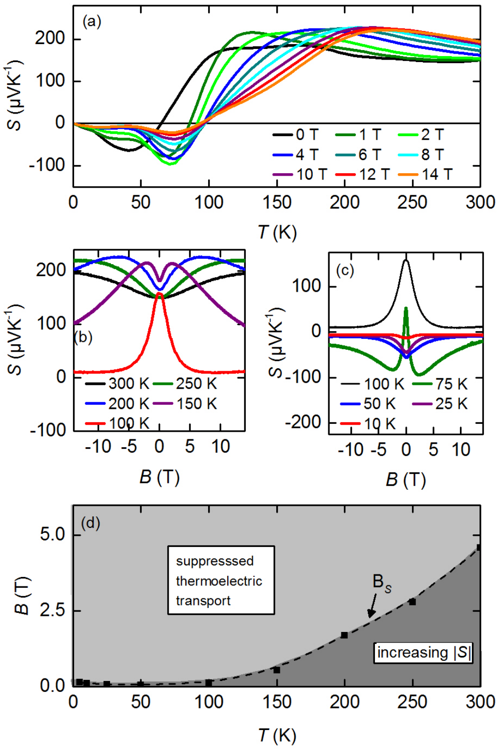

Figure 4.8: (a) The thermopower S as a function of the temperature T for different applied magnetic fields of up to 14 T. (b) S as a function of B for temperatures between 100 K and 300 K and (c) S as a function of B for low temperatures from 10 K to 100 K. (d) Depending on the T and B, either an increasing $|S|$ for increasing B or a suppressed thermoelectric transport can be observed. Figure taken from Ref. [IV]

When plotting ρ as a function of T as shown in **Fig. 4.7 a**, a resistivity anomaly peak can be observed at $T_p = 60\,K$, which was recently related to a temperature-induced Lifshitz transition[29] that occurs across T_p. In a temperature-induced Lifshitz transition, the Fermi surface topology transforms from an electron-like pocket below T_p to a hole-like pocket above T_p. At T_p, the Fermi level E_F lies in the energy gap between conduction and valence band and therefore a high resistivity is measured. When applying an external magnetic field, we observe an increased ρ over the whole T-range compared to $\rho(T)$ at zero magnetic field (**Fig. 4.7 a**). This increasingly strong semiconducting behavior due to the application of an increasingly strong magnetic field is commonly attributed to a small band gap semiconductor, which experiences an increasing gap opening due to an increasing applied magnetic field.[114,178]

In the MR measurements, we observe three different MR regimes, as shown in **Fig. 4.7 b** and **Fig. 4.7 c**. There is a positive quadratic MR for low magnetic fields across the whole T-range. At elevated magnetic fields, the quadratic MR transforms into a linear MR, and for $T \leq 100\,K$, we observe saturation of MR for even further increased B.

The transition points from quadratic to linear and from linear to a saturating MR are given in **Fig. 4.7 c** as $B_{\rho 1}$ and $B_{\rho 2}$, respectively.

Similar MR curves were recently observed on Cd_3As_2 and tied to a two-band transport model.[179] For $HfTe_5$, a two-band transport mechanism was recently shown by performing Hall measurements.[30] Furthermore, a positive linear MR is often interpreted as a signature of transport in the lowest Landau level[117,180] and was recently identified with strong changes in the band structure of a Dirac semimetal when the Dirac cone splits into two Weyl cones due to the application of an external magnetic field.[181,182] Nevertheless, in these two scenarios there has to be an additional mechanism to be responsible for the saturation of MR at elevated B and $T \leq 100\,\mathrm{K}$, which might be given by confinement effects.[183,184]

In our thermopower measurements, we observe a sign change in S at $T_\mathrm{p} = 60\,\mathrm{K}$ from a negative S below T_p to a positive S above T_p,as given in **Fig. 4.8 a**, which is in accordance with the temperature-induced Lifshitz transition.

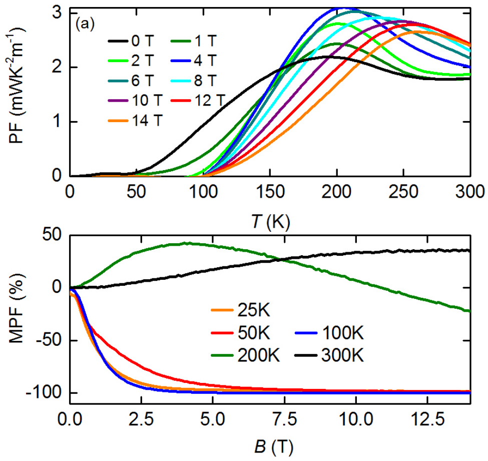

Figure 4.9: (a) The thermoelectric power factor PF ($PF = S^2/\rho$, with thermopower S and resistivity ρ) as a function of the temperature T for different applied magnetic fields B up to 14 T. (b) The magneto-power factor MPF (MPF = (PF$_B$-PF$_0$)/PF$_0$) as a function of B at different T. Figure taken from Ref. [IV]

Magneto-thermopower curves as a function of B for $T \geq 100\,\mathrm{K}$ and $T \leq 100\,\mathrm{K}$ are shown in **Fig. 4.8 b** and **Fig. 4.8 c**, respectively. For low magnetic fields, $|S|$ increases for increasing B over the whole T-range. At more elevated B, $|S|$ starts to decrease for increasing B, and for even higher magnetic fields and $T \leq 100\,\mathrm{K}$, $|S|$ approaches $0\,\mu\mathrm{V/K}$. From the $S(B)$-plots, we extracted the inflection points B_S, separating the increasing $|S|$ at low B from the decreasing $|S|$ at higher B, as depicted in **Fig. 4.8 d**. Comparing **Fig. 4.7 c** and **Fig. 4.8 d**, it can be seen that $B_{\rho 1}$ and B_S show good agreement across the whole T-range. The suppressed thermoelectric transport within an applied magnetic field was recently associated with transport at the lowest Landau level. Within the quantum limit, the electron density ρ is independent of T, whereas S is always proportional to $d\rho(T)/dT$ and the thermoelectric transport is accordingly suppressed in the quantum limit.[25,170] At $T \leq 50\,\mathrm{K}$, we observe the transition to the quantum limit to be at approx. 0.15 T, which is very similar to measurements on ZrTe$_5$, for which the transition to the quantum limit was recently observed to be at approx. 0.2 T.[120] To review the other possible transport mechanisms like the two-band transport model and the splitting of the Dirac cone into two Weyl cones, a theoretical description of the corresponding magneto-thermoelectric transport signatures is needed. These are promising subjects for further theoretical investigations.

The thermoelectric power factor PF (PF = S^2/ρ) of the HfTe$_5$ micro-ribbons is given in **Fig. 4.9 a** as a function of T for different applied B. For $T \leq 50\,\mathrm{K}$, the PF plateaus at a low value with PF(50 K, 0 T)=0.07 mWK^{-2}m^{-1} and for $T \geq 50\,\mathrm{K}$, we observe a steep increase of the PF. For $B = 0\,\mathrm{T}$, the thermoelectric PF between 150 K and 300 K plateaus at approx. 2 mWK^{-2}m^{-1}. This is comparable to the PF of HfTe$_5$ reported by Lowhorn *et al.*,[175] but a factor of three less than the PF of HfTe$_5$:Nd published in the same study. The magneto-power factor ratio MPF = (PF$_B$ - PF$_0$)/PF$_0$, with PF$_B$ being the power factor within a magnetic field and PF$_0$ being the power factor without an applied magnetic field, is shown in **Fig 4.9 b**. MPF increases up to 40 % when a magnetic field is applied for $T \geq 200\,\mathrm{K}$ which is the temperature range that is interesting for thermoelectric applications of HfTe$_5$ because in this temperature range the PF of HfTe$_5$ exceeds the PF of Bi$_2$Te$_3$.[31] The strong reduction of the PF for $T \leq 100\,\mathrm{K}$ of MPF ≈ -100 % corresponds to an almost complete suppression of the thermoelectric transport.

With the presented transport study on HfTe$_5$, we contribute to the identification of the transport mechanism as well as the optimization of the thermoelectric power output of this thermoelectric and topological non-trivial material.

4.2.2 [V] Berry Phase and Band Structure Analysis of the Weyl Semimetal NbP

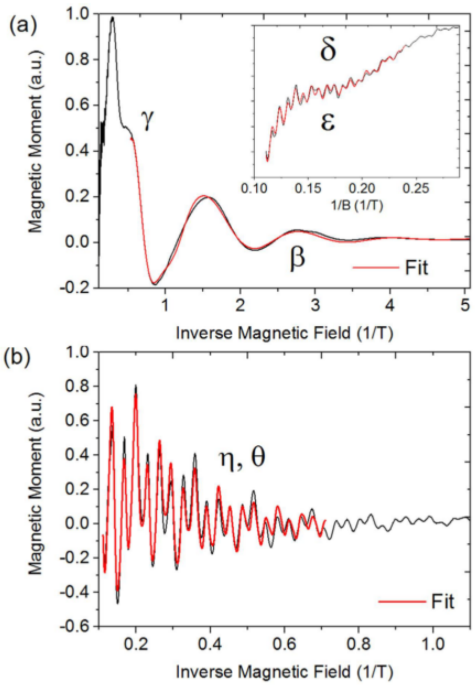

Figure 4.10: Fits of Eq. 4.4 to the raw data at 2.5 K for (a) k_x and k_y and (b) k_z. The full formula including all frequencies is always fitted; however, the fitting interval in $1/B$ is adjusted to a smaller region as shown in the graphs. Figure taken from Ref. [V]

A new class of topological materials was experimentally realized in 2015, when in ARPES measurements, TaAs was proven to be a Weyl semimetal.[101,102] TaAs is the most prominent member of the so-called TaAs inversion-breaking Weyl semimetal family, which also includes TaP, NbAs and NbP.[185,186] While all Weyl semimetals exhibit sets of two Weyl cones with different chirality which are separated in momentum space, TaAs – due to a large SOC – exhibits the largest separation of the two Weyl points in momentum space within the TaAs-family.[87] NbP has a much weaker SOC and the Weyl cones are less separated in momentum space, which leads to the existence of multiple, parallel conduction channels in NbP besides the Weyl cones.[88] Via the Shubnikov-de Haas (SdH)[88,114] and the de Haas-van Alphen (dHvA)[187,188] effect, the different conduction channels in Weyl semimetals can be dissolved in transport experiments. In SdH measurements with the magnetic field perpendicular to the applied current ($B \perp I$), transport in the Weyl bands should be strongly suppressed, due to the chiral symmetry.[32] In dHvA measurements both parabolic and topological bands can be identified via different effective masses, mobilities and Berry phases. A clear understanding of the position of the Fermi level and the different transport channels is crucial in Weyl semimetals, to analyze whether Weyl fermions take part in the electrical transport and and the precondition for e.g. the measurement of the chiral anomaly[129] is given.

In this study, we conducted dHvA measurements on a NbP single crystal along all three crystal axes of the body-centered tetragonal NbP crystal in a vibrating sample magnetometry (VSM) setup. The measured dHvA oscillations were plotted as a function of $1/B$ and the different oscillation frequencies F_i were extracted by Fourier analysis. For the [100]([010]) direction, we identified four bulk bands $(\beta, \gamma, \delta, \epsilon)$ and for the [001] direction, we found two bulk bands (η, θ). To calculate the Berry phase and the effective masses of each band it is necessary to obtain the temperature- and magnetic field-dependent damping factors for each oscillation frequency. To obtain these parameters, we fitted the measured magnetization M as the superposition of independent, dampened sine functions of F_i for both lattice directions:[115,189]

$$M = a_0 + \sum_{i=1}^{n} A_\mathrm{i} \cdot \sin(2\pi F_\mathrm{i} \frac{1}{B} - \varphi_\mathrm{i}) \cdot \mathrm{e}^{d_\mathrm{i} \frac{1}{B}}. \tag{4.4}$$

As fitted parameters, we obtained the oscillation amplitude A_i, the damping factor d_i, the phase φ_i and a global offset a_0. In **Fig. 4.10 a and b**, the fitted magnetization curves (red) together with the original measurement data (black) at 2.5 K can be seen for the [100] ([010]) and [001] direction, respectively. To examine the topological or trivial character of the bulk bands, we derived different properties from the fitted oscillation parameters.

Firstly, we calculated the Berry phase by using $-\varphi_\mathrm{i} = 2\pi(1/2 - \Gamma + \Delta)$ with the Berry phase $2\pi\Gamma$. Δ is an additional phase shift between ±1/8, which arises due to corrugated Fermi surfaces.[190, 191] For each transport direction, we found one band with a non-trivial Berry phase ≥ 0.25, namely the β-band in the [100] ([010]) direction ($\Gamma + \Delta = 0.54(5)$) and the Θ-band in the [001]-direction ($\Gamma + \Delta = 0.48(1)$). These non-trivial Berry phases hint at the topological, non-trivial nature of these bands. The other transport channels ($\gamma, \delta, \epsilon, \eta$) exhibit a Berry phase of $\Gamma + \Delta \leq 0.25$, which we attribute to a parabolic band structure.

To further explore the topological or trivial nature of the bulk conduction bands, we calculated the effective masses of each conduction band. For this, we used the temperature-dependent plot of the Lifshitz-Kosevich-Shoenberg (LKS)-formula,[18, 20, 113, 114] given by:

$$M(T, B) \propto B^{-\frac{1}{2}} \cdot e^{\lambda T_{\mathrm{D}} B} \cdot \frac{\chi T/B}{\sinh(\chi T/B)}, \tag{4.5}$$

with $\chi = \frac{4\pi^3 k_{\mathrm{B}} m^*}{eh}$ as the fitting parameter. k_{B} is the Boltzmann constant, T_{D} is the Dingle temperature, m^* is the effective mass of the charge carriers, τ is the mean carrier life time, and e is the elementary charge. For the fitting procedure, we used one pronounced oscillation peak at a fixed B for each oscillation frequency. The oscillation amplitude of this oscillation peak was then plotted as a function of the temperature T, as shown in **Fig. 4.11**. To fully distinguish between the magnetization signals from different oscillation frequencies, we used the fitted magnetization from Eq. 4.4 to calculate the effective masses using Eq. 4.5. We find a very low effective mass of $m^*_\beta = 0.048\,m_{\mathrm{e}}$ for the β-band. Combining this low effective mass with the non-trivial Berry phase, it is further indicated that β is indeed a Weyl band. For the Θ-band, we calculated an effective mass of $0.086\,m_{\mathrm{e}}$, which cannot be distinguished from the effective masses of the other, trivial bands ($m^*_\gamma = 0.110\,m_{\mathrm{e}}$, $m^*_\delta = 0.183\,m_{\mathrm{e}}$, $m^*_\epsilon = 0.255\,m_{\mathrm{e}}$, $m^*_\eta = 0.086\,m_{\mathrm{e}}$).

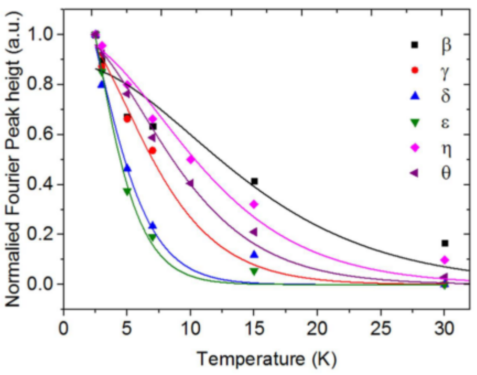

Figure 4.11: Best fits to the T-dependent LKS plots for all bands. There is a slight mismatch between the points and the fit at higher temperatures due to noise in the FFT data, which can lead to the determination of slightly lower effective masses than those in reality, particularly in ϵ and θ (blue and green graphs). Note that the formula only weakly depends on the values for higher temperatures, and the standard errors from the fitting procedure are on the order of 5 %. From the quantization condition $\omega_{\mathrm{C}} \geq k_{\mathrm{B}}T$, we expect oscillations from Weyl- pocket bands and consequently lower effective masses to sustain at higher T, as shown for the β band. Figure taken from Ref. [V]

In a next step, we calculated the carrier mobility μ and the mean carrier life time τ using the Dingle temperature T_{D} with $T_{\mathrm{D}} = h/(4\pi^2 k_{\mathrm{B}} \tau)$ and $\mu = e \cdot \tau / m^*$.[113] Also here, we find that the β-band has a significantly larger mobility ($\mu = 25800\,\mathrm{cm}^2/\mathrm{Vs}$) and mean carrier life time ($\tau = 0.73 \cdot 10^{-12}\,\mathrm{s}$) than the other transport channels (compare Ref. [V], Table 1), which further emphasizes that the β-conduction channel might belong to a Weyl cone, while the other transport channels might rather be of parabolic, non-topological nature.

For the β-band, we calculated the energy distance from the Fermi energy to Weyl node using $E_{\mathrm{F}} = (\hbar k_{\mathrm{F}})^2/m^*$. To determine the Fermi vector k_{F}, we used $A = F_{\mathrm{i}} \cdot 2\pi^2 \Phi_0$, with the Fermi surface cross section $A = \pi k_{\mathrm{F}}^2$ and the magnetic flux quantum Φ_0.[20] We determine the Fermi energy to be $E_{\mathrm{F}} = 3.74\,\mathrm{meV}$. Band structure calculations of NbP predicted two sets of Weyl cones W1 and W2, with E_{F} at 5 meV below and 57 meV above the Weyl cones, respectively.[188] Regarding our analysis, with respect to E_{F}, but also in accordance with the calculated values for m^*, $2\pi\Gamma$, μ, and τ, we identify the β-band with the W1 Weyl cone in NbP, while all other transport channels seem to be of parabolic nature.

Our findings show that due to the weak spin-orbit coupling in NbP,[88] Weyl bands as well as parabolic, non-topological bands are indeed present in NbP. We emphasize that judging the topological or trivial character of the conduction bands solely from the Berry phase may not be accurate, but a number of other charge carrier characteristics like the effective mass, the mobility, the mean charge carrier life time and the Fermi energy have to be taken into account.

4.2.3 [VI] Chiral Magnetoresistance in the Weyl Semimetal NbP

Weyl semimetals[23,24,101,102,192,193] have proven to be a ideal model system to investigate the breakdown of chiral symmetry,[32] a phenomenon that until 2015 had only been observed in particle physics, namely in the decay of a neutral pion into two photons.[127,128] The band structure of Weyl semimetals (as well as the band structure of Dirac semimetals[21,22] that are exposed to sufficiently strong magnetic fields) is characterized by pairs of Weyl cones of opposite chirality, which are spatially separated in momentum space. In general, the chirality – which gives the spin direction of the Weyl fermions with respect to its linear momentum – is a strictly conserved quantum number, which means that the two Weyl cones have to be equally populated. In parallel electric and magnetic fields ($E \parallel B$), there is a breakdown of the chiral symmetry (**Fig. 4.13 a**) and an additional axial current occurs, which can be measured as a negative magnetoresistance (NMR) in $E||B$.[129] NMR that is related to the broken chiral symmetry has been reported lately in numerous Dirac[97,131,132] and Weyl semimetals.[88,133–135] In the presented study (Ref. [VI]), we investigate the chiral anomaly in a NbP micro-ribbon. We utilize Shubnikov-de Haas (SdH)-oscillation measurements with combined band structure calculations to determine the Fermi level of our sample and test whether relativistic Weyl fermions take part in the electrical transport. To verify the chiral anomaly, we investigate the temperature-, magnetic field- and angle-dependence of the NMR of the NbP micro-ribbon for $E||B$.

Within our study, we worked with a NbP micro-ribbon of $50\,\mu\text{m} \times 2.46\,\mu\text{m} \times 526\,\text{nm}$ that was defined by Ga-focused ion beam (FIB) from a NbP bulk sample. The micro-ribbon was defined along the crystal axes of the NbP sample, which were identified by X-ray diffraction (XRD) measurements, compare Ref[VI]. We chose a micro-ribbon geometry for our sample (and applied contact lines over the whole width of the sample) to ensure a homogenous E-field distribution within the sample and avoid the effect of current jetting.[25] Energy dispersive X-ray spectroscopy measurements conducted in a scanning electron microscope showed a 53 % Nb, 45 % P and 2 % Ga composition on the surface of the micro-ribbon. The amorphous layer due to the Ga-FBI is about 20 nm and an exponentially decaying Ga-content deeper into the bulk of the micro-ribbon is assumed.[99] We note that such an amorphous surface layer has no influence on the topological properties on the ribbon.[99]

The NbP micro-ribbon was electrically contacted by laser lithography followed by a metallization process.[159] We conducted magneto-transport measurements from room temperature down to cryogenic temperatures with an applied magnetic field up to ±9 T. The current direction was applied along the [100]-axis and the magnetic field was varied from the [100]-axis (0° – longitudinal transport) to the [001] axis (90° – transverse transport).

To determine the position of the Fermi level in our sample, we conducted SdH-measurements with B applied perpendicular to the current direction I. We observed a positive MR that is proportional to the B^2 for low magnetic fields and proportional to B for high magnetic fields, when the quantum limit is reached.[180] For low T ($T < 50\,\text{K}$), we observe SdH-oscillations (**Fig. 4.12 a**) that are periodic in $1/B$ (**Fig. 4.12 b**). Conducting a Fourier analysis revealed that we observe in total six different SdH oscillation frequencies of 3.47 T, 17.37 T, 24.56 T, 34.63 T, 43.08 T and 71.36 T (**Fig. 4.12 c**). These SdH oscillations frequencies were identified with the different electron and hole pockets of NbP by performing band structure calculations (**Fig. 4.12 d**). At the Fermi surface, NbP exhibits two electron and two hole pockets (E_1, E_2, H_1, and H_2 in **Fig. 4.12 d**).[188] For applied magnetic fields

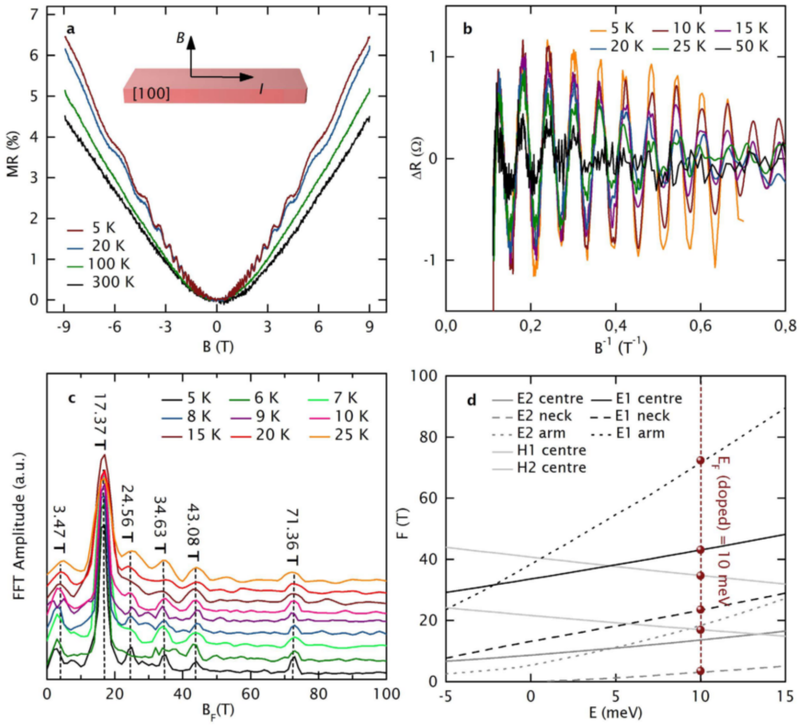

Figure 4.12: Transverse magneto-transport and SdH oscillation analysis. (a) The temperature-dependent, transverse MR reveals non-saturated linearity at high magnetic fields across the entire T range from 5 K – 300 K and SdH oscillations below 75 K. (b) After the subtraction of a non-oscillatory background, the SdH oscillations show a clear periodicity in B^{-1}. (c) FFT spectra from 5 K to 25 K reveal six fundamental SdH frequencies at $F_1 = 3.47\,\mathrm{T}$, $F_2 = 17.37\,T$, $F_3 = 24.56\,T$, $F_4 = 34.63\,T$, $F_5 = 43.08\,T$ and $F_6 = 71.36\,T$. (d) SdH oscillation frequencies F from ab-initio simulations are shown as a function of the energy E relative to the intrinsic Fermi level E_{F0}. Two electron pockets E1 and E2, which each have three extremal obits (neck, arm and center), and two hole pockets H1 and H2 with one extremal orbit are resolved. Matching our experimental data (red dots) to the simulations revealed that $E_{\mathrm{F(doped)}}$ is 10 meV above E_{F0} and consequently 5 meV above the W2 nodes. Figure taken from Ref. [VI].

along the [001] axis, electron pockets show 3 extremal orbits (labeled as neck, center and arm in **Fig. 4.12 d**) and hole pockets show one extremal orbit. From the fit of the experimental data to the theoretically calculated $F(E)$-diagram (**Fig. 4.12 d**), we determined a shift of the Fermi energy of our NbP micro-ribbon of E_{F}(doped)=+10 meV with respect to the intrinsic Fermi level of the bulk sample of E_{F0}.[188] While the W2 Weyl points of the bulk NbP are 5 meV above E_{F0}, which prevents these connected W2 points from exhibiting the chiral anomaly, in our NbP micro-ribbon, the Weyl points are 5 meV below E_{F}, which truly separates them and makes them active for the chiral anomaly.

When we tilted the magnetic field to be aligned parallel to the current direction ($B||I$), we observed a negative magnetoresistance over the whole temperature range from 5 K to 300 K (**Fig. 4.13 b**), which we relate to an additional axial current due to a breakdown of the chiral symmetry[129] (**Fig. 4.13 a**). Note that the longitudinal NMR at 300 K is enhanced by a factor of 2.9 compared to the NMR at 25 K. This observation is attributed to the ionization of Ga, which increases at elevated temperatures and pushes the Fermi level even closer to the W2 Weyl points. Angle-dependent MR measurements (**Fig. 4.13 c**) show that the NMR is extremely sensitive to the angle Φ between B and I. For angles larger than 10°, the NMR vanishes. Overall, the MR can be described by a $\cos^2(\Phi)$-term, which is in accordance with the chiral asymmetry. For low magnetic fields ($< 4\,\mathrm{T}$), we observe a magneto-conductance ($\mathrm{MC} = (G(B) - G(0))/G(B)$), with the conductance without an applied magnetic field $G(0)$ and with an applied magnetic field $G(B)$) that is proportional to B^2 (**Fig. 4.13 d**), which is in accordance with the predictions for the chiral anomaly.[130] For higher magnetic fields ($> 4\,\mathrm{T}$), we observe a linear MC, which is consistent with the transition from multi-Landau level transport for low

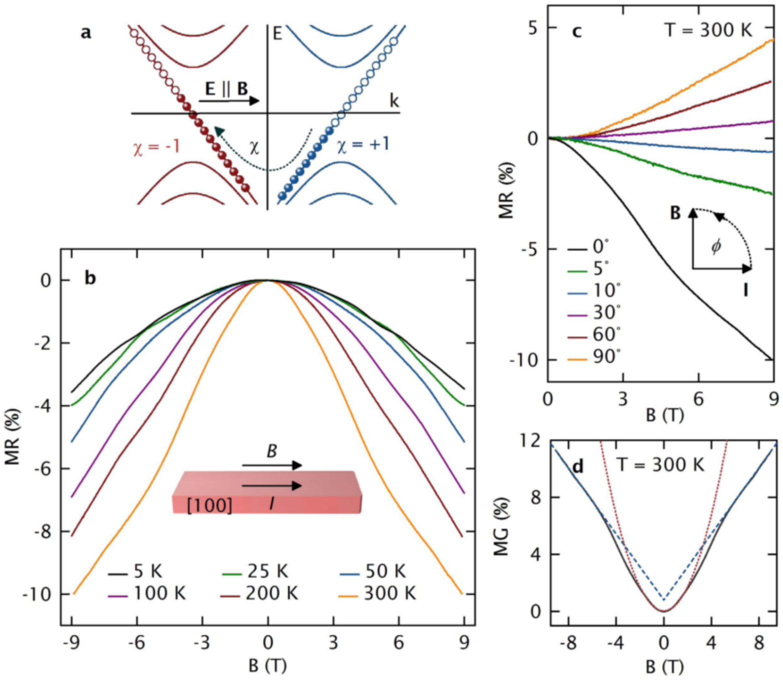

Figure 4.13: Longitudinal magneto-transport – Chiral anomaly-induced negative magnetoresistance. (a) Energy spectrum of left- and right-handed chirality fermions (red and blue, respectively) in parallel applied electric and magnetic fields. In the zeroth Landau level, left-handed particles and right-handed antiparticles have been produced, leading to an additional topological current. (b) Temperature dependence of the NMR in parallel magnetic fields. (c) Angle-dependent MR at 300 K. (d) Positive magneto-conductance at 300 K reveals a parabolic low-field regime that evolves into a linear regime under high magnetic fields. Figure taken from Ref. [VI]

magnetic fields to transport in the quantum limit, e.g. transport only in the lowest Landau level for higher magnetic fields.[180]

In conclusion, we showed that the Fermi level of the NbP-micro-ribbon is shifted by electron doping compared to the Fermi level of a bulk NbP sample[188] by 10 meV, which makes the W2 Weyl cones in NbP active for the chiral anomaly. The breakdown of the chiral symmetry for $B \parallel E$ was shown by the measured temperature, magnetic field and angle dependence of the NMR.

4.2.4 [VII] Experimental Signatures of the Mixed Axial-Gravitational Anomaly in the Weyl Semimetal NbP

The band structure of Weyl semimetals (**Fig. 4.14 a**) exhibits two Weyl cones with massless fermions of opposite chirality, which are well separated in momentum space.[23, 24] When a Weyl semimetal is exposed to parallel electric and magnetic fields ($E||B$), a breakdown of the chiral symmetry occurs - a phenomenon called the chiral anomaly.[32, 129] This configuration of parallel aligned electric and magnetic fields is one but not the only field configuration in which a breakdown of the chiral symmetry occurs. Three-dimensional chiral fermions are also theoretically predicted to exhibit a mixed axial-gravitational anomaly,[136, 137] which is the breakdown of the chiral symmetry in collinear gravitational fields and temperature gradients ($\nabla g||\nabla T$). This mixed axial gravitational anomaly has been proposed to be relevant for the vortical effect in the context of a quark-gluon plasma[111] and for the hydrodynamic description of neutron stars.[138] Experimental evidence for the existence of the mixed axial-gravitational anomaly for ($\nabla g||\nabla T$) has not been reported so far, for lack of experimental access to sufficiently large $\nabla g||\nabla T$. Nevertheless, the presence of the mixed axial-gravitational anomaly has recently been tied to the thermoelectric transport in Weyl semimetals with collinear magnetic fields and temperature gradients ($B||\nabla T$).[111, 112]

In this study, we used thermoelectric measurements conducted on a NbP micro-ribbon to investigate the breakdown of the chiral symmetry due to the mixed axial-gravitational anomaly. The measurements were performed on a NbP micro-ribbon ($50\,\mu\text{m} \times 2.5\,\mu\text{m} \times 500\,\text{nm}$) with the current direction along the [100] axis. We verified that the Weyl fermions of the W2-Weyl cones take part in the electrical transport by determining the Fermi level via SdH-measurements with combined band structure calculations, see Ref. [VI]. The electric and thermoelectric measurements were performed in a DynaCool PPMS system (QuantumDesign). We used the elongated geometry of the NbP sample and applied the contact lines across the full width of the micro-ribbon to provide a homogeneous field distribution and suppress current jetting.[25] To generate a temperature gradient along the NbP sample, we used a resistive heater, which supplies temperature differences of up to 350 mK.

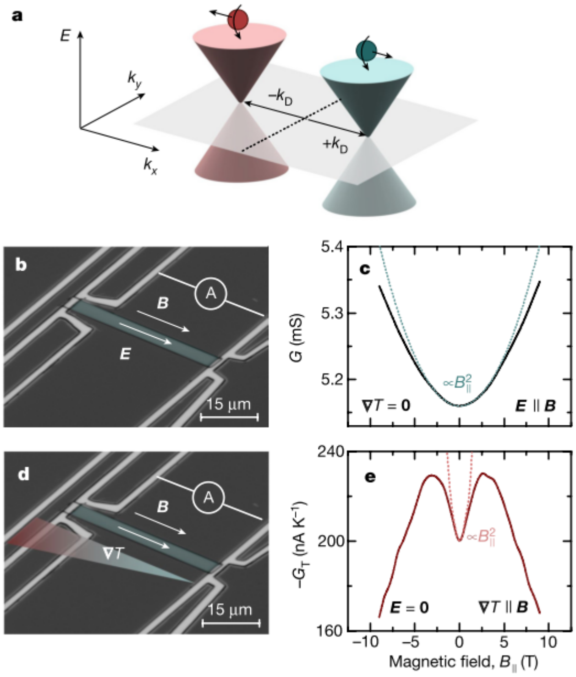

Figure 4.14: Positive magneto-conductance $G(B_{||})$ and magneto-thermoelectric conductance $G_\mathrm{T}(B_{||})$ in the Weyl semimetal NbP. (a) Sketch of two Weyl cones with distinct chiralities $+\chi$ and $-\chi$, represented in green and red, respectively. E, k_x and k_y are the energy and the components of the momentum vector k in x and y directions, respectively. k_D denotes the distance of the chiral nodes from their center point in momentum space. (b(and (c) False-colored optical micro-graphs of the devices used to measure the electrical conductance $G = J/E$ (b) and thermoelectric conductance $G_\mathrm{T} = J/|\nabla T|$ (c). The red and the green ends of the color gradient denote the hot and cold sides of the device, respectively. Four NbP micro-ribbons (green) were investigated, all showing similar results. The data for the first ribbon are presented here. (d) and (e) $G(E\|B)$ (d) and $-G_\mathrm{T}(\nabla T\|B)$ (e) as functions of the magnetic field $B\|$ at a cryostat base temperature of $T = 25\,\mathrm{K}$ (solid lines); the negative sign accounts for electron transport. The dotted lines show the predicted dependence ($\propto B^2$). Figure taken from Ref. [VII]

To verify the breakdown of the chiral symmetry due to the chiral anomaly, we conducted electrical conductance G measurements in parallel electric and magnetic fields (**Fig. 4.14 b**), revealing a positive magneto-conductance (**Fig. 4.14 c**). This positive magneto-conductance is associated with an increasing axial current for increasing magnetic fields as the breakdown of the chiral symmetry occurs.[129] The magneto-conductance changes from $\sim B^2$ as it is typical for multi-Landau-level transport[130] to $\sim B$ at the quantum limit (e.g. approx. 4 T at 25 K in the NbP micro-ribbon, compare Ref. [VI] and Ref. [VII]), where transport only takes place in the lowest Landau level.[180] The positive magneto-conductance analysis is equivalent to the analysis of the negative magnetoresistance measurements, presented in Ref. [VI].

The breakdown of the chiral symmetry due to the mixed axial-gravitational anomaly was investigated in a magnetic field that is applied parallel to a temperature gradient (**Fig. 4.14 d**).The total current J that is flowing through the sample is given by $J = GE + G_\mathrm{T}\nabla T$. We performed the magneto-thermoelectric measurements in a closed circuit setup to ensure $E = 0$ and $J = G_\mathrm{T}\nabla T$ to safely distinguish between measurement signals due to the chiral anomaly for $E||B$ and $\nabla T = 0$ and the mixed axial-gravitational anomaly for $\nabla T||B$ and $E = 0$. In a parallel magnetic field with respect to the temperature gradient and for low magnetic fields where multiple Landau levels contribute to the electric transport, we measure an increasing G_T for increasing B (**Fig. 4.14 e**). This positive magneto-thermoelectric conductance is attributed to an increasing axial current for increasing B, due to the breakdown of the chiral symmetry caused by the mixed axial-gravitational anomaly (**Fig. 4.15 a**). For higher magnetic fields, when transport takes place only in the lowest Landau level, we observe a decreasing $|G_\mathrm{T}|$ for increasing B with the thermoelectric signal approaching $0\,\mathrm{nA/K^{-1}}$, which is attributed to the thermoelectric transport after reaching the quantum limit.[25,194]

To investigate the axial-gravitational anomaly in more detail, we performed temperature- and angle-dependent magneto-thermoelectric conductance measurements. When performing temperature-dependent magneto-thermoelectric conductance measurements, we observe positive magneto-thermoelectric conductance over the whole measured T-range at low magnetic fields (e.g. $B \leq 4\,\mathrm{T}$ at $25\,\mathrm{K}$) from $25\,\mathrm{K}$ to $300\,\mathrm{K}$, as shown in **Fig. 4.15 b**. The decreasing magneto-thermoelectric conductance at higher magnetic fields (e.g. $B \geq 4\,\mathrm{T}$ at $25\,\mathrm{K}$), when the quantum limit is reached, can only be observed up to $150\,\mathrm{K}$. At higher temperatures, the thermal broadening of the density of states at the Fermi energy has become too large to realize electrical transport that is restricted to the lowest Landau level. When we rotate the magnetic field such that there is an angle $\phi > 0°$ between B and ∇T, we observe that the positive thermoelectric conductance is locked to collinear magnetic field and temperature gradient components.[112,139–142] For $\phi > 0°$, a much weaker positive magneto-thermoelectric conductance is observed than for $\phi = 0°$. For large angles, we even observe a negative magneto-thermoelectric conductance. Measuring the magneto-thermoelectric conductance at different angles, reveals a $\sim \cos^2(\phi)$-dependence of the magneto-thermoelectric conductance (**Fig. 4.15 d**), as it is also observed in angle-dependent magneto-conductance measurements (compare **Fig. 4.13 c**).

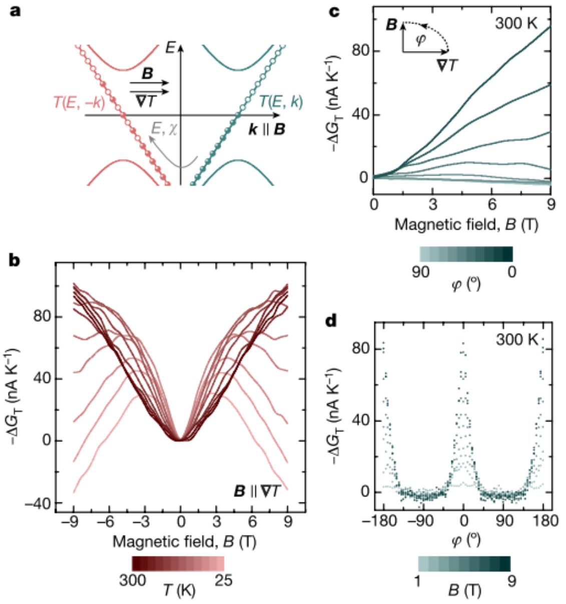

Figure 4.15: Evidence of the mixed axial-gravitational anomaly in NbP. (a) Parallel temperature gradients (∇T) and magnetic fields (B) result in a transfer of particles and energy (E) from one cone to the other. (b) Negative magneto-thermoelectric conductance without zero-field contributions ($-\Delta G_\mathrm{T}$) at selected temperatures (see colour scale), for $B \| \nabla T$. The negative sign accounts for electron transport. (c) $-\Delta G_\mathrm{T}$ versus $|B|$ for different angles φ (colour scale) between the temperature gradient and magnetic field (see inset), at $T = 300\,\mathrm{K}$. The magneto-conductance is negative for $\varphi > 30°$ at high fields. (d) Angular dependence of $-\Delta G_\mathrm{T}$ at $T = 300\,\mathrm{K}$, for varying magnetic field strength (colour scale). Figure taken from Ref. [VII]

In summary, we observed signatures of the mixed axial-gravitational anomaly in magnetic field-, temperature- and angle-dependent thermoelectric transport experiments in the Weyl semimetal NbP. By investigating the mixed axial-gravitational anomaly in a condensed matter system, we realized an experiment that remains elusive in the context of high-energy physics.

5 Conclusion and Outlook

In this thesis, different studies with a focus on thermoelectric transport were conducted to explore the transport phenomena in condensed matter systems belonging to two different research areas. In the beginning of this thesis, magnetic AMR and GMR nanowires were investigated by thermoelectric means in the framework of spincaloritronic transport studies. The second part of this this thesis deals with the band structure characterization by magnetometry as well as electric and thermoelectric transport measurements in the topological non-trivial materials $HfTe_5$ and NbP.

In the field of spincaloritronics, the thermoelectric power output of magnetic nanostructures from two different magnetoresistance regimes were investigated by performing magnetoresistance and magneto-thermopower measurements on CoNi alloy AMR and CoNi/Cu multilayered GMR nanowires.[I] We showed that the thermoelectric power generation from waste heat at the nanoscale is becoming a competitive scenario compared to conventional thermoelectric materials. The thermoelectric power factor of the magnetic nanowires can compete with the power factor of common thermoelectric bulk materials[154] such as Bi_2Te_3 and clearly exceeds the thermoelectric power factors of Bi_2Te_3 nanowires.[160] When we applied an external magnetic field to the magnetic nanowires, the thermoelectric power factor of the AMR wire increased by 13 % and the thermoelectric power factor of the GMR nanowires increased by 52 %, because the prevailing majority spin channel simultaneously exhibits the lower resistivity as well as the higher thermopower compared to the minority spin channel. Magnetic Nanostructures have a higher thermal conductivity[195] compared to the thermoelectric Bi–Sb–Te–Se materials.[196] Additionally the magnetic nanostructures can adjust their transport properties to changing loads and hot spots by an applied magnetic field. Therefore, we suggest magnetoresistive nanostructures for future heat dissipation applications in nano- and microscale electronic devices.

By utilizing current-perpendicular-to-plane magnetoresistance and magnetothermopower measurements on CoNi/Cu multilayered nanowires,[II] we confirmed the linear relation between the thermopower S and the electrical conductivity σ, with the magnetic field as an implicit variable, which is described by the Mott formula.[59] Compared to previous studies, which investigated this linear relation for ferromagnetic systems[7, 8, 74–82] we could additionally identify the thermopower offset value that arises in $S(\sigma)$ plot with the absolute thermopower of the electrical contact material. Thereby, we were able to establish a virtual tool to distinguish between the absolute thermopower contributions within a thermoelectric measurement circuit. Our model needs a thermoelectric measurement circuit that is composed of one non-magnetic material and one ferromagnetic material that is polycrystalline or nanostructured so that a diffusive thermoelectric transport can be assumed and the Mott formula can be applied. Utilizing our model, various systematic studies on the absolute thermopower on metallic, low thermopower materials are possible. For example, the size effect on the phonon-drag[39] in Pt thin films could be further investigated. Our model could be also utilized to distinguish the absolute thermopower contributions in other magnetoresistive systems for example in magnetic tunnel junctions exhibiting TMR.

On CoNi and FeNi nanowires, the magnetic switching process was investigated under the influence of elevated base temperatures and temperature gradients.[III] For increasing base temperatures, we observed decreasing coercive fields, in accordance with the concept of heat-assisted recording technology.[13,14] In contrast, we observed decreasing coercive fields in FeNi but increasing coercive fields in CoNi nanowires for increasing, applied temperature gradients along the nanowire axis. We attribute our observation to a stress-induced enhancement of the magneto-elastic anisotropy contribution to the effective anisotropy of the nanowires due to the applied temperature gradient. We were able to fit our measurements with a simple, quantitative model. With our results we highlight the quite distinct effect of elevated base temperatures and temperature gradients on the switching fields of magnetic nanostructures dependent on their magneto-elastic anisotropy constant and reveal potential engineering challenges in future heat-assisted recording devices.

In the research field of topological insulators and semimetals, we investigated $HfTe_5$, which hosts 2D/3D Dirac fermions[28–30] by means of magnetoresistance and magneto-thermopower measurements.[IV] When applying a magnetic field perpendicular to the transport direction, we observe a positive quadratic, positive linear and saturating magnetoresistance depending on the temperature and magnetic field range. Similar signatures were recently reported for a two-band transport model in Cd_3As_2.[179] For materials with a linear dispersion relation, the observed linear magnetoresistance is often associated with transport exclusively at the lowest Landau level,[117,180] but was recently also tied to a splitting of the Dirac cone when a magnetic field is applied.[181,182] Furthermore, we observe a vanishing magneto-thermoelectric transport for temperatures below 100 K and sufficiently strong magnetic fields, which is the thermoelectric transport signature of the quantum limit.[25,170] Nevertheless, for a final evaluation of the observed transport signatures in $HfTe_5$, the magneto-thermoelectric transport signatures of a two-channel transport model and for the splitting of the Dirac cone are needed. For temperatures between 150 K and 300 K, which is the temperature range that is relevant for thermoelectric applications of $HfTe_5$,[31] we observe an increased thermoelectric power output by up to 40 % for sufficiently strong applied magnetic fields compared to the power output at zero magnetic field. With our magneto-thermoelectric characterization of $HfTe_5$, we contributed to the investigation of the fundamental transport mechanisms in $HfTe_5$ as well as to the optimization of the thermoelectric power output of $HfTe_5$, which might be relevant for future applications.

On a bulk crystal of the Weyl semimetal NbP, we used magnetometry measurements to identify different conduction channels along all fundamental crystal axis.[V] We identified different dHvA oscillation frequencies and fitted the magnetization curves as independent, dampened sine functions of the different oscillation frequencies to calculate the effective mass, the Berry phase, the mobility and the mean charge carrier life time. Our detailed band structure analysis emphasizes that judging about the topological or topological-trivial character of a conduction band by only analyzing the Berry phase may not be sufficient, and other parameters also have to be taken into account. We found several parabolic bands, as expected due to the low SOC in NbP[88] as well as one Weyl band, which we identified with the NbP W2 Weyl band[188] via the calculated distance between the Weyl node and the Fermi energy. Experimental verification that Weyl fermions exist at the Fermi energy within a Weyl semimetal is crucial for the observation of Weyl physics in transport experiments. The presented band structure analysis of the bulk NbP crystal thereby sets the basis of the following NbP transport studies.

In a next step, we performed magnetoresistance measurements on a NbP micro-ribbon.[VI] The micro-ribbon geometry with a high aspect ratio and contact lines across the full width of the sample was chosen to suppress parasitic effects like current jetting.[25] In transverse magnetoresistance measurements, we observed SdH oscillations. Analyzing the SdH oscillation frequencies with combined band structure calculations revealed that the Fermi level of the NbP micro-ribbon was shifted to be 5 meV above the W2 Weyl points, which truly separates the W2 Weyl cones at the Fermi energy and makes them active for the chiral anomaly. The shifted Fermi energy of +10 meV compared to a study of bulk NbP might be caused electron doping due to the Ga-implantation from the FIB micro-ribbon definition. In longitudinal magnetoresistance measurements, we detected a negative magnetoresistance over the whole temperature range. The magnetic field- temperature-, and angle-dependence of the negative magnetoresistance is consistent with transport signatures of the broken chiral symmetry.

With our measurements we confirmed the breakdown of the chiral symmetry – like other recent studies[30,97,131,132,134,135,185] – in a condensed matter system, almost 50 years after the breakdown of the chiral symmetry was established by Adler, Bell and Jackiw[127,128] to explain the decay of a neutral pion into two photons in the research field of particle physics. A next step in the research on broken chiral symmetry in condensed matter systems is the detection of transport signatures of the chiral anomaly in other transport coefficients like the thermopower or the thermal conductivity.

In the last study of this thesis, thermoelectric measurements on a micro-ribbon of the Weyl semimetal NbP are presented.[VII] In collinear magnetic fields and temperature gradients, we observed a breakdown of the chiral symmetry, which results in an increasing thermoelectric conductivity for increasing magnetic fields below the quantum limit. Within the quantum limit, we observed vanishing thermoelectric transport. With different theoretical approaches, the breakdown of the chiral symmetry in collinear magnetic fields and temperature gradients in flat space time was tied to the breakdown of the chiral symmetry in curved space time with collinear magnetic and gravitational fields.[111,112] The breakdown of the chiral symmetry under these experimental conditions is accordingly referred to as the mixed, axial-gravitational anomaly. We confirmed the mixed, axial-gravitational anomaly in NbP with temperature-, magnetic field-, and angle-dependent, thermoelectric measurements. Thereby, we were able to realize an experiment that remains elusive in high-energy physics. Very recent and ongoing research on the mixed-axial-gravitational anomaly tries to verify the according transport signatures of a broken chiral symmetry in thermal conductivity measurements.[197]

Experimental Details

Table 5.1: Definition of the Ti/Pt electrical contact structure for contacting individual, magnetic nanowires.

Step	Process	Parameters
1	Spin coating of LOR-3B lift-off resist (MicroChem)	500 rpm, 5 s, 3500 rpm, 45 s
2	Soft baking on hot plate	180 °C, 4 min 10 s
3	Spin coating of maP-1205 photoresist (micro resist technology)	500 rpm, 5 s, 3500 rpm, 30 s
4	Soft baking on hot plate	100 °C, 30 s
5	Exposure using laser lithography (Heidelberg Instruments, μpG 101)	15 W, 65 %
6	Development using maD-331 (microresist technology)	42 s
7	rinsing with water	
8	drying with N_2	
9	Ar-sputter etching (Torr International, CRC-600)	7.4 mTorr, 30 W, 15 sccm, 10 min
10	Ar-*RF*-magnetron sputtering of Ti (Torr International, CRC-600)	7.4 mTorr, 80 W, 15 sccm, 2 min
11	Ar-DC-magnetron sputtering of Pt (Torr International, CRC-600)	7.4 mTorr, 50 mA, 15 sccm, 15 min
12	Lift-off in Microposit Remover 1165 (Shipley)	80 °C, 20 min
13	rinsing with water	
14	drying with N_2	

Table 5.2: Definition of the Ti/Pt electrical contact structure for contacting individual, NbP and $HfTe_5$ micro-ribbons.

Step	Process	Parameters
1	Spin coating of LOR-3B lift-off resist (MicroChem)	500 rpm, 5 s, 3500 rpm, 45 s
2	Soft baking on hot plate	180 °C, 4 min 10 s
3	Spin coating of maP-1205 photoresist (micro resist technology)	500 rpm, 5 s, 3500 rpm, 30 s
4	Soft baking on hot plate	100 °C, 30 s
5	Exposure using laser lithography (Heidelberg Instruments, μpG 101)	15 W, 65 %
6	Development using maD-331 (microresist technology)	42 s
7	rinsing with water	
8	drying with N_2	
9	Ar-sputter etching (Torr International, CRC-600)	7.4 mTorr, 30 W, 15 sccm, 10 min
10	Ar-RF-magnetron sputtering of Ti (Torr International, CRC-600)	7.4 mTorr, 80 W, 15 sccm, 5 min
11	Ar-DC-magnetron sputtering of Pt (Torr International, CRC-600)	7.4 mTorr, 50 mA, 15 sccm, 30 min
12	rotate the substrate in the sputtering machine by 180 °	
13	Ar-DC-magnetron sputtering of Pt (Torr International, CRC-600)	7.4 mTorr, 50 mA, 15 sccm, 30 min
14	Lift-off in Microposit Remover 1165 (Shipley)	80 °C, 20 min
15	rinsing with water	
16	drying with N_2	

Fundamental Constants

constant	**symbol**	**value**	**unit**
electron mass	m_e	$9.1094 \cdot 10^{-31}$	kg
electron charge	e	$1.6022 \cdot 10^{-19}$	As
Plank constant	$\hbar$	$1.0546 \cdot 10^{-34}$	Js
Boltzmann constant	k_B	$1.3806 \cdot 10^{-23}$	JK^{-1}

Bibliography

[1] H. J. Goldsmid. *Introduction to Thermoelectricity.* Springer Series in Material Science, 2009.

[2] G . J. Snyder and E. S. Toberer. Complex thermoelectric materials. *Nat. Mater.*, **7**(2), 2008.

[3] A. Shakouri. Recent Developments in Semiconductor Thermoelectric Physics and Materials. *Annu. Rev. Mater. Res.*, **41**: p. 399–431, 2011.

[4] G. E. W. Bauer, E. Saitoh, and B. J. van Wees. Spin caloritronics. *Nat. Mater.*, **11**(5), 2012.

[5] K. Uchida, S. Takahashi, K. Harii, J. Ieda, W. Koshibae, K. Ando, S. Maekawa, and E. Saitoh. Observation of the spin Seebeck effect. *Nature*, **45**(7214), 2008.

[6] D. Meier, D. Reinhardt, M. van Straaten, C. Klewe, M. Althammer, M. Schreier, S. T. B. Goennenwein, A. Gupta, M. Schmid, C. H. Back, J.-M. Schmalhorst, T. Kuschel, and G. Reiss. Longitudinal spin Seebeck effect contribution in transverse spin Seebeck effect experiments in Pt/YIG and Pt/NFO. *Nat. Commun.*, **6**: p. 8211, 2015.

[7] A. D. Avery, M. R. Pufall, and B. L. Zink. Determining the planar Nernst effect from magnetic-field-dependent thermopower and resistance in nickel and permalloy thin films. *Phys. Rev. B*, **86**(184408), 2012.

[8] J. Shi, S. S. P. Parkin, L. Xing, and M. B. Salamon. Giant magnetoresistance and magnetothermopower in Co/Cu multilayers. *J. Magn. Magn. Mater.*, **12**(3), 1993.

[9] M. Walter, J. Walowski, V. Zbarsky, M. Münzenberg, M. Schäfers, D. Ebke, G. Reiss, A. Thomas, P. Peretzki, M. Seibt, J. S. Moodera, M. Czerner, M. Bachmann, and C. Heiliger. Seebeck Effect in Magnetic Tunnel Junctions. *Nat. Mater.*, **10**(10), 2011.

[10] G. Pennelli. Review of nanostructured devices for thermoelectric applications. *Beilstein J. Nanotechnol.*, **5**(1), 2014.

[11] D. Zhao and G. Tan. A review of thermoelectric cooling: Materials, modeling and applications. *Appl. Therm. Eng.*, **66**(1-2), 2014.

[12] J. Lee, M. Asheghi, and K. E. Goodson. Impact of thermoelectric phenomena on phase-change memory performance metrics and scaling. *Nanotechnology*, **23**(205201), 2012.

[13] M. H. Kryder, E. C. Gage, T. W. McDaniel, Wi. A. Challener, R. E. Rottmayer, G. Ju, Y.-T. Hsia and M. F. Erden. Heat assisted magnetic recording. *Proc. IEEE*, **96**(11), 2008.

[14] R.E. Rottmayer, S. Batra, D. Buechel, W.A. Challener, J. Hohlfeld, Y. Kubota, L. Li, B. Lu, C. Mihalcea, K. Mountfield, K. Pelhos, C. Peng, T. Rausch, M.A. Seigler, D. Weller, and X. Yang. Heat-Assisted Magnetic Recording. *IEEE Trans. Magn.*, **42**(10), 2006.

[15] J. Gooth, G. Schierning, C. Felser, and K. Nielsch. Quantum materials for thermoelectricity. *MRS Bull.*, **43**(3), 2018.

[16] H. Zhang, C.-X. Liu, X.-L. Qi, X. Dai, Z. Fang, and S.-C. Zhang. Topological insulators in Bi_2Se_3, Bi_2Te_3 and Sb_2Te_3 with a single Dirac cone on the surface. *Nat. Phys.*, **5**(6), 2009.

[17] J. Zhang, C.-Z. Chang, Z. Zhang, J. Wen, X. Feng, K. Li, M. Liu, K. He, L. Wang, X. Chen, Q.-K. Xue, X. Ma, and Y. Wang. Band structure engineering in $(Bi_{1-x}Sb_x)_2Te_3$ ternary topological insulators. *Nat. Commun.*, **2**: p. 574, 2011.

[18] B. Hamdou, J. Gooth, A. Dorn, E. Pippel, and K. Nielsch. Surface state dominated transport in topological insulator Bi_2Te_3 nanowires. *Appl. Phys. Lett.*, **10**(193107), 2013.

[19] B. Hamdou, J. Gooth, A. Dorn, E. Pippel, and K. Nielsch. Aharonov-Bohm oscillations and weak antilocalization in topological insulator Sb_2Te_3 nanowires. *Appl. Phys. Lett.*, **10**(223110), 2013.

[20] J. Gooth, B. Hamdou, A. Dorn, R. Zierold, and K. Nielsch. Resolving the Dirac cone on the surface of Bi_2Te_3 topological insulator nanowires by field-effect measurements. *Appl. Phys. Lett.*, **10**(243115), 2014.

[21] S. M. Young, S. Zaheer, J. C Y Teo, C. L. Kane, E. J. Mele, and A. M. Rappe. Dirac semimetal in three dimensions. *Phys. Rev. Lett.*, **10**(140405), 2012.

[22] S. Borisenko, Q. Gibson, D. Evtushinsky, V. Zabolotnyy, B. Büchner, and R. J. Cava. Experimental realization of a three-dimensional Dirac semimetal. *Phys. Rev. Lett.*, **11**(027603), 2014.

[23] X. Wan, A. M. Turner, A. Vishwanath, and S. Y. Savrasov. Topological semimetal and Fermi-arc surface states in the electronic structure of pyrochlore iridates. *Phys. Rev. B*, **83**(205101), 2011.

[24] S.-Y. Xu, I. Belopolski, N. Alidoust, M. Neupane, G. Bian, C. Zhang, R. Sankar, G. Chang, Z. Yuan, C.-C. Lee, S.-M. Huang, H. Zheng, J. Ma, D. S. Sanchez, B. Wang, A. Bansil, F. Chou, P. P. Shibayev, H. Lin, S. Jia, and M. Z. Hasan. Discovery of a Weyl fermion semimetal and topological Fermi arcs. *Science*, **34**(6248), 2015.

[25] M. Hirschberger, S. Kushwaha, Z. Wang, Q. Gibson, S. Liang, C. A. Belvin, B. A. Bernevig, R. J. Cava, and N. P. Ong. The chiral anomaly and thermopower of Weyl fermions in the half-Heusler GdPtBi. *Nat. Mater.*, **15**(11), 2016.

[26] J. P. Moore and R. S. Graves. Absolute Seebeck coefficient of platinum from 80 to 340 K and the thermal and electrical conductivities of lead from 80 to 400 K. *J. Appl. Phys.*, **44**(1174), 1973.

[27] R. B. Roberts. The absolute scale of thermoelectricity II. *Philos. Mag. Part B*, **43**(6), 1981.

[28] H. Weng, X. Dai, and Z. Fang. Transition-Metal Pentatelluride $ZrTe_5$ and $HfTe_5$: A Paradigm for Large-Gap Quantum Spin Hall Insulators. *Phys. Rev. X*, **4**(011002), 2014.

[29] Y. Zhang, C. Wang, G. Liu, A. Liang, L. Zhao, J. Huang, Q. Gao, B. Shen, J. Liu, C. Hu, W. Zhao, G. Chen, X. Jia, L. Yu, L. Zhao, S. He, F. Zhang, S. Zhang, F. Yang, Z. Wang, Q. Peng, C. Xu, Z. Chen, and X. Zhou. Temperature-induced Lifshitz transition in topological insulator candidate $HfTe_5$. *Sci. Bull.*, **62**(950), 2017.

[30] H. Wang, C.-K. Li, H. Liu, J. Yan, J. Wang, J. Liu, Z. Lin, Y. Li, Y. Wang, L. Li, D. Mandrus, X. C. Xie, J. Feng, and J. Wang. Chiral anomaly and ultrahigh mobility in crystalline $HfTe_5$. *Phys. Rev. B*, **93**(165127), 2016.

[31] R. T . Littleton, T. M. Tritt, J. W. Kolis, and D. R. Ketchum. Transition-metal pentatellurides as potential low-temperature thermoelectric refrigeration materials. *Phys. Rev. B*, **60**(19), 1999.

[32] A. Burkov. Chiral anomaly without relativity. *Science*, **35**(6259), 2015.

[33] D. K. C. MacDonald. *Thermoelectricity - An Introduction to the Principles.* Dover Publications, New York, 2006.

[34] T. J. Seebeck. Ueber die magnetische Polarization der Metalle und Erze durch Temperaturdifferenz. *Ann. Phys.*, **82**(3), 1826.

[35] J. C. A. Peltier. Nouvelles expériences sur la caloricité des courants électrique. *Ann. Chim. Phys.*, **56**: p. 371, 1834.

[36] W. Thomson. On a Mechanical Theory of Thermo-Electric Currents. *Proc. R. Soc. Edinburgh*, **3**: p. 91–98, 1857.

[37] W. Thomson. IX. – On the Dynamical Theory of Heat. Part V. Thermoelectric Currents. *Trans. R. Soc. Edinburgh*, **21**(1), 1857.

[38] C. Herring, T. H. Geballe, and J. E. Kunzler. Phonon-Drag Thermomagnetic Effects in n-Type Germanium. I. General Survey. *Phys. Rev.*, **11**(1), 1958.

[39] R. P. Huebener. Size Effect on Phonon Drag in Platinum. *Phys. Rev.*, **14**(5A), 1965.

[40] C. Kittel. *Einführung in die Festkörperphysik.* Oldenbourg Wissenschaftsverlag GmbH, 2009.

[41] G. Wiedemann and R. Franz. Ueber die Wärme-Leitfähigkeit der Metalle. *Ann. der Phys. und Chemie*, **16**(8), 1853.

[42] G. S. Nolas, D. T. Morelli, and T. M. Tritt. SKUTTERUDITES: A Phonon-Glass-Electron Crystal Approach to Advanced Thermoelectric Energy Conversion Applications. *Annu. Rev. Mater. Res.*, **29**: p. 89–116, 1999.

[43] T. M. Tritt and M. A. Subramanian. Thermoelectric Materials, Phenomena, and Applications: A Bird's Eye View. *MRS Bull.*, **31**(3), 2006.

[44] L. E. Bell. Cooling, Heating, Generating Power, and Recovering Waste Heat with Thermoelectric Systems. *Science*, **32**(5895), 2008.

[45] L. D. Hicks and M. S. Dresselhaus. Effect of quantum-well structures on the thermomagnetic figure of merit. *Phys. Rev. B*, **47**(19), 1993.

[46] L. D. Hicks and M. S. Dresselhaus. Thermoelectric figure of merit of a one-dimensional conductor. *Phys. Rev. B*, **47**(24), 1993.

[47] J. Gooth, J. G. Gluschke, R. Zierold, M. Leijnse, H. Linke, and K. Nielsch. Thermoelectric performance of classical topological insulator nanowires. *Semicond. Sci. Technol.*, **30**(015015), 2015.

[48] M. Getzlaff. *Fundamentals of magnetism.* Springer Science & Business Media, 2007.

[49] S. Blundell. *Magnetism in condensed Matter.* Oxford University Press, 2001.

[50] L. Bergmann, C. Schäfer, and R. Kassinger. *Lehrbuch der Experimentalphysik 6. Festkörper.* De Grruyter, New York, Berlin, 2005.

[51] V. Vega, T. Böhnert, S. Martens, M. Waleczek, J. M. Montero-Moreno, D. Görlitz, V. M. Prida, and K. Nielsch. Tuning the magnetic anisotropy of Co–Ni nanowires: comparison between single nanowires and nanowire arrays in hard-anodic aluminum oxide membranes. *Nanotechnology*, **23**(46), 2012.

[52] L. G. Vivas, M. Vazquez, J. Escrig, S. Allende, D. Altbir, D. C. Leitao, and J. P. Araujo. Magnetic anisotropy in CoNi nanowire arrays: Analytical calculations and experiments. *Phys. Rev. B*, **85**(035439), 2012.

[53] T. R. McGuire and R. I. Potter. Anisotropic Magnetoresistance in Ferromagnetic 3d Alloys. *IEEE Trans. Magn.*, **11**(4), 1975.

[54] L. F. Yin, D. H. Wei, N. Lei, L. H. Zhou, C. S. Tian, G. S. Dong, X. F. Jin, L. P. Guo, Q. J. Jia, and R. Q. Wu. Magnetocrystalline anisotropy in permalloy revisited. *Phys. Rev. Lett.*, **97**(067203), 2006.

[55] C. Tannous and J. Gieraltowski. The Stoner–Wohlfarth model of Ferromagnetism. *Eur. J. Phys.*, **29**(3), 2008.

[56] A. Kumar, S. Fähler, H. Schlörb, K. Leistner, and L. Schultz. Competition between shape anisotropy and magnetoelastic anisotropy in Ni nanowires electrodeposited within alumina templates. *Phys. Rev. B*, **73**(064421), 2006.

[57] B. D. Cullity and C. D. Graham. *Introduction to Magnetic Materials.* John Wiley & Sons, 2011.

[58] R. K. Pirota, E. L Silva, D. Zanchet, D. Navas, M. Vázquez, M. Hernández-Vélez, and M. Knobel. Size effect and surface tension measurements in Ni and Co nanowires. *Phys. Rev. B*, **76**(233410), 2007.

[59] N. F. Mott and H. Jones. *The Theory of the Properties of Metals and Alloys.* Clarendon, Oxford, 1936.

[60] N. F. Mott. The Resistance and Thermoelectric Properties of the Transition Metals. *Proc. R. Soc. London A*, **15**: p. 368–382, 1936.

[61] A. Fert and I. A. Campbell. Two-Current conduction in Nickel. *Phys. Rev. Lett.*, **21**(16), 1968.

[62] W. Thomson. On the Electro-Dynamic Qualities of Metals: Effects of Magnetization on the Electric Conductivity of Nickel and of Iron. *Proc. R. Soc. London*, **8**: p. 546–550, 1856.

[63] M. N. Baibich, J. M. Broto, A. Fert, F. Nguyen Van Dau, F. Petroff, P. Eitenne, G. Creuzet, A. Friederich, and J. Chazelas. Giant magnetoresistance of (001)Fe/(001)Cr magnetic superlattices. *Phys. Rev. Lett.*, **61**(21), 1988.

[64] G. Binasch, P. Grünberg, F. Saurenbach, and W. Zinn. Enhanced magnetoresistance in layered magnetic structures with antiferromagnetic interlayer exchange. *Phys. Rev. B*, **39**(7), 1989.

[65] S. S. P. Parkin, Z. G. Li, and D. J. Smith. Giant magnetoresistance in antiferromagnetic Co/Cu multilayers. *Appl. Phys. Lett.*, **58**(2710), 1991.

[66] H. Kano, K. Kagawa, A. Suzuki, A. Okabe, K. Hayashi, and K. Aso. Substrate temperature effect on giant magnetoresistance of sputtered Co/Cu multilayers. *Appl. Phys. Lett.*, **63**(2839), 1993.

[67] P. R. Evans, G. Yi, and W. Schwarzacher. Current perpendicular to plane giant magnetoresistance of multilayered nanowires electrodeposited in anodic aluminum oxide membranes. *Appl. Phys. Lett.*, **76**(481), 2000.

[68] S. S. P. Parkin, N. More, and K. P. Roche. Oscillations in Exchange Coupling and Magnetoresistance in Metallic Superlattice Structures: Co/Ru, Co/Cr, and Fe/Cr. *Phys. Rev. Lett.*, **64**(19), 1990.

[69] R. Sizmann. Investigation of Electron Spin Polarization in Ferromagnets. *Nucl. Instruments Methods*, **13**: p. 523–533, 1976.

[70] R. Mitdank, M. Handwerg, C. Steinweg, W. Töllner, M. Daub, K. Nielsch, and S. F. Fischer. Enhanced magneto-thermoelectric power factor of a 70 nm Ni-nanowire. *J. Appl. Phys.*, **11**(104320), 2012.

[71] E. Villamor, M. Isasa, L. E. Hueso, and F. Casanova. Temperature dependence of spin polarization in ferromagnetic metals using lateral spin valves. *Phys. Rev. B*, **88**(18441), 2013.

[72] A. P. Mihai, J. P. Attané, A. Marty, P. Warin, and Y. Samson. Electron-magnon diffusion and magnetization reversal detection in FePt thin films. *Phys. Rev. B*, **77**(060401(R)), 2008.

[73] N. F. Mott and H. Jones. *The Theory of the Properties of Metals and Alloys.* Clarendon Press, Oxford, 1936.

[74] T. Böhnert, V. Vega, A.-K. Michel, V. M. Prida, and K. Nielsch. Magneto-thermopower and magnetoresistance of single Co-Ni alloy nanowires. *Appl. Phys. Lett.*, **10**(9), 2013.

[75] L. Gravier, A. Fábián, A. Rudolf, A. Cachin, J. E. Wegrowe, and J. Ph. Ansermet. Spin-dependent thermopower in Co/Cu multilayer nanowires. *J. Magn. Magn. Mater.*, **27**(2-3), 2004.

[76] J. Sakurai, D. Huo, T. Kuwai, K. Mori, T. Hihara, K. Sumiyama, and K. Suzuki. The Sign of Magneto-Thermoelectric Power of Magnetic Granular Alloys. *J. Phys. Soc. Jpn.*, **66**(8), 1997.

[77] J. Shi, K. Pettit, E. Kita, S. S. P. Parkin, R. Nakatani, and M. B. Salamon. Field-dependent thermoelectric power and thermal conductivity in multilayered and granular giant magnetoresistive systems. *Phys. Rev. B*, **54**(21), 1996.

[78] M. J. Conover, M. B. Brodsky, J. E. Mattson, C. H. Sowers, and S. D. Bader. Magnetothermopower of Fe/Cr superlattices. *J. Magn. Magn. Mater.*, **10**(1-2), 1991.

[79] J. Shi, R. C. Yu, S. S. P. Parkin, and M. B. Salamon. Magnetothermopower of Co/Cu multilayers. *J. Appl. Phys.*, **73**(5524), 1993.

[80] H. Sato, K. Honda, Y. Aoki, N. Kataoka, I. J. Kim, and K. Fukamichi. Transport properties in Co–Cu granular alloy. *J. Magn. Magn. Mater.*, **15**(1-2), 1996.

[81] J. Shi, E. Kita, L. Xing, and M. B. Salamon. Magnetothermopower of a $Ag_{80}Co_{20}$ granular system. *Phys. Rev. B*, **48**(21), 1993.

[82] H. Sato. Field dependence of transport properties correlated with the giant magnetoresistance. *Mater. Sci. Eng. B*, **31**(1-2), 1995.

[83] A. Soni and G. S. Okram. Size-dependent thermopower in nanocrystalline nickel. *Appl. Phys. Lett.*, **95**(013101), 2009.

[84] M. C. Cadeville and J. Rousse. Thermoelectric power and electronic structure of dilute alloys of nickel and cobalt with d transition elements. *J. Phys. F Met. Phys.*, **1**(686), 1971.

[85] J. S. Dugdale. *The Thermoelectrical Properties of Metals and Alloys.* Edward Arnold, London, 1977.

[86] R. D. Barnard. *Thermoelectricity in Metal and Alloys.* Taylor & Francis, London, 1972.

[87] Z. K. Liu, L. X. Yang, Y. Sun, T. Zhang, H. Peng, H. F. Yang, C. Chen, Y. Zhang, Y. F. Guo, D. Prabhakaran, M. Schmidt, Z. Hussain, S-.K. Mo, C. Felser, B. Yan, and Y. L. Chen. Evolution of the Fermi surface of Weyl semimetals in the transition metal pnictide family. *Nat. Mater.*, **15**(1), 2016.

[88] Z. Wang, Y. Zheng, Z. Shen, Y. Lu, H. Fang, F. Sheng, Y. Zhou, X. Yang, Y. Li, C. Feng, and Z.-A. Xu. Helicity-protected ultrahigh mobility Weyl fermions in NbP. *Phys. Rev. B*, **93**(121112(R)), 2016.

[89] M. Z. Hasan and C. L. Kane. Colloquium: Topological insulators. *Rev. Mod. Phys.*, **82**(4), 2010.

[90] C. H. Li, O. M. J. van't Erve, J. T. Robinson, Y. Liu, L. Li, and B. T. Jonker. Electrical detection of charge-current-induced spin polarization due to spin-momentum locking in Bi_2Se_3. *Nat. Nanotechnol.*, **9**(3), 2014.

[91] J. C. Y. Teo, L. Fu, and C. L. Kane. Surface states and topological invariants in three-dimensional topological insulators: Application to $Bi_{1-x}Sb_x$. *Phys. Rev. B*, **78**(045426), 2008.

[92] D. Hsieh, D. Qian, L. Wray, Y. Xia, Y. S. Hor, R. J. Cava, and M. Z. Hasan. A topological Dirac insulator in a quantum spin Hall phase. *Nature*, **45**(7190), 2008.

[93] A. Damascelli. Probing the Electronic Structure of Complex Systems by ARPES. *Phys. Scr.*, **TI**: p. 61, 2004.

[94] B. Hamdou, J. Gooth, T. Böhnert, A. Dorn, L. Akinsinde, E. Pippel, R. Zierold, and K. Nielsch. Thermoelectric Properties of Band Structure Engineered Topological Insulator $(Bi_{1-x}Sb_x)_2Te_3$ Nanowires. *Advvanced Energy Mater.*, **5**(11500280), 2015.

[95] N. P. Armitage and E. J. Mele. Weyl and Dirac semimetals in three-dimensional solids. *Rev. Mod. Phys.*, **90**(1), 2018.

[96] H. Weyl. Gravitation and the Electron. *Proc. Natl. Acad. Sci. U.S.A.*, **15**: p. 323–334, 1929.

[97] J. Xiong, S. K. Kushwaha, T. Liang, J. W. Krizan, M. Hirschberger, W. Wang, R. J. Cava, and N .P. Ong. Evidence for the chiral anomaly in the Dirac semimetal Na_3Bi. *Science*, **35**(6259), 2015.

[98] Q. Li, D. E. Kharzeev, C. Zhang, Y. Huang, I. Pletikosic, A. V. Fedorov, R. D. Zhong, J. A. Schneeloch, G. D. Gu, and T. Valla. Chiral magnetic effect in $ZrTe_5$. *Nat. Phys.*, **12**(6), 2016.

[99] P. J. W. Moll, N. L. Nair, T. Helm, A. C. Potter, I. Kimchi, A. Vishwanath, and J. G. Analytis. Transport evidence for Fermi-arc-mediated chirality transfer in the Dirac semimetal Cd_3As_2. *Nature*, **53**(7611), 2016.

[100] T. Ojanen. Helical Fermi arcs and surface states in time-reversal invariant Weyl semimetals. *Phys. Rev. B*, **87**(245112), 2013.

[101] L. X. Yang, Z. K. Liu, Y. Sun, H. Peng, H. F. Yang, T. Zhang, B. Zhou, Y. Zhang, Y. F. Guo, M. Rahn, D. Prabhakaran, Z. Hussain, S.-K. Mo, C. Felser, B. Yan, and Y. L. Chen. Weyl semimetal phase in the non-centrosymmetric compound TaAs. *Nat. Phys.*, **11**(9), 2015.

[102] B. Q. Lv, H. M. Weng, B. B. Fu, X. P. Wang, H. Miao, J. Ma, P. Richard, X. C. Huang, L. X. Zhao, G. F. Chen, Z. Fang, X. Dai, T. Qian, and H. Ding. Experimental discovery of Weyl semimetal TaAs. *Phys. Rev. X*, **5**(031013), 2015.

[103] S.-Y. Xu, N. Alidoust, I. Belopolski, Z. Yuan, G. Bian, T.-R. Chang, H. Zheng, V. N. Strocov, D. S. Sanchez, G. Chang, C. Zhang, D. Mou, Y. Wu, L. Huang, C.-C. Lee, S.-M. Huang, B. Wang, A. Bansil, H.-T. Jeng, T. Neupert, A. Kaminski, H. Lin, S. Jia, and M. Z. Hasan. Discovery of a Weyl fermion state with Fermi arcs in niobium arsenide. *Nat. Phys.*, **11**(9), 2015.

[104] Su.-Y. Xu, I. Belopolski, D. S. Sanchez, C. Zhang, G. Chang, C. Guo, G. Bian, Z. Yuan, H. Lu, T.-R. Chang, P. P. Shibayev, M. L. Prokopovych, N. Alidoust, H. Zheng, C.-C. Lee, S.-M. Huang, R. Sankar, F. Chou, C.-H. Hsu, H.-T. Jeng, A. Bansil, T. Neupert, V. N. Strocov, H. Lin, S. Jia, and M. Z. Hasan. Experimental discovery of a topological Weyl semimetal state in TaP. *Sci. Adv.*, **1**(10), 2015.

[105] A. A. Soluyanov, D. Gresch, Z. Wang, Q. Wu, M. Troyer, X. Dai, and B. A. Bernevig. Type-II Weyl semimetals. *Nature*, **52**(7579), 2015.

[106] P. Li, Y. Wen, X. He, Q. Zhang, C. Xia, Z.-M. Yu, S. A. Yang, Z. Zhu, H. N. Alshareef, and X.-X. Zhang. Evidence for topological type-II Weyl. *Nat. Commun.*, **8**(1), 2017.

[107] Y. Sun, S.-C. Wu, M. N. Ali, C. Felser, and B. Yan. Prediction of Weyl semimetal in orthorhombic $MoTe_2$. *Phys. Rev. B*, **92**(161107(R)), 2015.

[108] Z. Wang, D. Gresch, A. A. Soluyanov, W. Xie, S. Kushwaha, X. Dai, M. Troyer, R. J. Cava, and B. A. Bernevig. $MoTe_2$: A Type-II Weyl Topological Metal. *Phys. Rev. Lett.*, **11**(056805), 2016.

[109] T.-R. Chang, S.-Y. Xu, G. Chang, C.-C. Lee, S.-M. Huang, B. Wang, G. Bian, H. Zheng, D. S. Sanchez, I. Belopolski, N. Alidoust, M. Neupane, A. Bansil, H.-T. Jeng, H. Lin, and M. Z. Hasan. Prediction of an arc-tunable Weyl Fermion metallic state in $Mo_xW_{1-x}Te_2$. *Nat. Commun.*, **7**: p. 10639, 2016.

[110] H. Yang, Y. Sun, Y. Zhang, W.-J. Shi, S. S. P. Parkin, and B. Yan. Topological Weyl semimetals in the chiral antiferromagnetic materials Mn_3Ge and Mn_3Sn. *New J. Phys.*, **19**(015008), 2017.

[111] K. Landsteiner, E. Megías, and F. Pena-Benitez. Gravitational anomaly and transport phenomena. *Phys. Rev. Lett.*, **10**(021601), 2011.

[112] A. Lucas, R. A. Davison, and S. Sachdev. Hydrodynamic theory of thermoelectric transport and negative magnetoresistance in Weyl semimetals. *Proc. Natl. Acad. Sci.*, **11**(34), 2016.

[113] D. Shoenberg. *Magnetic oscillations in metals*. Cambridge University Press, Cambridge, 1984.

[114] C. Shekhar, A. K. Nayak, Y. Sun, M. Schmidt, M. Nicklas, I. Leermakers, U. Zeitler, Y. Skourski, J. Wosnitza, Z. Liu, Y. Chen, W. Schnelle, H. Borrmann, Y. Grin, C. Felser, and B. Yan. Extremely large magnetoresistance and ultrahigh mobility in the topological Weyl semimetal candidate NbP. *Nat. Phys.*, **11**(8), 2015.

[115] J. Hu, J. Y. Liu, D. Graf, S. M. A. Radmanesh, D. J. Adams, A. Chuang, Y. Wang, I. Chiorescu, J. Wei, L. Spinu, and Z. Q. Mao. π Berry phase and Zeeman splitting of Weyl semimetal TaP. *Sci. Rep.*, **6**: p. 18674, 2016.

[116] S.-Q. Shen. *Topological Insulators*. Springer Series in Solid-State Science, 2017.

[117] A . A. Abrikosov. Quantum linear magnetoresistance; solution of an old mystery. *J. Phys. A. Math. Gen.*, **36**(9119), 2003.

[118] K. Behnia, L. Balicas, and Y. Kopelevich. Signatures of Electron Fractionalization in Ultraquantum Bismuth. *Science*, **31**(5845), 2007.

[119] C.-l. Zhang, B. Tong, Z. Yuan, Z. Lin, J. Wang, J. Zhang, C.-Y. Xi, Z. Wang, S. Jia, and C. Zhang. Signature of chiral fermion instability in the Weyl semimetal TaAs above the quantum limit. *Phys. Rev. B*, **94**(205120), 2016.

[120] H. Wang, H. Liu, Y. Li, Y. Liu, J. Wang, J. Liu, Y. Wang, L. Li, J. Yan, D. Mandrus, X . C. Xie, and J. Wang. Discovery of Log-Periodic Oscillations in Ultra-Quantum Topological Materials. *arXiv:1704.00995v2*, 2018.

[121] D. C. Tsui, H. L. Stormer, and A. C. Gossard. Two-Dimensional Magnetotransport in the Extreme Quantum Limit. *Phys. Rev. Lett.*, **48**(22), 1982.

[122] A. V. Shytov, M. I. Katsnelson, and L. S. Levitov. Atomic collapse and quasi-Rydberg states in graphene. *Phys. Rev. Lett.*, **99**(246802), 2007.

[123] O. Ovdat, J. Mao, Y. Jiang, E. Y. Andrei, and E. Akkermans. Observing a scale anomaly and a universal quantum phase transition in graphene. *Nat. Commun.*, **8**(1), 2017.

[124] M. Sun. Magnetic Manifestation of Discrete Scaling Symmetry in Dirac Semimetals. *arXiv:1805.02074v1*, 2018.

[125] P. Zhang and H. Zhai. Efimov Effect in the Dirac Semi-metals. *arXiv:1711.03118v1*, 2017.

[126] H. Liu, H. Jiang, Z. Wang, R. Joynt, and X. C. Xie. Discrete Scale Invariance in Topological Semimetals. *arXiv:1807.02459v1*, 2018.

[127] S. L. Adler. Axial-vector vertex in spinor electrodynamics. *Phys. Rev.*, **17**(5), 1969.

[128] J. S. Bell and R. Jackiw. A PCAC puzzle: $\pi^0 \rightarrow \gamma\gamma$ in the σ-model. *Phys. Rev.*, **17**(2426), 1969.

[129] H. B. Nielsen and M. Ninomiya. The Adler-Bell-Jackiw anomaly and Weyl fermions in a crystal. *Phys. Lett.*, **13**(6), 1983.

[130] D. T. Son and B. Z. Spivak. Chiral anomaly and classical negative magnetoresistance of Weyl metals. *Phys. Rev. B*, **88**(104412), 2013.

[131] H. Li, H. He, H.-Z. Lu, H. Zhang, H. Liu, R. Ma, Z. Fan, S.-Q. Shen, and J. Wang. Negative Magnetoresistance in Dirac Semimetal Cd_3As_2. *Nat. Commun.*, **7**(10301), 2015.

[132] C. Z. Li, Li.-X. Wang, H. Liu, Jian Wang, Z.-M. Liao, and D.-P. Yu. Giant negative magnetoresistance induced by the chiral anomaly in individual Cd_3As_2 nanowires. *Nat. Commun.*, **6**: p. 10137, 2015.

[133] X. Huang, L. Zhao, Y. Long, P. Wang, D. Chen, Z. Yang, H. Liang, M. Xue, H. Weng, Z. Fang, X. Dai, and G. Chen. Observation of the chiral-anomaly-induced negative magnetoresistance: In 3D Weyl semimetal TaAs. *Phys. Rev. X*, **5**(031023), 2015.

[134] X. Yang, Y. Li, Z. Wang, Y. Zheng, and Z. Xu. Chiral anomaly induced negative magnetoresistance in topological Weyl semimetal NbAs. *arXiv:1506.03190v1*, 2015.

[135] Y. Wang, E. Liu, H. Liu, Y. Pan, L. Zhang, J. Zeng, Y. Fu, M. Wang, K. Xu, Z. Huang, Z. Wang, H.-Z. Lu, D. Xing, B. Wang, X. Wan, and F. Miao. Gate-Tunable Negative Longitudinal Magnetoresistance in the Predicted Type-II Weyl Semimetal WTe_2. *Nat. Commun.*, **7**: p. 13142, 2016.

[136] L. Alvarez-Gaumé and E. Witten. Gravitational anomalies. *Nucl. Phys. B*, **23**(2), 1983.

[137] T. Eguchi and G. O. Freund. Quantum Gravity and World Topology. *Phys. Rev. Lett.*, **37**(19), 1976.

[138] M. Kaminski, C. F. Uhlemann, M. Bleicher, and J. Schaffner-Bielich. Anomalous hydrodynamics kicks neutron stars. *Phys. Lett.*, **76**: p. 170–174, 2016.

[139] R. Lundgren, P. Laurell, and G. A. Fiete. Thermoelectric properties of Weyl and Dirac semimetals. *Phys. Rev.*, **90**(165115), 2014.

[140] K.-S. Kim. Role of axion electrodynamics in a Weyl metal: Violation of Wiedemann-Franz law. *Phys. Rev. B*, **90**(121108), 2014.

[141] G. Sharma, P. Goswami, and S. Tewari. Nernst and magnetothermal conductivity in a lattice model of Weyl fermions. *Phys. Rev. B*, **93**(035116), 2016.

[142] B. Z. Spivak and A. V. Andreev. Magnetotransport phenomena related to the chiral anomaly in Weyl semimetals. *Phys. Rev. B*, **93**(085107), 2016.

[143] J. M. Luttinger. Theory of thermal transport coefficients. *Phys. Rev.*, **13**(6A), 1964.

[144] J. Bachmann, R. Zierold, Y. T. Chong, R. Hauert, C. Sturm, R. Schmidt-Grund, B. Rheinländer, M. Grundmann, U. Gösele, and K. Nielsch. A practical, self-catalytic, atomic layer deposition of silicon dioxide. *Angew. Chemie - Int. Ed.*, **47**(33), 2008.

[145] J. Lee, S. Farhangfar, R. Yang, R. Scholz, M. Alexe, U. Gösele, J. Lee and K. Nielsch. A novel approach for fabrication of bismuth-silicon dioxide core-shell structures by atomic layer deposition. *J. Mater. Chem.*, **19**(38), 2009.

[146] M. S. Salem, P. Sergelius, R. Zierold, J. M. Montero Moreno, D. Görlitz, and K. Nielsch. Magnetic characterization of nickel-rich NiFe nanowires grown by pulsed electrodeposition. *J. Mater. Chem.*, **22**(17), 2012.

[147] T. Böhnert, A. C. Niemann, A.-K. Michel, S. Bäßler, J. Gooth, B. G. Tóth, K. Neuróhr, L. Péter, I. Bakonyi, V. Vega, V. M. Prida, and K. Nielsch. Magnetothermopower and magnetoresistance of single Co–Ni/Cu multilayered nanowires. *Phys. Rev. B*, **90**(165416), 2014.

[148] B. G. Tóth, L. Péter, J. Dégi, Á Révész, D. Oszetzky, G. Molnár, and I. Bakonyi. Influence of Cu deposition potential on the giant magnetoresistance and surface roughness of electrodeposited Ni–Co/Cu multilayers. *Electrochim. Acta*, **91**: p. 122–129, 2013.

[149] J. Martin and R. Gruehn. Zum chemischen Transport vom Monophosphiden MP (M=Zr,, Hf, Nb, Ta, Mo, W) und Diphosphiden MP2 (M=Ti, Zr, Hf). *Z. Krist.*, **18**: p. 180–182, 1988.

[150] F. Lévy and H. Berger. Single Crystals of Transition Metal Trichalcogenides. *J. Cryst. Growth*, **61**: p. 61–68, 1983.

[151] Y. Qi, W. Shi, P. G. Naumov, N. Kumar, W. Schnelle, O. Barkalov, C. Shekhar, H. Borrmann, C. Felser, B. Yan, and S. A. Medvedev. Pressure-driven superconductivity in the transition-metal pentatelluride $HfTe_5$. *Phys. Rev. B*, **94**(054517), 2016.

[152] S. Furuseth, L. Brattas, and A. Kjekshus. The Crystal Structure of $HfTe_5$. *Acta Chem. Scand.*, **27**: p. 2367–2374, 1973.

[153] D. A. Allwood, G. Xiong, M. D. Cooke, and R. P. Cowburn. Magneto-optical Kerr effect analysis of magnetic nanostructures. *J. Phys. D. Appl. Phys.*, **36**(18), 2003.

[154] J. W. G. Bos, H. W. Zandbergen, M.-H. Lee, N. P. Ong, and R. J. Cava. Structures and thermoelectric properties of the infinitely adaptive series $(\mathrm{Bi_2})_\mathrm{m}(\mathrm{Bi_2Te_3})_\mathrm{n}$. *Phys. Rev. B*, **75**(195203), 2007.

[155] S. Tehrani, J. M. Slaughter, E. Chen, M. Durlam, J. Shi, and M. DeHerrera. Progress and outlook for MRAM technology. *IEEE Trans. Magn.*, **35**(5), 1999.

[156] J. Smit. Magnetoresistance of ferromagnetic metals and alloys at low temperatures. *Physica*, **16**(6), 1951.

[157] S. Yuasa, T. Nagahama, A. Fukushima, Y. Suzuki, and K. Ando. Giant room-temperature magnetoresistance in single-crystal Fe/MgO/Fe magnetic tunnel junctions. *Nat. Mater.*, **3**(12), 2004.

[158] Seagate Product Manual, publication no: 100743772, rev A. 2013.

[159] E. Shapira, A. Tsukernik, and Y. Selzer. Thermopower measurements on individual 30 nm nickel nanowires. *Nanotechnology*, **18**(48), 2007.

[160] B. Hamdou, J. Kimling, A. Dorn, E. Pippel, R. Rostek, P. Woias, and K. Nielsch. Thermoelectric Characterization of Bismuth Telluride Nanowires, Synthesized Via Catalytic Growth and Post-Annealing. *Adv. Mater.*, **25**(2), 2013.

[161] A. Fert and I. A. Campbell. *Ferromagnetic Materials.* Wohlfarth, E.P., Amsterdam, 1982.

[162] N. Cusack and P. Kendall. The Absolute Scale of Thermoelectric Power at High Temperature. *Proc. Phys. Soc.*, **72**(898), 1958.

[163] T. Farrell and D. Greig. The thermoelectric power of nickel and its alloys. *J. Phys. C Solid State Phys.*, **3**(138), 1970.

[164] J. Sánchez-Barriga, M. Lucas, F. Radu, E. Martin, M. Multigner, P. Marin, A. Hernando, and G. Rivero. Interplay between the magnetic anisotropy contributions of cobalt nanowires. *Phys. Rev. B*, **80**(184424), 2009.

[165] W. P. Van Drent, M. D. Bijker, and J. C. Lodder. Effect of stress and magnetostriction on the anisotropy of CoNi/Pt multilayers. *J. Magn. Magn. Mater.*, **15**(1-3), 1996.

[166] F. C. Nix and D. MacNair. The thermal expansion of pure metals: Copper, gold, aluminum, nickel, and iron. *Phys. Rev.*, **60**(8), 1941.

[167] R. C. Hall. Single crystal anisotropy and magnetostriction constants of several ferromagnetic materials including alloys of NiFe, SiFe, AlFe, CoNi, and CoFe. *J. Appl. Phys.*, **30**(6), 1959.

[168] R. M. Bozorth and J. G. Walker. Magnetic crystal anisotropy and magnetization of iron-nickel alloys. *Phys. Rev.*, **89**(3), 1953.

[169] E. Liu, Y. Sun, N. Kumar, L. Muechler, A. Sun, L. Jiao, S.-Y. Yang, D. Liu, A. Liang, Q. Xu, J. Kroder, V. Süß, H. Borrmann, C. Shekhar, Z. Wang, C. Xi, W. Wang, W. Schnelle, S. Wirth, Y. Chen, S. T. B. Goennenwein, and C. Felser. Giant anomalous Hall effect in a ferromagnetic kagome-lattice semimetal. *Nat. Phys.*, **14**(11), 2018.

[170] J. Gooth, A. C. Niemann, T. Meng, A. G. Grushin, K. Landsteiner, B. Gotsmann, F. Menges, M. Schmidt, C. Shekhar, V. Sueß, R. Huehne, B. Rellinghaus, C. Felser, B. Yan, and K. Nielsch. Experimental signatures of the mixed axial–gravitational anomaly in the Weyl semimetal NbP. *Nature*, **54**(7663), 2017.

[171] M. Ikhlas, T. Tomita, T. Koretsune, M.-T. Suzuki, D. Nishio-Hamane, R. Arita, Y. Otani, and S. Nakatsuji. Large anomalous Nernst effect at room temperature in a chiral antiferromagnet. *Nat. Phys.*, **13**(November), 2017.

[172] M. Izumi, K. Uchinokura, and E. Matsuura. Anomalous electrical resistivity in $\mathrm{HfTe_5}$. *Solid State Commun.*, **37**: p. 641–642, 1981.

[173] T. Tritt, N. D. Lowhorn, R. T. Littleton, A. Pope, C. R. Feger, and J. W. Kolis. Large enhancement of the resistive anomaly in the pentatelluride materials $\mathrm{HfTe_5}$ and $\mathrm{ZrTe_5}$ with applied magnetic field. *Phys. Rev. B*, **60**(11), 1999.

[174] T. E. Jones, W. W. Fuller, T. J. Wieting, and F. Levy. Thermoelectric power of $\mathrm{HfTe_5}$ and $\mathrm{ZrTe_5}$. *Solid State Commun.*, 42(11): p. 793–798, 1982.

[175] N. D. Lowhorn, T. M. Tritt, E. E. Abbott, and J. W. Kolis. Enhancement of the power factor of the transition metal pentatelluride $\mathrm{HfTe_5}$ by rare-earth doping. *Appl. Phys. Lett.*, **88**(022101), 2006.

[176] R. T. Littelton, T. M. Tritt, J . W. Kolis, D. R. Ketchum, N. D. Lowhorn, and M. B. Korzenski. Suppression of the resistivity anomaly and corresponding thermopower behavior in the pentatelluride system by the addition of Sb: $\mathrm{Hf}_{1-x}\mathrm{Zr}_x\mathrm{Te}_{5-y}\mathrm{Sb}_y$. *Phys. Rev. B*, **64**(121104), 2001.

[177] Y. Zhang, C. Wang, L. Yu, G. Liu, A. Liang, J. Huang, S. Nie, X. Sun, Y. Zhang, B. Shen, J. Liu, H. Weng, L. Zhao, G. Chen, X. Jia, C. Hu, Y. Ding, W. Zhao, Q. Gao, C. Li, S. He, L. Zhao, F. Zhang, S. Zhang, F. Yang, Z. Wang, Q. Peng, X. Dai, Z. Fang, Z. Xu, C. Chen, and X. J. Zhou. Electronic evidence of temperature-induced Lifshitz transition and topological nature in $\mathrm{ZrTe_5}$. *Nat. Comm.*, **8**: p. 15512, 2017.

[178] M. N. Ali, J. Xiong, S. Flynn, J. Tao, Q. D. Gibson, L. M. Schoop, T. Liang, N. Haldolaarachchige, M. Hirschberger, N .P. Ong, and R. J. Cava. Large, non-saturating magnetoresistance in $\mathrm{WTe_2}$. *Nature*, **51**(7521), 2014.

[179] C.Z. Li, J.-G. Li, L.-X. Wang, L. Zhang, J.-M. Zhang, D. Yu, and Z.-M. Liao. Two-Carrier Transport Induced Hall Anomaly and Large Tunable Magnetoresistance in Dirac Semimetal $\mathrm{Cd_3As_2}$ Nanoplates. *ACS Nano*, **10**(6), 2016.

[180] A. A. Abrikosov. Quantum magnetoresistance. *Phys. Rev. B*, **58**(5), 1998.

[181] J. Feng, Y. Pang, D. Wu, Z. Wang, H. Weng, J. Li, X. Dai, Z. Fang, Y. Shi, and L. Lu. Large linear magnetoresistance in Dirac semimetal $\mathrm{Cd_3As_2}$ with Fermi surfaces close to the Dirac points. *Phys. Rev. B*, **92**(081306), 2015.

[182] T. Liang, Q. Gibson, M. N. Ali, M. Liu, R. J. Cava, and N. P. Ong. Ultrahigh mobility and giant magnetoresistance in the Dirac semimetal $\mathrm{Cd_3As_2}$. *Nat. Mater.*, **14**(3), 2015.

[183] R. G. Chambers. The conductivity of thin wires in a magnetic field. *Proc. R. Soc. London*, **20**(1070), 1950.

[184] J. Heremans, C. M. Thrush, Y.-M. Lin, S. Cronin, Z. Zhang, M. S. Dresselhaus, and J. F. Mansfield. Bismuth nanowire arrays : Synthesis and galvanomagnetic properties. *Phys. Rev. B*, **61**(4), 2000.

[185] S.-M. Huang, S.-Y. Xu, I. Belopolski, C.-C. Lee, G. Chang, B. Wang, N. Alidoust, G. Bian, M. Neupane, C. Zhang, S. Jia, A. Bansil, H. Lin, and M. Z. Hasan. A Weyl Fermion semimetal with surface Fermi arcs in the transition metal monopnictide TaAs class. *Nat. Commun.*, **6**: p. 7373, 2015.

[186] H. Weng, C. Fang, Z. Fang, B. A. Bernevig, and X. Dai. Weyl Semimetal Phase in Noncentrosymmetric Transition-Metal Monophosphides. *Phys. Rev. X*, **5**(011029), 2015.

[187] F. Arnold, M. Naumann, S. C. Wu, Y. Sun, M. Schmidt, H. Borrmann, C. Felser, B. Yan, and E. Hassinger. Chiral Weyl Pockets and Fermi Surface Topology of the Weyl Semimetal TaAs. *Phys. Rev. Lett.*, **11**(146401), 2016.

[188] J. Klotz, S. C. Wu, C. Shekhar, Y. Sun, M. Schmidt, M. Nicklas, M. Baenitz, M. Uhlarz, J. Wosnitza, C. Felser, and B. Yan. Quantum oscillations and the Fermi surface topology of the Weyl semimetal NbP. *Phys. Rev. B*, **93**(121105(R)), 2016.

[189] M. Tian, W. Ning, Z. Qu, H. Du, J. Wang, and Y. Zhang. Dual evidence of surface Dirac states in thin cylindrical topological insulator Bi_2Te_3 nanowires. *Sci. Rep.*, **3**: p. 1212, 2013.

[190] H. Murakawa, M. S. Bahramy, M. Tokunaga, Y. Kohama, C. Bell, Y. Kaneko, N. Nagaosa, H. Y. Hwang, and Y. Tokura. Detection of Berry's Phase in a Bulk Rashba Semiconductor. *Science*, **34**(6165), 2013.

[191] I. A. Luk'yanchuk and Y. Kopelevich. Phase Analysis of Quantum Oscillations in Graphite. *Phys. Rev. Lett.*, **93**(16), 2004.

[192] G. E. Volovik. *The Universe in A Helium Droplet.* Clarendon Press, Oxford, 2003.

[193] L. Balents. Weyl electrons kiss. *Physics (College. Park. Md).*, **4**(36), 2011.

[194] T. Liang, Q. Gibson, J. Xiong, M. Hirschberger, S. P. Koduvayur, R. J. Cava, and N. P. Ong. Evidence for massive bulk Dirac fermions in experiments $Pb_{1-x}Sn_xSe$ from Nernst and thermopower. *Nat. Commun.*, **4**: p. 2696, 2013.

[195] J. Kimling, J. Gooth, and K. Nielsch. Anisotropic magnetothermal resistance in Ni nanowires. *Phys. Rev. B*, **87**(094409), 2013.

[196] B. Hamdou, A. Beckstedt, J. Kimling, A. Dorn, L. Akinsinde, S. Bäßler, E. Pippel, and K. Nielsch. The influence of a Te-depleted surface on the thermoelectric transport properties of Bi_2Te_3 nanowires. *Nanotechnology*, **25**(365401), 2014.

[197] C. Schindler, S. N. Guin, W. Schnelle, N. Kumar, C. Fu, H. Borrmann, C. Shekar, Y. Zhang, Y. Sun, C. Felser, T. Meng, A. G. Grushin, and J. Gooth. Observation of an anomalous heat current in a Weyl fermion semimetal. *arXiv:1810.02300v1*, 2018.

Danksagung

Das Anfertigen dieser Arbeit wäre ohne die viele Unterstützung, die ich in den letzten fünf Jahren erfahren habe, nicht möglich gewesen. Für diese Unterstützung möchte ich mich herzlich bedanken.

Zuerst möchte ich mich bei **Prof. Kornelius Nielsch** für die fortwährende Betreuung seit dem Beginn meiner Masterarbeit bedanken. In den letzten fünf Jahren hatte ich die Gelegenheit an zahlreichen Konferenzen und Workshops in Deutschland, Europa und den USA teilzunehmen und darüber hinaus wurde mir ein zweimonatiger Auslandsaufenthalt in Minneapolis ermöglicht. Ich hatte nicht nur die Gelegenheit an der Universität Hamburg zu arbeiten sondern ich könnte auch die wissenschaftliche Arbeit an IFW Dresden und das Leben in dieser Stadt kennenlernen. Durch die vielen neuen Ort und die vielen Menschen, die ich kennerlernen durfte, konnte ich viele neue Erfahrungen sammeln. Außerdem möchte ich mich für die große Freiheit bei der wissenschaftlichen Themenwahl und den in dieser Arbeit untersuchten Materialien bedanken, die mir ermöglicht hat auf aktuellen Forschungsgebieten mitzuarbeiten.
Bei **Dr. Andy Thomas** möchte ich mich für die Aufnahme in die Arbeitsgruppe *Quantum Materials and Devices* am IFW Dresden, die nette Arbeitsatmosphäre sowie die wissenschaftliche Betreuung bedanken.
Dr. Johannes Gooth danke ich für die sehr gute wissenschaftliche Begleitung während der gesamten letzten fünf Jahre. Danke für die Begeisterung und die Ausdauer mit der alle Projekte betreut wurden.
Bei **Dr. Tim Böhnert** möchte ich mich für die Betreuung während meiner Masterarbeit und den fortwährenden wissenschaftlichen Austausch bedanken. Ohne die Unterstützung von **Dr. Robert Zierold** wäre der Übergang zwischen der Universität Hamburg und dem IFW Dresden nicht so reibungslos verlaufen. Für diese Unterstützung möchte ich mich herzlich bedanken.
Bei **Almut Pöhl** und **Tina Sturm** möchte ich mich für ihren großen Einsatz bei der Probenpräparation bedanken, ohne den viele Projekte nicht möglich gewesen wären.
Prof. Bethanie Stadtler möchte ich für den tollen Forschungsaufenthalt in ihrer Gruppe am *Department of Electrical and Computer Engineering* an der University of Minnesota danken. Des Weiteren gilt mein Dank **Daniel Shore**, der mir bei der Nanodrahtsynthese in Minneapolis immer zur Seite stand. Außerdem möchte ich mich bei **Prof. Imre Bakonyi** und **Prof. Victor M. Prida** sowie ihren Arbeitsgruppen am Wigner Research Center of Physics in Budapest und an der Universidad de Oviedo für die gute Zusammenarbeit in den Projekten über magnetische Nanodrähte bedanken.
Bei der Arbeitsgruppe von **Prof. Claudia Felser** Max Planck Institut für chemische Physik fester Stoffe in Dresden bedanke ich mich herzlich für die zur Verfügung gestellten Materialien und die gute Zusammenarbeit in den Projekten über topologische Isolatoren und Halbmetalle.
Der gesamten **Gruppe K am INF Hamburg** und dem gesamten **IMW am IFW Dresden** möchte ich für die gute Zusammenarbeit und die tolle Arbeitsatmosphäre während der letzten fünf Jahre danken.
Schließlich möchte ich mich bei **meiner Familie und meinen Freunden** für den Rückhalt und die Unterstützung in den letzten fünf Jahren bedanken. Vor allem danke **Michael** für die wunderschöne Zeit und deine Bereitschaft deiner geliebten Hansestadt für mich zeitweise den Rücken zuzukehren.

Eidesstattliche Versicherung

Hiermit versichere ich an Eides statt, die vorliegende Dissertationsschrift selbst verfasst und keine anderen als die angegebenen Hilfsmittel und Quellen benutzt zu haben. Die eingereichte schriftliche Fassung entspricht der auf dem elektronischen Speichermedium. Die Dissertation wurde in der vorgelegten oder einer ähnlichen Form nicht schon einmal in einem früheren Promotionsverfahren angenommen oder als ungenügend beurteilt.

Hamburg, den ______________________ Unterschrift: ______________________

I

Thermoelectric Power Factor Enhancement by Spin-Polarized Currents—A Nanowire Case Study

Anna Corinna Niemann, Tim Böhnert, Ann-Kathrin Michel, Svenja Bäßler, Bernd Gotsmann, Katalin Neuróhr, Bence Tóth, László Péter, Imre Bakonyi, Victor Vega, Victor M. Prida, Johannes Gooth, and Kornelius Nielsch

Reprinted with permission from *Advanced Electronic Materials* **2**, 9 (2016)
Copyright 2016 WILEY-VCH Verlag GmbH & Co. KGaA, Weinheim.

Author Contributions: T.B., A.-K.M., S.B., K.Ne., B.T., and V.V. synthesized the nanowires. A.C.N. and T.B. conducted the transport measurements. V.V. conducted the TEM study. A.C.N., T.B. and J.G. analyzed the data. A.C.N. wrote the manuscript. All authors significantly contributed to the scientific discussion during the data evaluation and manuscript preparation. I.B., V.M.P., D.G., and K.N. supervised the project.

Materials Views
www.MaterialsViews.com

ADVANCED ELECTRONIC MATERIALS
www.advelectronicmat.de

Thermoelectric Power Factor Enhancement by Spin-Polarized Currents—A Nanowire Case Study

Anna Corinna Niemann, Tim Böhnert, Ann-Kathrin Michel, Svenja Bäßler, Bernd Gotsmann, Katalin Neuróhr, Bence Tóth, László Péter, Imre Bakonyi, Victor Vega, Victor M. Prida, Johannes Gooth, and Kornelius Nielsch**

Thermoelectric (TE) measurements have been performed on the workhorses of today's data storage devices, exhibiting either the giant or the anisotropic magnetoresistance effect (GMR and AMR). The temperature-dependent (50–300 K) and magnetic field-dependent (up to 1 T) TE power factor (PF) has been determined for several Co—Ni alloy nanowires with varying Co:Ni ratios as well as for Co—Ni/Cu multilayered nanowires with various Cu layer thicknesses, which are all synthesized via a template-assisted electrodeposition process. A systematic investigation of the resistivity, as well as the Seebeck coefficient, is performed for Co—Ni alloy nanowires and Co—Ni/Cu multilayered nanowires. At room temperature, measured values of TE PFs up to 3.6 mW K^{-2} m^{-1} for AMR samples and 2.0 mW K^{-2} m^{-1} for GMR nanowires are obtained. Furthermore, the TE PF is found to increase by up to 13.1% for AMR Co—Ni alloy nanowires and by up to 52% for GMR Co—Ni/Cu samples in an external applied magnetic field. The magnetic nanowires exhibit TE PFs that are of the same order of magnitude as TE PFs of Bi—Sb—Se—Te based thermoelectric materials and, additionally, give the opportunity to adjust the TE power output to changing loads and hotspots through external magnetic fields.

A. C. Niemann, A.-K. Michel, S. Bäßler, Dr. J. Gooth, Dr. K. Nielsch
Institute of Nanostructure and Solid State Physics
Universität Hamburg
Jungiusstraße 11, D-20355 Hamburg, Germany
E-mail: aniemann@physnet.uni-hamburg.de

Dr. T. Böhnert
International Iberian Nanotechnology Laboratory
Av. Mestre Jose Veiga
Braga, 4715 Portugal

Dr. B. Gotsmann, Dr. J. Gooth
IBM Research-Zurich
Säumerstrasse 4, 8803 Rüschlikon, Switzerland

Dr. K. Neuróhr, Dr. B. G. Tóth, Dr. L. Péter, Dr. I. Bakonyi
Wigner Research Centre of Physics
Hungarian Academy of Sciences
Konkoly-Thege út 29-33, H-1121 Budapest, Hungary

Dr. V. Vega, Dr. V. M. Prida
Depto. Física
Universidad de Oviedo
E-33006 Oviedo, Spain

Dr. K. Nielsch
Leibniz Institute for Solid State and Material Research
Helmholtzstraße 20, D-01069 Dresden, Germany
E-mail: k.nielsch@ifw-dresden.de

DOI: 10.1002/aelm.201600058

1. Introduction

In recent years, the continuously increasing integration density of microelectronic devices has brought thermoelectric (TE) effects back into the focus of current research. Taking advantage of the nanostructuring capabilities of semiconductors, thermoelectric energy converters exploiting the Seebeck effect have been designed with the aim of recapturing the energy wasted by heat loss and converting it to electricity.[1] Furthermore, scaling toward lower device currents is concurrent with miniaturization; and, consequently, Peltier heating is becoming significant or even dominant over Joule heating due to an increasing interface density in microelectronic devices.[2] In addition, large temperature gradients change device currents through the Thomson effect.[3] Nanostructuring of thermoelectric materials has also been recently proposed as a novel route for properly tailoring the parameters of the figure-of-merit coefficient, ZT, due to the opportunity of tuning the various appropriate features of the materials at the nanoscale. Among others, downscaling may open the way to decouple the thermal and electrical conductivity together with a reduction of the thermal conductivity by increasing the scattering of phonons through interfaces or defects.[4,5]

Whether or not TE effects are advantageous or problematic for respective device performances depends on the specific application. In phase-change memory devices, for example, local heating is exploited as the mechanism for switching the resistance state of a nanoscale memristor,[6] Peltier effects modify localized hotspots in logic devices,[7] and local temperature gradients imposed within device structures can reach extreme values leading to Thomson and Peltier effects that can reach high magnitudes. By neglecting them, one may fail to predict device switching properties by more than 40%.[3]

An interesting class of integrated circuit elements is based on magnetoresistance (MR) effects, which nowadays provide an integral concept in omnipresent electronic devices such as reading heads for magnetic hard discs, magnetic sensors, and magnetoresistive random-access memories (MRAMs).[8] Both anisotropic magnetoresistance (AMR)[9–11] and giant

© 2016 WILEY-VCH Verlag GmbH & Co. KGaA, Weinheim

magnetoresistance (GMR)[12,13] effects that are based on spin-dependent transport in magnetic alloys and magnetic/nonmagnetic multilayers have found extensive application. Driven by the need for constantly increasing data storage densities and the corresponding enhancement of magnetoresistance sensitivity, tremendous progress in the miniaturization of MR devices has been made by downsizing toward the nanometer scale.

Recently, TE effects have also been considered in spintronic devices[14] and spin-dependent Seebeck effects were observed for various MR regimes, such as AMR,[15] GMR,[16] as well as tunneling MR.[17] Furthermore, macroscopic TE signals have been linked to nanoscopic spin configurations of domain walls in ferromagnetic nanostructures.[18]

In the present work, we study and compare the thermoelectric properties of standard magnetic materials in the Co—Ni—Cu systems. We chose two model systems: Co—Ni alloy nanowires representing the AMR regime on the one hand and Co—Ni/Cu multilayered nanowires representing the GMR regime on the other hand. Both have well-defined magnetization directions along the nanowire axis and in the plane of the magnetic layers, respectively. Not only the thermoelectric power (also called Seebeck coefficient S), but also its dependence on the external applied magnetic field, were investigated. Large TE power factors (PF = S^2/ρ, with ρ being the electrical resistivity) of up to 4 mW K^{-2} m^{-1} are observed, which can easily compete with common TE materials used specifically for power generation. Moreover, TE performances were modified by up to 52% of the zero-field values by applying an external magnetic field, allowing for adjustability to changing loads and hotspots. In the framework of the two-current model,[19] we show that this increase of performance owes to the fact that the spin channel, exhibiting a lower ρ, simultaneously has a higher S than the other spin channel, as depicted in **Figure 1**.

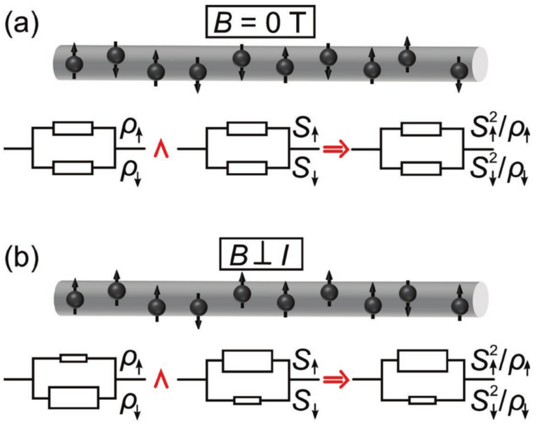

Figure 1. The two-current model for the resistivity as well as the thermopower S and the resulting thermoelectric power factor S^2/ρ. a) Without an external magnetic field, the majority and minority spin channel, ↑ and ↓, exhibit equal $\rho\uparrow$ and $\rho\downarrow$, as well as equal $S\uparrow$ and $S\downarrow$, resulting in equal S^2/ρ for both spin channels. b) With an externally applied magnetic field, ↑ exhibits lower ρ than ↓ and according to our observation $S\uparrow$ is increased compared to $S\downarrow$, which results in an increase of $S\uparrow^2/\rho\uparrow$ and, finally, in an increase of the thermoelectric power factor of the whole system.

2. Results and Discussion

2.1. Synthesis, Compositional, and Structural Characterization

The magnetic nanowires were synthesized by template-assisted electrodeposition into self-ordered, hard-anodized alumina (HAAO) membranes[20,21] with the internal walls of the membranes coated with SiO_2 in an atomic layer deposition (ALD) process in order to enhance the physical stability of the future nanowires and prevent them from oxidation after dissolving the alumina templates.[22,23] Alloy and multilayered nanowires were deposited by procedures which were described in detail by Vega et al.[24] and Tóth et al.[25] After the deposition process, we dissolved the HAAO templates in chromic–phosphoric acid aqueous solution and suspended the individual wires in ethanol.

The geometrical and compositional parameters of the alloy and multilayered nanowires investigated in the present work are summarized in **Table 1**.

Individual alloy nanowires were investigated by transmission electron microscopy (TEM), and their chemical composition was analyzed by electron dispersive X-ray spectroscopy (EDS) with the TEM, as shown in **Figure 2**a,b, respectively. In total, one Ni sample and three different Co—Ni alloy samples with Co content ranging from 24% up to 71% were prepared, as listed in Table 1a.

The crystalline phase of the Co—Ni alloy wires was characterized by X-ray diffraction (XRD).[24] Ni-rich nanowires (Ni, $Co_{24}Ni_{76}$, and $Co_{39}Ni_{61}$) exhibit a face centered cubic (fcc) structure, whereas in the Co-richest sample ($Co_{71}Ni_{29}$) the hexagonally close packed (hcp) phase and the fcc phase coexist.[24] The crystallite size of the nanowires obtained from XRD line width analysis[24] was 5 ± 2 nm for fcc crystals and 9 ± 2 nm for hcp crystals. The XRD results obtained on the crystal structure with the nanowires inside the membrane were supported by TEM selected-area electron diffraction (TEM-SAED) patterns on single fcc and hcp nanowires[26] as shown in the inset of Figure 2a for the hcp nanowire sample $Co_{71}Ni_{29}$.

In the same way, self-standing Co—Ni/Cu multilayered nanowires were analyzed by TEM and TEM-EDS,[27] as exemplified in Figure 2c,d, respectively. Bilayer thicknesses were measured over ten Co—Ni/Cu bilayers from high-resolution TEM images (HR-TEM) and the chemical composition of the nanowires was measured by TEM-EDS line scans performed on single nanowires, as given in Table 1b. From the EDS line scan, a counteroscillation of the Cu content and the amount of Co and Ni can be observed. The Co:Ni ratio in the magnetic layers of the six different multilayered nanowire samples ranges from 50:50 to 30:70. Also, a Cu content of about 2% can be estimated in the magnetic segments,[25] which is a value well below the absolute uncertainty of the chemical composition analysis of about 5%. From the bilayer thicknesses and the chemical composition, Cu layer thicknesses ranging from 0.2 up to 5.2 nm and Co—Ni layer thicknesses from 5.2 up to 17.4 nm were calculated, as shown in Table 1b.

In the following, alloy nanowires will be referred to according to their chemical composition (Ni and Co—Ni) and multilayered wires will be named according to their Cu spacer layer thickness Cu (x nm), since these are the main defining

© 2016 WILEY-VCH Verlag GmbH & Co. KGaA, Weinheim

Table 1. Geometrical and compositional parameters of alloy and multilayered nanowires: a) For alloy nanowires, the atomic ratio of cobalt and nickel atoms *r*(Co:Ni) determined by SEM- and TEM-EDS, the diameter, *d*, of the nanowire as determined from scanning electron microscopy images, and the electrical contact material of the microdevice are given for each sample. b) The multilayered nanowires were characterized by their bilayer thickness, l_{bilayer}, determined from transmission electron microscopy images and the atomic ratio of cobalt, nickel, and copper atoms *r*(Co:Ni:Cu) measured with TEM-EDS is given. The layer thickness of the magnetic Co—Ni layer, $l_{\text{Co–Ni}}$, and the non-magnetic Cu spacer layer, l_{Cu}, are calculated. Also, the diameter, *d*, of the nanowire and material of the microdevice are given.

(a) Alloy samples

Sample	*r*(Co:Ni) [%]	*D* [nm]	Material of the microdevice
$Co_{71}Ni_{29}$	71:29	140	Platinum
$Co_{39}Ni_{61}$	39:61	127	Gold
$Co_{24}Ni_{76}$	24:76	140	Gold
Ni	0:100	126	Platinum

(b) Multilayered samples

Sample	l_{bilayer} [nm]	*r*(Co:Ni:Cu) [%]	$l_{\text{Co–Ni}}$ [nm]	l_{Cu} [nm]	*D* [nm]	Material of the microdevice
Cu (0.2 nm)	Not measured	0.2	208	Platinum		
Cu (0.8 nm)		0.8	172	Platinum–chrome		
Cu (0.9 nm)	17.3 ± 1.3	32:64:3	16.4	0.9	257	Platinum
Cu (1.4 nm)	17.5 ± 1.5	47:47:6	16.1	1.4	205	Platinum
Cu (3.5 nm)	8.7 ± 1.0	25:43:41	5.2	3.5	155	Platinum–chrome
Cu (5.2 nm)	22.6 ± 1.1	23:54:22	17.4	5.2	159	Platinum

parameters of the anisotropic and giant magnetoresistance regime, respectively.

By using SEM, we determined the length between the electrical contacts, *l*, which was about 8 µm for all wires as well as the diameter, *d*, of the nanowires, which varied between 126 and 258 nm, as listed in Table 1a,b. To calculate the resistivity $\rho = R\pi d^2/4l$ of the nanowires with *R* being the resistance, we have also corrected the measured diameters for a 5 nm thick SiO_2 shell, since it does not contribute to the electrical transport.

2.2. Thermoelectric Characterization

Individual nanowires dispersed on a glass substrate were electrically contacted by defining a photoresist mask by laser beam lithography and subsequent sputtering of a Ti adhesion and a Pt layer. The inner part of the microstructure with an embedded nanowire can be seen on a SEM image of **Figure 3**a.

Transport measurements were conducted in a physical property measurement system (PPMS) at different base temperatures, *T*, from 50 to 325 K and at an applied magnetic field, $\mu_0 H_\perp$, perpendicular to the nanowire axis. To the heater line of the microdevice, DC voltages between 5 and 14 V were applied, which caused Joule heating between 1 and 8 mW. On a typical microdevice, this led to temperature differences between 5 and 10 K between the two resistive thermometers. The thermovoltage U_{thermo} was recorded as a dc voltage and *R* of the nanowire as well as of the two resistive thermometers were measured by employing standard lock-in techniques.

Plotting *R* as a function of $\mu_0 H_\perp$ gives typical magnetoresistance curves, as illustratively shown in Figure 3b for one GMR-sample of Cu (5.2 nm) and one AMR-nanowire of Ni (data obtained at room temperature). Magnetoresistance was calculated as $\text{MR} = (R_H - R_0)/R_0$, the resistance R_0 being obtained without an external magnetic field and the resistance R_H measured at a certain magnetic field *H*. While the Ni nanowire exhibits relatively small MR of –2.0% at the magnetization saturation field value, the multilayered Cu (5.2 nm) nanowire exhibits larger MR ratio of up to –11.0%, as shown in Figure 3c.

An enhanced absolute thermopower $S = U_{\text{thermo}}/(T_{\text{hot}} - T_{\text{cold}})$ was measured by increasing $\mu_0 H_\perp$ for alloy as well as multilayered nanowires, see Figure 3d. The observation that *S* increases and ρ decreases with increasing $\mu_0 H_\perp$ is in good agreement with several publications.[16,28–32] We quantified the thermopower change with $\mu_0 H_\perp$ by the magneto-thermoelectric power $\text{MTEP} = (S_H - S_0)/S_0$, with S_0 and S_H being the thermopower without an external magnetic field and at a certain applied magnetic field *H*, respectively.[33] Again, the Ni nanowire exhibits a relatively low magneto-thermoelectric power effect of MTEP = 4.6% at the magnetization saturation field, and the multilayered Cu (5.2 nm) nanowire has a larger MTEP of up to 14.3%, as shown in Figure 3e. Comparing MR and MTEP of all the alloy and multilayered nanowires investigated, the following key observations[26,27] have been made: First, MR of the alloy wires reaches bulk-like literature values,[10,11,34] except for $Co_{71}Ni_{29}$, which can be attributed to the strong magneto-crystalline anisotropy of the sample and therefore the non-negligible MR component in a magnetic field applied parallel to the nanowire axis. Second, at room temperature, multilayered wires with sufficiently thick Cu spacer layers show MR values from –6% up to –15%, comparable to the ones reported in other publications,[35–43] while wires with a Cu layer thickness below 1 nm show significantly reduced MR, ranging from –3.3% to –3.6%. This low performance can be attributed to pinholes in the nonmagnetic spacer layer and the resulting inability of the neighboring magnetic layers to establish an antiparallel (or, at least, random or non-parallel) magnetization alignment in

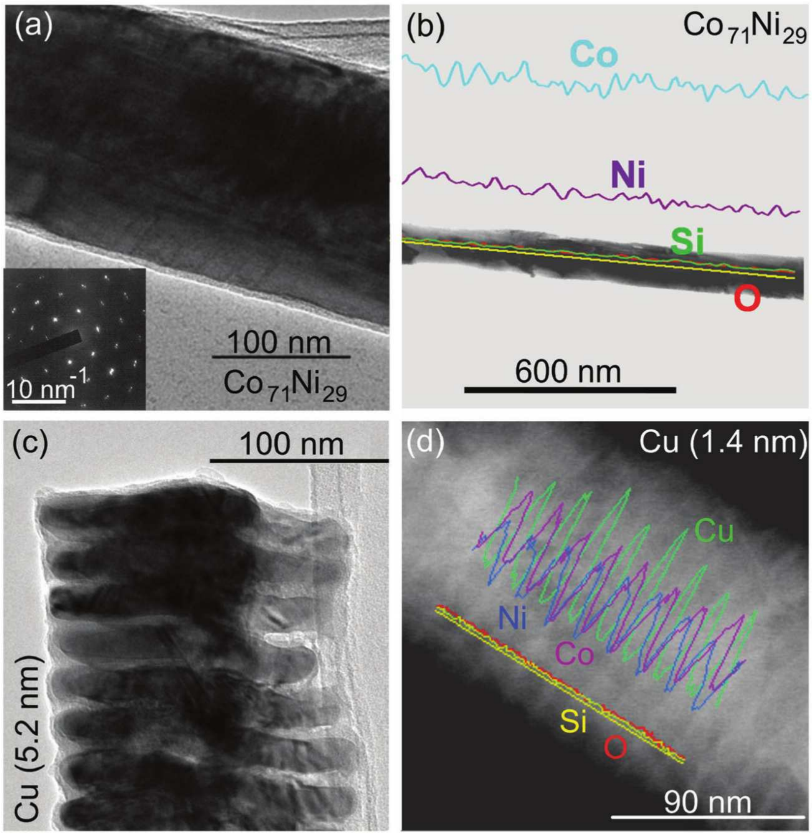

Figure 2. Structural, morphological, and compositional characterization of the magnetic nanowires: a) TEM image of sample $Co_{71}Ni_{29}$. The inset shows the SAED pattern of the nanowire, which reveals the [0001] zone axis of an hcp lattice. b) A broader TEM image of sample $Co_{71}Ni_{29}$ combined with superimposed TEM-EDS data obtained from a line scan along the nanowire length shows a fairly homogeneous Co:Ni ratio along the wire axis. c) TEM image of sample Cu (5.2 nm) revealing the multilayered structure of the nanowire. d) TEM image of the multilayered nanowire Cu (1.4 nm) with superimposed TEM-EDS data obtained from a line scan measured along the nanowire axis.

zero magnetic field.[44] Third, the thermopower change under an external applied magnetic field of all alloy and multilayered wires is in the same range as the corresponding MR effects of the samples. An in-depth discussion of MR and MTEP can be found in the recently published work by Böhnert et al.[26,27]

The resistivity, ρ, of alloy[26] and multilayered[27] samples exhibits a temperature dependence which is characteristic of metals in general. At room temperature, ρ of the alloy wires ranging from $\rho(\text{Ni}) = 13.2\ \mu\Omega$ cm to $\rho(Co_{24}Ni_{76}) = 21.7\ \mu\Omega$ cm is higher than the resistivity of the corresponding compositions in the bulk Ni-Co alloy system.[45] This deviation is well known in literature and is attributed to the nanocrystalline structure of electrodeposited materials.[45]

At the same time, ρ of the multilayered nanowires, ranging from ρ(Cu (5.2 nm)) = 28.7 μΩ cm to ρ(Cu (1.4 nm)) = 50.8 μΩ cm, is further enhanced when compared to ρ of the alloy wires, which we attribute to an additional scattering at the Co–Ni/Cu interfaces. The high uncertainty of the measured diameter and length of the nanowires leads to a high uncertainty of ρ up to 15%.

The resistivity and the absolute value of S show a similar increase with the mean sample temperature $\bar{T} = (T_{\text{hot}} + T_{\text{cold}})/2$ for both alloy[26] and multilayered[27] nanowires. S(300 K) of the alloy wires ranges between −15.6 μV K^{-1} (Ni) and −26.5 μV K^{-1} ($Co_{71}Ni_{29}$) and S(300 K) of the multilayered samples was measured between −10.5 μV K^{-1} (Cu (3.5 nm)) and −24.5 μV K^{-1} (Cu (0.2 nm)). Consequently, a local hotspot-induced temperature difference of 100 K along an MRAM device would cause local potential variations in the mV range. In fact, also the reverse effect, namely, the Peltier effect describing a temperature gradient across an interface resulting from a voltage drop may have a significant influence on the MR device performance, being particularly relevant for GMR devices. By using the Thomson relation, we have calculated the Peltier coefficient $\Pi = S \cdot \bar{T}$ of our samples to range from −3.15 mV (Cu (3.5 nm)) to −7.95 mV ($Co_{71}Ni_{29}$) at room temperature. Thus, a Peltier heat flow $\dot{Q} = \Pi \cdot I$ of the $Co_{71}Ni_{29}$ nanowire is generated, which is enhanced by as much as a factor of 8.0 ($R(Co_{71}Ni_{29})$ = 100 Ω) as compared to the heat generated by Joule heating when using a measurement current of 10 μA, and which, therefore, should not be neglected. One has to keep in mind that both S and Π coefficients refer not only to the nanowires but also to the other microdevice material Pt, Au, and Pt–Cr as listed in the legend of **Figure 4**.

The TE power output of the investigated nanowires, which is given by PF shown in Figure 4a,b, increases monotonically with $\bar{T}$ for all samples, except for $Co_{24}Ni_{76}$ and Cu (3.5 nm). At room temperature, the PF of the alloy samples ranges from 1.9 mW K^{-2} m^{-1} for Ni to 3.6 mW K^{-2} m^{-1} for the $Co_{71}Ni_{29}$ nanowire. In the case of the multilayered samples, the PF(300 K) ranges from 0.3 mW K^{-2} m^{-1} for Cu (3.5 nm) to 2.0 mW K^{-2} m^{-1} for Cu (0.2 nm). The TE power output of these magnetic nanowires can compete with PFs of the best TE bulk semiconductor materials like Bi_2Te_3,[46] which gives a PF of 1.9 mW K^{-2} m^{-1} at room temperature and it exceeds the PF of Bi_2Te_3 nanowires by a factor of five.[47] Thus, even if the magnetic metallic nanowires cannot reach values of S as high as the classical TE material ($S(Bi_2Te_{3,\text{bulk}})$ = −168 μV K^{-1}),[46] the resistivity of the latter is much higher ($\rho(Bi_2Te_{3,\text{bulk}})$ = 1430 μΩ cm),[46] and this allows the magnetic metallic nanowires to easily compete with and even exceed the TE power output of Bi–Se–Sb–Te material systems. Therefore, these materials may be interesting candidates for TE power generation under specific environments as well as heat management in micro- and nanoscale electronic devices.

The thermoelectric power output at—or slightly above—room temperature is probably most relevant for heat dissipation and device applications. We have recorded the magnetic field dependence of the PF at 300 K as shown in **Figure 5**a,c for alloy and multilayered nanowires, respectively. It can be observed that

© 2016 WILEY-VCH Verlag GmbH & Co. KGaA, Weinheim

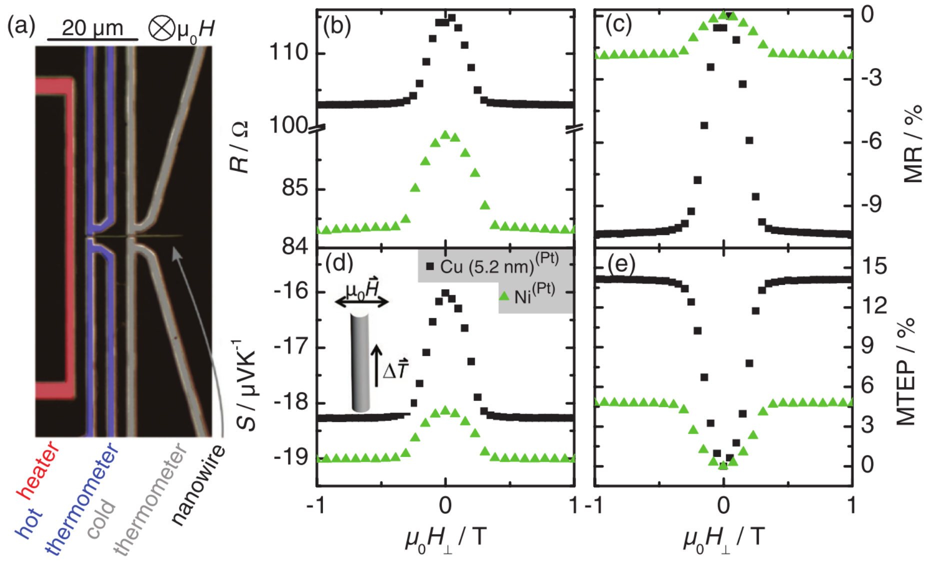

Figure 3. a) SEM image displaying the inner part of the microdevice, where the nanowire is embedded between the two resistive thermometers with an additional heater line. For a nickel nanowire (green triangles) and a multilayered nanowire Cu (5.2 nm) (black squares), b) the resistance R, c) thermopower S and corresponding magneto-effects, d) magnetoresistance MR (MR = $(R_H–R_0)/R_0$), and e) magneto-thermoelectric power MTEP (MTEP = $(S_H–S_0)/S_0$) are shown as a function of the external magnetic field, $\mu_0H_\perp$, applied perpendicular to the nanowire axis. The measurements are performed at 300 K. S and MTEP of both samples are measured with respect to a platinum microdevice.

the TE power output of all samples increases in an applied magnetic field until the magnetization saturation field is reached. Alloy samples reach PFs of up to 4.2 mW K^{-2} m^{-1} ($Co_{71}Ni_{29}$) and multilayered nanowires show PFs of up to 2.2 mW K^{-2} m^{-1} (Cu (0.2 nm)) at the magnetization saturation field. To quantify the change of PF in an applied magnetic field, we define the magneto-PF ratio MPF = $(PF_H–PF_0)/PF_0$, with PF_0 being the TE PF without an external applied magnetic field and PF_H the TE PF at a certain magnetic field applied perpendicular to the nanowire axis. The MPF is shown in Figure 5b,d as a function of $\mu_0H_\perp$ for alloy and multilayered nanowires, respectively. For alloy wires, the MPF ranges from 4.9% ($Co_{71}Ni_{29}$) up to 13.1% ($Co_{39}Ni_{61}$), while for multilayered wires an increase of the TE power output from 9.8% (Cu (0.2 nm)) to as high as 52.2% (Cu (3.5 nm)) is seen. For both the AMR and GMR systems, the improved TE performance in an increasing applied magnetic field can be understood within the framework of the two-current model,[19] which in this case describes two conducting spin channels in a parallel circuit, as depicted in Figure 1. The TE PF of AMR as well as GMR systems benefits from the fact that for a high degree of spin polarization, the prevailing low-resistivity majority spin channel simultaneously exhibits the highest thermopower within the system. To understand this, consider two conducting spin channels, the majority, ↑, and

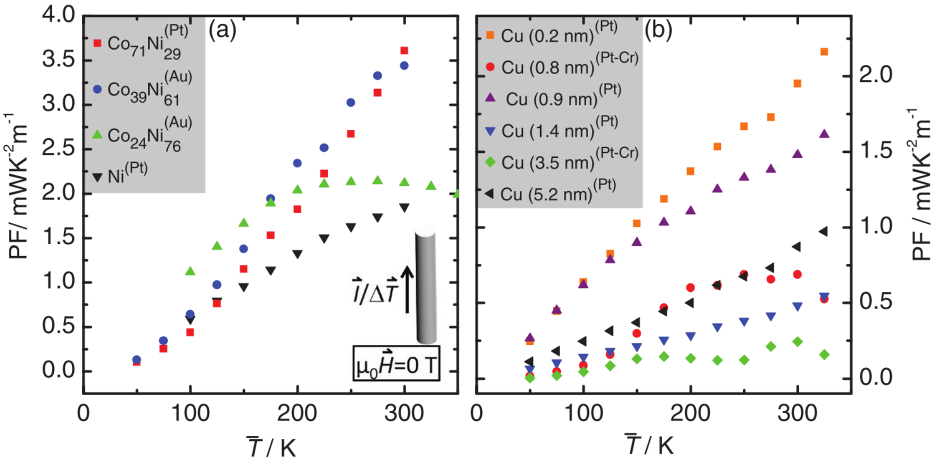

Figure 4. Thermoelectric power factor PF = S^2/ρ of a) single Ni and Co–Ni alloy nanowires and b) single Co–Ni/Cu multilayered nanowires measured with respect to the used electrical contact material (Pt = platinum, Au = gold, and Pt–Cr = platinum–chrome) is shown as a function of the mean temperature, $\bar{T}$, of the nanowires.

© 2016 WILEY-VCH Verlag GmbH & Co. KGaA, Weinheim

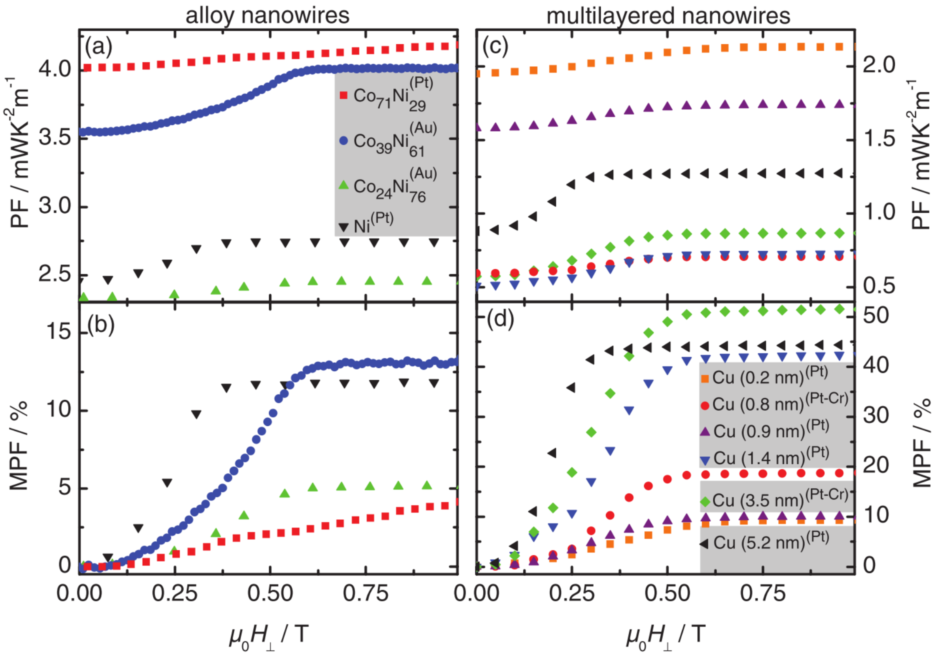

Figure 5. a) Thermoelectric power factor, PF, and b) magneto-power factor, MPF (MPF = $(\mathrm{PF_H}-\mathrm{PF_0})/\mathrm{PF_0}$) as a function of the external magnetic field, $\mu_0H_\perp$, applied perpendicular to the single Ni and Co–Ni alloy nanowire axis. Corresponding PF and MPF values for the Co–Ni/Cu multilayered nanowires are shown in (c) and (d), respectively. The base temperature was set to 300 K. Heating powers of 4.1 mW for the alloy samples and 2 mW for the multilayered samples were applied, which resulted in quite different mean temperatures $\bar{T}$ ($\bar{T} = (T_{\text{hot}} + T_{\text{cold}})/2$) of the nanowires [Co$_{71}Ni_{29}$: 320 K, Co$_{39}Ni_{61}$: 314 K, Co$_{24}Ni_{76}$: 342 K, Ni: 362 K, Cu (0.2 nm): 307 K, Cu (0.8 nm): 315 K, Cu (0.9 nm): 314 K, Cu (1.4 nm): 310 K, Cu (3.5 nm): 311 K, Cu (5.2 nm): 305 K] depending on the type of material and the thickness of the microdevice.

minority, ↓, channel. The total resistivity of the system is then given by $\rho_{\text{tot}} = (1/\rho\uparrow + 1/\rho\downarrow)^{-1}$ and it is well known that in high external magnetic fields the spin channel with the lower resistivity prevails. We assume that $\rho\uparrow \ll \rho\downarrow$, so that in the limit of full spin polarization $\rho_{\text{tot}}(\mu_0H \geq \mu_0H_{\text{sat}}) = \rho\uparrow > \rho_{\text{tot}}(\mu_0H = 0\ \text{T})$. The corresponding total thermopower of the system[48,49] is given by $S_{\text{tot}} = (S\uparrow/\rho\uparrow + S\downarrow/\rho\downarrow)/(1/\rho\uparrow + 1/\rho\downarrow)$, where $\min[S\uparrow, S\downarrow] < S_{\text{tot}} < \max[S\uparrow, S\downarrow]$. In large applied magnetic fields, it follows directly from $\rho\uparrow \ll \rho\downarrow$ that $S_{\text{tot}} \approx (S\uparrow/\rho\uparrow)\ /\ (1/\rho\uparrow) = S\uparrow$. Since in our experiments the thermopower increases with an increasing external magnetic field, $S_{\text{tot}} = \max[S\uparrow, S\downarrow]$ and $S\uparrow \gg S\downarrow$ follows. Consequently, the thermoelectric power for the AMR as well as for the GMR samples is maximized for highest spin polarization.

We note that regarding heat management in nanostructured devices, also the thermal conductivity, κ, is of major interest. Commonly, the Wiedemann-–Franz law $\kappa\cdot\rho = L\cdot\bar{T}$ is used to calculate κ from ρ, with the Lorenz number L being the Sommerfeld value $L_0 = 2.45 \times 10^{-8}$ V^2 K^{-2} for bulk metals above the Debye temperature.[50] These considerations lead to κ(300 K) values from 14.41 W m^{-1} K^{-1} (Cu (1.4 nm)) up to 55.45 W m^{-1} K^{-1} (Ni) for the metallic magnetic nanowires investigated here. Furthermore, the thermoelectric figure of merit ZT ($\mathrm{ZT} = S^2T/\rho\kappa = S^2/L_0$) ranges from 0.005 up to 0.009 at room temperature. However, in-plane measurements of ρ and κ on Co/Cu multilayered thin films[51,52] and Ni nanowires[53] have recently shown that their L value deviates from L_0 and depends on the magnetic configuration. Consequently, a calculation of κ and ZT for our nanowires using the Wiedemann–Franz law combined with L_0 is only a rough estimation and measuring both ρ and κ of magnetic nanostructures remains an interesting challenge and highly anticipates further studies in the near future.

3. Conclusions

To address emerging challenges and opportunities caused by heat management at the micro- and nanoscale, we studied the TE performance of magnetic nanowires for two different magnetoresistance regimes, namely, anisotropic magnetoresistance and giant magnetoresistance.

At room temperature, for the AMR nanowires PFs of up to 3.6 mW K^{-2} m^{-1} (Co$_{71}$Ni$_{29}$) and for the GMR wires PFs of up to 2.0 mW K^{-2} m^{-1} (Cu (0.2 nm)) have been found. The TE PF of both alloy and multilayered nanowires increases with increasing mean temperature of the nanowires. Thus, for heat dissipating structures which might be operated above room temperature, even higher TE power outputs can be expected. Our data show that TE power outputs of magnetic nanowires can compete with the power outputs of classical TE bulk semiconductor materials like Bi$_2$Te$_3$[46] and clearly exceed the PF of nanostructured thermoelectric Bi$_2$Te$_3$ nanowires.[47] Additionally, the metallic nanowires can also be expected to exhibit a higher thermal conductivity than Bi–Sb–Te–Se material systems. By applying an external magnetic field, the TE power outputs of the AMR as well as of the GRM nanowires can be further increased, due to the unique property of such systems that the dominating majority spin channel simultaneously exhibits lowest resistivity and highest thermopower in the system. At room temperature, the largest enhancement of PF in an applied magnetization saturation field was measured to be 13.1% for $Co_{39}Ni_{61}$ alloy AMR wires and 52% for Cu (3.5 nm) multilayered GMR wires.

Therefore, we propose that MR nanodevices are interesting for heat dissipating applications due to the adjustability of their transport properties to changing loads and local hotspots by an applied magnetic field in nano- and microscale electronics. Furthermore, we showed that TE power generation from waste heat on the nanoscale is becoming into a competitive scenario compared to conventional thermoelectric materials since the magnetic nanowires can achieve equally high or even higher PFs than the semiconductor TE materials. Finally, this study also revealed the importance of taking significant TE effects into account when designing MR operational units.

4. Experimental Section

Nanowire Synthesis: The nanowires were electrodeposited into self-ordered HAAO membranes which exhibit a nanoporous structure with a pore diameter between 136 and 268 nm. Before the anodization process, cleaned and electropolished high-purity aluminum foils (Al 99.999%) were pre-anodized under mild anodization conditions ($U = 80$ V, $t = 10$ min) in a 0.3 M oxalic acid aqueous solution containing 5 vol% of ethanol. The applied voltage was increased by 0.08 V s^{-1} to perform the hard anodization process at 140 V ($t = 1.5$ h, 0 °C < T < 3 °C). After anodization, the Al backside of the AAO membranes was removed by wet chemical etching in $CuCl_2$/HCl aqueous solution. Subsequently, the alumina bottom layer of the membrane pore structure as well as the protective mild anodized layer at the top side of the membrane were opened by immersing the membrane in a 5 wt% H_3PO_4 solution ($t = 2.5$ h, $T = 30$ °C). Using ALD technique, the porous structure of the alumina membranes was homogeneously covered with a 5 nm thick SiO_2 layer. Reactive ion etching removes the SiO_2 layer at the top and backsides of the membrane. The backside of the AAO membrane was then again sealed by sputtering and electrodeposition of a gold layer. The deposition process of the nanowires took place in a three-electrode setup with the gold layer at the membrane backside acting as the working electrode, a platinum mesh serving as the counter electrode, and an Ag/AgCl (3 M) KCl reference electrode. Alloy nanowires with a length of 15–30 µm were electrodeposited at 35 °C and under potentiostatic conditions (–0.8 V > U > –1 V vs reference electrode) from a Watts-type electrolyte containing different compositions of Co^{2+} and Ni^{2+} ions as described by Vega et al.[24] The multilayered nanowires were grown by two-pulse plating from a single electrolyte according to a recipe published by Tóth et al.[25] Co—Ni and Cu layers were deposited at –1.5 and –0.58 V versus reference electrode, respectively. The desired Co—Ni and Cu layer thicknesses were achieved by properly adjusting the deposited charge equivalent. After the deposition process, the gold electrode was removed from the backside of the HAAO membrane by using (0.6 M)KI·(0.1 M)I_2 aqueous solution and then the membranes in chromic–phosphoric acid aqueous solution (1.8 wt% CrO_3, 6 wt% H_3PO_4) were dissolved for ≈48 h at 45 °C. The released nanowires were first filtrated and rinsed with deionized water and afterward stored in ethanol.

Structural and Compositional Characterization: The morphology and chemical composition of the alloy nanowire arrays inside the membrane were characterized using a scanning electron microscope (Supra 55-Zeiss) equipped with EDS. The crystalline phase of the Co—Ni nanowire arrays was determined by XRD (X'Pert PRO-PANalytical) in a θ–2θ setup using CuKα1 radiation ($\lambda = 1.54056$ Å). Individual alloy and multilayered nanowires were investigated by HR-TEM (JEM 2100). A chemical analysis of the multilayered nanowires was performed using TEM-EDS operating in scanning transmission electron microscope (STEM) mode. Layer thicknesses of the Cu and Co—Ni layers were calculated by combining measured Co—Ni/Cu bilayer thicknesses from TEM images (averaged over ten bilayers) with chemical composition data from TEM-EDS. Layer thicknesses for sample Cu (0.2 nm) and Cu (0.8 nm) were determined by fitting the nominal layer thicknesses to the ratio of nominal and measured layer thickness of analyzed samples. To cross-check the crystalline phase of single alloy nanowires, SAED (JEM 2100) was performed.

Application of the Microdevice: Diluted nanowire solution was dropped on a 150 µm thick glass substrate. The dried substrate was coated with a bilayer of lift-off and positive photoresist (Micro Chem LOR-3B and ma-P 1205) and the electrical contact structure was defined as shown in Figure 3a, using a laser lithography system (Heidelberg Instruments µpg 101). This system was equipped with an optical microscope and a micrometer-step motor, which allows for optically scanning of the nanowires and manual definition of the contact structure position and orientation. Subsequently, the exposed parts of the resist (developer ma-D331, $t = 45$ s, $T = 20$ °C) were removed until an undercut structure could be observed at the edges of the developed parts, which guarantees a clean removal of the metal layer in the lift-off process. Prior to the metallization, in situ argon sputtering ($t = 15$ min, $p = 7.4 \times 10^{-3}$ Torr, $\text{flow}_{Ar} = 15$ sccm, $P = 20$ W) was performed to remove the protective Si_2O layer from the nanowire at the exposed contact areas. A titanium layer ($d_{Ti} = 5$ nm) was sputtered. It serves as an adhesion promoter before a platinum layer ($d_{Pt} = 100$ nm)—or a gold or platinum–chrome layer—was applied. Finally, residual metallic parts were removed in a lift-off process (Remover 1165, 2 × : $t = 15$ min, $T = 80$ °C, intermediate and final cleaning with deionized water and purged nitrogen).

Measurements: In a cryostatic system (PPMS DynaCool from Quantum Design), transport measurements were performed on single nanowires embedded in a microdevice, see Figure 3a, which consists of two resistive thermometers and one heater line. Voltages between 5 and 14 V were applied (Agilent E3644A DC Power Supply) to the heater. The two resistive thermometers were used not only to measure the absolute temperature at both ends of the nanowire, but also to make electrical contact to the nanowire itself. The resistances of both thermometers were measured via four-point measurement by standard lock-in technique ($I_{ac} = 10$ µA, $f_1 = 128$ Hz, $f_2 = 189$ Hz) using the cryostats' integrated measurement devices. The thermovoltage U_{thermo} was recorded by an additionally applied nanovoltmeter (Keithley 2184A) and the resistance R of the nanowire was measured employing lock-in technique ($I_{ac} = 10$ µA, $f = 189$ Hz) supplied by the cryostatic system. The measurements were performed in a temperature range between 50 and 325 K and at a nitrogen pressure of 4×10^{-3} mbar to avoid convection. The external magnetic field, applied perpendicular to the nanowire axis, was changed in steps from –1 to 1 T to achieve the magnetization saturation of the nanowire samples. U_{thermo} and R were each measured with the same applied temperature gradient to directly compare them at the very same temperature conditions.

Acknowledgements

The authors gratefully acknowledge financial support via the German Academic Exchange Service, Spanish MINECO grant under research Project No. MAT2013-48054-C2-2-R, the German Priority Program SPP 1536 "SpinCAT" funded by the Deutsche Forschungsgemeinschaft (DFG), and the excellence clusters "The Hamburg Centre for Ultrafast Imaging" funded by the DFG and "Nanospintronics" funded by the State of Hamburg. Scientific support from the University of Oviedo SCTs is also acknowledged. Work carried out in Budapest was supported by the Hungarian Scientific Research Fund under Grant No. OTKA K 104696.

Received: February 15, 2016
Published online:

[1] G. Pennelli, *Beilstein J. Nanotechnol.* **2014**, *5*, 1268.
[2] D. Zhao, G. Tan, *Appl. Therm. Eng.* **2014**, *66*, 15.
[3] J. Lee, M. Asheghi, K. E. Goodson, *Nanotechnology* **2012**, *23*, 205201.
[4] M. S. Dresselhaus, G. Chen, M. Y. Tang, R. G. Yang, H. Lee, D. Z. Wang, Z. F. Ren, J.-P. Fleurial, P. Gogna, *Adv. Mater.* **2007**, *19*, 8.
[5] A. J. Minnich, M. S. Dresselhaus, Z. F. Ren, G. Chen, *Energy Environ. Sci.* **2009**, *2*, 5.
[6] H.-S. P. Wong, S. Raoux, S. B. Kim, J. Liang, J. P. Reifenberg, B. Rajendran, M. Asheghi, K. E. Goodson, *Proc. IEEE* **2010**, *98*, 2201.
[7] A. Martinez, J. R. Barker, M. Aldegunde, R. Valin, *IEEE Electron Device Lett.* **2015**, *36*, 2.
[8] S. Tehrani, J. M. Slaughter, E. Chen, M. Durlam, J. Shi, M. DeHerren, *IEEE Trans. Magn.* **1999**, *35*, 2814.
[9] W. Thomson, *Proc. R. Soc. London* **1857**, *8*, 546.
[10] T. R. McGuire, R. I. Potter, *IEEE Trans. Magn.* **1975**, *11*, 1018.
[11] J. Smit, *Physica* **1951**, *17*, 612.
[12] M. N. Baibich, J. M. Broto, A. Fert, F. N. Van Dau, F. Petroff, P. Etienne, G. Creuzet, A. Friederich, J. Chazelas, *Phys. Rev. Lett.* **1988**, *61*, 2472.
[13] G. Binasch, P. Grünberg, F. Saurenbach, W. Zinn, *Phys. Rev. B* **1989**, *39*, 4828.
[14] G. E. W. Bauer, E. Saitoh, B. J. van Wees, *Nat. Mater.* **2012**, *11*, 391.
[15] A. D. Avery, M. R. Pufall, B. L. Zink, *Phys. Rev. B* **2012**, *86*, 184408.
[16] J. Shi, S. S. P. Parkin, L. Xing, M. B. Salamon, *J. Magn. Magn. Mater.* **1993**, *125*, L251.
[17] A. Boehnke, M. Walter, N. Roschewsky, T. Eggebrecht, V. Drewello, K. Rott, M. Münzenberg, A. Thomas, G. Reiss, *Rev. Sci. Instrum.* **2013**, *84*, 063905.
[18] P. Krzysteczko, X. Hu, N. Liebing, S. Sievers, H. W. Schumacher, *Phys. Rev. B* **2015**, *92*, 140405.
[19] I. A. Campbell, A. Fert, in *Ferromagnetic Materials*, Vol. *3* (Ed: E. P. Wohlfarth), North-Holland, Amsterdam **1982**, p. 747, Ch. 9.
[20] W. Lee, R. Ji, U. Gösele, K. Nielsch, *Nat. Mater.* **2006**, *5*, 741.
[21] V. Vega, J. R. García, J. M. Montero-Moreno, B. Hernando, J. Bachmann, V. M. Prida, K. Nielsch, *ACS Appl. Mater. Interfaces* **2015**, *7*, 28682.
[22] J. Bachmann, R. Zierold, Y. T. Chong, R. Hauert, C. Sturm, R. Schmidt-Grund, B. Rheinländer, M. Grundmann, U. Gösele, K. Nielsch, *Angew. Chem. Int. Ed.* **2008**, *47*, 6177.
[23] J. Lee, S. Farhangfar, R. Yang, R. Scholz, M. Alexe, U. Gösele, J. Lee, K. Nielsch, *J. Mater. Chem.* **2009**, *19*, 7050.
[24] V. Vega, T. Böhnert, S. Martens, M. Waleczek, J. M. Montero-Moreno, D. Görlitz, V. M. Prida, K. Nielsch, *Nanotechnology* **2012**, *23*, 465709.
[25] B. G. Tóth, L. Péter, J. Dégi, Á. Révész, D. Oszetzky, G. Molnár, I. Bakonyi, *Electrochim. Acta* **2013**, *91*, 122.
[26] T. Böhnert, V. Vega, A.-K. Michel, V. M. Prida, K. Nielsch, *Appl. Phys. Lett.* **2013**, *103*, 092407.
[27] T. Böhnert, A. C. Niemann, A.-K. Michel, S. Bäßler, J. Gooth, B. G. Tóth, K. Neuróhr, L. Péter, I. Bakonyi, V. Vega, V. M. Prida, K. Nielsch, *Phys. Rev. B* **2014**, *90*, 165416.
[28] M. J. Conover, M. B. Brodsky, J. E. Mattson, C. H. Sowers, S. D. Bader, *J. Magn. Magn. Mater.* **1991**, *102*, L5.
[29] Y. Kobayashi, Y. Aoki, H. Sato, T. Ono, T. Shinjo, *J. Phys. Soc. Jpn.* **1996**, *65*, 1910.
[30] J. Sakurai, D. Huo, T. Kuwai, K. Mori, T. Hihara, K. Sumiyama, K. Suzuki, *J. Phys. Soc. Jpn.* **1997**, *66*, 2240.
[31] J. Shi, R. C. Yu, S. S. P. Parkin, M. B. Salamon, *J. Appl. Phys.* **1993**, *73*, 5524.
[32] J. Shi, K. Pettit, E. Kita, S. S. P. Parkin, R. Nakatani, M. B. Salamon, *Phys. Rev. B* **1996**, *54*, 15273.
[33] L. Gravier, A. Fábián, A. Rudolf, A. Cachin, J.-E. Wegrowe, J.-P. Ansermet, *J. Magn. Magn. Mater.* **2004**, *271*, 153.
[34] H. C. Van Elst, *Physica* **1959**, *25*, 708.
[35] A. Blondel, J. P. Meier, B. Doudin, J.-P. Ansermet, *Appl. Phys. Lett.* **1994**, *65*, 3019.
[36] P. R. Evans, G. Yi, W. Schwarzacher, *Appl. Phys. Lett.* **2000**, *76*, 481.
[37] L. Gravier, J.-E. Wegrowe, T. Wade, A. Fabian, J.-P. Ansermet, *IEEE Trans. Magn.* **2002**, *38*, 2700.
[38] L. Gravier, S. Serrano-Guisan, F. Reuse, J.-P. Ansermet, *Phys. Rev. B* **2006**, *73*, 52410.
[39] X. Huang, L. Tan, H. Cho, B. J. H. Stadler, *J. Appl. Phys.* **2009**, *105*, 07D128.
[40] K. Liu, K. Nagodawithana, P. C. Searson, C. L. Chien, *Phys. Rev. B* **1995**, *51*, 7381.
[41] F. Nasirpouri, P. Southern, M. Ghorbani, A. I. Zad, W. Schwarzacher, *J. Magn. Magn. Mater.* **2007**, *308*, 35.
[42] L. Piraux, J.-M. George, J. F. Despres, C. Leroy, E. Ferain, R. Legras, K. Ounadjela, A. Fert, *Appl. Phys. Lett.* **1994**, *65*, 2484.
[43] X.-T. Tang, G.-C. Wang, M. Shima, *Phys. Rev. B* **2007**, *75*, 134404.
[44] I. Bakonyi, E. Simon, B. G. Tóth, L. Péter, L. F. Kiss, *Phys. Rev. B* **2009**, *79*, 174421.
[45] B. G. Tóth, L. Péter, Á. Révész, J. Pádár, I. Bakonyi, *Eur. Phys. J. B* **2010**, *75*, 167.
[46] J. W. G. Bos, H. W. Zandbergen, M.-H. Lee, N. P. Ong, R. J. Cava, *Phys. Rev. B* **2007**, *75*, 195203.
[47] B. Hamdou, J. Kimling, A. Dorn, E. Pippel, R. Rostek, P. Woias, K. Nielsch, *Adv. Mater.* **2013**, *25*, 239.
[48] R. D. Barnard, *Thermoelectricity in Metal and Alloys*, Taylor and Francis, London **1972**.
[49] J. S. Dugdale, *The Electrical Properties of Metals and Alloys*, Edward Arnold, London **1997**.
[50] G. K. White, S. B. Woods, *Philos. Trans. R. Soc. London, A* **1959**, *251*, 273.
[51] J. Kimling, K. Nielsch, K. Rott, G. Reiss, *Phys. Rev. B* **2013**, *87*, 134406.
[52] F. Tsui, B. Chen, J. Wellman, C. Uher, R. Clarke, *J. Appl. Phys.* **1997**, *81*, 4586.
[53] J. Kimling, J. Gooth, K. Nielsch, *Phys. Rev. B* **2013**, *87*, 094409.

© 2016 WILEY-VCH Verlag GmbH & Co. KGaA, Weinheim

II

Magnetothermopower and magnetoresistance of single Co-Ni/Cu multilayered nanowires
Tim Böhnert, Anna Corinna Niemann, Ann-Kathrin Michel, Svenja Bäßler, Johannes Gooth, Bence G. Tóth, Katalin Neuróhr, László Péter, Imre Bakonyi, Victor Vega, Victor M. Prida, and Kornelius Nielsch

Reprinted with permission from *Physical Review B* **90**, 165416 (2014)
Copyright 2014 American Physical Society.

Author Contributions: T.B., A.-K.M., S.B., B.G.T., K.Ne., and V.V. synthesized the nanowires. A.C.N. and T.B. conducted the transport measurements. V.V. conducted the TEM study. T.B., A.C.N., and J.G. analyzed the data. T.B. wrote the manuscript. All authors significantly contributed to the scientific discussion during the data evaluation and manuscript preparation. I.B., V.M.P. and K.N. supervised the project.

PHYSICAL REVIEW B **90**, 165416 (2014)

Magnetothermopower and magnetoresistance of single Co-Ni/Cu multilayered nanowires

Tim Böhnert,[1] Anna Corinna Niemann,[1] Ann-Kathrin Michel,[1] Svenja Bäßler,[1] Johannes Gooth,[1] Bence G. Tóth,[2]
Katalin Neuróhr,[2] László Péter,[2] Imre Bakonyi,[2] Victor Vega,[3] Victor M. Prida,[3] and Kornelius Nielsch[1]
[1]*Institute of Applied Physics, Universität Hamburg, D-20355 Hamburg, Germany*
[2]*Wigner Research Centre for Physics, Hungarian Academy of Sciences, H-1121 Budapest, Hungary*
[3]*Departamento de Física, Universidad de Oviedo, s/n 33007 Oviedo, Spain*

(Received 26 May 2014; revised manuscript received 5 September 2014; published 14 October 2014)

The magnetothermopower and the magnetoresistance of single Co-Ni/Cu multilayered nanowires with various thicknesses of the Cu spacer are investigated. Both kinds of measurement are performed as a function of temperature (50–325 K) and under applied magnetic fields perpendicular to the nanowire axis, with magnitudes up to −15% at room temperature. A linear relation between thermopower S and electrical conductivity σ of the nanowires is found, with the magnetic field as an implicit variable. Combining the linear behavior of the S vs σ relation and the Mott formula, the energy derivative of the resistivity is determined. In order to extract the true nanowire materials parameters from the measured thermopower, a simple model based on the Mott formula is employed to distinguish the individual thermopower contributions of the sample. By assuming that the nondiffusive thermopower contributions of the nanowire can be neglected, it is found that the magnetic-field-induced changes of thermopower and resistivity are equivalent. The emphasis in the present paper is on the comparison of the magnetoresistance and magnetothermopower results and it is found that the same correlation is valid between the two sets of data for all samples, irrespective of the relative importance of the giant magnetoresistance or anisotropic magnetoresistance contributions in the various individual nanowires.

DOI: 10.1103/PhysRevB.90.165416 PACS number(s): 75.47.De, 72.15.Jf, 73.63.−b, 81.15.Pq

I. INTRODUCTION

The thermopower, or Seebeck coefficient, S describes the redistribution of charge carriers driven by an applied temperature gradient. Experiments show a linear behavior between thermopower S and electrical conductivity σ [1–14], with the magnetic field as an implicit variable, in metals with anisotropic magnetoresistance (AMR) [15–17] or giant magnetoresistance (GMR) [18,19] effects. Comparing this linear relation to the Mott formula [20], which describes the diffusive part of the thermopower, a direct proportionality between S and σ is predicted in materials with negligible nondiffusive contributions. On the contrary, the experimental results do not obey these clear predictions and often a more complicated relationship is presumed. The major experimental difficulty is that only relative Seebeck coefficients of the specimen with respect to the contact material are accessible. In order to obtain absolute thermopower values, the measured data have to be corrected by the absolute values of the contact material. These absolute literature values are calculated ultimately from observations of the Thomson effect of pure bulk samples [21,22]. Since the thermopower is very sensitive to impurities [23] and shows size effects [24,25], deviations between the literature values and properties of materials used in the experiments should be considered. However, an evaluation of a material's absolute Seebeck coefficient directly from thermopower measurements has not been challenged to date. In this work, the different thermopower contributions are distinguished utilizing a simple model based on the Mott formula. This enables us to separate the different thermopower contributions of the specimen and the electrical contact structure.

Currently, the interest in the magnetothermopower (MTP) of magnetic nanostructures is high, as recent publications reporting on measurements on single nanowires [26,27], tunnel junctions [28], and spin valves [29,30] show. Especially multilayered nanowires constitute a perfect model system to experimentally investigate spin-dependent transport in the current-perpendicular-to-plane (CPP) mode. The CPP transport is of particular interest in the concept of spin heat accumulation, which is proposed to cause a violation of the Wiedemann-Franz law [31].

According to the literature, electrodeposited Co-Ni/Cu nanowires [32–36] exhibit higher GMR values (between −23% and −35%) than Co/Cu nanowires [1,37–44] (between −14% and −15%). The magnetic-field dependence of S in materials that show AMR or GMR effects is explained either by two spin-dependent Seebeck coefficients [1,2] or through the Mott formula using the resistivity instead of the electrical conductivity of the sample [1–9]. The latter approach has been applied by Conover *et al.* [3] and is used to predict equivalent MTP and magnetoresistance (MR) behavior. However, in spite of several related publications, this prediction has not been convincingly demonstrated [8,27,45]. One of the few publications on this topic is by Costache *et al.* [46], who managed to separate the magnon contribution from the diffusive thermopower of ferromagnetic thin films. In addition, the energy derivative of the resistivity from the Mott formula can be calculated, which can be correlated with the transmission function serving as a starting point in theoretical models.

To contribute to a deeper insight into the interplay between heat and spin, Co-Ni/Cu multilayered nanowires are electrochemically deposited into nanoporous alumina templates. Electrical contacts are lithographically defined on top of single nanowires on a glass substrate in contrast to measurement approaches performed on platforms [47–50], in which the particular nanowire had to be assembled on top of a predefined structure. The thermopower and magnetoresistance of several single nanowires have been measured in a wide temperature

©2014 American Physical Society

range as a function of the magnetic field. The relation between these two properties is compared to the Mott formula in order to extract the absolute thermopower of the nanowire materials. The paper is organized as follows. Section II gives a definition and the theoretical background for the main experimental quantities (MR and MTP) investigated in the present paper. In Sec. III, the nanowire synthesis and the measurement setup is explained in detail. The results of MR and MTP measurements are presented in Sec. IV, while Sec. V is devoted to a discussion of their correlation based on the Mott formula. Finally, the conclusions are summarized in Sec. VI.

II. THEORETICAL BACKGROUND

A. Magnetoresistance

The crucial parameters for an understanding of the magnetotransport phenomena in nanowires are the resistivity ρ and the magnetoresistance [15–17]. In the following, two definitions of the MR ratio r_{MR} are compared to the MTP ratio r_{MTP}, namely, the conservative $r_{\text{MR}} = (\rho_H - \rho_0)/\rho_0$ and the inflationary (also called optimistic) $r_{\text{MR,inf}} = (\rho_H - \rho_0)/\rho_H$, with the zero-magnetic-field resistivity ρ_0 and the resistivity in the magnetic field ρ_{H}.

In multilayered nanowires, which are the subject of the present study, an appropriate alternating sequence of magnetic and nonmagnetic segments leads to spin-dependent scattering events that result in a GMR effect [18,19] and simultaneously the spin-dependent scattering events within the magnetic layer lead to an AMR effect [15–17]. The relative importance of the GMR and AMR effects in a given nanowire depends on the individual layer thicknesses, interfacial features, and the eventual presence of pinholes in the nonmagnetic spacer layer.

B. Thermopower

The origin of the thermopower or Seebeck coefficient lies in the temperature-dependent average energy of the electrons, which generally leads to a diffusion towards the cold side. The accumulation of charge carriers at the cold side builds up the so-called thermoelectric voltage. The proportionality factor between the thermoelectric voltage U_{thermo} and the temperature difference ΔT across a sample is called the Seebeck coefficient S. This coefficient is an intrinsic material property and is defined either absolutely against a superconductor or relative to a specific metallic material (mostly platinum). Per definition, the Seebeck coefficient is negative if electrons diffuse towards the cold side of the sample. The Mott formula is a first-order approximation of the Boltzmann transport equation and describes S in the free-electron model [20]. Substituting the electrical conductivity for the resistivity, the following expression for the Mott formula is derived:

$$S = -\frac{cT}{\rho}\left(\frac{d\rho(E)}{dE}\right)_{E=E_F}, \tag{1}$$

with $c = \pi^2 k_B^2/3q$, q being the charge of the carriers, k_B the Boltzmann constant, ρ the electrical resistivity, and E the energy of the charge carriers. The energy derivatives of the resistivity are attainable by first-principle calculations, but only a few publications consider the band structure [10,51].

The thermopower expressed by the Mott formula describes solely diffusive contributions of the thermopower, which is valid only if the charge carriers are scattered dominantly by impurities and lattice defects. However, at certain temperatures, electron-phonon and electron-magnon collisions can give rise to additional thermopower contributions called phonon drag and magnon drag, respectively [52–54]. The diffusive thermopower is independent of the phonon drag, as it does not change the heat capacity of the electrons [23,52]. Therefore, the diffusive and nondiffusive thermopower contributions are independent of each other and simply add up.

The relative change of the Seebeck coefficient in an applied magnetic field is called magnetothermoelectric power (MTEP) ratio and is defined as:

$$r_{\text{MTEP}} = \frac{U_{\text{thermo}}(H) - U_{\text{thermo}}(0)}{U_{\text{thermo}}(0)}. \tag{2}$$

Here U_{thermo} describes the measured thermoelectric voltage with respect to the contact material. In the case of opposite signs of the thermopower of the nanowire and the contact material, the r_{MTEP} can reach infinite values and should be treated with caution. The term magnetothermopower ratio will be used to describe the magnetic-field-induced effect relative to the absolute Seebeck coefficient of the nanowire sample and is defined as:

$$r_{\text{MTP}} = \frac{S_{\text{NW}}^{\text{abs}}(H) - S_{\text{NW}}^{\text{abs}}(0)}{S_{\text{NW}}^{\text{abs}}(0)} = \frac{U_{\text{thermo}}(H) - U_{\text{thermo}}(0)}{U_{\text{thermo}}(0) - S_{\text{contact}}^{\text{abs}}(0)\Delta T}, \tag{3}$$

with the absolute thermopower values S^{abs}. Obtaining the r_{MTP} is experimentally challenging due to uncertainties of the absolute Seebeck coefficient value of the contact materials $S_{\text{contact}}^{\text{abs}}$. Absolute literature values for most metals from low temperature to room temperature (RT) are available [55], but the Seebeck coefficient is very sensitive to impurities [23] and size effects [24,25]. Therefore, it depends on the fabrication technique and deviations between the literature values and properties of materials used in the experiments should be considered.

The magnetic field dependence of the energy derivatives of the resistivity in the Mott formula and the relation between r_{MTP} and r_{MR} are the focus of the present work. One of the few publications on this topic by Conover *et al.* [3] directly relates r_{MTP} and r_{MR} by utilizing the linear relationship between S and σ discovered by Nordheim and Gorter [56,57]. Up to now, in several magnetic systems, such as granular alloys, magnetic/nonmagnetic multilayers, spin valve structures, and alloys, a linear dependence of the Seebeck coefficient on the electrical conductivity in an applied magnetic field has been found [1–14]. By comparing the linear relationship to Eq. (1), it seems reasonable to assume that the quantity $d\rho/dE$ at the Fermi energy does not depend on the magnetic field.

III. EXPERIMENT

A. Sample preparation and characterization

In this work, self-ordered anodized aluminum oxide membranes exhibiting a hexagonal nanoporous structure [58] were used as templates for the preparation of Co-Ni/Cu multilayered

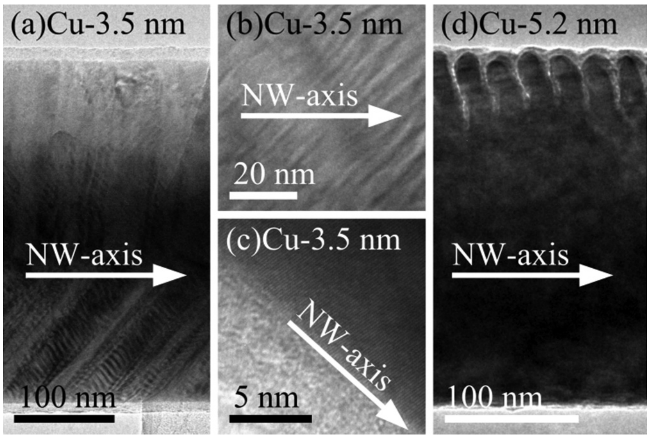

FIG. 1. (a) Transmission electron microscope image of a single nanowire (NW) of the 3.5-nm Cu sample with an average bilayer thickness of 8.7 nm. The fringes at the bottom are not related to the bilayered structure, but are rather artifacts that are associated with electron scattering at twin boundaries in the material because of the large nanowire diameter. (b) Magnification of the bilayers and (c) high-resolution transmission electron microscope image of the edge of the same nanowire and the SiO_2 shell in the bottom left. (d) Transmission electron microscope image of the 5.2-nm Cu sample.

TABLE I. Bilayer lengths l_{bilayer} and magnetic $l_{\mathrm{Co-Ni}}$ and nonmagnetic l_{Cu} layer thicknesses of the investigated nanowires. The atomic ratios of Co:Ni:Cu and Co:Ni were obtained from the overall nanowire compositions measured by the transmission electron microscope (data given after a correction for the Cu grid background) or the scanning electron microscope (these data are marked with an asterisk). The bilayer thicknesses were determined as described in the text. The two thinnest l_{Cu} values are roughly approximated.

l_{Cu} sample	l_{bilayer} (nm)	$l_{\mathrm{Co-Ni}}$ (nm)	Co:Ni:Cu	Co:Ni
0.2-nm Cu	not measured		not measured	
0.8-nm Cu	not measured		not measured	
0.9-nm Cu	17.3 ± 1.3	16.4	32:64:3	33:66
1.4-nm Cu	17.5 ± 1.5	16.1	47:47:6	50:50
3.5-nm Cu	8.7 ± 1	5.2	25:43:41	42:58
	9.2*	5.4*	29:29:42*	50:50*
5.2-nm Cu	22.6 ± 1.1	17.4	23:54:22	30:70

nanowires. In order to passivate the surface of the nanowires, the pores of the alumina template were coated by atomic layer deposition with a SiO_2 shell having a thickness of about 5 nm [59,60]. The multilayered Co-Ni/Cu nanowires were prepared by two-pulse plating from a single bath by using an Ivium CompactStat potentiostat. The Cu layers were electrodeposited at a potential of −0.58 V with respect to an Ag/AgCl electrode, while the Co-Ni layers were electrodeposited at a potential of −1.5 V vs an Ag/AgCl electrode. A $Co_{0.5}Ni_{0.5}$ composition was chosen to maximize the GMR effect [61] according to the recipe published by Tóth *et al.* [62]. The applied Cu deposition potential corresponds to the electrochemically optimized value [62] at which neither a dissolution of the magnetic layer during the Cu deposition nor a codeposition of magnetic atoms into the Cu spacer layer occurs. A Cu content of about 2% is estimated in the magnetic layers based on the ratio of the current densities during the two pulses [62]. According to the results of Pullini and Busquets-Mataix on multilayered nanowires [63], the current efficiencies can be expected slightly below the value of 100% known from depositions on thin films [62]. Furthermore, in agreement with previous reports [63], there is some uncertainty of the effective cathode area due to a canting of layer planes with respect to the nanowire axis up to 45° [see Figs. 1(a) and 1(b)] and due to an unknown amount of filled pores. Thus, the nominal deposition values have significant unsystematic errors and detailed electron microscopy investigations are conducted to get a reliable estimate of the actual layer thicknesses by using the bilayer thickness and the analyzed nanowire composition. The multilayered nanowire samples will be identified by the Cu layer thickness obtained from these studies in a manner as described below.

After electrodeposition of the nanowires, a mixture of chromic acid and phosphoric acid was used to dissolve the template selectively. The single nanowires with diameters around 240 nm were separated by filtration from the solution, diluted in ethanol, and finally deposited on a glass substrate with a thickness of 150 μm. Transmission electron microscope micrographs of different nanowire sections of the 3.5- and 5.2-nm Cu samples are shown in Fig. 1. A chemical analysis of the 0.9-, 1.4-, 3.5-, and 5.2-nm Cu samples was performed by transmission electron microscopy energy dispersive x-ray spectroscopy (TEMEDX) (JEM 2100) on single nanowires placed on a fine-mesh copper grid. For the 3.5-nm Cu sample, the composition was also measured by scanning electron microscopy energy dispersive x-ray spectroscopy (ZEISS SIGMA) on the cross section of the membrane. The overall composition of the Co-Ni/Cu nanowires is given in columns 4 and 5 of Table I. The uncertainty of the composition analysis is around 5% for each element and the statistical deviation between individual nanowires of the same sample is in the same range. The homogeneity of the composition along and across the nanowire axis was confirmed by TEMEDX. The TEM analysis results were corrected for the average Cu background signal due to the transmission electron microscope copper grid, which leads to an additional error for the TEMEDX results. The large scatter of the Co-Ni composition in the magnetic layers of different samples, exceeding the measurement error, may be from the preparation conditions. The composition of the magnetic layer is known to change very rapidly with the ionic concentration ratio in the template and the deposition current density [64]. These factors are difficult to control due to complex diffusion conditions in the template and might contribute to the differences observed in the magnetic layer compositions of the various samples.

In addition to the quantitative chemical analysis, the bilayer thickness was determined from TEMEDX line scans along the nanowires at several positions and averaged. For the 3.5-nm Cu sample, the bilayer length was also estimated from scanning electron microscope micrographs by dividing the average nanowire length by the number of bilayer pulses during electrodeposition. With information about the bilayer thickness and the overall nanowire composition, the average thickness of the magnetic and nonmagnetic layers was determined with an uncertainty of about ± 2 nm. Compared to the uncertainty of the layer thicknesses, the amount of Cu in the magnetic layer is insignificant and was neglected. Nevertheless, these are average values only and do not necessarily agree with the actual data of the individual nanowire used in the magnetotransport measurements. Despite all the uncertainties, the SEM and TEM results are in good agreement (as shown in Table I for the 3.5-nm Cu sample), which gives a hint at the reliability of the analysis. The determination of the layer thicknesses of electrodeposited multilayered nanowires is still a remaining problem [32].

It should be kept in mind that the uncertainties of the chemical composition as well as the bilayer length and the individual layer thicknesses do not have a significant impact on the analysis of the measured magnetotransport data. This is because the main emphasis in the present paper is on a comparison of the magnetoresistance and magnetothermopower results measured on the same individual nanowire. As will be presented in Sec. IV, the same correlation was found to be valid between the two sets of data for all samples, irrespective of the relative importance of the GMR or AMR contributions, which is finally determined by the actual thicknesses of the magnetic and nonmagnetic layers. Therefore, the geometrical and compositional properties are rather used to label the samples.

For the determination of the resistivity, knowledge of the diameter and length of the nanowire is necessary. These are determined from scanning electron microscope micrographs of each nanowire and corrected for the passivating SiO_2 layer thickness determined from transmission electron microscope images such as those shown in Fig. 1. Figure 1(d) shows part of a nanowire with a damaged SiO_2 layer. The upper part of the Cu layers is dissolved, which leads to the high contrast of the micrograph and is not representative for all samples.

For the present work, six multilayered nanowire samples were altogether prepared with different deposition parameters, which were grouped according to their measured magnetoresistance characteristics as shown in Fig. 2. The 3.5-nm Cu sample was designed to have approximately equal magnetic and nonmagnetic layer thicknesses and exhibited the largest GMR effect with a very small AMR contribution. The other five samples were designed to have various Cu layer thicknesses and a constant magnetic layer thickness. The 0.8-, 1.4-, and 5.2-nm Cu samples exhibit significant GMR and AMR contributions, while the 0.2- and 0.9-nm Cu samples show solely the AMR effect.

B. Magnetotransport measurements

In the present work, the magnetotransport has been measured on single nanowires with the help of lithographically defined measurement platforms on a glass substrate. For this purpose, a double layer of photoresist (ma-P 1205, microresist technology) and lift-off resist (LOR-3B, Micro Chem) was applied. Using a laser writer (μPG 101, Heidelberg Instruments), the photoresist was exposed and developed. An *in situ* radio-frequency argon sputter etching was applied for 15 min to remove the SiO_2 shell and surface oxides of the nanowire in order to achieve low-resistance Ohmic contacts. The electrical contacts consisted of a few-nanometer-thick titanium adhesion layer and a 60-nm-thick platinum layer, both sputtered prior to the lift-off process. A scanning electron microscope micrograph of a typical electrical contact structure for thermoelectric characterization of a single nanowire is shown in Fig. 3(a). The microheater was located perpendicular

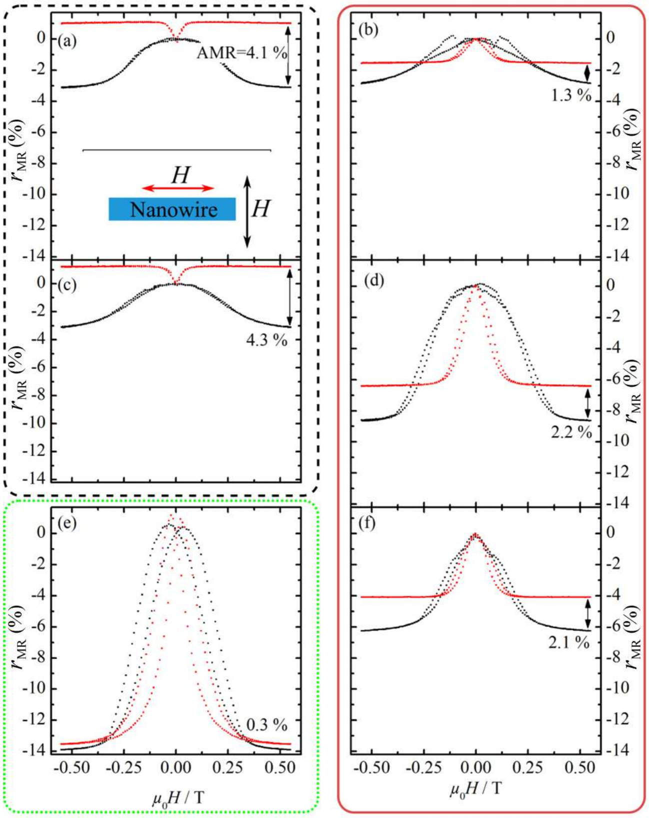

FIG. 2. (Color online) Plot of the $r_{MR}(H)$ curves of the Co-Ni/Cu multilayered nanowires in parallel and perpendicular directions of the magnetic field with respect to the nanowire axis (electrical current direction) at RT for (a) 0.2-nm Cu, (b) 0.8-nm Cu, (c) 0.9-nm Cu, (d) 1.4-nm Cu, (e) 3.5-nm Cu, and (f) 5.2-nm Cu samples. The samples within the dashed black border show AMR-dominated behavior due to pinholes in the nonmagnetic layers. The samples within the red border show significant GMR effects due to continuous bilayers and the sample within the dotted green border shows a dominating GMR effect. The saturation fields are not reached for all of the samples and the actual saturation values are slightly higher.

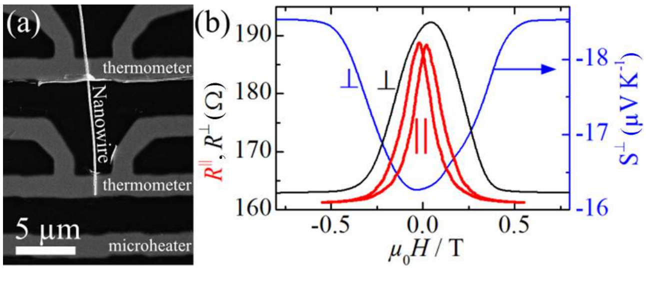

FIG. 3. (Color online) (a) Scanning electron microscope image of a nanowire and the electrical contact structure. (b) Parallel (probe station setup) and perpendicular (cryostat) resistance measurements at RT and a Seebeck coefficient measurement (cryostat) in a magnetic field for the 3.5-nm Cu sample.

to the nanowire to create a temperature gradient of 3 K μm^{-1} via Joule heating. Two resistance thermometers were placed at a distance of 8 μm along the nanowire and served three purposes: probing the temperature difference ΔT as well as measuring both the resulting thermovoltage U_{thermo} between the hot and the cold contacts to the nanowire and the electrical conductivity σ. This electrical contacting method has been described elsewhere [9].

With the setup introduced above, temperature-dependent measurements could be performed with the magnetic field perpendicular to the nanowire axis in a cryostat. During a full measurement cycle, the temperature of the cryostat T_{cryostat} was changed stepwise between 50 and 325 K. At each increment, the magnetic field was varied stepwise up to ±3 T and electric powers of roughly 1, 2, and 5 mW were applied to the heater. The resistance or the thermovoltage of the nanowire was measured separately at thermal equilibrium, which is necessary to reduce the noise level. All resistance values were measured with the four-point technique at 128 and 189 Hz by the lock-in amplifier of the cryostat with a feedback-controlled alternating current source at 10 μA. The thermovoltage was measured by a 2182A nanovoltmeter (Keithley) with an input impedance greater than 10 GΩ and corrected by the offset at zero heat voltage (about 1 μV). To probe the temperature difference, the ac resistance of both thermometers was measured and calibrated against T_{cryostat} at zero heat power. The temperature difference $\Delta T = T_{\text{hot}} - T_{\text{cold}}$ is about one-third of the rise of the average temperature of the nanowire $\bar{T} = (T_{\text{HOT}} + T_{\text{COLD}})/2$ for the electrical contact structure shown in Fig. 3(a). A so-called probe-station setup was used for measurements at RT with the magnetic field perpendicular and parallel to the nanowire axis.

The measured r_{MR} and r_{MTP} data include contributions from GMR, AMR, and magnon-related magnetoresistance. Below the saturation field, the GMR and AMR effects dominate, while above the saturation field, the magnon-related magnetoresistance dominates the magnetotransport [65]. Nernst effects of the contact structure and time-dependent changes due to a continuous temperature rise of the microstructure were determined from the slopes above saturation and were corrected, which resulted in symmetric hysteresis loops. The correction of these deviations, typically below 0.06 μV K^{-1} at 1 T and RT, are important for the following comparisons of S and σ.

IV. RESULTS

A. Magnetoresistance

The resistivities of the multilayered nanowires at RT vary between 28 and 50 $\mu\Omega$ cm, as shown in Fig. 4(a), with no clear dependence on the Cu layer thickness in contrast to the literature [66,67]. It seems that the zero-field resistivity is dominated by nonsystematic changes of the impurity concentration, the crystallinity, and lattice defects, but not the spin-dependent scattering, which should depend on the Cu layer thickness. The residual resistivity values obtained from the temperature behavior can be expected to be between 16 and 35 $\mu\Omega$ cm. These values are a factor of 2–5 higher than measured for electrochemically deposited Co-Ni alloy nanowires [9] and thin films [68], which seems reasonable by considering the additional scattering due to Cu impurities, interfaces, and spin-dependent scattering. Errors in the diameter measurement have to be considered and might lead to deviations up to 15% of the resistivity. Lenczowski *et al.* [66] investigated the current-in-plane (CIP) resistivity of electrochemically deposited Co/Cu thin films and found a decrease from 15 $\mu\Omega$ cm at 1-nm Cu layer thickness to 5 $\mu\Omega$ cm at 5 nm.

The Cu layer thickness has a major influence on the GMR effect, which reaches a maximum for electrodeposited nanowires (CPP geometry) between 3 and 5 nm [35,42,69,70]. Bakonyi and Peter published a comprehensive review on

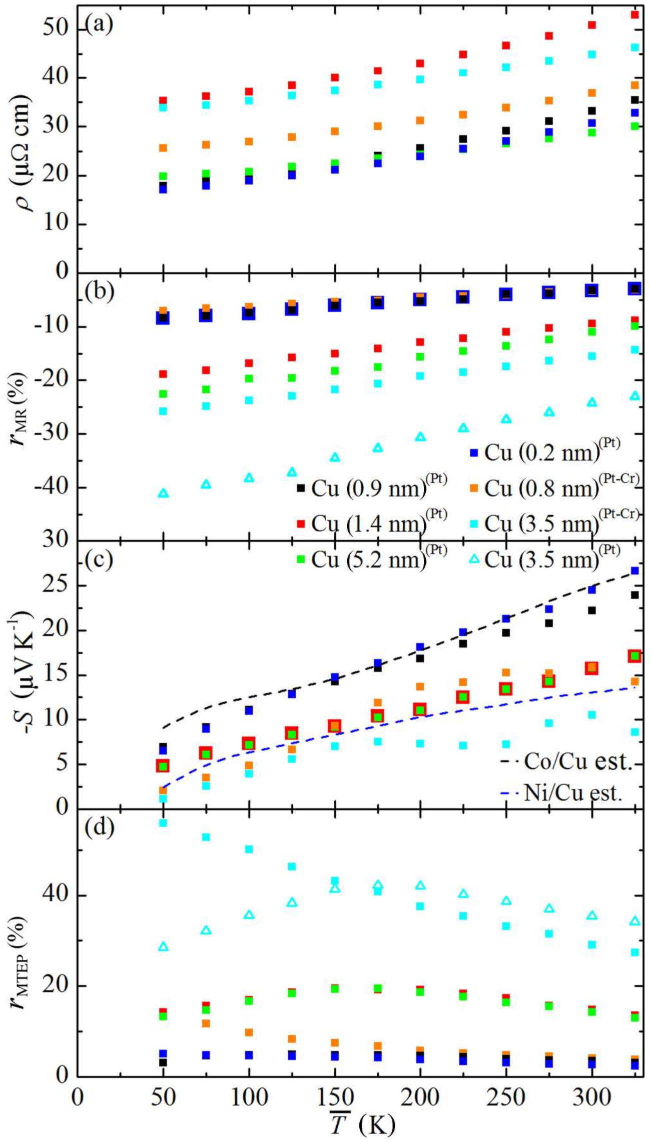

FIG. 4. (Color online) Temperature dependence of the (a) zero-field resistivity, (b) r_{MR}, (c) thermopower, and (d) r_{MTEP} of the multilayered nanowires. The r_{MR} and r_{MTEP} data were measured in perpendicular magnetic fields of 3 T. Also shown are (c) estimated thermopower values for Co/Cu and Ni/Cu multilayer with a layer thickness ratio of 5:1 using the literature bulk data for S_{Co}, S_{Ni}, and S_{Cu}. (b) and (d) Two 3.5-nm Cu samples were measured 21 months apart, which caused a reduction of the effect magnitudes.

TABLE II. Room temperature values of resistivities, $r_{\mathrm{MR}\perp}$, $r_{\mathrm{MR}||}$, $r_{\mathrm{AMR}} = r_{\mathrm{MR}||} - r_{\mathrm{MR}\perp}$, thermopower S, and magnetothermoelectric power ratio r_{MTEP}. The $r_{\mathrm{MR}||}$ and $r_{\mathrm{MR}\perp}$ data were obtained in a magnetic field of 0.55 T parallel and perpendicular to the nanowire axis, respectively, as shown in Fig. 2. The saturation fields are not reached for all samples and the actual values are slightly higher. The r_{MTEP} data were obtained in the perpendicular magnetic field up to 3 T.

l_{Cu} sample	ρ ($\mu\Omega$ cm)	$r_{\mathrm{MR}\perp}$ (%)	$r_{\mathrm{MR}\|\|}$ (%)	r_{AMR} (%)	S (μV K^{-1})	r_{MTEP} (%)
0.2-nm Cu	30.7	− 3.1	1.0	4.1	− 24.5	2.7
0.8-nm Cu	36.8	− 2.9	− 1.6	1.3	− 18.5	4.1
0.9-nm Cu	33.2	− 3.1	1.2	4.3	− 22.2	3.6
1.4-nm Cu	50.8	− 8.6	− 6.4	2.2	− 15.7	14.8
3.5-nm Cu	44.9	− 13.9	− 13.5	0.3	− 15	29.0
5.2-nm Cu	28.7	− 6.2	− 4.1	2.1	− 15.7	14.3

the progress and difficulties regarding GMR multilayered film depositions [71]. The magnitude of the GMR effect is independent of the direction of the applied magnetic field. On the other hand, in the case of the bulk AMR effect, the resistivity increases for a magnetic field parallel to the measuring current and decreases if the current and magnetic field are perpendicularly aligned. Therefore, the GMR and AMR contributions can be distinguished by comparing the r_{MR} values above the saturation field in parallel and perpendicular directions to the nanowire axis, as shown in Fig. 2. In Table II the total perpendicular $r_{\mathrm{MR}\perp}$, parallel $r_{\mathrm{MR}||}$, and the difference of the values in both directions, the AMR effect r_{AMR}, are given. According to Liu *et al.* [72], three regimes can be distinguished in electrochemically deposited multilayers: continuous bilayers, pinholes in the nonmagnetic layer, and pinholes in the magnetic layer. At continuous Cu layers, the GMR effect typically decreases as the Cu layer thickness increases. Below a certain spacer thickness, pinholes form in the Cu layer and a direct exchange coupling leads to a parallel alignment of the magnetic layers in zero field. The 0.8-, 1.4-, and 5.2-nm Cu samples indicate a pinhole-dominated behavior with the increasing GMR effect with increasing spacer thickness. The 3.5-nm Cu nanowire has thinner magnetic segments and, as a result, a higher GMR effect. At thinner spacer thicknesses, the GMR effect vanishes and only the AMR effect remains (0.2- and 0.9-nm Cu samples). In the third case (not observed) the so-called superparamagnetic magnetoresistance occurs, due to magnetic islands embedded in the nonmagnetic matrix that act like magnetic nanoparticles. Our perpendicular magnetoresistance values above the saturation fields at RT are comprised between −3.3% and −15.5% [see Fig. 4(b)], while the highest value for electrodeposited Co-Ni/Cu multilayered nanowires in the literature is −35% (derived from the $r_{\mathrm{MR,inf}}$ value of −55% given in Ref. [32]). The decrease of the general MR magnitudes between the two 3.5-nm Cu measurements 21 months apart can be ascribed to aging of the nanowires that are stored at RT in ethanol. Subsequent measurements three and seven months later show a further decrease of both the r_{MR} value and the electrical conductivity.

B. Magnetothermopower

The thermopower or Seebeck coefficient of a multilayered nanowire can be described as a series of Co-Ni and Cu segments, which results in a relation known from the so-called Nordheim-Gorter rule [52,73,74]. Using the compositional and geometrical data given in Table I and the thermopower values of Co-Ni alloy nanowires reported elsewhere [9], the literature bulk values of S_{Cu} [75], and bulk resistivities [16], the overall thermopower at RT is roughly estimated. Two effects increase the estimated thermopower with decreasing Cu layer thickness from −17 to −25 μ V K^{-1}: These are the increasing ratio of Co-Ni to Cu and, more importantly, the compositional change of the magnetic layer (the latter resulting in a change of $S_{\mathrm{Co-Ni}}$ from −18 to −24 μV K^{-1}). The measured thermopowers at RT vary between −15 and −24.5 μV K^{-1} and fit well to the calculation. These thermopower RT values are given in Table II; the values of some samples are extrapolated from the trend at low temperatures, due to errors in the determination of ΔT above 150 K. The Seebeck coefficients in Fig. 4(c), interpolated at 25-K steps for clarity, show a monotonic increase with the temperature, as expected for most metals due to a single type of charge carrier and by the dominating diffusive thermopower [52].

As explained above, the thermopower for Co/Cu and Ni/Cu multilayers is estimated from the literature values for bulk in reference to Pt [16,21,76–78]. Since the composition has a stronger influence than the layer thicknesses, the Co-Ni to Cu ratio is set to 5:1. It seems that the measured values of the 0.9-nm Cu sample are shifted upward, while the values of the 3.5-nm Cu sample are shifted downward in comparison with the estimation. The phonon-drag peak around 75 K in the estimated curves is due to the bulk Pt values. This peak is not visible in the nanowire measurements as expected due to the nanostructuring of the Pt contacts. Above 150 K, some measurements show irreversible deviations of ΔT. Wherever possible, the faulty data are replaced by thermometer data of a comparable sample and scaled to fit the low-temperature region. At each temperature step, the magnetic field dependence of the thermopower is measured. The relative change due to the applied magnetic field (the r_{MTEP} value) is shown in Fig. 4(d). The RT values of the r_{MTEP} are 2.7% for 0.2-nm Cu, 4.2% for 0.8-nm Cu, 3.5% for 0.9-nm Cu, 14.7% for 1.4-nm Cu, 29.1% for 3.5-nm Cu, and 14.5% for 5.2-nm Cu. These values are similar to the available literature values for Co/Cu thin films and nanowires, which range between 5% and 32% [1,2,44,73,74,79,80].

The measured r_{MTEP} values are higher than the r_{MR} values, which is in agreement with most nanowire and CPP thin-film literature [1,44,74,79,80]. On the contrary, two publications on CIP thin-film measurements show the opposite behavior with higher r_{MR} than the r_{MTEP} [2,73]. Kobayashi *et al.* [81] studied the difference between CIP and CPP measurements on the same sample and found no systematic difference between the measurement directions. (More precisely, a current-at-angle-to-plane contribution is measured that involves a CPP contribution.) Therefore, this variation in the literature data might not be due to the alignment of the current with respect to the multilayer planes, but rather due to the contact materials used and measurement setup. The r_{MTEP} [Eq. (2)] depends on the thermopower of the electrical contact structure. Because

Co/Cu and Co-Ni/Cu multilayers have negative Seebeck coefficients, positive/negative absolute Seebeck coefficients of the electrical contacts $S^{\mathrm{abs}}_{\mathrm{contact}}$ will lead to decreased/increased r_{MTEP} magnitudes compared to the r_{MR} values (Fe, Au, and Cu are positive and Pt is negative at RT). In publications that specify the contact material, the decreased/increased r_{MTEP} magnitudes seem to correlate with positive/negative $S^{\mathrm{abs}}_{\mathrm{contact}}$. Shi *et al.* [2] used Fe as contact material and measured decreased r_{MTEP} values. Gravier *et al.* [1,44,74,79] state to have measured systematically too low Seebeck coefficients (despite stating Au as the contact material), which nevertheless explains the repeatedly observed increased r_{MTEP} value [82]. Previous results on Co-Ni alloy nanowires with Pt and Au contacts behaved accordingly [9].

Our measured r_{MTEP} at temperatures above 200 K is similar in absolute magnitude to the r_{MR}, but at lower temperatures, the samples can be arranged into two groups. The r_{MTEP} of the 0.8- and 3.5-nm Cu samples continuously increases with decreasing temperature, while the rest of the samples reach a maximum around 180 K. In the case of the 3.5-nm Cu nanowire, both behaviors occur; therefore, the deviation is not due to the nanowires themselves. The explanation is that the r_{MTEP} includes the thermopower of the electrical contact structure. Due to inconsistencies of the sputtering setup, the electrical contact structure of the 0.8- and 3.5-nm Cu samples incorporated Cr, which is known to diminish the phonon drag, e.g., in Au [83]. As shown by Huebener [24], the absolute thermopower of Pt crosses zero around 180 K and reaches a maximum around 70 K due to the phonon drag. Although no phonon-drag-related peak is observed in the thermopower measurements, the Pt contacts still lead to a maximum of the r_{MTEP} at 180 K by decreasing/increasing the measured thermopower at lower/higher temperatures. In other words, the thermopower of the Pt contacts still shows the typical zero crossing between 150 and 200 K. By incorporating the Cr impurities, this zero crossing seems to be suppressed and the thermopower of Pt-Cr contact adds an approximately constant increase to the r_{MTEP} value.

The absolute change of the Seebeck coefficient due to the magnetic field ΔS is between 0.66 and 4.4 $\mu\mathrm{V K}^{-1}$. The ΔS is independent of the contact material, therefore, it is a useful property to compare the magnitudes of the effects of different materials. The highest ΔS values of around 8 $\mu\mathrm{V K}^{-1}$ at RT are measured by Shi *et al.* [2] and Nishimura *et al.* [73] on sputtered Co/Cu thin films with a nonmagnetic layer thickness of 1 nm. These thin films showed CIP GMR effects of about 50%.

V. CORRELATION BETWEEN THERMOPOWER AND RESISTANCE

The $S(H)$ and the corresponding $R(H)$ curves displayed in Fig. 3(b) indicate a typical linear relation between S and R^{-1} with a certain deviation above the saturation. It is important for the analysis that the conditions (e.g., temperature gradient and average temperature) during thermopower and resistivity measurement are identical; otherwise the dependences are not comparable. The linear relation between S and R^{-1}_{res}, with R_{res} being the residual resistance, was first found by Nordheim and Gorter [57] and was described more comprehensively by Gold *et al.* [56] with the impurity concentration as an implicit variable. Conover *et al.* [3] then predicted equal r_{MTP} and r_{MR} magnitudes and attempted to verify this experimentally. In the present work, the magnetic field is varied between ± 3 T as an implicit variable and a linear relation between $S(H)$ and $R(H)^{-1}$ is found at each temperature, as shown in Fig. 5(a). This linear relationship in combination with the Mott formula [see Eq. (1)] indicates a magnetic-field-independent $d\rho/dE$ at the Fermi energy [1–14]. By fitting S versus the conductance scaled by the average temperature of the nanowire ($\bar{T}R^{-1}$), the temperature-dependent energy derivative of the resistivity can be extracted from the slope and S_{offset} can be extracted from the offset, as shown in Figs. 5(b) and 5(c).

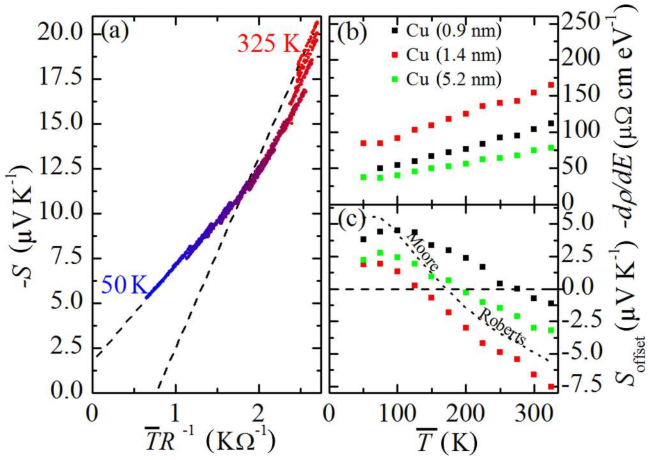

FIG. 5. (Color online) (a) Seebeck coefficient versus average temperature times the conductance of the 1.4-nm Cu sample in 25-K steps from 50 to 325 K with the applied magnetic field as an implicit variable. For simplicity, only data for $U_{\mathrm{heater}} = 5$ V are shown, which correspond to a ΔT of 3 K at 25 K to 2 K at 325 K. (b) Energy derivative of the resistivity at the Fermi energy derived from Eq. (5) against the temperature. (c) Offset from Eq. (5) and the absolute literature values of Pt [21,77].

A temperature-dependent increase of the slope has been published on Co/Cu multilayers by Baily *et al.* [80] and by Shi *et al.* [2,6,10], on Cu/Co/Cu/Ni-Fe multilayers by Kobayashi *et al.* [81], and on Fe-Ag granular alloys by Sakurai *et al.* [5]. Figure 5(c) shows the temperature-dependent offset S_{offset} of the linear fits on the data shown in Fig. 5(a). The measured Seebeck coefficient is in reference to the contact material, while the resistance measurement gives the resistance of the nanowire. Any magnetic field dependence of the measured Seebeck coefficient S_{measured} should be caused by the nanowire. In the following S_{NW} and S_{contact} refer to absolute thermopowers. Due to a magnetic-field-independent $d\rho/dE$ at the Fermi energy as discussed earlier, the Mott formula (1) predicts that the magnetic field dependence of the Seebeck coefficient is proportional to the nanowire conductivity $\rho_{\mathrm{NW}}(H)^{-1}$ at any given temperature. This can be summarized in the following two formulas for the measured Seebeck coefficients:

$$S_{\mathrm{measured}}(H) = S_{\mathrm{NW}}(H) - S_{\mathrm{contact}}, \tag{4}$$

$$S_{\mathrm{measured}}(H) = -cT\left(\frac{d\rho}{dE}\right)_{E=E_F}\rho_{\mathrm{NW}}(H)^{-1} - S_{\mathrm{offset}}. \tag{5}$$

In general, S_{offset} can arise from the following thermopower contributions: (i) thermopower of the electrical contacts (S_{contact}), (ii) nondiffusive thermopower of the sample (drag effects), and (iii) a magnetic-field-dependent energy derivative of the resistivity. The linear temperature behavior of the Seebeck coefficient of the investigated samples suggests a dominating diffusive behavior. In polycrystalline nanostructured samples of Co, Ni, and Cu, a nondiffusive thermopower can be most likely excluded, as discussed previously. Therefore, point (ii) can be neglected, but the thermopower contribution below 100 K should be carefully treated in general due to the high uncertainties and a wide range of possible effects. In the observed magnetic field range, the energy derivative of the resistivity is magnetic field independent as stated in the literature several times. Therefore, point (iii) is carefully rejected, leaving only point (i). For this material system, it follows that $S_{\text{contact}} = S_{\text{offset}}$ and, as already predicted for Fe-Cr by Conover *et al.* [3],

$$\begin{aligned} r_{\text{MTP}} &= [S(H) - S_0]/S_{\text{NW},0} \\ &= -[R(H) - R_0]/R(H) = -r_{\text{MR,inf}}. \end{aligned} \tag{6}$$

At the same time, the $r_{\text{MTP,inf}}$ is equal to $-r_{\text{MR}}$. By comparing the r_{MTP} to $r_{\text{MR,inf}}$ or S_{contact} to S_{offset}, a quantitative statement about the previous assumptions can be made. Figure 5 shows S_{offset} and the absolute bulk Pt literature values, which fit qualitatively. The temperature-dependent literature values for absolute S_{Pt} are a combination of the data by Roberts [21] (above 270 K) and Moore and Graves [77] (below 270 K), representing the most reliable literature data in each temperature region. Deviations are expected due to two effects: Size effects should reduce the phonon-drag peak [24] and impurities of the materials used in measurement setups can be expected to cause deviations from the pure bulk literature value [83]. The surface is likely contaminated by the necessary ac sputter cleaning process of 15-min duration. The Ti adhesion layer sputtered prior to the Pt deposition leads to a parallel circuit [84] of the Ti and the Pt layers and a deviation of about 0.5 μVK^{-1} at RT [21,77,85–87]. The offsets of the three samples deviate from each other. Since all three electrical contact structures show very similar heating and resistance behavior, the deviations are unexpected and might be a sign for nondiffusive thermopower contributions of the nanowires. This seems questionable close to RT and is in conflict with the previous discussion on point (ii). Independently of the origin of the deviation between the samples, the calculation of the absolute thermopower leads to very good results, as shown in the following.

In Figs. 6(a) and 6(b), the temperature behavior of the absolute thermopower of three nanowires is calculated using the bulk Pt literature value [Fig. 6(a)] and $S_{\text{contact}} = S_{\text{offset}}$ [Fig. 6(b)]. Theoretical values of the absolute thermopower for Co/Cu and Ni/Cu multilayers with 5:1 layer thicknesses are estimated by using the absolute bulk literature values [16,21,76–78] The correction by the absolute bulk literature value of Pt shifts each curve by a fixed value and changes the curvature in opposite direction, which suggests a positive phonon-drag or magnon-drag contribution similar to the results of Farrell and Greig [88] for bulk Ni. In general, bulk Co, Ni, and Cu metals show a significant phonon-drag contribution at 70 K, which is decreased in bulk Ni by adding Co impurities as Farrell and Greig showed [88]. In nanocrystalline metals, phonon transport is restricted and the phonon-electron scattering probability is thus reduced [89–91]. Hence, the phonon-drag thermopower in electrochemically deposited materials is typically negligible [9,27].

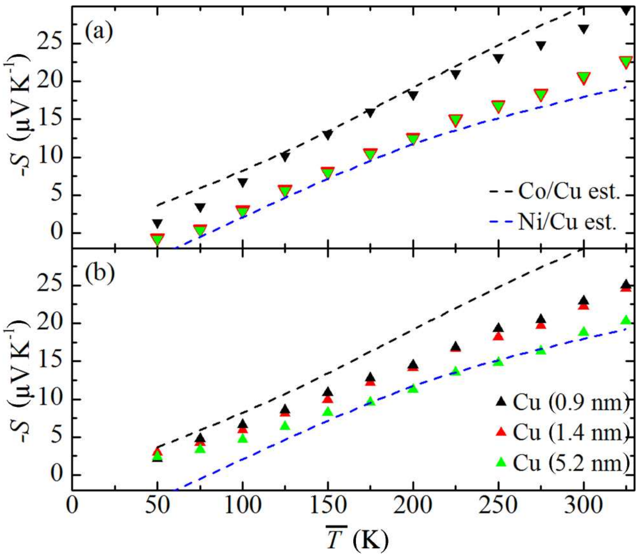

FIG. 6. (Color online) (a) Absolute thermopower obtained by correcting by the literature values for S_{Pt} [21,77], $S + S_{\text{Pt}}^{\text{abs}}$, and (b) the absolute thermopower obtained by correcting by S_{offset}, $S + S_{\text{offset}}$. The dashed lines indicate the estimated absolute thermopower values for Co/Cu and Ni/Cu multilayers with 5:1 layer thicknesses [21,76,78].

Overall, the deviations in Fig. 6(a) from the diffusive behavior are unreasonable and almost certainly are due to an artifact of the correction by inappropriate bulk values. The individual correction by S_{offset} for each sample leads to the curves shown in Fig. 6(b). The curvatures are almost completely removed and the thermopower shows the expected linear temperature behavior without an offset at absolute zero. Comparing Figs. 6(a) and 6(b) leads to the conclusion that the correction by S_{offset} is more appropriate for this material system.

The r_{MTEP} values are corrected by S_{offset} to obtain the r_{MTP} values, which are compared to the $r_{\text{MR,inf}}$ values. The r_{MTP} and $r_{\text{MR,inf}}$ curves shown in Fig. 7 have to match according to Eq. (6) and any deviations arise from variation from the linear fits in Fig. 7. The uncorrected r_{MTEP} curves are added to the figure as lines, illustrating the significance of the correction. Nonmonotonic deviations as shown by the r_{MTEP} curves are commonly attributed to drag effects of the sample [12,89,92]. Although these effects can dominate depending on the sample properties, the influence of measurement artifacts due to the contact material should be carefully considered. For instance, the r_{MTEP} at RT decreased by up to 3% due to the influence of the electrical contacts, which explains why published r_{MTEP} values deviate from the r_{MR} values as discussed in the previous section. In the case of samples with dominating drag effects, this model can be used to quantify the deviations from the

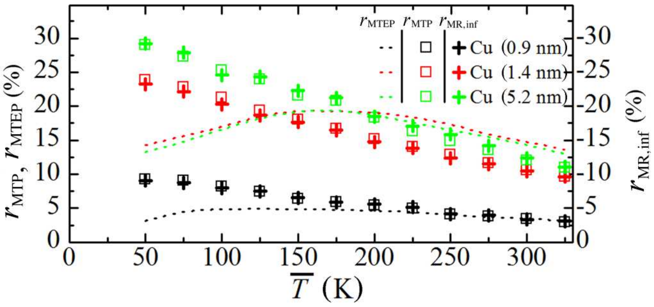

FIG. 7. (Color online) Temperature dependence of $r_{\mathrm{MR,inf}}$, r_{MTEP}, and r_{MTP} values, which are corrected under the assumption of $S_{\mathrm{contact}} = S_{\mathrm{offset}}$. The expected relation between r_{MTP} and $r_{\mathrm{MR,inf}}$ according to Eq. (6) is observed.

Mott formula by minimizing the contribution of the electrical contacts.

Several other coherent conclusions follow from this line of thought. According to Eq. (6), a finite r_{MR} value and vanishing absolute S result in a vanishing change ΔS of S due to the magnetic field. In addition, a sign change of the absolute S induces a sign change of ΔS, which is exactly the result of one of the first r_{MTEP} measurements by Piraux *et al.* [51] on Fe/Cr multilayers. The sign of S is given by the charge of the carriers and the energy derivative of the resistivity. Therefore, in metals the sign of the energy derivative of the resistivity determines the sign of S and ΔS. In contrast, the r_{MTEP} can have either sign or value due to various possible contact offsets, which is in agreement with experimental results and density of states evaluations by Tsymbal *et al.* [93] (The quantity r_{MTEP} is used with the meaning of the quantity r_{MTP} in Ref. [93].)

VI. CONCLUSION

Current-perpendicular-to-plane MTP and GMR measurements on single Co-Ni/Cu multilayered nanowires are presented with varying thickness of the Cu spacer. The thermopower values of electrochemically deposited multilayered nanowires are measured to be -15 to $-24.5\,\mu\mathrm{V\,K^{-1}}$ at RT, which convincingly agrees with estimated values between -17 and $-25\,\mu\mathrm{V\,K^{-1}}$. Magnetoresistance measurements in parallel and perpendicular magnetic fields show that the thinnest Cu spacers are not continuous and these samples show negligible GMR effects. For samples with thicker Cu layers, the GMR effects are between -9% and -25% at RT. A linear relationship between the magnetic-field-dependent Seebeck coefficient S and the electrical conductivity σ, with the magnetic field as an implicit variable, is found, as expected from the Mott formula, which describes the diffusive thermopower contribution. Disregarding nondiffusive thermopower contributions, a simple model is proposed to separate the absolute thermopower of the sample from the magnetic-field-independent thermopower of the contact material, without relying on the literature values of the latter. The temperature dependence of the thermopower offset agrees qualitatively with the literature values of the absolute Seebeck coefficient of the contact material. The absolute thermopower, the r_{MTP} values, and the energy derivative of the resistivity are calculated as a function of temperature. In accordance with the model, equal magnitudes of $r_{\mathrm{MR,inf}}$ and r_{MTP} values are the consequence. Although open questions remain, the methods presented provide a powerful tool to quantify and separate the different thermovoltage contributions.

ACKNOWLEDGMENTS

The authors gratefully acknowledge financial support via the German Academic Exchange Service, Spanish MINECO under research Projects No. MAT2010-20798-C05-04 and No. MAT2013-48054-C2-2-R, the German Priority Program SPP 1536 "SpinCAT" funded by the Deutsche Forschungsgemeinschaft (DFG), and the excellence clusters "The Hamburg Centre for Ultrafast Imaging" funded by the DFG and "Nanospintronics" funded by the State of Hamburg. Scientific support from the University of Oviedo SCTs is also recognized. Work carried out in Budapest was supported by the Hungarian Scientific Research Fund under Grant No. OTKA K104696.

[1] L. Gravier, A. Fabian, A. Rudolf, A. Cachin, J.-E. Wegrowe, and J.-P. Ansermet, J. Magn. Magn. Mater. **271**, 153 (2004).
[2] J. Shi, R. C. Yu, S. S. P. Parkin, and M. B. Salamon, J. Appl. Phys. **73**, 5524 (1993).
[3] M. J. Conover, M. B. Brodsky, J. E. Mattson, C. H. Sowers, and S. D. Bader, J. Magn. Magn. Mater. **102**, L5 (1991).
[4] D. K. C. MacDonald and W. B. Pearson, Proc. R. Soc. London Ser. A **241**, 257 (1957).
[5] J. Sakurai, D. Huo, T. Kuwai, K. Mori, T. Hihara, K. Sumiyama, and K. Suzuki, J. Phys. Soc. Jpn. **66**, 2240 (1997).
[6] J. Shi, K. Pettit, E. Kita, S. S. P. Parkin, R. Nakatani, and M. B. Salamon, Phys. Rev. B **54**, 15273 (1996).
[7] H. Itoh, J. Inoue, and S. Maekawa, Phys. Rev. B **47**, 5809 (1993).
[8] A. D. Avery, M. R. Pufall, and B. L. Zink, Phys. Rev. B **86**, 184408 (2012).
[9] T. Böhnert, V. Vega, A.-K. Michel, V. M. Prida, and K. Nielsch, Appl. Phys. Lett. **103**, 092407 (2013).
[10] J. Shi, S. S. P. Parkin, L. Xing, and M. B. Salamon, J. Magn. Magn. Mater. **125**, L251 (1993).
[11] H. Sato, K. Honda, Y. Aoki, N. Kataoka, I. J. Kim, and K. Fukamichi, J. Magn. Magn. Mater. **152**, 109 (1996).
[12] J. Shi, E. Kita, L. Xing, and M. B. Salamon, Phys. Rev. B **48**, 16119 (1993).
[13] H. Sato, Mater. Sci. Eng. B **31**, 101 (1995).
[14] A. D. Avery, R. Sultan, D. Bassett, D. Wei, and B. L. Zink, Phys. Rev. B **83**, 100401 (2011).
[15] L. Berger, Physica **30**, 1141 (1964).
[16] T. R. McGuire and R. I. Potter, IEEE Trans. Magn. **11**, 1018 (1975).
[17] H. C. Van Elst, Physica **25**, 708 (1959).

[18] M. N. Baibich, J. M. Broto, A. Fert, F. Nguyen Van Dau, F. Petroff, P. Etienne, G. Creuzet, A. Friederich, and J. Chazelas, Phys. Rev. Lett. **61**, 2472 (1988).

[19] G. Binasch, P. Grünberg, F. Saurenbach, and W. Zinn, Phys. Rev. B **39**, 4828(R) (1989).

[20] N. F. Mott and H. Jones, *The Theory of the Properties of Metals and Alloys* (Clarendon, Oxford, 1936), p. 309.

[21] R. B. Roberts, Philos. Mag. B **43**, 1125 (1981).

[22] N. Cusack and P. Kendall, Proc. Phys. Soc. **72**, 898 (1958).

[23] M. C. Cadeville and J. Roussel, J. Phys. F **1**, 686 (1971).

[24] R. P. Huebener, Phys. Rev. **140**, A1834 (1965).

[25] A. Soni and G. S. Okram, Appl. Phys. Lett. **95**, 013101 (2009).

[26] E. Shapira, A. Holtzman, D. Marchak, and Y. Selzer, Nano Lett. **12**, 808 (2012).

[27] E. Shapira, A. Tsukernik, and Y. Selzer, Nanotechnology **18**, 485703 (2007).

[28] M. Walter, J. Walowski, V. Zbarsky, M. Muenzenberg, M. Schaefers, D. Ebke, G. Reiss, A. Thomas, P. Peretzki, M. Seibt, J. S. Moodera, M. Czerner, M. Bachmann, and C. Heiliger, Nat. Mater. **10**, 742 (2011).

[29] F. K. Dejene, J. Flipse, and B. J. van Wees, Phys. Rev. B **86**, 024436 (2012).

[30] H. Yu, S. Granville, D. P. Yu, and J.-P. Ansermet, Phys. Rev. Lett. **104**, 146601 (2010).

[31] T. T. Heikkilä, M. Hatami, and G. E. W. Bauer, Phys. Rev. B **81**, 100408 (2010).

[32] P. R. Evans, G. Yi, and W. Schwarzacher, Appl. Phys. Lett. **76**, 481 (2000).

[33] X.-T. Tang, G.-C. Wang, and M. Shima, Phys. Rev. B **75**, 134404 (2007).

[34] K. Attenborough, R. Hart, W. Schwarzacher, J.-P. Ansermet, A. Blondel, B. Doudin, and J. P. Meier, in *Magnetic Ultrathin Films, Multilayers and Surfaces*, edited by E. E. Marinero, B. Heinrich, W. F. Egelhoff, Jr., A. Fert, H. Fujimori, G. Guntherodt, and R. L. White, MRS Proceedings Vol. 384 (MRS, Pittsburgh, 1995), p. 3.

[35] W. Schwarzacher, K. Attenborough, A. Michel, G. Nabiyouni, and J. P. Meier, J. Magn. Magn. Mater. **165**, 23 (1997).

[36] F. Nasirpouri, P. Southern, M. Ghorbani, A. Irajizad, and W. Schwarzacher, J. Magn. Magn. Mater. **308**, 35 (2007).

[37] L. Gravier, S. Serrano-Guisan, F. Reuse, and J.-Ph. Ansermet, Phys. Rev. B **73**, 052410 (2006).

[38] S. Serrano-Guisan, L. Gravier, M. Abid, and J.-P. Ansermet, J. Appl. Phys. **99**, 08T108 (2006).

[39] X. Huang, L. Tan, H. Cho, and B. J. H. Stadler, J. Appl. Phys. **105**, 07D128 (2009).

[40] L. Piraux, J. M. George, J. F. Despres, C. Leroy, E. Ferain, R. Legras, K. Ounadjela, and A. Fert, Appl. Phys. Lett. **65**, 2484 (1994).

[41] A. Blondel, J. P. Meier, B. Doudin, and J.-P. Ansermet, Appl. Phys. Lett. **65**, 3019 (1994).

[42] K. Liu, K. Nagodawithana, P. C. Searson, and C. L. Chien, Phys. Rev. B **51**, 7381 (1995).

[43] A. Fert and L. Piraux, J. Magn. Magn. Mater. **200**, 338 (1999).

[44] L. Gravier, J.-E. Wegrowe, T. Wade, A. Fabian, and J.-P. Ansermet, IEEE Trans. Magn. **38**, 2700 (2002).

[45] A. D. Avery, M. R. Pufall, and B. L. Zink, Phys. Rev. Lett. **109**, 196602 (2012).

[46] M. V. Costache, G. Bridoux, I. Neumann, and S. O. Valenzuela, Nat. Mater. **11**, 199 (2012).

[47] F. Völklein, H. Reith, M. Schmitt, M. Huth, M. Rauber, and R. Neumann, J. Electron. Mater. **39**, 1950 (2010).

[48] A. I. Boukai, Y. Bunimovich, J. Tahir-Kheli, J.-K. Yu, W. A. Goddard, III, and J. R. Heath, Nature (London) **451**, 168 (2008).

[49] P. Kim, L. Shi, A. Majumdar, and P. L. McEuen, Phys. Rev. Lett. **87**, 215502 (2001).

[50] A. Mavrokefalos, A. L. Moore, M. T. Pettes, L. Shi, W. Wang, and X. Li, J. Appl. Phys. **105**, 104318 (2009).

[51] L. Piraux, A. Fert, P. Schroeder, R. Loloee, and P. Etienne, J. Magn. Magn. Mater. **110**, L247 (1992).

[52] D. MacDonald, *Thermoelectricity: An Introduction to the Principles* (Wiley, New York, 1962).

[53] C. Herring, T. H. Geballe, and J. E. Kunzler, Phys. Rev. **111**, 36 (1958).

[54] L. Gurevich, Acad. Sci. USSR J. Phys. **9**, 477 (1945).

[55] C. L. Foiles, in *Metals: Electronic Transport Phenomena. Electrical Resistivity, Thermoelectrical Power and Optical Properties*, edited by K.-H. Hellwege and J. L. Olsen, Landolt-Börnstein, New Series, Group III, Vol. 15, Pt. B (Springer, Berlin, 1985).

[56] A. V. Gold, D. K. C. MacDonald, W. B. Pearson, and I. M. Templeton, Philos. Mag. **5**, 765 (1960).

[57] L. Nordheim and C. J. Gorter, Physica **2**, 383 (1935).

[58] K. Nielsch, F. Müller, A.-P. Li, and U. Gösele, Adv. Mater. **12**, 582 (2000).

[59] J. Bachmann, R. Zierold, Y. T. Chong, R. Hauert, C. Sturm, R. Schmidt-Grund, B. Rheinländer, M. Grundmann, U. Gösele, and K. Nielsch, Angew. Chem. Int. Ed. Engl. **47**, 6177 (2008).

[60] J. Lee, S. Farhangfar, R. Yang, R. Scholz, M. Alexe, U. Gösele, J. Lee, and K. Nielsch, J. Mater. Chem. **19**, 7050 (2009).

[61] G. Nabiyouni, W. Schwarzacher, Z. Rolik, and I. Bakonyi, J. Magn. Magn. Mater **253**, 77 (2002).

[62] B. G. Tóth, L. Péter, J. Dégi, L. Á. Révész, D. Oszetzky, G. Molnár, and I. Bakonyi, Electrochim. Acta **91**, 122 (2013).

[63] D. Pullini and D. Busquets-Mataix, ACS Appl. Mater. Interfaces **3**, 759 (2011).

[64] B. G. Tóth, L. Péter, J. Dégi, and I. Bakonyi, J. Electrochem. Soc. **160**, D307 (2013).

[65] B. Raquet, M. Viret, E. Sondergard, O. Cespedes, and R. Mamy, Phys. Rev. B **66**, 024433 (2002).

[66] S. K. J. Lenczowski, C. Schönenberger, M. A. M. Gijs, and W. J. M. de Jonge, J. Magn. Magn. Mater. **148**, 455 (1995).

[67] I. Bakonyi, E. Simon, B. G. Tóth, L. Péter, and L. F. Kiss, Phys. Rev. B **79**, 174421 (2009).

[68] B. G. Tóth, L. Péter, Á. Révész, J. Pádár, and I. Bakonyi, Eur. Phys. J. B **75**, 167 (2010).

[69] B. Voegeli, A. Blondel, B. Doudin, and J.-P. Ansermet, J. Magn. Magn. Mater. **151**, 388 (1995).

[70] B. Doudin, A. Blondel, and J.-P. Ansermet, J. Appl. Phys. **79**, 6090 (1996).

[71] I. Bakonyi and L. Peter, Prog. Mater. Sci. **55**, 107 (2010).

[72] Q. X. Liu, L. Péter, J. Tóth, L. F. Kiss, Á. Cziráki, and I. Bakonyi, J. Magn. Magn. Mater. **280**, 60 (2004).

[73] K. Nishimura, J. Sakurai, K. Hasegawa, Y. Saito, K. Inomata, and T. Shinjo, J. Phys. Soc. Jpn. **63**, 2685 (1994).

[74] L. Gravier, S. Serrano-Guisan, and J.-P. Ansermet, J. Appl. Phys. **97**, 10C501 (2005).

[75] M. J. Laubitz, Can. J. Phys. **45**, 3677 (1967).

[76] M. J. Laubitz and T. Matsumura, Can. J. Phys. **51**, 1247 (1973).

[77] J. P. Moore and R. S. Graves, J. Appl. Phys. **44**, 1174 (1973).
[78] T. Maeda and T. Somura, J. Phys. Soc. Jpn. **44**, 148 (1978).
[79] L. Gravier, S. Serrano-Guisan, F. Reuse, and J.-P. Ansermet, Phys. Rev. B **73**, 024419 (2006).
[80] S. A. Baily, M. B. Salamon, and W. Oepts, J. Appl. Phys. **87**, 4855 (2000).
[81] Y. Kobayashi, Y. Aoki, H. Sato, T. Ono, and T. Shinjo, J. Phys. Soc. Jpn. **65**, 1910 (1996).
[82] L. Gravier, A. Fábián, A. Rudolf, A. Cachin, K. Hjort, and J.-P. Ansermet, Meas. Sci. Technol. **15**, 420 (2004).
[83] D. K. C. MacDonald, W. B. Pearson, and I. M. Templeton, Proc. R. Soc. London Ser. A **266**, 161 (1962).
[84] H. J. Goldsmid, *Introduction to Thermoelectricity*, Springer Series in Materials Science Vol. 121 (Springer, Berlin, 2009).
[85] H. W. Worner, Au. S. R. A **4**, 62 (1951).
[86] W. Haynes and D. Lide, *CRC Handbook of Chemistry and Physics: A Ready-Reference Book of Chemical and Physical Data* (CRC, Boca Raton, 2011).
[87] G. W. Scovil, J. Appl. Phys. **27**, 1196 (1956).
[88] T. Farrell and D. Greig, J. Phys. C **3**, 138 (1970).
[89] F. J. Blatt, D. J. Flood, V. Rowe, P. A. Schroeder, and J. E. Cox, Phys. Rev. Lett. **18**, 395 (1967).
[90] B. L. Zink, A. D. Avery, R. Sultan, D. Bassett, and M. R. Pufall, Solid State Commun. **150**, 514 (2010).
[91] K. Pekala and M. Pekala, Nanostruct. Mater. **6**, 819 (1995).
[92] F. J. Blatt, Can. J. Phys. **50**, 2836 (1972).
[93] E. Y. Tsymbal, D. G. Pettifor, J. Shi, and M. B. Salamon, Phys. Rev. B **59**, 8371 (1999).

III

Temperature gradient-induced magnetization reversal of single ferromagnetic nanowires
Ann-Kathrin Michel, Anna Corinna Niemann, Tim Boehnert, Stephan Martens, Josep M Montero Moreno, Detlef Goerlitz, Robert Zierold, Heiko Reith, Victor Vega, Victor M Prida, Andy Thomas, Johannes Gooth & Kornelius Nielsch

Reprinted from *Journal of Physics D: Applied Physics* **50**, 494007 (2017)
Copyright 2017 IOP Publishing Ltd.
License: Creative Commons Attribution 3.0 Unported (CC BY 3.0)

Author Contributions: A.-K.M., T.B., J.M.M.M., and V.V. fabricated the samples. A.-K.M., T.B., S.M., J.M.M.M., R.Z. V.V., and J.G. conducted the measurements. A.-K.M., A.C.N., T.B., S.M., R.Z., V.V., and J.G. analyzed the data. A.C.N. wrote the manuscript. All authors significantly contributed to the scientific discussion during the data evaluation and manuscript preparation. D.G. and K.N. supervised the project.

OPEN ACCESS
IOP Publishing
Journal of Physics D: Applied Physics
J. Phys. D: Appl. Phys. **50** (2017) 494007 (6pp)
https://doi.org/10.1088/1361-6463/aa9444

Temperature gradient-induced magnetization reversal of single ferromagnetic nanowires

Ann-Kathrin Michel[1], Anna Corinna Niemann[1,2], Tim Boehnert[1,3], Stephan Martens[1], Josep M Montero Moreno[1], Detlef Goerlitz[1], Robert Zierold[1], Heiko Reith[2], Victor Vega[4], Victor M Prida[4], Andy Thomas[2], Johannes Gooth[1,5] and Kornelius Nielsch[1,2,6,7]

[1] Institute of Nanostructure and Solid State Physics, Universität Hamburg, Jungiusstrasse 11 B, 20355, Hamburg, Germany
[2] Leibniz Institute for Solid State and Material Research, Helmholtzstraße 20, D-01069, Dresden, Germany
[3] INL International Iberian Nanotechnology Laboratory, Av. Mestre José Veiga, 4715-330, Braga, Portugal
[4] Depto. Física, Fac. Ciencias, Universidad de Oviedo, C/Federico García Lorca 18, E-33007, Oviedo, Spain
[5] IBM Research-Zurich, Säumerstrasse 4, 8803 Rüschlikon, Switzerland
[6] Technische Universität Dresden, Institute of Materials Science, 01062 Dresden, Germany
[7] Technische Universität Dresden, Institute of Applied Physics, 01062 Dresden, Germany

E-mail: a.niemann@ifw-dresden.de and k.nielsch@ifw-dresden.de

Received 8 September 2017, revised 13 October 2017
Accepted for publication 18 October 2017
Published 17 November 2017

Abstract

In this study, we investigate the temperature- and temperature gradient-dependent magnetization reversal process of individual, single-domain $Co_{39}Ni_{61}$ and $Fe_{15}Ni_{85}$ ferromagnetic nanowires via the magneto-optical Kerr effect and magnetoresistance measurements. While the coercive fields (H_C) and therefore the magnetic switching fields (H_{SW}) generally decrease under isothermal conditions at elevated base temperatures (T_{base}), temperature gradients (ΔT) along the nanowires lead to an increased switching field of up to 15% for $\Delta T = 300\,K$ in $Co_{39}Ni_{61}$ nanowires. This enhancement is attributed to a stress-induced, magneto-elastic anisotropy term due to an applied temperature gradient along the nanowire that counteracts the thermally assisted magnetization reversal process. Our results demonstrate that a careful distinction between locally elevated temperatures and temperature gradients has to be made in future heat-assisted magnetic recording devices.

Keywords: magnetic nanowires, nanoelectronics, magneto-optical Kerr effect

(Some figures may appear in colour only in the online journal)

Magnetic memory devices are the workhorses of modern digital data storage [1]. The first commercial magnetic hard disk drives were introduced in 1957 by IBM [2] and held a storage capacity of 2 kb in^{-2}. Since then, tremendous progress in the optimization of magnetic memory devices has been made to the extent that in 2014, Seagate [3] announced a device with a memory capacity of 826 Gb in^{-2}. However, the main reason for this track record is the continuous down-scaling of the geometrical single magnetic bit unit sizes, which is restricted by the superparamagnetic limit. Accordingly, reliable data storage is inhibited below a certain particle size because the thermal activation energy induces random bit flipping. Driven by the

Original content from this work may be used under the terms of the Creative Commons Attribution 3.0 licence. Any further distribution of this work must maintain attribution to the author(s) and the title of the work, journal citation and DOI.

© 2017 IOP Publishing Ltd Printed in the UK

need to overcome this limit, alternative concepts for future magnetic data storage have emerged. One of the most distinct approaches is heat-assisted magnetic recording (HAMR) [4, 5], where the shape or crystal anisotropy enhances the magnetic switching fields, H_{SW}, (and therefore the coercivity, H_C) and suppresses the superparamagnetic limit, while a heating laser pulse that decreases H_C for a short period of time is used to allow for a magnetic bit writing process. In fact, for highly anisotropic FePt HAMR devices, a data storage areal density of 1.4 Tb in^{-2} has recently been demonstrated in a laboratory environment [6].

Parallel to the efforts to incorporate heat pulses into magnetic memory devices, the research field of spin-caloritronics [7] evolved, seeking a fundamental understanding of the interplay between charge, spin and heat. While the HAMR technique basically relies on induced magnetic switching at elevated temperature pulses, temperature gradients were also found to generate numerous spin-caloritronic effects. Currently, classical thermoelectric effects in ferromagnetic materials systems are quite well-established. The so-called spin-dependent Seebeck effect has been observed in anisotropic magnetoresistance (MR) [8, 9], giant MR [10, 11] and tunnel MR [12, 13] regimes. The spin-Seebeck effect (SSE) [14, 15], which describes the generation of a pure spin current due to a temperature gradient in a ferromagnetic material, is currently under intense investigation. Furthermore, the thermal spin transfer torque (TSTT) has attracted much attention because the effect on the magnetic switching behavior of magnetic tunnel junctions is three orders of magnitude larger than its spintronic equivalent effect (the spin transfer torque) can account for, due to charge currents generated by the spin-dependent Seebeck effect [16].

In this study, we directly compare the influence of the base temperature, T_{base}, and temperature gradients, ΔT, on the magnetization reversal of ferromagnetic nanostructures. Therefore, magneto-optical Kerr (MOKE) measurements and MR measurements were performed on individual $Co_{39}Ni_{61}$ and $Fe_{15}Ni_{85}$ nanowires under an externally applied magnetic field, $\mu_0 H$, at different ΔT and T_{base} values. We show that H_{SW} generally decreases with increasing T_{base}, while the magnetic switching field of $Co_{39}Ni_{61}$ nanowires increases for increasing ΔT. We attribute this increase in H_{SW} for increasing ΔT to a stress-induced enhancement of the magneto-elastic anisotropy and develop a simple approach to estimate the H_C values as a function of the applied ΔT.

Cylindrical ferromagnetic nanowires with an average diameter of 150 nm and lengths of up to 30 μm were grown by template-assisted electrodeposition into self-ordered, nanoporous alumina (AAO) membranes [17]. Two types of soft magnetic alloy nanowires—$Fe_{15}Ni_{85}$ and $Co_{39}Ni_{61}$—were synthesized according to previously followed procedures from Salem *et al* [18] and Vega *et al* [19], respectively. Prior to electrodeposition, the internal walls of the alumina membranes had been coated with an approx. 10 nm thick layer of SiO_2 by atomic layer deposition [20, 21]. The SiO_2 cover layer protects the nanowires from oxidation and additionally supplies mechanical stability when the nanowires are suspended in ethanol after being released from the AAO template by selective chemical etching.

Two types of micro-devices (A and B) were designed to measure the optical and electrical properties of the individual nanowires (figures 1(a) and 2(a), respectively). Therefore, the suspended nanowire/ethanol solution was applied dropwise to a 150 μm thick quartz substrate, and the micro-devices were defined by laser beam lithography followed by a metallization process [9].

Micro-device A consists of two Ti/Pt lines—one at each end of the nanowire—which are not in electrical contact with the nanowire (figure 1(a)) and which have been simultaneously used as heater lines and as resistive thermometers. DC currents up to 10 mA generated temperature gradients via Joule heating in the heater line, which led to temperatures up to 680 K at the hot thermometer and 380 K at the cold thermometer. Hence, temperature gradients, ΔT, up to 300 K were generated along the nanowire (figure 1(b)). We note that the actual temperature difference along the nanowire is slightly below the measured temperature difference, because the nanowire is about 1 μm shorter than the distance between the thermometers.

Micro-device A was used to measure the coercive fields of $Co_{39}Ni_{61}$ and $Fe_{15}Ni_{85}$ nanowires as a function of the applied temperature gradients via the longitudinal MOKE [22]. A NanoMOKE™2 from *Durham Magneto Optics* equipped with an (45°) incidence continuous wave-laser light with a power output of 1.9 mW and with an in-plane focused spot size of approximately 3 μm was used. Alternating magnetic fields up to ± 0.08 T could be applied with a quadrupole magnet in the plane of incidental beam of light and thus parallel to the nanowire axis, as described in detail by Vega *et al* [19]. With a distance of approx. 500 nm between the nanowire and the heater line, the estimated maximum Oersted fields induced by the heater lines to the nanowire were in the order of 10^{-4} T and could be excluded from having an impact on the magnetization reversal of the nanowire. Furthermore, the temperature rise due to the incidental laser beam could be neglected in this study due to an estimated heating of less than 1 K. The recorded hysteresis loops show no deviation whether the laser spot was focused on the wire's edges or on its center, and the square-like MOKE hysteresis curves exhibited symmetric Barkhausen jumps for $Fe_{15}Ni_{85}$ and the $Co_{39}Ni_{61}$ nanowires. In figure 1(c), the hysteresis loop of the $Co_{39}Ni_{61}$ nanowire measured at $T_{\mathrm{base}} = 300$ K and for $\Delta T = 0$ K was exemplarily given with a coercive field of 424 G. Due to the low signal-to-noise ratio, it became necessary to successively average data over several hundred single shot hysteresis loops.

Micro-device B (figure 2(a)) corresponded with the typical experimental setup [9, 23] for measuring the thermopower, S ($S = U_{\mathrm{th}}/\Delta T$, with U_{th} being the thermo-voltage induced by the temperature gradient ΔT), of nanowires. The micro-device consisted of one resistive heater line (yellow) and two resistive thermometers (red and blue for the hot and cold thermometer, respectively). For the thermoelectric characterization, applied DC currents flowing through the resistive heater line generated a temperature gradient along the nanowire. Employing both resistive thermometers, ΔT was determined, and U_{th} was measured along the nanowire. For a general characterization of our sample we determined the resistivity, ρ, and S of the nanowires. Resistance measurements were conducted

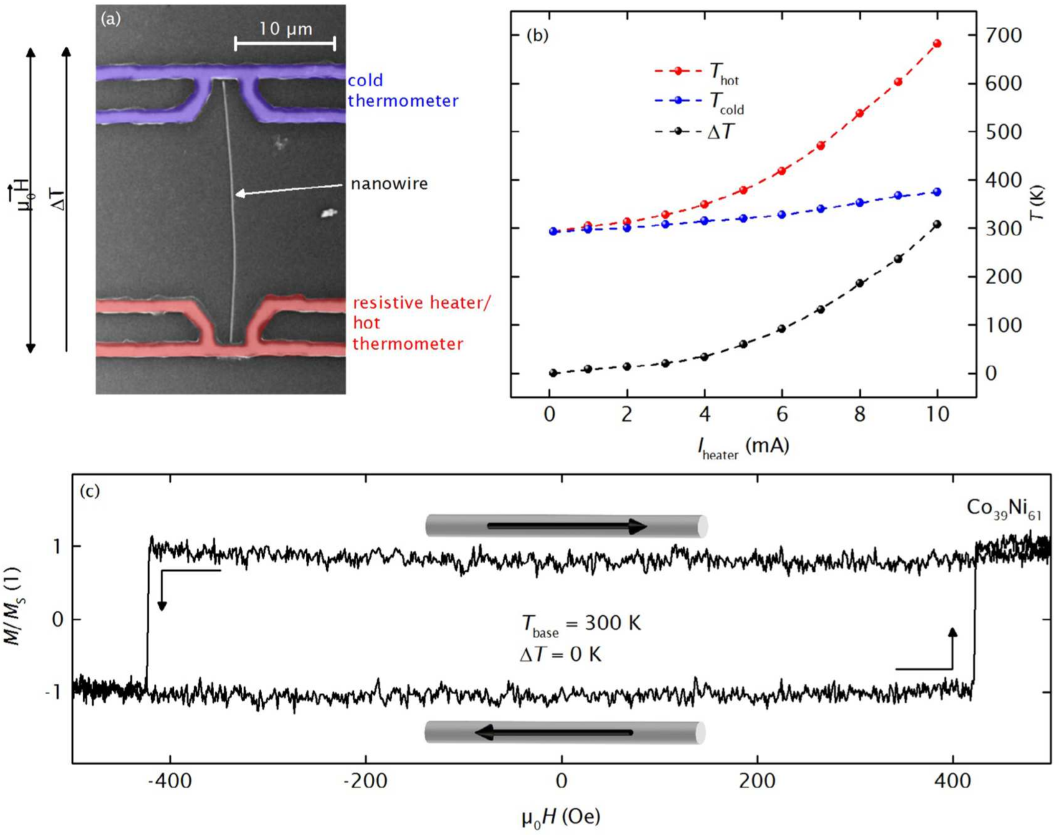

Figure 1. MOKE measurements: (a) the experimental setup for the MOKE measurements is sketched on a scanning electron microscopy image of the utilized micro-device A. The nanowire is surrounded by two Ti/Pt lines, which are not in electrical contact with the nanowire and serve as both Joule heaters and resistive thermometers, simultaneously. An external magnetic field was applied parallel to the nanowire axis, and a linear polarized laser beam was focused on the nanowire for longitudinal MOKE measurements as a function of the applied temperature gradient. (b) The temperatures at both resistive thermometers $T_{\rm hot}$ and $T_{\rm cold}$ and the resulting temperature difference ΔT are shown as a function of the DC heating current $I_{\rm heater}$, which is supplied to the Joule heater. (c) Hysteresis loop of a $Co_{39}Ni_{61}$ nanowire measured at room temperature and without an applied temperature gradient. The nanowire (gray rod) and its magnetization (black arrow) are sketched for the upper and lower branch of the hysteresis curve.

in a four-point measurement geometry, for which we used the hot and cold thermometers (figure 2(a)) as the electrodes. We observed metallic $\rho(T)$-curves for both material systems with room temperature values of $\rho(Fe_{15}Ni_{85}) = 34.5\ \mu\Omega$ cm and $\rho(Co_{39}Ni_{61}) = 19.7\ \mu\Omega$ cm, which are higher than the corresponding bulk literature values of $\rho(Fe_{15}Ni_{85}, \text{bulk}) = 14\ \mu\Omega$ cm and $\rho(Co_{39}Ni_{61}, \text{bulk}) = 11\ \mu\Omega$ cm [24]. These enhanced resistivity values of the nanostructures compared to bulk materials are commonly observed and attributed to the nanocrystalline nature of the electrodeposited nanowires [25]. The thermopower of $Fe_{15}Ni_{85}$ and $Co_{39}Ni_{61}$ nanowires is displayed as a function of $T_{\rm base}$ in figure 2(b). At 300 K, we measured $S(Fe_{15}Ni_{85}) = -32\ \mu V\ K^{-1}$ and $S(Co_{39}Ni_{61}) = -26\ \mu V\ K^{-1}$. For comparison, Co and Ni bulk samples have a thermopower [26, 27] of $S(\text{Co}) = -30, 8\ \mu V\ K^{-1}$ and $S(\text{Ni}) = -18, 4\ \mu V\ K^{-1}$, respectively while the Fe–Ni bulk samples [28] showed a room temperature thermopower of $S(\text{Fe–Ni}) = -35\ \mu V\ K^{-1}$.

Additionally, micro-device B was also used to determine the temperature-dependent coercive fields of $Co_{39}Ni_{61}$ and $Fe_{15}Ni_{85}$ nanowires. In a probe station setup, we therefore performed MR measurements with the externally applied magnetic field up to 0.5 T parallel to the nanowire axis and in the temperature range from 290 K to 350 K. Distinct resistance jumps on the order of 50 mΩ can be observed at the switching field values as exemplarily shown for a $Fe_{15}Ni_{85}$ nanowire with a coercive field of 178 G (figure 2(c)).

For $\Delta T = 0$ K, H_C for $Fe_{15}Ni_{85}$ as well as $Co_{39}Ni_{61}$ nanowires decreased in the MR measurements with increasing $T_{\rm base}$ (figure 3(a)). The reduction of the temperature normalized coercive field, taken as the coercivity measured at any temperature referred to the value at T = 300 K, ($H_C(T)/H_C(300\,\text{K})$) for $Fe_{15}Ni_{85}$ nanowires (4% from 300 K to 350 K) is slightly steeper than for the one of $Co_{39}Ni_{61}$ nanowires (1% from 300 K to 350 K). Such decrease in H_C value with increasing T was a consequence of the thermally assisted switching process—the basic concept of HAMR devices.

In a next step, H_C of the $Co_{39}Ni_{61}$ and $Fe_{15}Ni_{85}$ nanowires as a function of ΔT was investigated in the NanoMOKE setup. Longitudinal MOKE hysteresis loops for $Co_{39}Ni_{61}$ and $Fe_{15}Ni_{85}$ nanowires were measured with applied ΔT between 0 K and 300 K along the nanowire axis, and the applied magnetic field $\mu_0 H$ parallel to the nanowire axis as shown in figure 3(b). For $Fe_{15}Ni_{85}$ nanowires, we observed a decrease

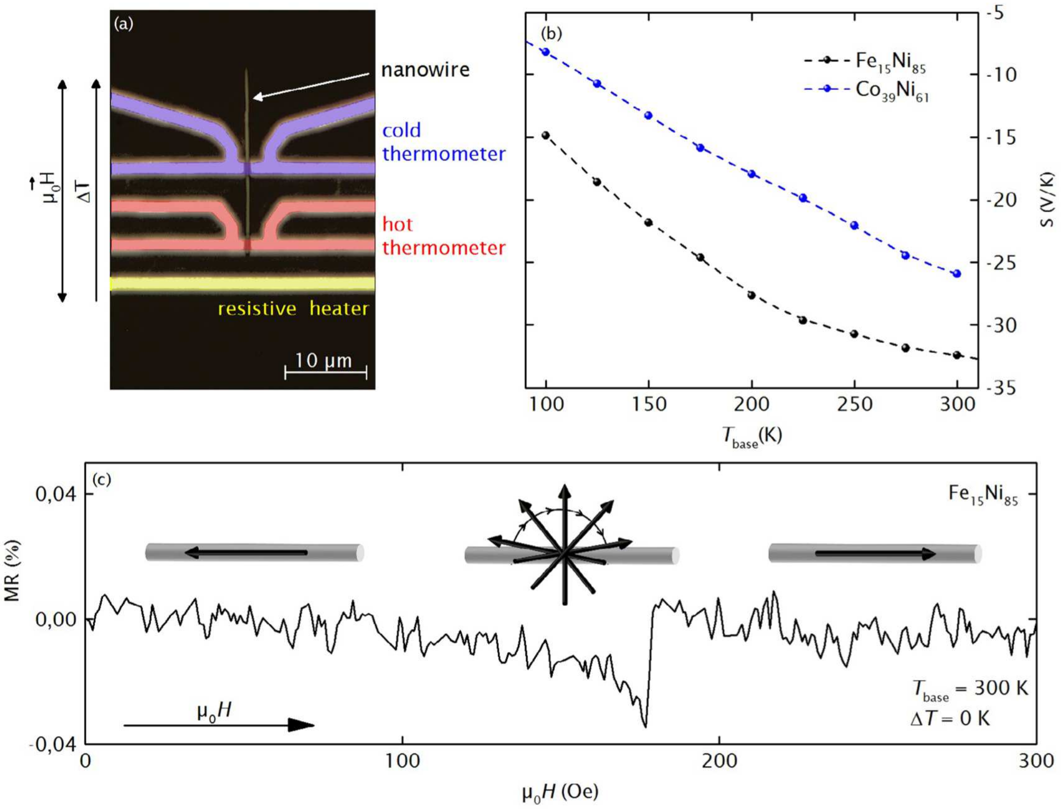

Figure 2. MR and thermopower measurements: (a) micro-device B for measuring the thermopower, S, consists of one heater line (yellow) and two resistive thermometers (red and blue) that are in electrical contact with the nanowire. Additionally, MR measurements were performed on this device with an external magnetic field, $\mu_0 H$, parallel to the nanowire axis. (b) S, as a function of the temperature, T, for $\mathrm{Co_{39}Ni_{61}}$ and $\mathrm{Fe_{15}Ni_{85}}$ nanowires. (c) MR (MR = $(R_\mathrm{H} - R_0)/R_0$) as a function of $\mu_0 H$ for $\mathrm{Fe_{15}Ni_{85}}$ nanowires, measured at room temperature and without applied temperature gradients. At the coercive field, H_C, a jump in the MR signal can be observed. The nanowire (gray rod) and its magnetization (black arrow) are sketched before, during and after the magnetization reversal process at the corresponding field values $\mu_0 H$.

of H_C with increasing ΔT of 4% for $\Delta T = 100\,\mathrm{K}$. In contrast, we surprisingly found an increasing H_C for increasing ΔT for the $\mathrm{Co_{39}Ni_{61}}$ nanowires. This observation remained valid even when we changed the material of the micro-device from Pt to Au to exclude any influence by the electrical contact material (figure 3(b)). Therefore, we conclude that the increase in H_C with increasing ΔT has an intrinsic origin that counteracts the average temperature-assisted switching mechanism.

To explain the unexpected $H_\mathrm{C}(\Delta T)$ dependence of the $\mathrm{Co_{39}Ni_{61}}$ nanowires, we will discuss possible origins in the following, whereas we start with considering stress-induced changes on the magnetic switching mechanism.

Our first hypothesis is an axial stress-induced enhancement of H_C due to an increasing ΔT along the nanowire axis. To establish an easy, quantitative model for $H_\mathrm{C}(\Delta T)$, we start with [29]

$$H_\mathrm{C} = \frac{2K_\mathrm{eff}}{\mu_0 M_\mathrm{s}} |\cos(\theta)| \qquad (1)$$

with the vacuum permeability μ_0, the saturation magnetization M_S, the angle θ between external magnetic field $\mu_0 H$ and the magnetization vector, and the effective anisotropy constant K_eff of the nanowires, which is given by $K_\mathrm{eff} \approx$. $K_\mathrm{shape} + K_\mathrm{me}$, with the shape anisotropy constant K_shape and the magneto-elastic anisotropy constant K_me. Note that we neglect the magneto-crystalline anisotropy in our nanowire because it is rather small regarding the magneto-crystalline anisotropy constants [30, 31] of 5 kJ $\mathrm{m^{-3}}$ and 7.5 kJ $\mathrm{m^{-3}}$ for $\mathrm{Co_{39}Ni_{61}}$ and $\mathrm{Fe_{15}Ni_{85}}$, respectively. Due to their high aspect ratio, the magnetization of the nanowires and therefore their magnetization reversal in the relaxed state without induced stress are dominated by shape anisotropy. The shape anisotropy constant of an infinitely long wire is given by [32]

$$K_\mathrm{shape} = \frac{1}{4}\mu_0 M_\mathrm{s}^2. \qquad (2)$$

Using the literature values [32, 33] of the saturation magnetization $M_\mathrm{s}(\mathrm{Co_{50}Ni_{50}}) = 1060$ kA $\mathrm{m^{-1}}$ and $M_\mathrm{s}(\mathrm{Fe_{20}Ni_{80}}) = 795$ kA $\mathrm{m^{-1}}$ a shape anisotropy constant of $K_\mathrm{shape}(\mathrm{Co_{39}Ni_{61}}) \approx 350$ kJ $\mathrm{m^{-3}}$ and of $K_\mathrm{shape}(\mathrm{Fe_{15}Ni_{85}}) \approx 200$ kJ $\mathrm{m^{-3}}$ is obtained. The magneto-elastic anisotropy constant is given by [34]

$$K_\mathrm{me} = \frac{3}{2}\lambda_\mathrm{me}\sigma. \qquad (3)$$

λ_me is the magnetostriction coefficient, and σ is the axial stress given by $\sigma = \alpha_\mathrm{Co/Ni/Fe} Y \Delta T$. Here, Y is the Young's modulus ($Y_\mathrm{Ni,Co,Fe} \approx 209$ GJ $\mathrm{m^{-3}}$), and $\alpha_\mathrm{Co/Ni/Fe}$ reflects the thermal expansion coefficients [35] $\alpha_\mathrm{Co} = 13.0 \cdot 10^{-6}\ \mathrm{K^{-1}}$,

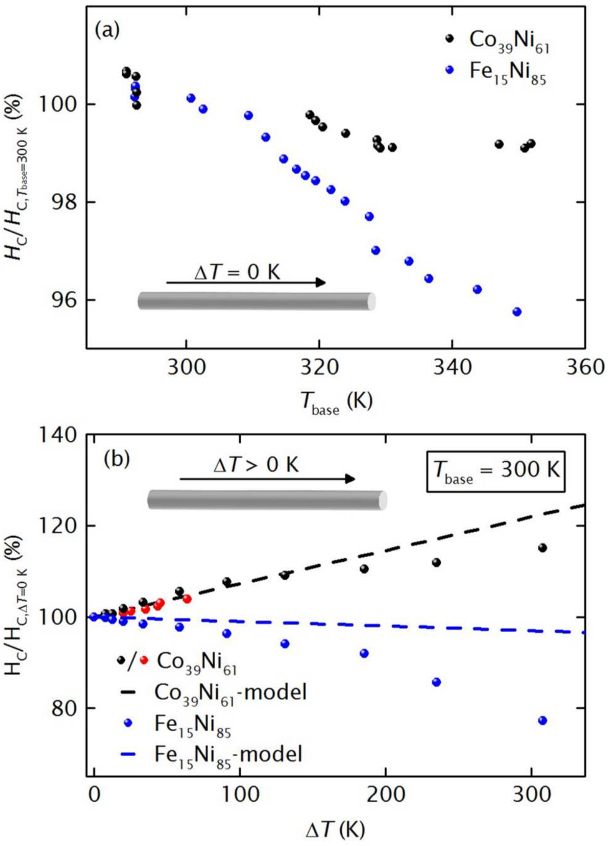

Figure 3. Temperature- and temperature gradient-dependent coercive fields of $Co_{39}Ni_{61}$ and $Fe_{15}Ni_{85}$ nanowires: (a) temperature normalized coercive fields $H_C/H_C(T_{base} = 300\,K)$ for $Co_{39}Ni_{61}$ and $Fe_{15}Ni_{85}$ nanowires as a function of T_{base} and with $\Delta T = 0\,K$. (b) $H_C/H_C(\Delta T = 0\,K)$ for $Co_{39}Ni_{61}$ and $Fe_{15}Ni_{85}$ nanowires as a function of the applied ΔT at $T_{base} = 300\,K$. Black dots correspond to a $Co_{39}Ni_{61}$ nanowire contacted with platinum leads, blue dots correspond to a Fe15Ni85 nanowire contacted with platinum leads, and the red dots correspond to a $Co_{39}Ni_{61}$ nanowire contacted with gold leads.

$\alpha_{Ni} = 13.4 \cdot 10^{-6}\ K^{-1}$, and $\alpha_{Fe} = 11.8 \cdot 10^{-6}\ K^{-1}$ of Co, Ni and Fe at 300 K, respectively. Thus, a temperature gradient of 300 K along the nanowire leads to a stress of about $\sigma(\Delta T = 300\,K) \approx 800\,MJ\ m^{-3}$ along the nanowire axis in all investigated material systems. Now, for $\Delta T = 300\,K$ the relatively low magnetostriction coefficient [36] of the $Fe_{15}Ni_{85}$ ($\lambda_{me} = -5 \times 10^{-6}$) leads to a minor contribution of $K_{me} = -6\,kJ\ m^{-3}$ even for the highest thermal stress, such that $K_{eff} \approx K_{shape}$. For the $Co_{39}Ni_{61}$ system with the ten-times higher magnetostriction coefficient [37] $\lambda_{me} = 65 \times 10^{-6}$, however, we obtain $K_{me} = 78\ kJ\ m^{-3}$ for $\Delta T = 300\,K$, which is one order of magnitude higher than $K_{me}(Fe_{15}Ni_{85})$ and provides a significant contribution to the magnetic configuration in the nanowire. In fact, for $\Delta T = 300\,K$ and using equation (1), we obtain a relative change in the coercive field of $\frac{H_C(\Delta T=300\,K)}{H_C(\Delta T=0\,K)} = 1.22$ for the $Co_{39}Ni_{61}$ nanowires as indicated by the dashed line in figure 3(b). We find a very good agreement between our estimation and the experimental data for $\Delta T < 200\,K$. At higher ΔT, the measured $H_C(\Delta T)$ deviates to a less steep increase than that predicted by our model, which we attribute to the heat-assisted magnetization reversal process due to the elevated average temperature of the nanowire caused by the high applied ΔT. For the $Co_{39}Ni_{61}$, the deviation between the measured $H_C(\Delta T)$ and the calculated $H_C(\Delta T)$ is 7% at $\Delta T = 300\,K$. Performing the same estimation of $H_C(\Delta T)$ for the $Fe_{15}Ni_{85}$ nanowire only yields a stress-induced decrease of the normalized H_C to 0.97 at $\Delta T = 300\,K$, as shown by the blue dotted line in figure 3(b). As a result, the heat-assisted switching process determines $H_C(\Delta T)$ for the $Fe_{15}Ni_{85}$ nanowires, and the measured $H_C(\Delta T)$ is significantly smaller than the estimated values regarding the stress-induced magneto-elastic anisotropy component, which leads to a difference of 20% between the measured $H_C(\Delta T)$ and the normalized $H_C(\Delta T)$ estimated with our model at $\Delta T = 300\,K$. Extrapolating the $H_C(T_{base})$ (see figure 3(a)) of the nanowires to $T_{base} = 600\,K$ ($\Delta T = 300\,K$) gives a decrease of $H_C(T_{base})$ of 5% for the $Co_{39}Ni_{61}$ nanowire and 20% for the $Fe_{15}Ni_{85}$ nanowire, which is for both material systems in good agreement with the difference between measured and calculated values of $H_C(\Delta T)$ at $\Delta T = 300\,K$.

Increasing H_C with increasing ΔT for the $Co_{39}Ni_{61}$ nanowires due to increasing radial stress-induced by the nanowire-core/SiO_2-shell is unlikely because radial stress is also present for the measurements with increasing base temperature, where we observed a decreasing H_C for increasing T_{base}.

To our knowledge, saturation magnetostriction $\lambda_S(\sigma, T)$, affecting the hysteretic behavior of ferromagnetic nanowires has so far only been reported for nanowire arrays within the template, which are exposed to uniform temperature enhancements. Kumar *et al* [34] observed increasing H_C with increasing T for Ni nanowires in an AAO template with a thick Al backside. Due to the different thermal expansion coefficients of Ni, AAO and Al, they calculated magneto-elastic anisotropy constants between $-42\ kJ\ m^{-3}$ and $-96\ kJ\ m^{-3}$. Silva *et al* [38] investigated Co nanowires in AAO templates and found that longer nanowire segments experience a stronger thermal expansion and therefore more stress in the AAO templates for decreasing T than shorter nanowires, which leads to change in the easy magnetization axis from parallel to perpendicular direction to the nanowire axis that occurs nearer to the electrodeposition temperature of 300 K for longer Co nanowire than for shorter Co segments. Pirota *et al* [39] intensified this study on Ni nanowires in AAO templates and calculated (thermal) induced stresses between $-170\ kJ\ m^{-3}$ for short ($l = 0.5\ \mu m$) nanowires and $-780\ kJ\ m^{-3}$ for longer ($l = 2.2\ \mu m$) segments.

Another effect that might have a noticeable influence on the switching mechanism of magnetic nanowires under a temperature gradient is the TSTT. It has been recently demonstrated that the TSTT has a much higher effect on the magnetization reversal characteristics of tunnel MR structures than the STT due to a spin-dependent Seebeck effect accounting for [16]. One underlying mechanism for this observation in our samples geometry could be a pure spin current due to the longitudinal SSE [15] that can have a stabilizing or destabilizing effect on the magnetization of the nanowire and therefore decreases or increases the coercivity H_C. Overall, we believe that the interplay of the stress-induced contributions of the magneto-elastic anisotropy and an intrinsic thermally assisted switching mechanism described in this work fits the data accurately. Thus, we conclude that no major influences of the TSTT and the longitudinal SSE are observed in these samples.

In summary, we synthesized $Co_{39}Ni_{61}$ and $Fe_{15}Ni_{85}$ nanowires to investigate temperature- and temperature-gradient dependent magnetization reversal process of ferromagnetic nanostructures. Performing MR measurements, we found that the magnetic switching fields (and therefore their coercivities) decreased with increasing the base temperature for both $Co_{39}Ni_{61}$ and $Fe_{15}Ni_{85}$ nanowires. MOKE measurements with applied temperature gradients at room temperature showed a decrease in the coercive field values for $Fe_{15}Ni_{85}$ nanowires while H_C increases up to 5% per 100 K for $Co_{39}Ni_{61}$ nanowires. We attribute this increase in H_C for $Co_{39}Ni_{61}$ nanowires to a stress-induced enhancement in the magneto-elastic anisotropy contribution to the effective anisotropy due to an applied temperature gradient, and we were able to fit the measured $H_C(\Delta T)$ increase with a simple model. Our results highlight the quite distinct effects of elevated temperatures and applied temperature gradients on the switching fields and therefore on the magnetization reversal mechanisms of ferromagnetic nanostructures and reveal the challenges of future heat-assisted, magnetic recording device design.

Acknowledgments

The authors thank R Meissner and L Akinsinde for technical support. This work was supported by the German research society via the excellence cluster 'The Hamburg Centre for Ultrafast Imaging-Structure, Dynamics and Control of Matter at the Atomic Scale, and the SPP 1538 'Spin Caloric Transport'. Spanish MINECO funds form research projects N° MAT2013-48054-C2-2-R and MAT2016-76824-C3-3-R are also gratefully recognized.

ORCID iDs

Anna Corinna Niemann https://orcid.org/0000-0003-2996-7808
Tim Boehnert https://orcid.org/0000-0002-2659-1481
Detlef Goerlitz https://orcid.org/0000-0002-3496-5519

References

[1] Tehrani S, Slaughter J M, Chen E, Durlam M and Shi J 1999 *IEEE Trans. Magn.* **35** 2814–9
[2] Harker J M, Brede D W, Pattison R E, Santana G R and Taft L G 1981 *IBM J. Res. Dev.* **25** 677–90
[3] *Seagate Product Manual* Dec 2013 publication no: 100743772, rev A
[4] Rausch T, Gage E and Dykes J 2015 *Springer Proc. Phys.* **159** 200–2
[5] Rottmayer R E *et al* 2006 Heat-assisted magnetic recording *IEEE Trans. Magn.* **42** 2417–21
[6] Ju G *et al* 2015 *IEEE Trans. Magn.* **51** 11
[7] Bauer G E W, Saitoh E and van Wees B J 2012 *Nat. Mater.* **11** 391–9
[8] Avery A D, Pufall M R and Zink B L 2012 *Phys. Rev.* B **86** 1–5
[9] Böhnert T, Vega V, Michel A-K, Prida V M and Nielsch K 2013 *Appl. Phys. Lett.* **103** 092407
[10] Shi J, Parkin S S P, Xing L and Salamon M B 1993 *J. Magn. Magn. Mater.* **125** 251–6
[11] Böhnert T *et al* 2014 *Phys. Rev.* B **90** 165416
[12] Yuasa S, Nagahama T, Fukushima A, Suzuki Y and Ando K 2004 *Nat. Mater.* **3** 868–71
[13] Böhnert T, Serrano-Guisan S, Paz E, Lacoste B and Ferreira R 2017 *J. Phys.: Condens. Matter.* **29** 185303
[14] Uchida K, Takahashi S, Harii K, Ieda J, Koshibae W, Ando K, Maekawa S and Saitoh E 2008 *Nature* **455** 778–81
[15] Meier D *et al* 2015 *Nat. Commun.* **6** 8211
[16] Pushp A, Phung T, Rettner C, Hughes B P, Yang S-H and Parkin S S P 2015 *Proc. Natl Acad. Sci. USA* **112** 6585–90
[17] Nielsch K, Choi J, Schwirn K, Wehrspohn R B and Gösele U 2002 *Nano Lett.* **2** 677–80
[18] Salem M S, Sergelius P, Zierold R, Montero Moreno J M, Görlitz D and Nielsch K 2012 *J. Mater. Chem.* **22** 8549
[19] Vega V, Böhnert T, Martens S, Waleczek M, Montero-Moreno J M, Görlitz D, Prida V M and Nilesch K 2012 *Nanotechnology* **23** 465709
[20] Bachmann J, Zierold R, Chong Y T, Hauert R, Sturm C, Schmidt-Grund R, Rheinländer B, Grundmann M, Gösele U and Nielsch K 2008 *Angew. Chem., Int. Ed. Engl.* **47** 6177–9
[21] Lee J, Farhangfar S, Yang R, Schulz R, Alexe M, Gösele U, Lee J and Nielsch K 2009 *J. Mater. Chem.* **19** 7050
[22] Allwood D A, Gang X, Cooke M D and Cowburn R P 2003 *J. Phys. D.: Appl. Phys.* **36** 2175–82
[23] Shapira E, Tsukernik A and Selzer Y 2007 *Nanotechnology* **18** 485703
[24] McGuire T R and Potter R I 1975 *IEEE Trans. Magn.* **11** 4
[25] Srivastav A K and Shekhar R 2014 *J. Magn. Magn. Mater.* **349** 21–6
[26] Laubitz M J and Matsumura T 1973 *Can. J. Phys.* **51** 12
[27] Laubitz M J and Matsumura T 1976 *Can. J. Phys.* **54** 1
[28] Ho C Y, Chi T C, Bogaard R H, Havill T N and James H M 1983 *Thermal Conductivity* vol 17 ed J G Hust (New York: Plenum Press)
[29] Sánchez-Barriga J, Lucas M, Radu F, Martin E, Multigner M, Marin P, Hernando A and Rivero G 2009 *Phys. Rev.* B **80** 1–8
[30] Vivas L G, Vazquez M, Escrig J, Allende S, Altbir D, Leitao D C and Araujo J P 2012 *Phys. Rev.* B **85** 1–8
[31] Yin L F *et al* 2006 *Phys. Rev. Lett.* **97** 1–4
[32] Tannous C and Gieraltowski J 2006 *Eur. J. Phys.* **29** 475–7
[33] Van Drent W P, Bijker M D and Lodder J C 1996 *J. Magn. Magn. Mater.* **156** 309–10
[34] Kumar A, Fähler S, Schlörb H, Leistner K and Schultz L 2006 *Phys. Rev.* B **73** 1–5
[35] Nix F C and MacNair D 1941 *Phys. Rev.* **60** 597–605
[36] Bozorth R M and Walker J G 1953 *Phys. Rev.* **89** 624–62
[37] Hall R C 1959 *J. Appl. Phys.* **30** 816–9
[38] Silva E L, Nunes W C, Knobel M, Denardin J C, Zanchet D, Pirota K, Navas D and Vázquez M 2006 *Physica* B **384** 22–4
[39] Pirota K R, Silva E L, Zanchet D, Navas D, Vázquez M, Hernández-Vélez M and Knobel M 2007 *Phys. Rev.* B **76** 233410

IV

Magneto-thermoelectric characterization of a $HfTe_5$ micro-ribbon

Anna C. Niemann, Johannes Gooth, Yan Sun, Felix Thiel, Andy Thomas, Chandra Shekhar, Vicky Süß, Claudia Felser, & Kornelius Nielsch

Reprinted with permission from *Applied Physics Letters* **115**, 072109 (2019)
Copyright 2019, AIP Publishing LLC.

Author Contributions:
A.C.N. conceived the original idea for the project. V.S. and C. S. synthesized the sample. A.C.N. performed the transport measurements. F.T. characterized the crystal structure. All authors analyzed the results. A.C.N. wrote the manuscript with substantial contributions from all authors. C.F. and K.N. supervised the project.

Applied Physics Letters ARTICLE scitation.org/journal/apl

Magneto-thermoelectric characterization of a $HfTe_5$ micro-ribbon

Cite as: Appl. Phys. Lett. **115**, 072109 (2019); doi: 10.1063/1.5116788
Submitted: 2 July 2019 · Accepted: 29 July 2019 ·
Published Online: 16 August 2019

Anna Corinna Niemann,[1,a)] Johannes Gooth,[2] Yan Sun,[2] Felix Thiel,[1] Andy Thomas,[1] Chandra Shekhar,[2] Vicky Süß,[2] Claudia Felser,[2] and Kornelius Nielsch[1,3,4]

AFFILIATIONS

[1]Leibniz Institute for Solid State and Materials Research Dresden (IFW Dresden), Institute for Metallic Materials, Helmholtzstrasse 20, 01069 Dresden, Germany
[2]Max Planck Institute for Chemical Physics of Solids, Nöthnitzer Straße 40, 01187 Dresden, Germany
[3]Technische Universität Dresden, Institute of Materials Science, 01062 Dresden, Germany
[4]Technische Universität Dresden, Institute of Applied Physics, 01062 Dresden, Germany

[a)]Author to whom correspondence should be addressed: a.niemann@ifw-dresden.de

ABSTRACT

$HfTe_5$ is a promising low-temperature thermoelectric material. Its thermoelectric power output has been investigated at different temperatures and with different dopants. Recently, research has focused on the nontrivial topological band structure of $HfTe_5$. Whereas band structure simulations and angle-resolved photoemission spectroscopy experiments put $HfTe_5$ at the transition between a weak and a strong topological insulator, observations of the chiral magnetic effect indicate that $HfTe_5$ is instead a Dirac semimetal. In this study, we contribute to the investigation of transport phenomena in $HfTe_5$ by magnetoresistance (MR) and magnetothermopower (MS) measurements on a single-crystalline $HfTe_5$ microribbon measuring $20\,\mu m \times 2.1\,\mu m \times 0.7\,\mu m$, with a magnetic field applied perpendicular to the transport direction. Interestingly, we see an almost complete suppression of the thermopower for elevated magnetic fields at temperatures of $T \leq 100$ K, while an increased magnetothermopower is observed for increasing magnetic fields at $T \geq 150$ K. First, we analyze the magnetic field-dependence of the magnetoresistance and magnetothermopower for different temperatures and propose several possible transport mechanisms responsible for the vanishing magnetothermoelectric transport at low temperatures. Furthermore, we report on an increase in the thermoelectric power factor by up to 40% due to an applied magnetic field and for temperatures between 150 K and 300 K, which is the temperature range relevant for thermoelectric applications of $HfTe_5$.

Published under license by AIP Publishing. https://doi.org/10.1063/1.5116788

In recent years, theoretical and experimental band structure investigations have sparked renewed interest in thermoelectric materials known for several decades. For example, Bi-Te-Sb-Se based materials like Bi_2Te_3, which have primarily been investigated for their thermoelectric power generation, have proven to be topological insulators.[1] For thermoelectric characterization, measurements of the electrical resistivity ρ, the thermopower S, and the thermal conductivity are performed. In Dirac[2,3] and Weyl[4,5] semimetals, electrical transport measurements are commonly used to investigate new transport phenomena like the chiral anomaly caused by the breakdown of chiral symmetry between the Weyl nodes[6,7] or the anomalous Hall effect (AHE) that arises due to a Berry curvature associated with the Weyl nodes.[8] Additionally, thermoelectric transport phenomena have been investigated in Dirac and Weyl semimetals, like the thermoelectric response to the breakdown of chiral symmetry[9,10] and the anomalous Nernst effect,[11] which is the thermoelectric equivalent to the AHE.

Lately, there has also been renewed interest in isostructural, layered materials $HfTe_5$ and $ZrTe_5$. $HfTe_5$ and $ZrTe_5$ have an orthorhombic crystal structure[12] with the space group *Cmcm*. They are characterized by a layered structure with sheets in the a-c plane, which are stacked along the b-axis. $HfTe_5$ and $ZrTe_5$ have been investigated since the 1980s and were first studied for their resistivity anomaly[13,14] and thermoelectric transport.[15] They are interesting materials for thermoelectric low-T applications because they possess a higher thermoelectric power factor (PF) than Bi_2Te_3 between 150 K and 300 K.[16] To further enhance the PF of $HfTe_5$ and $ZrTe_5$, the effect of doping was intensively studied.[16–18] Doping of single-crystalline $HfTe_5$ and Hf_x-$Zr_{1-x}Te_5$ showed remarkable thermoelectric PF of up to $6\,mW/K^2m$ for $HfTe_5$:Nd at 300 K.[17] Thermoelectric transport

Published under license by AIP Publishing

experiments on polycrystalline $ZrTe_5$ and polycrystalline iodine-doped $ZrTe_5$ explain the observed transport phenomena in polycrystalline as well as single-crystalline flux- and vapor-grown $ZrTe_5$ by a two-band model, consisting of a valence band with a high mobility and a conduction band with high effective masses.[19] Recently, the nontrivial topological band structure of $HfTe_5$ and $ZrTe_5$ has been investigated in theoretical and experimental studies.[20–23] While *ab initio* band simulations[20] as well as angle-resolved photoemission spectroscopy investigations[21] show that $HfTe_5$ and $ZrTe_5$ are located at a phase transition between a weak and a strong topological insulator, the reported chiral anomaly[22,23] indicates the existence of 3D-Dirac bands in $HfTe_5$ and $ZrTe_5$. Additionally, a temperature-induced Lifshitz transition, in which the Fermi level is shifted across the Dirac point as the temperature increases, was reported to be responsible for the resistivity anomaly in $HfTe_5$ and $ZrTe_5$.[21,24]

In this study, we conducted magnetoresistance (MR) and magnetothermopower (MS) measurements on a single-crystalline $HfTe_5$ microribbon with the magnetic field perpendicular to the transport direction from room temperature down to cryogenic temperatures and for magnetic fields of up to ± 14 T. While we observe a PF growing continuously up to 35% for increasing magnetic fields at room temperature, we see vanishing thermoelectric transport for $T \leq 100$ K and elevated magnetic fields. Analyzing the MR and MS curves, we propose different transport mechanisms including a two-carrier transport model, transport exclusively at the lowest Landau level, and a splitting of the Dirac cone into two Weyl cones that fit the observed MR curves and might be responsible for the almost complete suppression of S.

The $HfTe_5$ single crystal used in this study was grown by chemical vapor transport.[25] Single-crystal x-ray diffraction showed that the $HfTe_5$ samples adopted the *Cmcm* structure and the probed lattice constants[26] of $a = 3.974$ Å, $b = 14.481$ Å, and $c = 13.720$ Å are in good agreement with the previously reported values for $HfTe_5$.[12] Energy-dispersive X-ray spectroscopy (EDXS) shows a near-stoichiometric composition of 1 : 4.97 Hf - Te in our sample.[26]

For the magnetotransport measurements, an $HfTe_5$ microribbon was mechanically extracted from the bulk crystal using a micromanipulator. The $HfTe_5$ microribbon ($20\,\mu m \times 2.1\,\mu m \times 0.7\,\mu m$) was placed on a glass substrate and electrically contacted by laser lithography combined with a Ti/Pt metallization process. The electrical contact structure consists of one resistive heater line and two resistive thermometers. The same contact structure is used to measure ρ [Fig. 1(a)] as well as S[27,28] [Fig. 1(b)]. We chose a microribbon geometry for our measurement setup to ensure a one-dimensional temperature gradient. The orientation of the crystal axes within the microribbon was identified by electron backscattering diffraction (EBSD) within a scanning electron microscope. We confirmed that electrical transport occurs along the [100] axis. The magnetotransport measurements were performed between 1.7 K and room temperature with an external magnetic field up to ± 14 T. The electric current (100 nA) used for the resistivity measurement and the temperature gradient ($\Delta T = 0.29\,\mathrm{K} \pm 0.04\,\mathrm{K}$) used for the thermopower measurement were applied along the [100] axis, and the magnetic field was applied perpendicular to the current direction, along the [010] axis.

For temperatures T of room temperature and below, we observe nearly constant $\rho(T)$ until approximately 150 K with a room temperature resistivity of 1.2 mΩ cm [Fig. 1(c)]. Toward lower T, the resistivity anomaly peak appears at the transition temperature of $T_p \approx 60$ K, which is slightly shifted downward compared to literature data for bulk samples[13] ($T_{p,\mathrm{lit.}} \approx 74$ K). Using angle-resolved photoemission spectroscopy (ARPES) measurements, this resistivity anomaly peak was recently identified to result from a temperature-induced Lifshitz transition that occurs across T_p.[21] The Fermi surface topology transforms from an electronlike pocket below T_p to a holelike pocket above T_p. At T_p, the Fermi level E_F lies in the energy gap between the valence and conduction bands, resulting in increased resistivity at T_p. Accordingly, we observe a transition from an n-type semimetal for $T < T_p$ to a p-type semimetal for $T > T_p$. In our thermopower measurements, we observed a positive S at room temperature [$S(300\,\mathrm{K}) = 150\,\mu V\,K^{-1}$] and a sign change to a negative S below T_p [Fig. 1(d)]. Compared to the literature data,[15] we observe an increased positive S above T_p but a decreased negative S below T_p. We therefore conclude that E_F in our $HfTe_5$ microribbon is shifted toward the valence band compared to the depicted literature data.[15] We would like to note that the resistivity and the thermopower have uncertainties of 6% and 14%, respectively, caused by uncertainties in the determination of the geometry and temperature gradient.

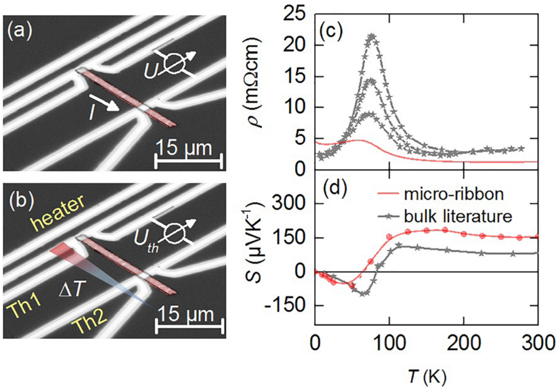

FIG. 1. False color, optical micrograph of the $HfTe_5$ microribbon ($20\,\mu m \times 2.1\,\mu m \times 0.7\,\mu m$) (red) and the electrical contact structure in the configuration for electrical resistivity measurements (a) and thermopower measurements (b). In (b), the resistive heater line and the two resistive thermometers are labeled as the heater and Th1/Th2, respectively. (c) The resistivity ρ and (d) the thermopower S as a function of temperature T. The measured resistivity and thermopower of the microribbon (red) are compared with literature values[13,15] (gray) for several $HfTe_5$ bulk samples.

For any applied external magnetic field, the resistivity as a function of temperature $\rho(T)$ is increased over the entire temperature range of 2 K to 300 K as compared to no applied field [Fig. 2(a)]. At 300 K, there is a moderate positive MR of 25% with an applied magnetic field of 14 T. At 2 K, we observe a positive MR of 95% when applying a magnetic field of 14 T. Additionally, we observe that the resistivity anomaly peak shifts to higher T when an external magnetic field is applied. The observed increasingly strong semiconducting behavior for increasingly strong magnetic fields is normally associated with small gap semiconductors, which exhibit an increasing gap opening due to the external magnetic field.[29,30]

In the next step, we recorded the MR [$\mathrm{MR} = (R_B - R_0)/R_0$], with R_0 being the resistance at zero magnetic field and R_B being the resistance within a magnetic field as shown in Fig. 2(b). Depending on T and B, we observe three different MR regimes. First, there is a positive, quadratic MR at low magnetic fields across the whole T-range. For

Published under license by AIP Publishing

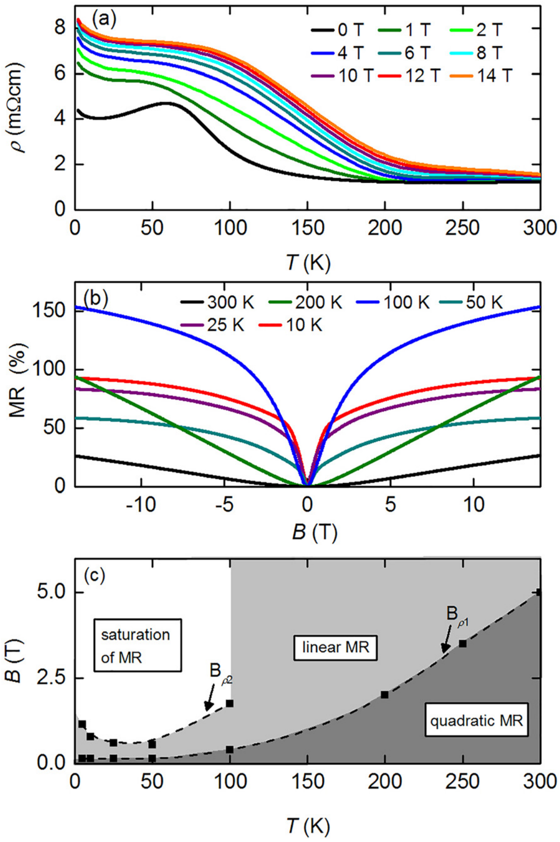

FIG. 2. (a) Resistivity ρ as a function of temperature T for different applied magnetic fields B up to 14 T. (b) MR [MR = $(\rho_B - \rho_0)/\rho_0$] as a function of B at different T values. (c) The three different regimes of the MR (quadratic, linear, and saturating) depending on T and B. The transition magnetic fields from quadratic to linear and from linear to saturating MR are labeled as $B_{\rho 1}$ and $B_{\rho 2}$, respectively.

higher magnetic fields, this quadratic MR becomes a linear MR. The corresponding transition magnetic field $B_{\rho 1}$ from quadratic to linear MR is 0.15 T at 5 K and increases to 5 T at 300 K [Fig. 2(c)]. For $T \leq 100$ K, we observe an additional saturation in MR for a further increased B beyond the linear MR regime [Fig. 2(b)]. The transition magnetic field $B_{\rho 2}$ from linear MR to a saturating MR is also given in Fig. 2(c).

MR signatures similar to those observed by us – namely, a strong increase in the MR for increasing B combined with a saturating MR at further increased B – have previously been observed in the Dirac semimetal Cd_3As_2 and were associated with a two-carrier transport behavior.[31] For $HfTe_5$, a two-carrier transport mechanism was recently found in Hall measurements.[22] Furthermore, the MR curves for $T \leq 100$ K might, at first glance, look similar to MR peaks caused by weak antilocalization (WAL).[32] Nevertheless, we note that WAL is usually associated with much weaker magnetic fields as well as lower temperatures. Our observed values of more than 1 T and up to 100 K are therefore highly uncharacteristic of the WAL, respectively. Thus, exclude WAL as an explanation for the measured signatures.

Another approach to analyze the measured MR curves is to consider the different MR regimes independently. Particularly, the linear MR, which we observe for $T > 100$ K for the whole B range and for $T \leq 100$ K in intermediate B ranges [compare Fig. 2(c)], is widely discussed for materials with linear band crossings in their band structure. It can be caused by different phenomena. First, a linear MR can be caused by disorder-induced mobility fluctuations,[33] which we exclude because of the single crystalline nature of our sample. Second, a linear MR can be a signature of the quantum limit which means that transport exclusively takes place at the lowest Landau level.[34,35] Third, a linear MR has recently been associated with strong changes in the electronic structure of Dirac semimetals, where the Dirac cone splits into two Weyl cones due to an applied magnetic field.[36,37] Nevertheless, considering the linear MR as an independent transport signature requires an additional mechanism to be responsible for the saturation of MR at elevated B and $T \leq 100$ K. One possible mechanism for the saturation of MR might be confinement effects.[38,39]

The thermopower as a function of T for different elevated magnetic fields shows an increase in S at high T well above the p-n transition and a decrease in $|S|$ for T below the p-n transition [Fig. 3(a)].

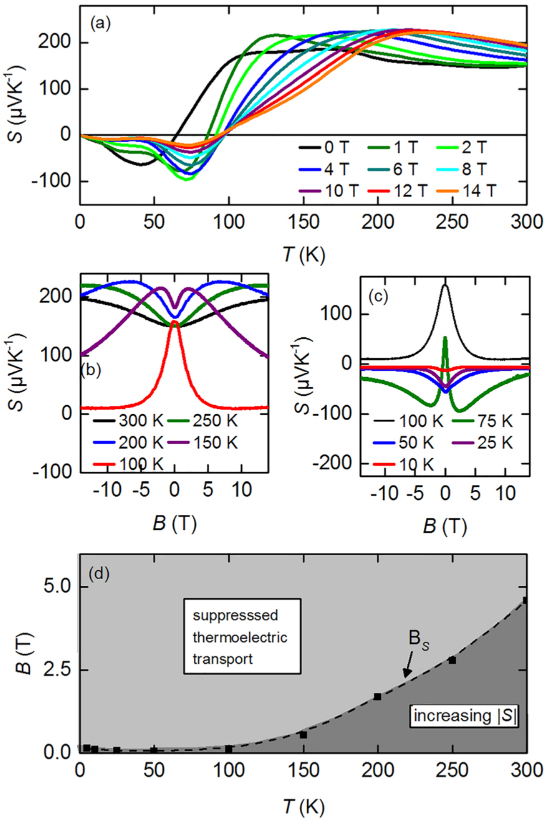

FIG. 3. (a) Thermopower S as a function of temperature T for different applied magnetic fields up to 14 T. (b) S as a function of B for temperatures between 100 K and 300 K and (c) S as a function of B for low temperatures from 10 K to 100 K. (d) Depending on T and B, either an increasing $|S|$ for increasing B or a suppressed thermoelectric transport can be observed.

Published under license by AIP Publishing

Additionally, the temperature of the p-n transition increases from 60 K at zero magnetic field to 96 K at an applied magnetic field of 14 T, which is in agreement with the shift of the resistivity anomaly peak toward higher *T* at elevated magnetic fields.

The thermopower plotted as a function of *B* for different *T* values is shown in Figs. 3(b) and 3(c) for $T \geq 100$ K and $T \leq 100$ K, respectively. At low magnetic fields, we obtain an increasing $|S|$ with increasing *B*. At higher magnetic fields, $|S|$ starts to decrease with further increasing *B*, and for even more elevated *B* at $T \leq 100$ K, $|S|$ approaches 0 μV K^{-1} and maintains this constant value as *B* increases. From the $S(B)$-plots, we extracted the magnetic field values of the inflection points B_S separating the increasing *S* at low magnetic fields from the decreasing *S* at higher magnetic fields, as shown in Fig. 3(d). B_S increases from 0.14 T at 5 K to 4.6 T at 300 K. Comparing the magnetic field values of transition B_S with the field values $B_{\rho 1}$ for the transition from quadratic to linear MR, there is good agreement across the whole temperature range. We emphasize that the magnetic field value of constant $S(B) \approx 0\,\mu$V/K decreases with decreasing *T* [Fig. 3(c)]. At 100 K, $S(B) \approx 0\,\mu$V/K is approached at 9.5 T, while for 5 K, $S(B)$ already plateaus at 1.8 T.

The magnetothermoelectric transport curves might indicate the transport mechanisms in $HfTe_5$ which we introduced for the analysis of the MR curves. Vanishing thermoelectric transport for elevated magnetic fields is a transport signature for the transition from multi-Landau level transport to transport at the lowest Landau level. In general, *S* is proportional to the temperature derivative of the density of states (DOS). In the quantum limit, the DOS is independent of *T*. Therefore, the thermoelectric transport is suppressed in the quantum limit.[9,10] The matching values of $B_{\rho 1}$ and B_S show that the signatures of reaching the quantum limit in the magnetoresistance and magnetothermoelectric transport appear at identical magnetic field values. With $B_{\rho 1}/B_S$ at approx. 0.15 T for $T \leq 50$ K, the quantum limit of $HfTe_5$ would be extremely low. Nevertheless, Wang *et al.* claim to observe the quantum limit in $ZrTe_5$,[40] which is isostructural to $HfTe_5$ for comparable magnetic field values. To review the other possible transport mechanisms, like the two-carrier transport and the splitting of the Dirac cone into two Weyl cones, a theoretical description of the corresponding magnetothermoelectric transport signatures is needed. These are promising subjects for further theoretical investigations.

The thermoelectric power factor PF ($PF = S^2/\rho$) of the $HfTe_5$ microribbons, which quantifies the thermoelectric power output, is given in Fig. 4(a) as a function of *T* for different applied *B* values. For $T \leq 50$ K, the PF plateaus at a low value with PF(50 K, 0 T) = 0.07 mW/K^{2}m. For $T \geq 50$ K, there is a steep increase in the PF. At zero magnetic field, the thermoelectric PF between 150 K and 300 K plateaus at approx. 2 mW/K^{2}m, which is comparable to the values for $HfTe_5$ reported by Lowhorn *et al.*,[17] but is lower by a factor of three than that for $HfTe_5$:Nd from the same study. Figure 4(a) shows that applying a magnetic field to the $HfTe_5$ microribbon leads to an increase in the PF for $T \geq 150$ K compared to the PF at zero magnetic field.

To quantify the changes of the PF within the magnetic field, we calculate the magnetopower factor ratio $MPF = (PF_B - PF_0)/PF_0$, with PF_B being the power factor within a magnetic field and PF_0 being the power factor without an applied magnetic field, as shown in Fig. 4(b). For $T \geq 200$ K, MPF increases up to 40% when a magnetic field is applied. Thus, the PF can be enhanced by applying a magnetic field in a temperature range that is interesting for thermoelectric applications of $HfTe_5$ because in this temperature range, the PF of $HfTe_5$ exceeds the PF of Bi_2Te_3.[16] Furthermore, we observe a strong reduction of the PF for $T \leq 100$ K to MPF ≈ –100% which corresponds to an almost complete suppression of the thermoelectric transport.

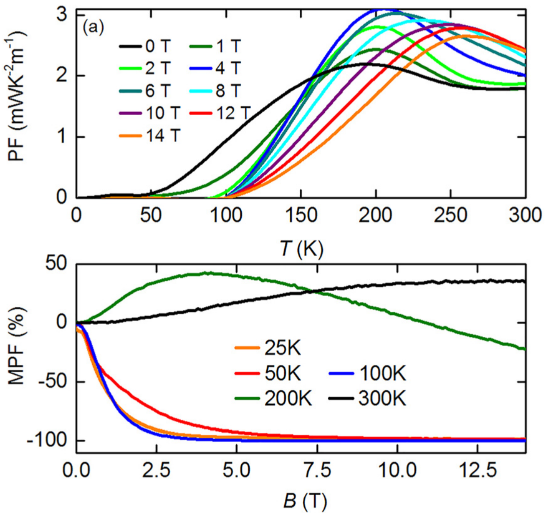

FIG. 4. (a) The thermoelectric power factor PF ($PF = S^2/\rho$, with thermopower *S* and resistivity ρ) as a function of the temperature *T* for different applied magnetic fields *B* up to 14 T. (b) The magnetopower factor MPF [$MPF = (PF_B - PF_0)/PF_0$] as a function of *B* at different *T* values.

In conclusion, we have performed resistance and thermopower measurements on an $HfTe_5$ microribbon with the magnetic field perpendicular to the transport direction in order to present the first detailed study of magnetothermoelectric transport in this layered thermoelectric material with a nontrivial topological band structure. The MR shows a positive quadratic, positive linear and saturating MR depending on *T* and *B*, which was previously reported as a signature of a two-channel transport in the Dirac semimetal Cd_3As_2.[31] Moreover, the observed linear MR in materials with a linear dispersion relation is also a signature of transport within the quantum limit[34,35] or changes in the band structure due to a splitting of the Dirac cone.[36,37] There is a vanishing thermoelectric transport for increasing *B* and $T \leq 100$ K, which was recently connected to the thermoelectric transport within the quantum limit.[9,10] Nevertheless, a theoretical description of the magnetothermoelectric signatures of transport in a two-carrier transport model and for splitting Dirac cones is of high interest and needed for a final evaluation of the presented data. Additionally, we find that the PF can be increased up to 40% by applying a magnetic field between 150 K and 300 K which is the temperature range that is relevant for thermoelectric applications of $HfTe_5$.

The authors thank Almut Pöhl and Tina Sturm for experimental support. The authors gratefully acknowledge financial support from the Deutsche Forschungsgemeinschaft DFG via DFG-RSF-Project No. (NI 616/22-1) “Influence of the topological states on the thermoelectric properties of Weyl semimetals.”

REFERENCES

[1] H. Zhang, C.-X. Liu, X.-L. Qi, X. Dai, Z. Fang, and S.-C. Zhang, Nat. Phys. **5**, 438 (2009).

[2]S. M. Young, S. Zaheer, J. C. Y. Teo, C. L. Kane, E. J. Mele, and A. M. Rappe, Phys. Rev. Lett. **108**, 140405 (2012).
[3]S. Borisenko, Q. Gibson, D. Evtushinsky, V. Zabolotnyy, B. Büchner, and R. J. Cava, Phys. Rev. Lett. **113**, 027603 (2014).
[4]X. Wan, A. M. Turner, A. Vishwanath, and S. Y. Savrasov, Phys. Rev. B **83**, 205101 (2011).
[5]S.-Y. Xu, I. Belopolski, N. Alidoust, M. Neupane, G. Bian, C. Zhang, R. Sankar, G. Chang, Z. Yuan, C.-C. Lee, S.-M. Huang, H. Zheng, J. Ma, D. S. Sanchez, B. Wang, A. Bansil, F. Chou, P. P. Shilbayev, S. Lin, S. Jia, and M. Z. Hasan, Science **349**, 613–617 (2015).
[6]H. Li, H. He, H.-Z. Lu, H. Zhang, H. Liu, R. Ma, Z. Fan, S.-Q. Shen, and J. Wang, Nat. Commun. **7**, 10301 (2016).
[7]X. Huang, L. Zhao, Y. Long, P. Wang, D. Chen, Z. Yang, H. Liang, M. Xue, H. Weng, Z. Fang, X. Dai, and G. Chen, Phys. Rev. X **5**, 031023 (2015).
[8]E. Liu, Y. Sun, N. Kumar, L. Muechler, A. Sun, L. Jiao, S.-Y. Yang, D. Liu, A. Liang, Q. Xu, J. Kroder, V. Süß, H. Borrmann, C. Shekhar, Z. Wang, C. Xi, W. Wang, W. Schnelle, S. Wirth, Y. Chen, S. T. B. Goennenwein, and C. Felser, Nat. Phys. **14**, 1125 (2018).
[9]J. Gooth, A. C. Niemann, T. Meng, A. G. Grushin, K. Landsteiner, B. Gotsmann, F. Menges, M. Schmidt, C. Shekhar, V. Süß, R. Hühne, B. Rellinghaus, C. Felser, B. Yan, and K. Nielsch, Nature **547**, 324–327 (2017).
[10]M. Hirschberger, S. Kushwaha, Z. Wang, Q. Gibson, S. Liang, C. A. Belvin, R. J. Cava, and N. P. Ong, Nat. Mater. **15**, 1161 (2016).
[11]M. Ikhlas, T. Tomita, T. Koretsune, M.-T. Suzuki, D. Nishio-Hamane, R. Arita, Y. Otani, and S. Nakatsuji, Nat. Phys. **13**, 1085 (2017).
[12]S. Furuseth, L. Brattas, and A. Kjekshus, Acta Chem. Scand. **27**, 2367–2374 (1973).
[13]M. Izumi, K. Uchinokura, and E. Matsuura, Solid State Commun. **37**, 641–642 (1981).
[14]T. M. Tritt, N. D. Lowhorn, R. T. Littleton IV, A. Pope, C. R. Feger, and J. W. Kolis, Phys. Rev. B **60**, 7816 (1999).
[15]T. E. Jones, W. W. Fuller, T. J. Wieting, and F. Levy, Solid State Commun. **42**, 793 (1982).
[16]R. T. Littleton IV, T. M. Tritt, J. W. Kolis, and D. R. Ketchum, Phys. Rev. B **60**, 13453 (1999).
[17]N. D. Lowhorn, T. M. Tritt, E. E. Abbott, and J. W. Kolis, Appl. Phys. Lett. **88**, 022101 (2006).
[18]R. T. Littleton IV, T. M. Tritt, J. W. Kolis, D. R. Ketchum, N. D. Lowhorn, and M. B. Korzenski, Phys. Rev. B **64**, 121104 (2001).
[19]S. A. Miller, I. Witting, U. Aydemir, L. Peng, A. J. E. Rettie, P. Gorai, D. Young Chung, M. G. Kanatzidis, M. Grayson, V. Stevanovic, E. S. Toberer, and G. J. Snyder, Phys. Rev. Appl. **9**, 014025 (2018).
[20]H. Weng, X. Dai, and Z. Fang, Phys. Rev. X **4**, 011002 (2014).
[21]Y. Zhang, C. Wang, G. Liu, A. Liang, L. Zhao, J. Huang, Q. Gao, B. Shen, J. Liu, C. Hu, W. Zhao, G. Chen, X. Jia, L. Yu, L. Zhao, S. He, F. Zhang, S. Zhang, F. Yang, Z. Wang, Q. Peng, Z. Xu, C. Chen, and X. Zhou, Sci. Bull. **62**, 950 (2017).
[22]H. Wang, C.-K. Li, H. Liu, J. Yan, J. Wang, J. Liu, Z. Lin, Y. Li, Y. Wang, L. Li, D. Mandrus, X. C. Xie, J. Feng, and J. Wang, Phys. Rev. B **93**, 165127 (2016).
[23]Q. Li, D. E. Kharzeev, C. Zhang, Y. Huang, I. Pletikosic, A. V. Fedorov, R. D. Zhong, J. A. Schneeloch, G. D. Gu, and T. Valla, Nat. Phys. **12**, 550 (2016).
[24]Y. Zhang, C. Wang, L. Yu, G. Liu, A. Liang, J. Huang, S. Nie, X. Sun, Y. Zhang, B. Shen, J. Liu, H. Wenig, L. Zhao, G. Chen, X. Jia, C. Hu, Y. Ding, W. Zhao, Q. Gao, C. Li, S. He, L. Zhao, F. Zhang, S. Zhang, F. Yang, Z. Wang, Q. Peng, X. Dai, Z. Fang, Z. Xu, C. Chen, and X. J. Zhou, Nat. Commun. **8**, 15512 (2017).
[25]F. Levy and H. Berger, J. Cryst. Growth **61**, 61–68 (1983).
[26]Y. Qi, W. Shi, P. G. Naumov, N. Kumar, W. Schnelle, O. Barkalov, C. Shekhar, H. Borrmann, C. Felser, B. Yan *et al.*, Phys. Rev. B **94**, 054517 (2016).
[27]T. Böhnert, V. Vega, A.-K. Michel, V. M. Prida, and K. Nielsch, Appl. Phys. Lett. **103**, 092407 (2013).
[28]E. Shapira, A. Tsukernik, and Y. Selzer, Nanotechnology **18**, 485703 (2007).
[29]C. Shekhar, A. K. Nayak, Y. Sun, M. Schmidt, M. Nicklas, I. Leermakers, U. Zeitler, Y. Skourski, J. Wosnitza, Z. Liu *et al.*, Nat. Phys. **11**, 645 (2015).
[30]M. N. Ali, J. Xiong, S. Flynn, J. Tao, Q. D. Gibson, L. M. Schoop, T. Liang, N. Haldolaarachchige, M. Hirschberger, N. P. Ong *et al.*, Nature **514**, 205–208 (2014).
[31]C.-Z. Li, J.-G. Li, L.-X. Wang, L. Zhang, J.-M. Zhang, D. Yu, and Z.-M. Liao, ACS Nano **10**, 6 (2016).
[32]S. Hikami, A. I. Larkin, and Y. Nagaoka, Prog. Theor. Phys. **63**, 707 (1980).
[33]M. M. Parish and P. B. Littlewood, Nature **426**, 162 (2003).
[34]A. A. Abrikosov, Phys. Rev. B **58**, 2788 (1998).
[35]A. A. Abrikosov, J. Phys. A **36**, 9119 (2003).
[36]J. Feng, Y. Pang, D. Wu, Z. Wang, H. Weng, J. Li, X. Dai, Z. Fang, Y. Shi, and L. Lui, Phys. Rev. B **92**, 081306 (2015).
[37]T. Liang, Q. Gibson, M. N. Ali, M. Liu, R. J. Cava, and N. P. Ong, Nat. Mater. **14**, 280 (2015).
[38]R. G. Chambers, Proc. R. Soc. London, Ser. A **202**, 378 (1950).
[39]J. Heremans, C. M. Thrush, Y.-M. Lin, S. Cronin, Z. Zhang, M. S. Dresselhaus, and J. F. Mansfield, Phys. Rev. B **61**, 2921 (2000).
[40]H. Wang, H. Liu, Y. Li, Y. Liu, J. Wang, J. Liu, Y. Wang, L. Li, J. Yan, D. Mandrus, X. C. Xie, and J. Wang, Sci. Adv. **4**, 11 (2018).

Published under license by AIP Publishing

V

Berry phase and band structure analysis of the Weyl semimetal NbP

Philip Sergelius, Johannes Gooth, Svenja Bäßler, Robert Zierold, Christoph Wiegand, Anna Niemann, Heiko Reith, Chandra Shekhar, Claudia Felser, Binghai Yan & Kornelius Nielsch

Reprinted from *Scientific Reports* **6**, 33859 (2016)

Copyright 2016 Springer Nature Publishing AG.
License: Creative Commons Attribution 4.0 International (CC BY 4.0).

Author Contributions:

P.S. and J.G. conducted the measurements. J.G., S.B., R.Z., C.W., A.N., H.R. and B.Y. assisted in data evaluation, C.S. grew the samples. P.S. wrote the manuscript, and B.Y. wrote parts of the introduction. J.G., C.F. and K.N. conceived the study, supervised the project and assisted in data evaluation and manuscript finalization. All authors significantly contributed to the scientific discussion during data evaluation and manuscript preparation. All authors conducted a final proof reading.

www.nature.com/scientificreports

SCIENTIFIC REPORTS

OPEN

Received: 16 May 2016
Accepted: 04 September 2016
Published: 26 September 2016

Berry phase and band structure analysis of the Weyl semimetal NbP

Philip Sergelius[1], Johannes Gooth[1,2], Svenja Bäßler[1], Robert Zierold[1], Christoph Wiegand[1], Anna Niemann[1], Heiko Reith[1,3], Chandra Shekhar[4], Claudia Felser[4], Binghai Yan[4,5] & Kornelius Nielsch[1,3]

Weyl semimetals are often considered the 3D-analogon of graphene or topological insulators. The evaluation of quantum oscillations in these systems remains challenging because there are often multiple conduction bands. We observe de Haas-van Alphen oscillations with several frequencies in a single crystal of the Weyl semimetal niobium phosphide. For each fundamental crystal axis, we can fit the raw data to a superposition of sinusoidal functions, which enables us to calculate the characteristic parameters of all individual bulk conduction bands using Fourier transform with an analysis of the temperature and magnetic field-dependent oscillation amplitude decay. Our experimental results indicate that the band structure consists of Dirac bands with low cyclotron mass, a non-trivial Berry phase and parabolic bands with a higher effective mass and trivial Berry phase.

Topological insulators, Dirac semimetals and most recently Weyl semimetals (WSM) are the subject of considerable research interest in both fundamental physics[1–3] and with respect to applications[4–6]. The band structure of a WSM exhibits a crossing of two bulk bands, which results in two so-called Weyl points with opposing parity[7,8]. These pairs are expected to be notably robust but are only realised in 3D systems, where either time-reversal or inversion symmetry is broken[3,7,9]. Similar to the well-known 2D case in graphene or topological insulators, there is no energy gap, and a linear dispersion relation is present in all directions in k-space away from a single Weyl point[3,10]. On the surface of a Weyl metal, Fermi arcs were theoretically predicted[3] and experimentally shown *via* angle-resolved photoelectron emission spectroscopy (ARPES) for NbP[11] and other Weyl metals[12–15]. Both Weyl fermions and surface states are expected to cause numerous exotic quantum effects[2]. Low effective masses are expected for Dirac systems, and with the high mobilities, extremely large magnetoresistance (MR) effects have been observed, particularly in NbP with up to $8 \cdot 10^5$% MR at cryogenic temperatures and 250% at room temperature and 9 T[5]. Particularly interesting for high-performance electronics are their expected and recently demonstrated ultrahigh mobilities[5,7]. These characteristic traits of the materials may become important for future device applications such as magnetic field sensors or transistors[16].

Moreover, Weyl and Dirac semimetals exhibit new and exotic quantum effects such as chiral anomaly and negative magnetoresistance because of their non-trivial topology and associated Berry Phase. However, in contrast to other Weyl metals such as TaAs, the spin orbit coupling in NbP is much weaker due to the lower atomic mass of Nb, which may lead to the existence of additional, parabolic semimetal bands apart from the Dirac bands[7]. Because ARPES measurements resolve the surface states, which only allow for indirect investigation of the bulk band structure, the quantum oscillations must be analysed to reconstruct the Fermi surface. Electric measurements on NbP single crystals have shown strong Shubnikov-de Haas (SdH) oscillations and evidence for Dirac-like dispersions[5,7], but the individual conduction band's Berry phases have not been clearly analysed. In fact, *ab-initio* band structure calculations have predicted that the conduction bands in NbP will generally be trivial[17] because the theoretical position of the Fermi level encompasses the Weyl nodes. To realize a Berry phase, the chiral anomaly and other related effects to Weyl metals, the Fermi level must be as close as possible to the Weyl points. A possible route may be controlled electron doping, which will shift the Fermi level to a more desired position, but in reality, due to slight variations during material synthesis, an uncontrolled shift on the order of a few meV may easily be induced.

[1]Institute of Nanostructure and Solid-State Physics, University of Hamburg, 20355 Hamburg, Germany. [2]IBM Research GmbH, 8803 Rueschlikon, Switzerland. [3]Leibniz Institute for Solid State and Materials Research (IFW) Dresden, 01171 Dresden, Germany. [4]Max Planck Institute for Chemical Physics of Solids, 01187 Dresden, Germany. [5]Max Planck Institute for the Physics of Complex Systems, 01187 Dresden, Germany. Correspondence and requests for materials should be addressed to P.S. (email: Philip.Sergelius@physnet.uni-hamburg.de)

In this publication, we present de Haas-van Alphen (dHvA) measurements of a NbP single crystal with an intrinsic Fermi level as close as 3.7 meV to the Weyl nodes. A 9 T physical property measurement system (*Quantum Design*) was used with a mounted option to enable Vibrating Sample Magnetometry (VSM). For band structure investigations, VSM is more beneficial than electric measurements because of the trivial sample mounting and the possibility of easily rotating the sample to investigate different crystal orientations while maintaining the possibility to extract transport properties such as effective mass and carrier mobility. Along the major crystal axes ([100] or k_x, [010] or k_y and [001] or k_z) of the body-centred tetragonal NbP crystal[5,18], we find two fundamentally different behaviours, which are associated to the coexistence of Dirac and parabolic bands. We fit the experimental data to a superposition of up to seven sinusoidal, independent functions, each of which has a frequency, a phase and a damping parameter. The fit enables us to independently extract all relevant parameters. We observe that two bands exhibit relatively low cyclotron masses and a non-trivial Berry phase, and we find evidence for parabolic bands with comparably higher effective masses and trivial Berry phases.

Results and Discussion

The experimental data in Fig. 1 show the superpositions of multiple quantum oscillations of the magnetic moment as a function of the applied (a,b) and inverse magnetic field (c,d) and the respective Fourier transforms (e,f) for all three crystal orientations.

Fourier analysis is simultaneously conducted over the entire inverse magnetic field range. For the [100] and [010] directions, the transformation yields several peaks that were indexed by α, β, γ, δ, ε and higher harmonics. For [001], we find three peaks indexed by ζ, η and θ. We attribute peaks α and ζ to a general background curvature of the measurement data with no physical relevance. All other bands can be identified as different bulk conduction bands. For δ and η, we assign higher-order harmonic numbers to peaks where the frequency is harmonically related; however, the higher harmonic has a larger intensity (Fig. 1e,f), which is contrary to common expectation. A possible reason for this effect is the spin orbit coupling, which induces spin splitting, as discussed by Jalan *et al.*[19] and Moetakef *et al.*[20]. Additionally, the higher harmonics may be the result of non-sinusoidal components in the oscillations, which can easily occur due to noise.

The raw data (Fig. 1a,b) show multiple oscillations with different frequencies and magnitudes. If only one type of oscillation is present, it is straightforward to calculate the Landau level diagrams, temperature and field-dependent damping of the amplitudes. However, in our case, only the most prominent oscillations can be distinguished by eye, and determining any damping from the raw data is elusive. Therefore, following the argumentation of Tian *et al.*[21] and Hu *et al.*[22], we fit the raw data for T = 2.5 K with a superposition of damped sine-functions for each frequency as in Eq. (1)

$$M = a_0 + \sum_{i=1}^{n} A_i \ \sin\left(2\pi F_i \frac{1}{B} - \varphi_i\right) e^{-d_i \frac{1}{B}}, \tag{1}$$

where we sum over the frequencies (F_i with $i = \alpha, \beta, \gamma \ldots$) from the Fourier transform. The fit parameters are the associated oscillation amplitude A_i, damping factor d_i, phase φ_i and a global offset a_0. If higher harmonics are visible, they are incorporated into the sum, but they share an identical damping factor and phase to the respective first harmonic. Note that for oscillations in the magnetic moment, a sine function must be used, whereas the oscillations in the resistivity oscillate as a cosine function[23], which is important in the Berry phase calculation. Figure 2 shows that Eq. 1 fits the experimental data well, which enables us to extract the individual properties of each band using Onsager relations and the Lifshitz-Kosevich-Shoenberg (LKS) formula[23]. Note that we cannot fit the k_x and k_y data between 0.25 and 0.5 T^{-1} because the β-band reaches its quantum limit and stops oscillating as early as 3 T. In addition, the SdH oscillations become visible as early as 0.2 T, which corresponds to a magnetic length of $l_B = \sqrt{\hbar/eB} = 57$ nm and emphasizes the high sample quality[17].

If a sine function is used as in Eq. 1, the phase is $-\varphi_i = 2\pi(\frac{1}{2} - \Gamma + \Delta)$. $2\pi\Gamma$ is the Berry phase, and Δ is an additional phase shift between $\pm 1/8$, which may arise because of the corrugated Fermi surfaces[24,25]. Note that if the dHvA oscillation minima are manually evaluated, an additional summand of $\frac{1}{4}$ is necessary[26]. In this case, Lifshitz-Onsager quantization rule is $\frac{A_f \hbar}{e}\frac{1}{B} = 2\pi(n + \frac{1}{2} + \frac{1}{4} + \Gamma + \Delta)$.

We emphasize that the precise determination of the Berry phase is often a challenging procedure because the axis intercept is inherently prone to scattering, particularly if only high-index Landau levels can be resolved. However, we can fit the raw data over a multitude of oscillation periods while considering all other superposed oscillations. Thus, we can extract the axis intercept with high accuracy. The standard error from the fits to the phase is less than 1% in all cases, except the $\delta-$band, which is not evaluated because only three periods can be fitted. To cross check our calculations, all minima that are unambiguously visible in the raw data are also manually counted with identical results. The errors are further assessed as shown in the supporting information.

In the [100] and [010] directions, we identify β as a Dirac band with an axis intercept of $\Gamma + \Delta = 0.48(1)$, which displays a non-trivial Berry phase. A similar behaviour is found in the [001] direction, where θ shows an axis intercept of $\Gamma + \Delta = 0.54(5)$. All other bands have axis intercepts of $\Gamma + \Delta < 0.25$, which indicates a parabolic behaviour. We investigate the effective mass to further elucidate the carrier characteristics, band topology and whether the fermi surface has been shifted to a more desired position, as previously introduced.

From the Onsager relation $A_f = F \cdot 2\pi^2/\phi_0$ with ϕ_0 as the magnetic flux quantum, we determine the size of the Fermi surface cross section; if we approximate it as a circle, the k-vectors are $A_f = \pi k^2$. The values are summarized in Table 1. The effective mass is calculated using the temperature-dependent part of the LKS theory, as shown in Eq. (2):

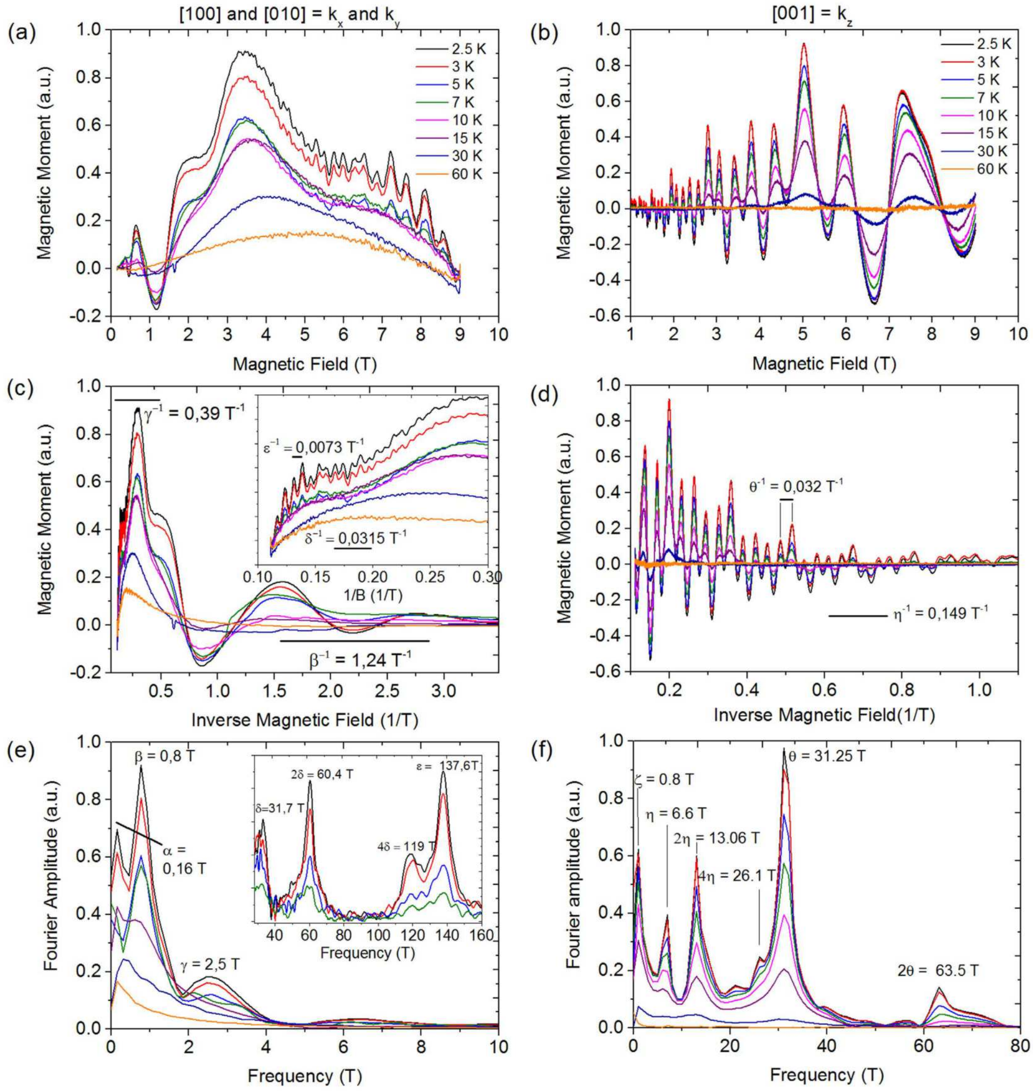

Figure 1. Left column shows the [100] and [010] orientations (k_x and k_y, respectively). The right column shows [001] or k_z. (**a,b**) Display dHvA oscillations of the magnetic moment as a function of the magnetic field between 2.5 K and 60 K. In the graphs, the raw data are shown with a subtracted linear background. Several superpositions of different oscillation frequencies are visible. (**c,d**) Display the identical data in 1/B. The inset in (**c**) displays the narrow region that corresponds to large magnetic fields >3 T. (**e,f**) Show the fast Fourier transforms of the measurement data. Several oscillation peaks and their higher harmonics can be observed. The small peak at 21 T is neglected in the data evaluation because it may be noise or a notably weakly contributing band. In any case, a temperature dependence of the peak height cannot be extracted. (**f**) The inset in (**e**) displays the higher frequency oscillations.

$$M(T, B) \propto B^{-\frac{1}{2}} \cdot e^{-\chi T_D B} \cdot \frac{\chi T/B}{\sinh(\chi T/B)}, \tag{2}$$

with $\chi = 4\pi^3 k_B m^\star/eh$ as the fitting parameter[5,23,27,28]. k_B is Boltzmann's constant, T_D is the Dingle temperature, $m^\star$ is the effective mass and e is the elemental charge. A well-pronounced, single oscillation is often selected (imposing $B = \text{const.}$), and its amplitude decay with temperature is fitted to Eq. (2). If several oscillations with severely different damping and amplitudes are superposed, this procedure cannot be performed. Therefore, we fit the temperature decay of the peak heights of the Fourier spectra[29]. To calculate $m^\star$, B must be set to the centre point of the magnetic field interval where the respective oscillations are present, e.g., 5.5 T if the oscillations are visible at 2–9 T[22]. The graphs of the LKS fits are shown in Fig. 3. The respective values of the effective mass are summarized in Table 1. As noted above, the cyclotron mass of the Dirac band, $m^*_\beta = 0.048$, is found to be significantly lower than that for all other bands. We therefore believe that β lies within the Weyl pocket. For the θ-Band, we find an effective mass of $m^*_\theta = 0.086$, which is of a similar magnitude as the parabolic γ or η band. These findings

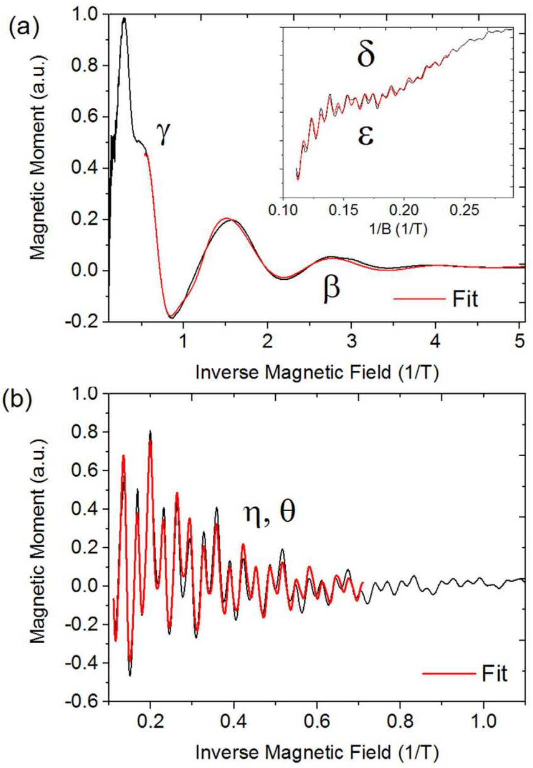

Figure 2. Fits of Eq. 1 to the raw data at 2.5 K for (**a**) k_x and k_y and (**b**) k_z. The full formula including all frequencies is always fitted; however, the fitting interval in 1/B is adjusted to a smaller region as shown in the graphs.

	F (T)	Phase $\Gamma + \Delta$	m^* (m_0)	A_{Fermi} (10^{-5} Å^{-2})	k (10^{-3} Å^{-1})	E (meV)	τ (10^{-12} s)	μ (cm^2/Vs)
α	0.16							
β	0.8	0.48(1)	0.048	7.64	4.93	3.74	0.73	25800
γ	2.5	0.19(5)	0.110	23.9	8.72	2.62	0.42	6700
δ	31.7	—	0.183	303	31.0	39.7	0.33	3200
ε	137.6	0.24(7)	0.255	1314	64.7	62.4	0.30	2100
ζ	0.98							
η	6.6	0.15(0)	0.086	63.0	14.2	8.93	0.36	7400
θ	31.25	0.54(5)	0.086	298	30.8	42.2	0.37	7600

Table 1. α to ε displays [100] and [010] or k_x and k_y, whereas ζ to θ displays [001] or k_z. A discussion of the errors can be found in the supporting information. The columns correspond to the oscillation frequency F, phase $\Gamma + \Delta$, effective mass m^*, size of the Fermi surface A_{Fermi}, corresponding k-vectors, energy distance from the Fermi level E, scattering lifetime τ and mobility μ. Note that $\Gamma + \Delta$ is the value of the phase extracted from the fits to Equation (1) and $\Delta = \pm 1/8$ has not been added in either direction yet.

may show that deriving conclusions about the existence of Weyl points simply from the Berry phase may not be sufficient, especially because the additional phase shift $\Delta = \pm 1/8$ allows for additional freedom.

The Dingle temperature $T_D = \hbar / 2\pi k_B \tau$ is inversely proportional to the carrier lifetime τ and mobility $\mu = e\tau/m^*$[23]. For $T = 2.5$ K, the field-dependent damping of the dHvA amplitude (A) is known from the fit procedure of the raw M vs. $1/B$-data to Eq. (1).

$$e^{-d_i \frac{1}{B}} = e^{-\chi T_D \frac{1}{B}} \tag{3}$$

The Dingle temperature, carrier lifetime and mobility are summarized in Table 1. Similar to the effective- mass evaluation, we find a significantly larger mobility for β than for all other bands, which further indicates that it may indeed be part of the Weyl pocket. When evaluated individually for each band, the mobility of β is two orders of magnitude smaller than reported by Shekhar *et al.* and Wang *et al.* from Hall measurements[5,7]. By determining the mobilities from Hall measurements, one imposes a one-carrier and one-channel model, which may explain a

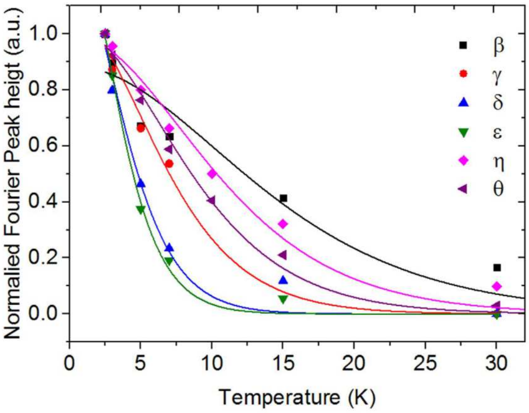

Figure 3. Best fits to the T-dependent LKS plots for all bands. There is a slight mismatch between the points and the fit at higher temperatures due to noise in the FFT data, which can lead to the determination of slightly lower effective masses than those in reality, particularly in ε and θ (blue and green graphs). Note that the formula only weakly depends on the values for higher temperatures, and the standard errors from the fitting procedure are on the order of 5%. From the quantization condition $\hbar\omega_c \geq k_B T$, we expect oscillations from Weyl-pocket bands and consequently lower effective masses to sustain at higher T, as shown for the β band[7].

significant deviation, particularly because NbP shows a notably large magneto resistance. This magneto resistance results from the electron-hole-resonance, which significantly affects any type of electric transport.

In the parabolic case, the energy distance of the Fermi level is calculated by $E = \frac{(\hbar k)^2}{2m^*}$ as summarized in Table 1 (Dirac case lacks the factor 1/2). As expected, the Dirac β-band lies very close to the Fermi energy (3.74 meV), whereas the energy distance of θ is unexpectedly large (42.2 meV). The band structure calculations predict two Weyl pockets: one approximately 5 meV above the Fermi energy and another 57 meV below[17]. The latter does not contribute to the conduction. Considering the Berry phase, low effective mass and close proximity to the Fermi energy, we can safely assign β to the first Weyl pocket. Thus, we reinforce the theoretical predictions that a slight shift of the Fermi level towards the Weyl points may incur numerous exotic effects[17]. New experiments on the electric transport in structured NbP thin films are in preparation. The finding of nontriviality for the θ-Band raises an open question of whether the analysis of the Berry phase alone can strongly prove the existence of Weyl points.

Conclusion and Outlook. In summary, we analyse the bulk magnetometry of the Fermi surface of the Weyl semimetal NbP for the fundamental crystal orientations. We demonstrate that a fit of the raw data enables us to separate superposed oscillations. Low effective masses and nontrivial Berry phases are obtained for one band, which experimentally proves that a slight shift of the Fermi level activates the Weyl nodes in the electric transport of NbP. Simultaneously, we find evidence for parabolic bands with higher effective masses and zero Berry phase, which confirms that the low spin-orbit coupling strength enable the presence of both types of bands in NbP. We emphasize that a careful, individual assessment of each conduction band is important to correctly interpret the quantum oscillatory measurement data. Positioning the Fermi level as close as possible to the Weyl nodes is crucial in the ongoing experimental effort to characterize Weyl semimetals. For potential applications of Weyl semimetals in electric devices, a route to miniaturize the bulk crystals must be developed. We propose using tailored growth substrates in a crystal growth furnace or using a focused ion beam to shape the desired nanostructures. The effect of possible surface states will be of great interest, such as in thickness-dependent thin-film studies.

Methods

Polycrystalline NbP powder was synthesized in a direct reaction of Nb powder (99.9%) and red phosphorous pieces (99.999%) in an evacuated silica tube for 48 h at 800 °C. Single NbP crystals were grown from this powder in a chemical transport reaction with iodine as a transport agent. The source and sink were set to 950 °C and 850 °C, respectively. The VSM measurements were conducted in a *Quantum Design PPMS* cryostat with a VSM Option.

References

1. Lundgren, R., Laurell, P. & Fiete, G. A. Thermoelectric properties of Weyl and Dirac semimetals. *Phys. Rev. B* **90,** 165115 (2014).
2. Shekhar, C. *et al.* Large and unsaturated negative magnetoresistance induced by the chiral anomaly in the Weyl semimetal TaP. *preprint at arXiv:1506.06577* (2015).
3. Wan, X., Turner, A. M., Vishwanath, A. & Savrasov, S. Y. Topological semimetal and Fermi-arc surface states in the electronic structure of pyrochlore iridates. *Phys. Rev. B* **83,** 205101 (2011).
4. Parameswaran, S. A., Grover, T., Abanin, D. A., Pesin, D. A. & Vishwanath, A. Probing the Chiral Anomaly with Nonlocal Transport in Three-Dimensional Topological Semimetals. *Phys. Rev. X* **4,** 031035 (2014).
5. Shekhar, C. *et al.* Extremely large magnetoresistance and ultrahigh mobility in the topological Weyl semimetal candidate NbP. *Nat. Phys.* **11,** 645−+ (2015).

6. Weng, H., Fang, C., Fang, Z., Bernevig, B. A. & Dai, X. Weyl Semimetal Phase in Noncentrosymmetric Transition-Metal Monophosphides. *Phys. Rev. X* **5,** 011029 (2015).
7. Wang, Z. *et al.* Helicity protected ultrahigh mobility Weyl fermions in NbP. *Phys. Rev. B* **93,** 121112 (2016).
8. Sun, Y., Wu, S.-C. & Yan, B. Topological surface states and Fermi arcs of the noncentrosymmetric Weyl semimetals TaAs, TaP, NbAs, and NbP. *Phys. Rev. B* **92,** 115428 (2015).
9. Ojanen, T. Helical Fermi arcs and surface states in time-reversal invariant Weyl semimetals. *Phys. Rev. X* **87,** 245112 (2013).
10. Huang, S.-M. *et al.* A Weyl Fermion semimetal with surface Fermi arcs in the transition metal monopnictide TaAs class. *Nat. Commun.* **6,** 7373 (2015).
11. Di-Fei, X. *et al.* Observation of Fermi Arcs in Non-Centrosymmetric Weyl Semi-Metal Candidate NbP. *Chin. Phys. Lett.* **32,** 11006 (2015).
12. Xu, N. *et al.* Observation of Weyl nodes and Fermi arcs in TaP. *Nat. Commun.* **7** (2016).
13. Xu, S.-Y. *et al.* Discovery of a Weyl fermion state with Fermi arcs in niobium arsenide. *Nat. Phys.* **11,** 748−+ (2015).
14. Xu, S. Y. *et al.* TOPOLOGICAL MATTER Discovery of a Weyl fermion semimetal and topological Fermi arcs. *Science* **349,** 613–617 (2015).
15. Lv, B. Q. *et al.* Experimental Discovery of Weyl Semimetal TaAs. *Phys. Rev. X* **5,** 031013 (2015).
16. Ali, M. N. *et al.* Large, non-saturating magnetoresistance in WTe2. *Nature* **514,** 205 (2014).
17. Klotz, J. *et al.* Quantum oscillations and the Fermi surface topology of the Weyl semimetal NbP. *Phys. Rev. B* **93,** 121105 (2016).
18. Xu, J. *et al.* Crystal structure, electrical transport, and magnetic properties of niobium monophosphide. *Inorg. Chem.* **35,** 845–849 (1996).
19. Jalan, B., Stemmer, S., Mack, S. & Allen, S. J. Two-dimensional electron gas in delta-doped SrTiO3. *Phys. Rev. B* **82,** 081103 (2010).
20. Moetakef, P. *et al.* Quantum oscillations from a two-dimensional electron gas at a Mott/band insulator interface. *Appl. Phys. Lett.* **101,** 151604 (2012).
21. Tian, M. *et al.* Dual evidence of surface Dirac states in thin cylindrical topological insulator Bi2Te3 nanowires. *Sci. Rep.* **3,** 1212 (2013).
22. Hu, J. *et al.* pi Berry phase and Zeeman splitting of Weyl semimetal TaP. *Sci. Rep.* **6,** 18674–18674 (2016).
23. Shoenberg, D. *Magnetic Oscillations in metals.* Cambridge University Press, Cambridge (1984).
24. Murakawa, H. *et al.* Detection of Berry's Phase in a Bulk Rashba Semiconductor. *Science* **342,** 1490–1493 (2013).
25. Luk'yanchuk, I. A. & Kopelevich, Y. Phase analysis of quantum oscillations in graphite. *Phys. Rev. Lett.* **93,** 166402 (2004).
26. Pariari, A., Dutta, P. & Mandal, P. Probing the Fermi surface of three-dimensional Dirac semimetal Cd3As2 through the de Haas-van Alphen technique. *Phys. Rev. B* **91,** 155139 (2015).
27. Gooth, J., Hamdou, B., Dorn, A., Zierold, R. & Nielsch, K. Resolving the Dirac cone on the surface of Bi2Te3 topological insulator nanowires by field-effect measurements. *Appl. Phys. Lett.* **104,** 243115 (2014).
28. Hamdou, B., Gooth, J., Dorn, A., Pippel, E. & Nielsch, K. Surface state dominated transport in topological insulator Bi2Te3 nanowires. *Appl. Phys. Lett.* **103,** 193107 (2013).
29. Xiang, F.-X., Veldhorst, M., Dou, S.-X. & Wangs, X.-L. Multiple Fermi pockets revealed by Shubnikov-de Haas oscillations in WTe2. *preprint at arXiv:1504.01460* (2015).

Acknowledgements

We would like to thank Prof. Wolfgang Hansen for the useful discussion.

Author Contributions

P.S. and J.G. conducted the measurements. J.G., S.B., R.Z., C.W., A.N., H.R. and B.Y. assisted in data evaluation, C.S. grew the samples. P.S. wrote the manuscript, and B.Y. wrote parts of the introduction. J.G., C.F. and K.N. conceived the study, supervised the project and assisted in data evaluation and manuscript finalization. All authors significantly contributed to the scientific discussion during data evaluation and manuscript preparation. All authors conducted a final proof reading.

Additional Information

Supplementary information accompanies this paper at http://www.nature.com/srep

Competing financial interests: The authors declare no competing financial interests.

How to cite this article: Sergelius, P. *et al.* Berry phase and band structure analysis of the Weyl semimetal NbP. *Sci. Rep.* **6**, 33859; doi: 10.1038/srep33859 (2016).

This work is licensed under a Creative Commons Attribution 4.0 International License. The images or other third party material in this article are included in the article's Creative Commons license, unless indicated otherwise in the credit line; if the material is not included under the Creative Commons license, users will need to obtain permission from the license holder to reproduce the material. To view a copy of this license, visit http://creativecommons.org/licenses/by/4.0/

© The Author(s) 2016

VI

Chiral magnetoresistance in the Weyl semimetal NbP

Anna Corinna Niemann, Johannes Gooth, Shu-Chun Wu, Svenja Bäßler, Philip Sergelius, Ruben Hühne, Bernd Rellinghaus, Chandra Shekhar, Vicky Süß, Marcus Schmidt, Claudia Felser, Binghai Yan & Kornelius Nielsch

Reprinted from *Scientific Reports* **7**, 43394 (2017)
Copyright 2017 Springer Nature Publishing AG.
License: Creative Commons Attribution 4.0 International (CC BY 4.0).

Author Contributions:
J.G. conceived the original idea for the project. A.C.N. performed the electrical measurements with the help of J.G., S.B. and P.S., R.H. characterized the crystal structure. B.R. supervised the micro-ribbon definition and the compositional analysis. S.-C.W. and B.Y. calculated the band structure. V.S. and M.S. synthesized the single crystal samples. All authors analyzed the results. J.G. and A.C.N. wrote the manuscript with substantial contributions from all authors. C.F. and K.N. supervised the project.

www.nature.com/scientificreports

SCIENTIFIC REPORTS

OPEN

Chiral magnetoresistance in the Weyl semimetal NbP

Anna Corinna Niemann[1,2,*], Johannes Gooth[1,3,*], Shu-Chun Wu[4], Svenja Bäßler[1], Philip Sergelius[1], Ruben Hühne[2], Bernd Rellinghaus[2], Chandra Shekhar[4], Vicky Süß[4], Marcus Schmidt[4], Claudia Felser[4], Binghai Yan[4,5] & Kornelius Nielsch[1,2]

Received: 21 November 2016
Accepted: 20 January 2017
Published: 06 March 2017

NbP is a recently realized Weyl semimetal (WSM), hosting Weyl points through which conduction and valence bands cross linearly in the bulk and exotic Fermi arcs appear. The most intriguing transport phenomenon of a WSM is the chiral anomaly-induced negative magnetoresistance (NMR) in parallel electric and magnetic fields. In intrinsic NbP the Weyl points lie far from the Fermi energy, making chiral magneto-transport elusive. Here, we use Ga-doping to relocate the Fermi energy in NbP sufficiently close to the W2 Weyl points, for which the different Fermi surfaces are verified by resultant quantum oscillations. Consequently, we observe a NMR for parallel electric and magnetic fields, which is considered as a signature of the chiral anomaly in condensed-matter physics. The NMR survives up to room temperature, making NbP a versatile material platform for the development of Weyltronic applications.

Weyl semimetals[1–3] are a recently realized, new topological matter[4–7] in which conduction and valence bands touch linearly near the Fermi energy (E_F). Weyl states are closely related to the well-known Dirac states[8–11], where both time reversal and inversion symmetries are preserved. In contrast, Weyl states emerge when one of these symmetries is broken. The band touching points in a Weyl semimetal – so-called Weyl nodes – always come in spatially separated pairs of opposite chirality ($\chi = \pm 1$), as sketched in Fig. 1a, which distinguish them from Dirac semimetals having two degenerate Weyl nodes of opposite chirality that form one Dirac node. Therefore, exotic features of Weyl semimetals include Fermi arcs, which connect two Weyl nodes of opposite chirality. This occurs even in the absence of an external magnetic field, which would be required for the realization of Fermi arcs in Dirac semimetals.

For relativistic Weyl and Dirac fermions, chirality is, in principle, a strictly conserved quantum number, which gives the direction of the fermion spin relative to the direction of its linear momentum. Nevertheless, when these relativistic fermions are subjected to electromagnetic fields with parallel electric and magnetic field components ($E||B$), the gauge invariance also has to be taken into account, and a breakdown of chiral symmetry occurs. The physical origin of this phenomenon lies in the splitting of the band structure into Landau levels in the presence of a magnetic field. In this scenario, only the zeroth Landau level of the Weyl band exhibits uni-directional fermion velocity, forward or backward along the magnetic field direction depending on its chirality. Without an additional electric field, the forward and backward moving zeroth Landau levels are equally filled; however, applying $E||B$ leads to chiral charge pumping between the two branches, with a flow rate that is proportional to $E \cdot B$. The electrons are forced to move – for example – in the forward direction, and consequently, the forward moving zeroth Landau level is filled more than the backward moving one. Such breaking of the chiral symmetry is referred to as the Adler-Bell-Jackiw or chiral anomaly[12,13]. In electrical transport measurements this anomaly leads to an additional topological current in parallel to the aligned electric and magnetic fields, decreasing the resistance of a Weyl semimetal with increasing magnetic field. Such a negative magnetoresistance (NMR) is considered to be a strong signature of broken chiral symmetry in condensed matter systems[14,15]. In the limit of weak B, Son and Spivak showed, in fact, that the resistance - in a condensed matter system with broken chiral symmetry and $E||B$ - is inverse proportional to the squared magnetic field ($R \sim 1/B^2$)[16]. NMR related to broken chirality has already

[1]Institute of Nanostructure and Solid State Physics, Universität Hamburg, Jungiusstraße 11, 20355 Hamburg, Germany. [2]Leibniz Institute for Solid State and Materials Research Dresden, Institute for Metallic Materials, Helmholtzstraße 20, 01069 Dresden, Germany. [3]IBM Research-Zurich, Säumerstrasse 4, 8803 Rüschlikon, Switzerland. [4]Max Planck Institute for Chemical Physics of Solids, Nöthnitzer Straße 40, 01187 Dresden, Germany. [5]Max Planck Institute for Physics of Complex Systems, Nöthnitzer Straße 38, 01187 Dresden, Germany. *These authors contributed equally to this work. Correspondence and requests for materials should be addressed to A.C.N. (email: aniemann@physnet.uni-hamburg.de)

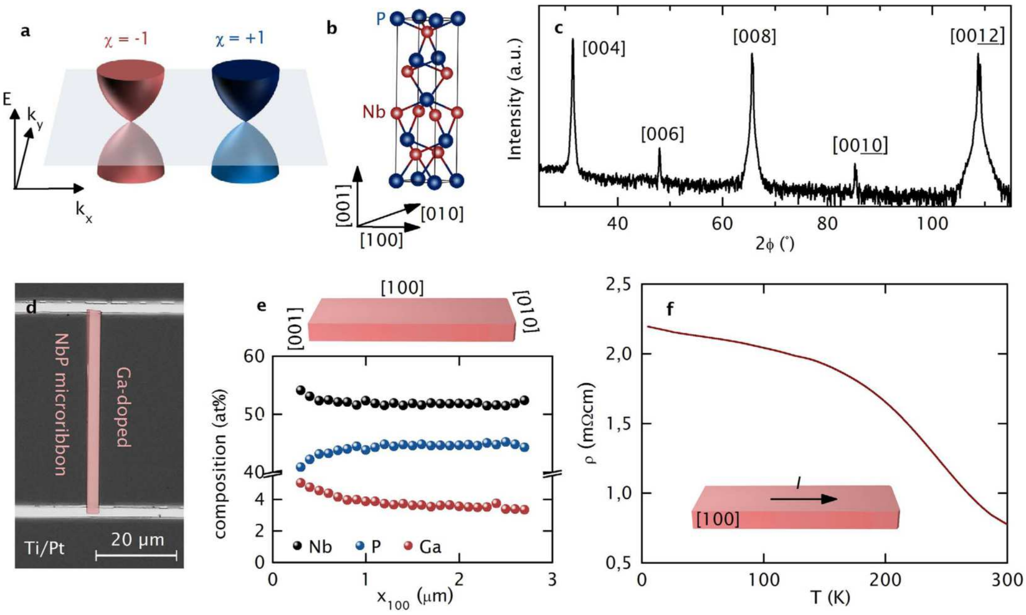

Figure 1. Topological semimetal NbP micro-ribbon device. (**a**) Sketch of a Weyl semimetal, represented as two spatially separated, massless Weyl nodes with distinct chiralities $\chi = -1$ (red cone) and $+1$ (blue cone). (**b**) The non-centrosymmetric crystal structure in a tetragonal lattice (space group I_41md) of NbP and (**c**) the XRD spectrum with a logarithmic intensity scale of the bulk NbP measured at room temperature. (**d**) Optical micrograph of the NbP micro-ribbon, which has been defined by Ga-FIB. (**e**) SEM-EDX data of the first 3 µm from the left sample edge along the [100] direction of the NbP micro-ribbon reveals an average 53% Nb, 45% P and 2% Ga composition. (**f**) Plot of the resistivity ρ versus temperature T.

been reported for Dirac semimetals such as Cd_3As_2 and Na_3Bi and the Weyl metals TaAs, NbAs, Zn-doped NbP and the predicted type-II Weyl semimetal WTe_2[17–23]. In contrast, NMR in TaP has been related to the effect of current jetting[24].

For TaAs-family compounds, which are recently discovered inversion-breaking Weyl semimetals[4–6,25–28], two groups of Weyl points were found and classified into four pairs in the $k_z = 0$ plane (called W1) and eight pairs off the $k_z = 0$ plane (called W2) in the first Brillouin zone[29]. NbP is the lightest member of the TaAs family. It has a non-centrosymmetric crystal structure in a tetragonal lattice (space group I_41md), as sketched in Fig. 1b. Intrinsic NbP has been intensively studied by magneto-transport[29] and quantum oscillation measurements[30,31]. Ultrahigh mobility ($5 \cdot 10^6\,\mathrm{cm^2\,V^{-1}\,s^{-1}}$ at 9 T and 1.85 K)[29] and huge magnetoresistance ($8.5 \cdot 10^5$% at 9 T and 1.85 K) attributed to electron-hole resonance[32] have been observed[29]. Quantum oscillation measurements combined with *ab initio* calculations revealed that the W1 and W2 Weyl nodes are located −57 meV and +5 meV away from the intrinsic Fermi level (E_{F0}) of the pristine NbP sample without intentional doping[30]. In contrast, Wang *et al.* reported that they were able to activate the W1 Weyl cones in Zn-doped NbP for chiral anomaly. For their samples, the W1 Weyl points are 15 meV above the Fermi level[22].

For the magneto-transport measurements, elongated, Ga-doped NbP micro-ribbons of 50 µm × 2.46 µm × 526 nm were prepared by Ga focused ion beam (FIB) etching into the bulk sample. The XRD pattern of the (001) surface of the NbP bulk sample, as given in Fig. 1c, shows the good quality of the sample with the full-width half-maximum being no larger than 0.15 degrees. The NbP micro-ribbon was extracted from the bulk sample using a micromanipulator and electrically contacted using laser lithography, followed by a Ti/Pt metallization process. A micrograph of the electrically contacted sample can be seen in Fig. 1d. The high aspect ratio of the micro-ribbon with contact lines across the full width of the sample is chosen to supress current jetting and to ensure a homogenous *E*-field distribution, respectively[33]. The Ga concentration on the surface of the micro-ribbon (analysed by scanning electron microscopy energy dispersive x-ray spectroscopy (SEM-EDX)) revealed an average composition of 53% Nb, 45% P and 2% Ga with a slight Ga and Nb increase and a P decrease at the edge of the sample (Fig. 1e). Ga etching leads to a few nanometer-thick surface defect layer as commonly introduced by this fabrication technique and an exponentially decaying Ga-concentration deeper in the bulk of the micro-ribbon[34]. However, we note that, as stated by Moll *et al.*[34], such an amorphous surface layer has no influence on the topological properties of the ribbon. Magneto-transport measurements from cryogenic temperatures up to room temperature and with applied magnetic fields up to ±9 T were performed with the current (100 nA) along the [100] axis and the magnetic field varying from the [100] axis (0°) to the [001] axis (90°).

At room temperature, the zero-field resistivity of the Ga-doped NbP micro-ribbon is enhanced by a factor of 15 compared to the intrinsic NbP bulk sample. A non-metallic resistivity ρ versus temperature T profile is observed (Fig. 1f). Lowering E_F in Na_3Bi and Cd_2As_3 to observe the NMR has previously resulted in a similar

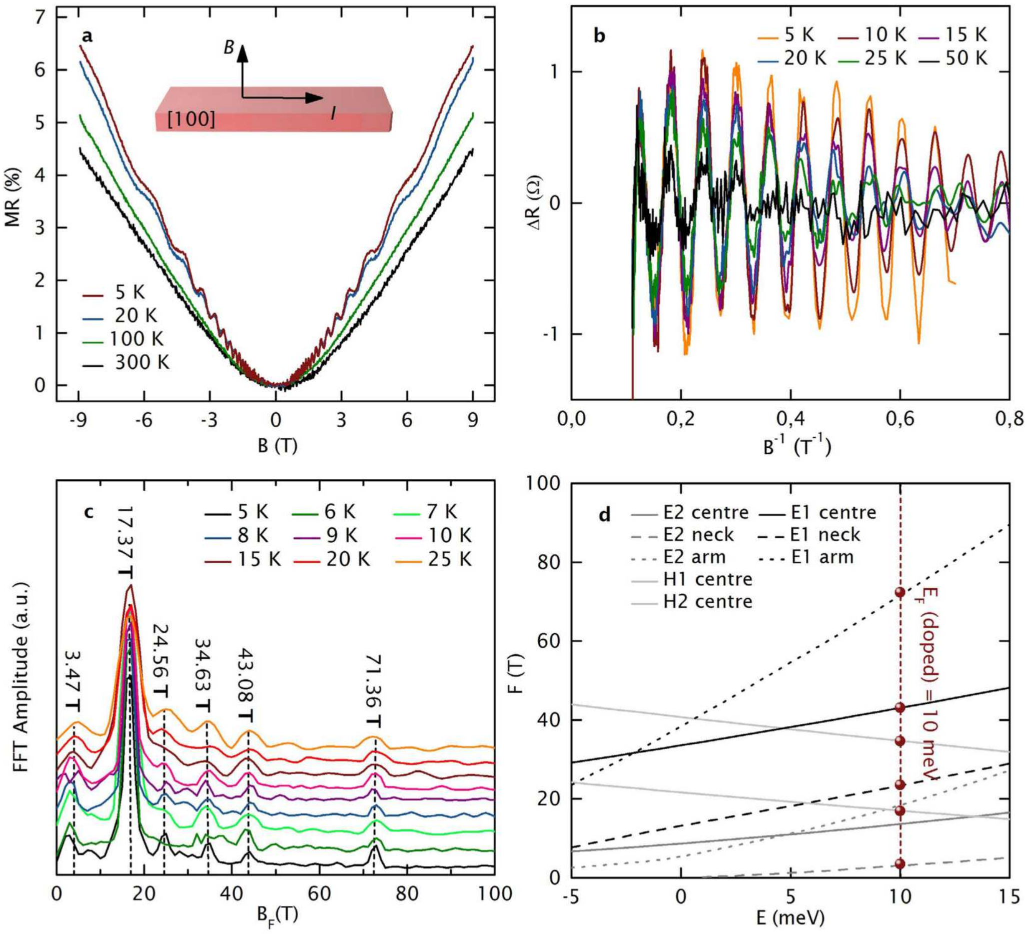

Figure 2. Transverse magneto-transport and SdH oscillation analysis. (**a**) The temperature-dependent, transverse MR reveals non-saturated linearity at high magnetic fields across the entire T range from 5 K–300 K and SdH oscillations below 75 K. (**b**) After the subtraction of a non-oscillatory background, the SdH oscillations show a clear periodicity in B^{-1}. (**c**) FFT spectra from 5 K to 25 K reveal six fundamental SdH frequencies at $F_1 = 3.47$ T, $F_2 = 17.37$ T, $F_3 = 24.56$ T, $F_4 = 34.63$ T, $F_5 = 43.08$ T and $F_6 = 71.36$ T. (**d**) SdH oscillation frequencies F from *ab initio* simulations are shown as a function of the energy E relative to the intrinsic Fermi level E_{F0}. Two electron pockets E1 and E2, which each have three extremal obits (neck, arm and centre), and two hole pockets H1 and H2 with one extremal orbit are resolved. Matching our experimental data (red dots) to the simulations revealed that E_F(doped) is 10 meV above E_{F0} and consequently 5 meV above the W2 nodes.

$\rho(T)$, which was ascribed to thermal activation of holes across the gapless energy band due to the close vicinity of the Fermi level to the neutrality point[17,19].

A quadratic low-field MR ($MR = (\rho(B) - \rho(0))/\rho(B) \cdot 100\%$, with $\rho(0)$ for zero magnetic field and $\rho(B)$ for an applied magnetic field B) and an unsaturated linear high-field magnetoresistance MR are observed in transverse magnetic fields (Fig. 2a). The MR at high fields is attributed to Abrikosov's linear quantum MR[35], resulting from thermal excitation into the lowest Landau level, which is consistent with the non-metallic $\rho(T)$. Linearity induced by strong disorder[36] is rather unlikely due to the high crystalline quality of our samples. Ultrahigh MR, as observed in intrinsic NbP, is not obtained in our samples (MR(300 K) = 4.46% to MR(5 K) = 6.42%), which probably originates from the absence of electron-hole resonance[32] due to a Ga doping-induced Fermi level shift.

Our interpretation is supported by the analysis of strong Shubnikov-de Haas (SdH) oscillations (Fig. 2a), observed below 50 K. After subtracting a smooth background (Fig. 2b), Fast Fourier Transformation (FFT) (Fig. 2c) reveals six fundamental SdH oscillation frequencies - $F_1 = 3.47$ T, $F_2 = 17.37$ T, $F_3 = 24.56$ T, $F_4 = 34.63$ T, $F_5 = 43.08$ T and $F_6 = 71.36$ T - which are correlated with the corresponding electron and hole pockets by performing band structure calculations. NbP exhibits two electron and two hole pockets (E1, E2, H1 and H2) at the Fermi surface[30]. For applied magnetic fields along the [001] axis, hole pockets show one extremal orbit, while electron pockets exhibit 3 extremal orbits (labelled as neck, centre and arm in Fig. 2d). From the best fits of the experimentally observed SdH oscillation frequencies to the F versus E plot obtained from band structure calculations, F_1 was identified with the E_2 electron pocket, F_2 with the H_2 hole pocket, F_3, F_5 and F_6 with the E_1 electron pocket, and F_4 with the H_1 hole pocket. Accordingly, the Fermi energy in our Ga-doped NbP micro-ribbons is shifted to E_F (doped) = +10 meV above the intrinsic Fermi level E_{F0} (compare in Fig. 2d). While the W2 points

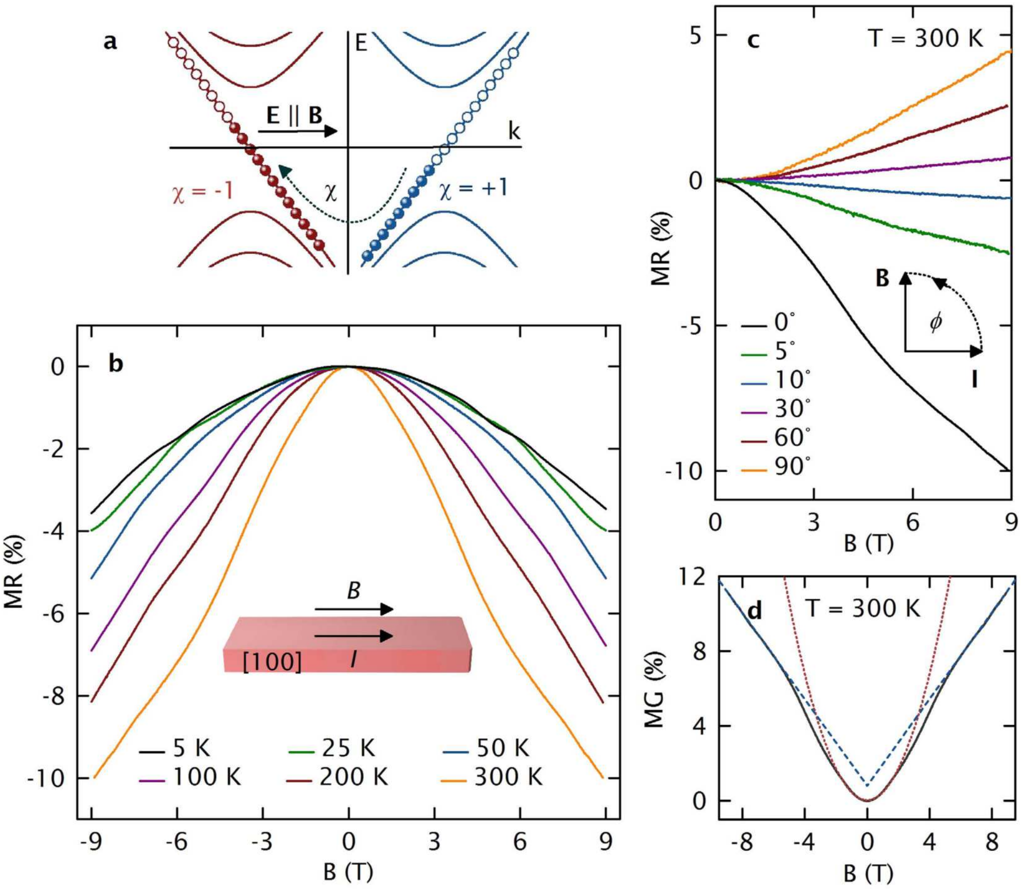

Figure 3. Longitudinal magnetotransport – Chiral anomaly-induced negative magnetoresistance. (**a**) Energy spectrum of left- and right-handed chirality fermions (red and blue, respectively) in parallel applied electric and magnetic fields. In the zeroth Landau level, left-handed particles and right-handed antiparticles have been produced, leading to an additional topological current. (**b**) Temperature dependence of the NMR in parallel magnetic fields. (**c**) Angle-dependent MR at 300 K. (**d**) Positive magneto-conductance at 300 K reveals a parabolic low-field regime that evolves into a linear regime under high magnetic fields.

of intrinsic NbP are 5 meV above E_{F0}, which prevents these connected W2 points from exhibiting NMR[30], in the doped NbP, the Weyl points 5 meV below E_F are truly separated, which makes them active for chiral anomaly. Given the theoretical position of the Fermi level, oscillation frequencies at 14.02 T and 20.04 T should also be experimentally observable. However, the broad peak at 17.37 T does not allow for sufficient resolution. From the position of the Fermi level, carrier concentrations of $n_h = 1.95 \cdot 10^{19}\,\mathrm{cm}^{-3}$ and $n_e = 4.19 \cdot 10^{19}\,\mathrm{cm}^{-3}$ were calculated such that electron-hole resonance and therefore ultrahigh MR are suppressed. Furthermore, for the most prominent SdH frequency ($F_2 = 17.37$), we obtain a high mobility of $7.1 \cdot 10^5\,\mathrm{cm}^2/\mathrm{Vs}$ at 5 K and a relatively low effective mass $m_c = 0.064\,m_0$ from the magnetic field- and temperature-damping of the oscillations[37].

Tilting the magnetic field parallel to the applied current, we observe a distinct NMR, which we explain via the chiral anomaly, (Fig. 3a,b). Based on the above analysis, the W2 points should be active for the chiral anomaly along the [100] axis. The NMR is very robust against temperature enhancement, as it is observed between 5 and 300 K. Although of the same order of magnitude, in contrast to the positive MR in transverse magnetic fields, the longitudinal NMR at 300 K is enhanced by a factor of 2.9 compared to the NMR at 25 K. We attribute this observation to the ionization of Ga, which increases at elevated temperatures, pushing the Fermi level even closer to the W2 points. Angle-dependent MR measurements (Fig. 3c) show that the observed NMR is sensitive to the angle (ϕ) between B and I, and can be well traced by a $\cos^2(\phi)$-term at low fields, underscoring our assignment to chiral asymmetry. Moreover, at low magnetic fields the inverse of the NMR, the longitudinal positive magnetoconductance MC (Fig. 3d), is well described by B^2- function, in accordance with the prediction of Son and Spivak[16]. At higher fields, however, the longitudinal MC becomes linear. This observation is in agreement with the theoretical description of a transition from a multi-Landau level chiral anomaly to the limit, where only one Landau level is occupied[35]. We note that the temperature broadening of the Fermi distribution will activate charge carriers that do not contribute to the NMR. Even at low temperatures likely several band as indicated in Fig. 2(d) will contribute to the transport in parallel to the Weyl cones at zero magnetic field. However, up to the highest temperature of

300 K measured here, we observe that the chiral anomaly seems to dominate the B-dependence of R, which could be interesting for Weyltronic applications[28].

In conclusion, we have provided experimental evidence of chiral anomaly in Ga-doped NbP, which originates from the W2 cones. Our analysis is based on magneto-transport studies of Ga-doped NbP micro-ribbons combined with band structure simulations. The observation of a non-metallic temperature dependence of the resistivity and Abrikosov's linear quantum MR, as well as the evaluation of the observed SdH oscillations, revealed that electron doping shifts the Fermi level in NbP as close as 5 meV above the W2 points, making them active for chiral anomaly. In fact, with parallel magnetic and electric fields, we observe a negative magnetoresistance, whose temperature, magnetic field and angle dependences are consistent with broken chiral symmetry. We believe that this work can pave the way to systematically accessing the unique properties of massless Weyl fermions near the Weyl nodes by material engineering, providing a versatile platform for the development of Weyltronic components.

Methods

Crystal growth. Polycrystalline NbP powder was synthesized by a direct reaction of niobium (Chempur 99.9%) and red phosphorus (Heraeus 99.999%) which were kept in an evacuated fused silica tube ($t = 48$ h, $T = 800$ °C). Subsequently, high-quality single crystals of NbP were grown from this microcrystalline powder via a chemical vapour transport reaction in a temperature gradient starting from 850 °C (source) to 950 °C (sink) using iodine (Alfa Aesar 99.998%)[38] with a concentration of 13.5 mgcm^{-3} as a transport agent.

Crystal structure analysis. The XRD measurements were performed in a Panlaytical X'Pert four-circle diffractometer using Cu-K$_\alpha$ radiation. The sample was oriented with the help of the Euler cradle in the device. Afterwards, a $\theta - 2\theta$ was taken using a high-resolution optics with a Goebel mirror in the primary beam path and narrow soller slits on the detector side.

Definition of the micro-ribbon. From the NbP bulk sample, a 50 μm × 2.46 μm × 526 nm large micro-ribbon was cut with a dual-beam focused ion beam system (FIB) of the type FEI Helios 600i using 30 keV Ga$^+$ ions ($I = 65$ nA $- 80$ pA). In order to avoid electrostatic repulsion, the as-cut NbP micro-ribbon was picked up *ex-situ* with a glass needle and transferred to a glass substrate.

Compositional analysis of the micro-ribbon. The compositional analysis was carried out *in-situ* in the FIB by energy dispersive X-ray analysis (EDX) using 15 keV electrons.

Definition of the electrical contacts. The NbP micro-ribbon placed on a 150 μm thick glass substrate was covered with a double layer of photo resist, composed of a layer lift-off resist covered with a layer of positive resist (Micro Chem LOR 3B and maP-1205). The electrical contact structure was defined as shown in Fig. 1d using a laser lithography system (Heidelberg Instruments μpg 101). Afterwards, the exposed parts of the photoresist were developed (developer ma-D331, $t = 45$ s, $T = 20$ °C) until an undercut structure was observed at the edges of the developed parts, which ensures a clean removal of the metal layer in the lift-off process. Before the metallization, the NbP contact areas were cleaned by Ar etching ($t = 5$ min, $p = 7.4 \times 10^{-3}$ Torr, flow$_{\text{Ar}} = 15$ sccm and $P = 20$ W) and subsequently 10 nm of Ti and 500 nm of Pt were sputtered without breaking the vacuum. In the lift-off process (Remover 1165, $T = 80$ °C, $t = 1$ h) residual metal parts were removed.

Transport measurements. Transport measurements were performed in a cryostatic system (PPMS DynaCool from Quantum Design) equipped with a 9 T electromagnet. The resistance measurements ($I_{\text{ac}} = 100$ nA, $f = 189$ Hz) were performed on a rotary sample holder at temperatures between 5 K and 300 K and at a nitrogen pressure of 4×10^{-3} mbar.

Band structure calculations. The ab initio band structure calculations were performed within the framework of density functional theory (DFT), which are implemented in the Vienna ab initio simulation package[39]. The core electrons were represented by the projector-augmented-wave potential. Generalized gradient approximation (GGA) is employed for the exchange correlation functional. Maximally localized Wannier functions (MLWFs) were used to interpolate the bulk Fermi surface[40].

References

1. Volovik, G. E. *The Universe in a Helium Droplet*. (Clarendon Press, 2003).
2. Wan, X. *et al.* Topological semimetal and Fermi-arc surface states in the electronic structure of pyrochlore iridates. *Phys. Rev. B* **83,** 205101 (2011).
3. Balents, L. Weyl electrons kiss. *Physics (College. Park. Md).* **4,** 36 (2011).
4. Lv, B. Q. *et al.* Experimental discovery of Weyl semimetal TaAs. *Phys. Rev. X* **5,** 31013 (2015).
5. Xu, S.-Y. *et al.* Discovery of a Weyl Fermion semimetal and topological Fermi arcs. *Science* **349,** 6248 (2015).
6. Yang, L. X. *et al.* Weyl semimetal phase in the non-centrosymmetric compound TaAs. *Nat. Phys.* **11,** 728–732 (2015).
7. Belopolski, I. *et al.* Discovery of a new type of topological Weyl fermion semimetal state in $Mo_xW_{1-x}Te_2$. *Nat. Commun.* **7,** 13643 (2016).
8. Young, S. M. *et al.* Dirac semimetal in three dimensions. *Phys. Rev. Lett.* **108,** 140405 (2012).
9. Borisenko, S. *et al.* Experimental realization of a three-dimensional Dirac semimetal. *Phys. Rev. Lett.* **113,** 027603 (2014).
10. Schoop, L. M. *et al.* Dirac Cone Protected by Non-Symmorphic Symmetry and 3D Dirac Line Node in ZrSiS. *Nat. Commun.* **7,** 11696 (2015).
11. Wang, X. *et al.* Evidence of Both Surface and Bulk Dirac Bands and Anisotropic Nonsaturating Magnetoresistance in ZrSiS. *Adv. Electron. Mater.* **2,** 1600228 (2016).
12. Adler, S. L. Axial-vector vertex in spinor electrodynamics. *Phys. Rev*. **177,** 5 (1969).
13. Bell, J. S. & Jackiw, R. A PCAC puzzle: $\pi^0 \rightarrow \gamma\gamma$ in the σ-model. *Nuovo Cim.* **A60,** 4 (1969).
14. Nielsen, H. B. & Ninomiya, M. The Adler-Bell-Jackiw anomaly and Weyl fermions in a crystal. *Phys. Lett. B* **130,** 6 (1983).

15. Burkov, A. Chiral anomaly without relativity. *Science* **350,** 6259 (2015).
16. Son, D. T. & Spivak, B. Z. Chiral anomaly and classical negative magnetoresistance of Weyl metals. *Phys. Rev. B* **88,** 104412 (2013).
17. Li, H. *et al.* Negative Magnetoresistance in Dirac Semimetal Cd_3As_2. *Nat. Commun.* **7,** 10301 (2015).
18. Li, C. *et al.* Giant negative magnetoresistance induced by the chiral anomaly in individual Cd_3As_2 nanowires. *Nat. Commun.* **6,** 10137 (2015).
19. Xiong, J. *et al.* Evidence for the chiral anomaly in the Dirac semimetal Na_3Bi. *Science* **350,** 6259 (2015).
20. Huang, X. *et al.* Observation of the chiral-anomaly-induced negative magnetoresistance: In 3D Weyl semimetal TaAs. *Phys. Rev. X* **5,** 031023 (2015).
21. Yang, X. *et al.* Chiral anomaly induced negative magnetoresistance in topological Weyl semimetal NbAs. arXiv: 1506.03190 (2015).
22. Wang, Z. *et al.* Helicity-protected ultrahigh mobility Weyl fermions in NbP. *Phys Rev. B* **93,** 121112(R) (2016).
23. Wang, Y. *et al.* Gate-Tunable Negative Longitudinal Magnetoresistance in the Predicted Type-II Weyl Semimetal WTe_2. *Nat. Commun.* **7,** 13142 (2016).
24. Arnold, F. *et al.* Negative magnetoresistance without well-defined chirality in the Weyl semimetal TaP. *Nat. Commun.* **7,** 11615 (2016).
25. Arnold, F. *et al.* Chiral Weyl Pockets and Fermi Surface Topology of the Weyl Semimetal TaAs. *Phys. Rev. Lett.* **117,** 146401 (2016).
26. Liu, Z. K. *et al.* Evolution of the Fermi surface of Weyl semimetals in the transition metal pnictide family. *Nat. Mater.* **15,** 4457 (2016).
27. Xu, N. *et al.* Observation of Weyl nodes and Fermi arcs in tantalum phosphide. *Nat. Comm.* **7,** 11006 (2015).
28. Xu, S.-Y. *et al.* Discovery of a Weyl fermion state with Fermi arcs in niobium arsenide. *Nat. Phys.* **11,** 3437 (2015).
29. Shekhar, C. *et al.* Extremely large magnetoresistance and ultrahigh mobility in the topological Weyl semimetal candidate NbP. *Nat. Phys.* **11,** 3372 (2015).
30. Klotz, J. *et al.* Quantum oscillations and the Fermi surface topology of the Weyl semimetal NbP. *Phys. Rev. B* **93,** 121105 (2016).
31. Sergelius, P. *et al.* Berry phase and band structure analysis of the Weyl semimetal NbP. *Sci. Rep.* **6,** 33859 (2016).
32. Ali, M. N. *et al.* Large, non-saturating magnetoresistance in WTe_2. *Nature* **514,** 13763 (2014).
33. Hirschberger, M. *et al.* The chiral anomaly and thermopower of Weyl fermions in the half-Heusler GdPtBi. *Nat. Mat*. 4684 (2016).
34. Moll, P. J. W. *et al.* Transport evidence for Fermi-arc-mediated chirality transfer in the Dirac semimetal Cd_3As_2. *Nature* **535,** 266–270 (2016).
35. Abrikosov, A. A. Quantum magnetoresistance. *Phys. Rev. B* **58,** 5 (1998).
36. Parish, M. M. & Littlewood, P. B. Non-saturating magnetoresistance in heavily disordered semiconductors. *Nature* **426,** 162–165 (2003).
37. Shoenberg, D. *Magnetic oscillations in metals*. (Cambridge University Press, 1984).
38. Martin, J. & Gruehn, R. Zum chemischen Transport vom Monophosphiden MP (M=Zr, Hf, Nb, Ta, Mo, W) und Diphosphiden MP2 (M=Ti, Zr, Hf). *Z. Krist.* **182,** 180–182 (1988).
39. Kresse, G. & Furthmüller, J. Efficient iterative schemes for ab initio total-energy calculations using a plane-wave basis set. *Phys. Rev. B* **54,** 11169–11186 (1996).
40. Mostofi, A. A. *et al.* wannier90: A tool for obtaining maximally-localised Wannier functions. *Comput. Phys. Commun.* **178,** 685–699 (2008).

Acknowledgements

The authors gratefully acknowledge the work of Tina Sturm and Almut Pöhl defining the NbP micro-ribbon and conducting the compositional analysis and Andy Thomas for helpful discussion. This work was financially supported by the Deutsche Forschungsgemeinschaft DFG via Project DFG-SFB 1143 and DFG-RSF-Project No. (NI 616/22-1) 'Influence of the topological states on the thermoelectric properties of Weyl-Semimetals' and by the ERC Advanced Grant No. (291472) 'Idea Heusler'.

Author Contributions

J.G. conceived the original idea for the project. A.C.N. performed the electrical measurements with the help of J.G., S.B. and P.S., R.H. characterized the crystal structure. B.R. supervised the micro-ribbon definition and the compositional analysis. S.-C.W. and B.Y. calculated the band structure. V.S. and M.S. synthesized the single crystal samples. All authors analysed the results. J.G. and A.C.N. wrote the manuscript with substantial contributions from all authors. C.F. and K.N. supervised the project.

Additional Information

Competing Interests: The authors declare no competing financial interests.

How to cite this article: Niemann, A. C. *et al.* Chiral magnetoresistance in the Weyl semimetal NbP. *Sci. Rep.* **7**, 43394; doi: 10.1038/srep43394 (2017).

Publisher's note: Springer Nature remains neutral with regard to jurisdictional claims in published maps and institutional affiliations.

This work is licensed under a Creative Commons Attribution 4.0 International License. The images or other third party material in this article are included in the article's Creative Commons license, unless indicated otherwise in the credit line; if the material is not included under the Creative Commons license, users will need to obtain permission from the license holder to reproduce the material. To view a copy of this license, visit http://creativecommons.org/licenses/by/4.0/

© The Author(s) 2017

VII

Experimental signatures of the mixed axial–gravitational anomaly in the Weyl semimetal NbP

Johannes Gooth, Anna C. Niemann, Tobias Meng, Adolfo G. Grushin, Karl Landsteiner, Bernd Gotsmann, Fabian Menges, Marcus Schmidt, Chandra Shekhar, Vicky Süß, Ruben Hühne, Bernd Rellinghaus, Claudia Felser, Binghai Yan & Kornelius Nielsch

Reprinted with permission from *Nature* **547**, 7663 (2017)

Copyright 2017, Springer Nature.

Author Contributions:

J.G. conceived the experiment. M.S., C.S. and V.S. synthesized the single-crystal bulk samples. R.H. characterized the crystal structure. B.R. supervised the micro-ribbon definition and the compositional analysis. A.C.N. fabricated the samples. J.G. carried out the thermoelectric transport measurements with the help of A.C.N. J.G., A.C.N., F.M., B.G., T.M. and A.G.G. analyzed the data. B.G., C.F., B.Y. and K.N. supervised the project. A.G.G., T.M. and K.L. provided the theoretical background for the work. All authors contributed to interpreting the data and writing the manuscript.

LETTER

doi:10.1038/nature23005

Experimental signatures of the mixed axial–gravitational anomaly in the Weyl semimetal NbP

Johannes Gooth[1,2], Anna C. Niemann[1,3], Tobias Meng[4], Adolfo G. Grushin[5], Karl Landsteiner[6], Bernd Gotsmann[2], Fabian Menges[2], Marcus Schmidt[7], Chandra Shekhar[7], Vicky Süß[7], Ruben Hühne[3], Bernd Rellinghaus[3], Claudia Felser[7], Binghai Yan[7,8] & Kornelius Nielsch[1,3]

The conservation laws, such as those of charge, energy and momentum, have a central role in physics. In some special cases, classical conservation laws are broken at the quantum level by quantum fluctuations, in which case the theory is said to have quantum anomalies[1]. One of the most prominent examples is the chiral anomaly[2,3], which involves massless chiral fermions. These particles have their spin, or internal angular momentum, aligned either parallel or antiparallel with their linear momentum, labelled as left and right chirality, respectively. In three spatial dimensions, the chiral anomaly is the breakdown (as a result of externally applied parallel electric and magnetic fields[4]) of the classical conservation law that dictates that the number of massless fermions of each chirality are separately conserved. The current that measures the difference between left- and right-handed particles is called the axial current and is not conserved at the quantum level. In addition, an underlying curved space-time provides a distinct contribution to a chiral imbalance, an effect known as the mixed axial–gravitational anomaly[1], but this anomaly has yet to be confirmed experimentally. However, the presence of a mixed gauge–gravitational anomaly has recently been tied to thermoelectrical transport in a magnetic field[5,6], even in flat space-time, suggesting that such types of mixed anomaly could be experimentally probed in condensed matter systems known as Weyl semimetals[7]. Here, using a temperature gradient, we observe experimentally a positive magneto-thermoelectric conductance in the Weyl semimetal niobium phosphide (NbP) for collinear temperature gradients and magnetic fields that vanishes in the ultra-quantum limit, when only a single Landau level is occupied. This observation is consistent with the presence of a mixed axial–gravitational anomaly, providing clear evidence for a theoretical concept that has so far eluded experimental detection.

Weyl semimetals are materials in which electrons behave as a type of massless relativistic particle known as a Weyl fermion. Massless chiral fermions exist where conductance and valence bands in these materials touch in isolated points, so-called Weyl nodes. At energies near these points the electrons are effectively described by the Weyl Hamiltonian[8,9], which implies that the energy of these Weyl fermions scales linearly with their momentum. Weyl nodes occur in pairs of opposite chirality[10] that, in the absence of additional symmetries, are topologically stable when they are separated in momentum space (Fig. 1a). Chiral Weyl fermions are subject to a chiral anomaly, which results in a strong positive magneto-conductance that can be detected experimentally[4,11]. Inspired by the pioneering studies of the chiral anomaly in pion physics[2,3], several research groups have recently reported on the observation of chiral-anomaly-induced positive longitudinal magneto-conductance in Na_3Bi (ref. 12), TaAs (ref. 13), NbP (ref. 14), GdPtBi (ref. 15), Cd_2As_3 (ref. 16), TaP (ref. 17) and RPtBi (ref. 18). Three-dimensional chiral fermions are theoretically predicted to also exhibit a mixed axial–gravitational anomaly[19,20]. In curved space-time, this anomaly contributes to the violation of the covariant conservation laws of the axial current, which are relevant to the chiral anomaly, and to the conservation law for the energy–momentum tensor[21]. The energy–momentum tensor encodes the density and flux of energy and momentum of a system. The mixed axial–gravitational anomaly has been suggested to be relevant to the hydrodynamic description of neutron stars[22], and to the chiral vortical effect in the context of quark–gluon plasmas[5]. However, a clear experimental signature has yet to be reported.

Although the flatness of space-time would imply that gravitational anomalies are irrelevant for condensed matter systems, it has been recently understood that the presence or absence of a positive magneto-thermoelectric conductance for Weyl fermions is tied to the presence or absence of a mixed axial–gravitational anomaly in flat space-time[5,6]. The connection between the mixed axial–gravitational anomaly and the observed positive magneto-thermoelectric conductance can be understood by a calculation based on the conservation laws for charge and energy, and the standard Kubo formalism for the conductivities (Methods). Because the Weyl semimetal lives in a flat space-time, the mixed axial–gravitational anomaly does not affect the conservation laws for charge and energy directly. An anomalous contribution to the energy current has nevertheless been identified in the Kubo formalism[22]. Inserting this contribution into the conservation laws and using a simple approximation for the relaxation time, we find that thermoelectric transport in flat space-time is explicitly modified as a result of the presence of the mixed axial–gravitational anomaly in the underlying field theory.

The connection between thermal transport and the mixed axial–gravitational anomaly is also apparent in a relativistic quantum field theory computation of transport properties[5] and in the hydrodynamic formalism of the effective chiral electron liquid[6]. In the latter approach, the presence of a mixed axial–gravitational anomaly modifies the thermodynamic constitutive relations of the current and energy–momentum tensor in terms of gradients of the relevant hydrodynamic variables: temperature, chemical potential and velocity[6]. These modifications can be viewed as the hydrodynamic equivalent of the anomalous contributions to the energy current identified in the Kubo formalism. Although the Kubo-based calculation (Methods) is thus qualitatively consistent with the hydrodynamic calculation[6], transport in current Weyl semimetal samples is not consistent with the hydrodynamic regime, which involves strong interactions and features fast energy–momentum relaxation between the nodes. The predicted positive magneto-thermoelectric conductance is also consistent with

[1]Institute of Nanostructure and Solid State Physics, Universität Hamburg, Jungiusstraße 11, 20355 Hamburg, Germany. [2]IBM Research -Zurich, Säumerstrasse 4, 8803 Rüschlikon, Switzerland. [3]Leibniz Institute for Solid State and Materials Research Dresden, Institute for Metallic Materials, Helmholtzstraße 20, 01069 Dresden, Germany. [4]Institute for Theoretical Physics, Technical University Dresden, Zellescher Weg 17, 01062 Dresden, Germany. [5]Department of Physics, University of California, Berkeley, California 94720, USA. [6]Instituto de Física Teórica UAM/CSIC, Nicolás Cabrera 13–15, Universidad Autónoma de Madrid, Cantoblanco, 28049 Madrid, Spain. [7]Max Planck Institute for Chemical Physics of Solids, Nöthnitzer Straße 40, 01187 Dresden, Germany. [8]Department of Condensed Matter Physics, Weizmann Institute of Science, 7610001 Rehovot, Israel.

© 2017 Macmillan Publishers Limited, part of Springer Nature. All rights reserved.

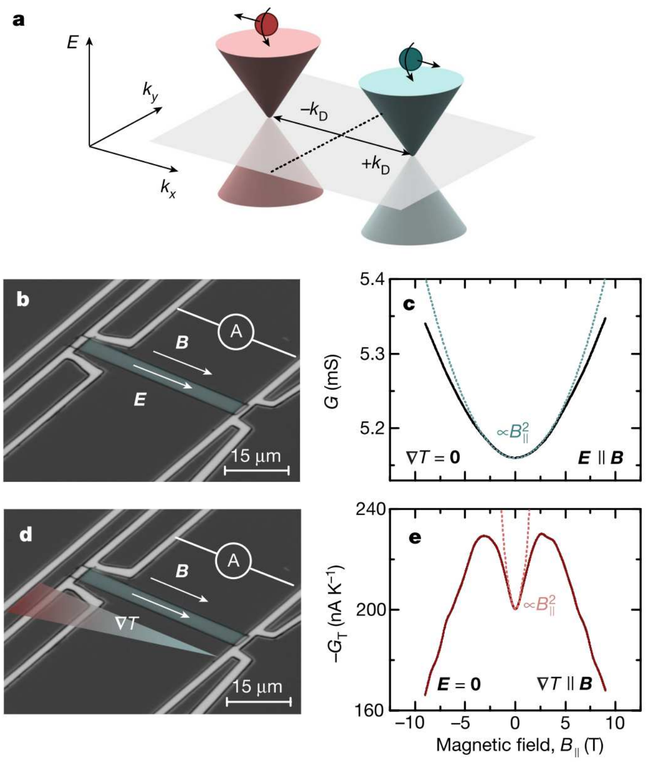

Figure 1 | Positive magneto-conductance $G(B_{\parallel})$ and magneto-thermoelectric conductance $G_T(B_{\parallel})$ in the Weyl semimetal NbP. **a**, Sketch of two Weyl cones with distinct chiralities $+\chi$ and $-\chi$, represented in green and red, respectively. E, k_x and k_y are the energy and the components of the momentum vector $\boldsymbol{k}$ in x and y directions, respectively. k_D denotes the distance of the chiral nodes from their centre point in momentum space. **b**, **c**, False-coloured optical micrographs of the devices used to measure the electrical conductance $G = J/E$ (**b**) and thermoelectric conductance $G_T = J/|\nabla T|$ (**c**). The red and the green ends of the colour gradient denote the hot and cold sides of the device, respectively. Four NbP micro-ribbons (green) were investigated, all showing similar results. The data for the first ribbon are presented here. **d**, **e**, $G(\boldsymbol{E} \parallel \boldsymbol{B})$ (**d**) and $-G_T(\nabla \boldsymbol{T} \parallel \boldsymbol{B})$ (**e**) as functions of the magnetic field $B_{\parallel}$ at a cryostat base temperature of $T = 25$ K (solid lines); the negative sign accounts for electron transport. The dotted lines show the predicted dependence ($\propto B_{\parallel}^2$).

the semi-classical approach based on the Boltzmann equation[23–26], which so far lacks a simple connection to the anomalous origin of this contribution. This consistency of different theoretical approaches illustrates that anomalies affect transport on a fundamental level; their effect can consistently be derived from any calculation that keeps track of conservation laws and symmetries, and that correctly captures the topological character of a Weyl node.

The positive magneto-conductance and magneto-thermoelectric conductance are fundamentally linked to the response of the charge current $\boldsymbol{J}$ when an electric field $\boldsymbol{E}$ and a thermal gradient ∇T are applied through the relation $\boldsymbol{J} = G\boldsymbol{E} + G_T \nabla T$. Here, $G = J/E$ denotes the electric conductance, which characterizes the response of the electrical current to electric fields, and $G_T = J/|\nabla T|$ is the thermoelectric conductance, which characterizes the electrical current in the Weyl metal that is induced by a temperature gradient. (Note that we define the coordinate system such that the applied temperature gradient has only one non-zero component.) In low magnetic fields, the mixed axial–gravitational anomaly and the chiral anomaly implies a positive magneto-current contribution to the transport coefficients $G = d_e + c_1 a_c^2 B_{\parallel}^2$ and $G_T = d_{th} + c_2 a_c a_g B_{\parallel}^2$, with $c_{1,2} > 0$ accounting for details of the band structure. Here d_e and d_{th} express the classical electrical and thermal Drude parts, the coefficients a_c and a_g account for the contributions of the chiral and mixed axial–gravitational anomalies, respectively[6,23,24,27], and $B_{\parallel}$ denotes the component of the magnetic field that is parallel to the electric field or thermal gradient. In the ultra-quantum limit at high magnetic fields, when only the lowest Landau level contributes to transport, G depends linearly on the magnetic field and the gravitational anomaly does not contribute to G_T (see Methods). Analogously to the positive magneto-conductance, which requires parallel electric and magnetic fields as determined by the chiral anomaly, the positive magneto-thermoelectric conductance is expected to be locked to the magnetic-field direction as a result of the anomalous contribution[6,23–26]. The combined measurement of (i) a finite value of a_g, (ii) the functional dependence for $\nabla T \cdot \boldsymbol{B} \neq 0$ of the positive magneto-thermoelectric conductance at low fields ($\boldsymbol{B}$ is the magnetic field), and (iii) the absence of positive magneto-thermoelectric conductance at high fields represents the experimental signature of the mixed axial–gravitational anomaly in thermal transport.

The magneto-thermoelectrical conductance of the half-Heusler alloy GdPtBi (ref. 15) has recently been calculated from separate measurements of thermopower and electrical conductance, revealing a positive magneto-thermoelectric conductance contribution at low magnetic fields. However, this contribution was interpreted as a signature of the node creation process, which depends on the magnetic field. To obtain experimental signatures of the presence of the mixed axial–gravitational anomaly, it is therefore desirable to go beyond these experiments and investigate the electrical response of intrinsic Weyl semimetals to temperature gradients in collinear magnetic fields.

For our experiments, we used micro-ribbons (50 μm × 2.5 μm × 0.5 μm) cut out from single-crystalline bulk samples of the Weyl semimetal NbP with a gallium focused-ion beam. The transport direction in our samples matches the [100] axis of the crystal (see Methods for details). An on-chip micro-strip line heater near the micro-ribbon generates a temperature gradient along the length of the ribbon, with the resulting temperature differences (less than 350 mK) sufficiently small to ensure that the measurement is in the linear response regime (Extended Data Fig. 6). The temperature gradient ∇T was measured by resistance thermometry using two metal four-probe thermometer lines located at the ends of the NbP micro-ribbon (Fig. 1d). The metal lines for thermometry also serve as electrodes for applying an electrical bias and for measuring the current response of the ribbon. The elongated geometry of the micro-ribbons, with contact lines across the full widths of the samples, was chosen to ensure that current jetting is suppressed and to provide homogenous field distributions[15,17]. To justify the description of the carriers in terms of Weyl fermions, it is essential that the Fermi level E_F is as close as possible to the Weyl nodes of NbP (refs 28, 29). By means of gallium doping, we recently showed that E_F is located only 5 meV above the Weyl points, in the electron cone of our NbP sample[14].

In a first set of transport experiments of electrical conductance measurements under isothermal conditions ($\nabla T = \mathbf{0}$), we establish that the NbP micro-ribbon can be accurately described by Weyl fermions. For this purpose, a voltage $V = 1$ mV is applied along the ribbon, which sets an electric field $\boldsymbol{E}$, and the corresponding current $\boldsymbol{J}$ is measured through a near-zero-impedance (1 Ω) ammeter. When the magnetic field is switched on, the Weyl nodes split into Landau levels. For each Weyl node, the zeroth Landau level disperses linearly with momentum along $\boldsymbol{B}$ (Fig. 2a) and is thus chiral, unlike the remaining Landau levels, which disperse quadratically. Aligned electric and magnetic fields ($\boldsymbol{E} \parallel \boldsymbol{B}$) generate a chiral flow of charge between the two valleys of different chirality[4], with a rate that is proportional to $\boldsymbol{E} \cdot \boldsymbol{B}$. To equilibrate the induced chiral imbalance between the left- and right-handed fermions, large-momentum internode scattering is required, which in general depends on $\boldsymbol{B}$ (refs 11, 27). In the low-field regime, in which many Landau levels are filled, it is possible to solve the corresponding Boltzmann[11] or hydrodynamic[6] transport equation, resulting in a chiral-anomaly-induced positive magneto-conductance contribution of $G = d_e + c_1 a_c^2 B_{\parallel}^2$. In the high-field limit, in which only the lowest Landau levels contribute to transport, the magneto-conductance

© 2017 Macmillan Publishers Limited, part of Springer Nature. All rights reserved.

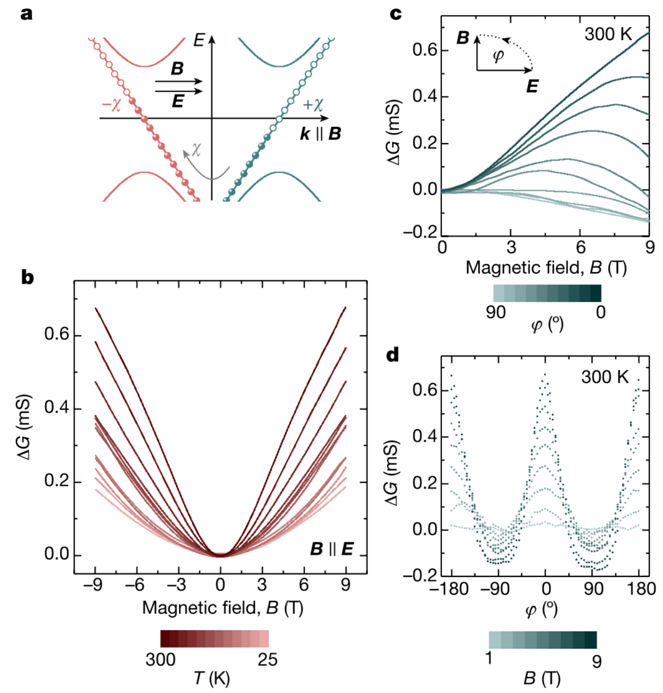

Figure 2 | Chiral anomaly in NbP. a, In a strong magnetic field, the Weyl nodes quantize into Landau levels. The lowest Landau levels exhibit a linear dispersion with distinct chirality ($\pm\chi$). Parallel electric (***E***) and magnetic (***B***) fields pump chiral charges from one cone into the other, which breaks chiral symmetry. **b**, Magneto-conductance without zero-field contributions (ΔG) at selected temperatures (see colour scale), for $\boldsymbol{E} \parallel \boldsymbol{B}$. **c**, ΔG versus $|\boldsymbol{B}|$ for different angles φ (colour scale) between the electric and magnetic fields (see inset), at $T = 300$ K. **d**, Angular dependence of ΔG at $T = 300$ K, for varying magnetic field strength (colour scale).

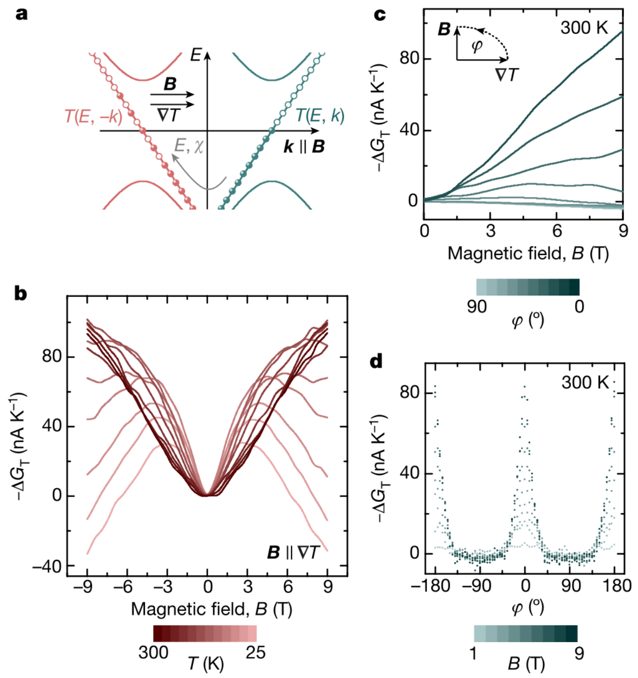

Figure 3 | Evidence of the mixed axial–gravitational anomaly in NbP. a, Parallel temperature gradients (∇T) and magnetic fields (***B***) result in a transfer of particles and energy (E) from one cone to the other. **b**, Negative magneto-thermoelectric conductance without zero-field contributions ($-\Delta G_T$) at selected temperatures (see colour scale), for $\boldsymbol{B} \parallel \nabla T$. The negative sign accounts for electron transport. **c**, $-\Delta G_T$ versus $|\boldsymbol{B}|$ for different angles φ (colour scale) between the temperature gradient and magnetic field (see inset), at $T = 300$ K. The magneto-conductance is negative for $\varphi > 30°$ at high fields. **d**, Angular dependence of $-\Delta G_T$ at $T = 300$ K, for varying magnetic field strength (colour scale).

behaves linearly with applied field. This is the transport fingerprint of the chiral anomaly. As shown in Fig. 2b, we observe a large positive magneto-conductance up to room temperature for $\boldsymbol{E} \parallel \boldsymbol{B}$, which is sensitive to misalignments (Fig. 2c). Whereas the low-field regime is well described by a quadratic fit ($\Delta G \propto B_\parallel^2$), in agreement with the Boltzmann description for chiral anomaly, the linear high-field regime can be explained by a transition from a multi-level state to the limit in which only the lowest chiral Landau levels contribute to the transport[14]. Accordingly, with chiral charge pumping, the positive magneto-conductance at low magnetic fields is well approximated by $\cos^2(\varphi)$, where φ is the angle between ***E*** and ***B*** (Fig. 2d). The narrowing of the angular width at higher fields is caused by strong collimation of the axial beams[12]. The observed locking pattern and the consistent quadratic dependence in the low-field regime are the fundamental signatures of the chiral anomaly[11] and support the description of the system in terms of chiral Weyl fermions.

We now turn to testing the mixed axial–gravitational anomaly in the NbP micro-ribbon. We use a transport experiment, but in this case apply a thermal gradient instead of a voltage bias. Because the NbP sample is short-cut through a near-zero-impedance ammeter, no net electric field is imposed. Excluding electric fields is essential for a clear distinction from the chiral anomaly, which is induced by a finite $\boldsymbol{E} \parallel \boldsymbol{B}$. Instead, applying $\nabla T \parallel \boldsymbol{B}$ leads to a net difference in energy density between the two chiral valley fluids[6,21], proportional to $\nabla T \cdot \boldsymbol{B}$, that is equilibrated through an intervalley energy transfer (Fig. 3a) The resulting imbalance leads to a charge current, owing to the chiral magnetic effect, which then leads to a positive magneto-thermoelectric conductance contribution of $G_T = d_{th} + c_2 a_c a_g B_\parallel^2$ (refs 2, 6, 21, 23–26). This phenomenon allows us to probe the presence of the mixed axial–gravitational anomaly through its effect on thermoelectric transport in a condensed matter system. The data corresponding to these measurements are shown in Fig. 3b, c. The applied temperature gradient indeed appears to result in magneto-transport features that are similar to those that result from the application of an electric field. When $\nabla T \parallel \boldsymbol{B}$, the thermoelectrical conductance at low magnetic fields exhibits a positive magneto-thermoelectric conductance that fits to $G_T \propto B_\parallel^2$ with the same $\cos^2(\varphi)$ locking pattern as the positive magneto-conductance (Fig. 3d). At high temperatures ($T > 150$ K), the observed dependence of the magneto-transport on the field strength is consistent with the presence of a mixed axial–gravitational anomaly and its corresponding thermoelectric transport prediction[6,23–26]. At lower temperatures, however, we observe a decrease in G_T. This decrease occurs in the same magnetic field range as the crossover from a quadratic to a linear field dependence in ΔG, in agreement with the fact that both effects can be explained by the crossover to a one-dimensional dispersion that Weyl metals show along ***B*** in the ultra-quantum limit[15,30]. As we show in Methods, the suppression of thermoelectric transport at high magnetic fields occurs because ΔG_T is proportional to the derivative of the electron density ρ with respect to temperature ($\Delta G_T \propto \partial\rho/\partial T$). Because the density of states is independent of the temperature in the ultra-quantum limit, the electron density at large magnetic fields is independent of temperature and $\Delta G_T = 0$.

The ratio G_T/G should correspond to another measurable transport coefficient, the thermopower S. Starting from the relation $\boldsymbol{J} = G\boldsymbol{E} + G_T \nabla T$, the thermopower S can be determined either from a measurement using an open circuit ($\boldsymbol{J} = \boldsymbol{0}$) or from combining the above experiments at $\boldsymbol{E} = \boldsymbol{0}$ and $\nabla T = \boldsymbol{0}$. The thermopower S expresses the response of the open-circuit voltage to a temperature gradient. To carry out this test, we removed the short-cutting ammeter from our experiment and measured the response of the open-circuit voltage to a temperature gradient in a collinear magnetic field (Fig. 1a). As shown

© 2017 Macmillan Publishers Limited, part of Springer Nature. All rights reserved.

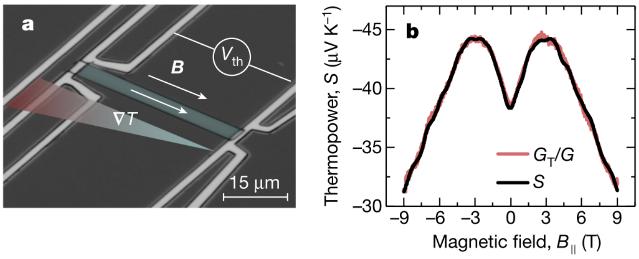

Figure 4 | Longitudinal thermopower. a, False-coloured optical micrograph of the thermopower measurement device. The thermopower $S = V_{th}/|\nabla T|$ is measured along a NbP micro-ribbon (green) by applying a temperature gradient ∇T and measuring the response of the open-circuit voltage V_{th}. **b**, The measured magneto-thermopower S and calculated magneto-thermopower G_T/G of the anomalous transport coefficients match quite well, as demonstrated for $T = 25$ K.

in Fig. 4b, the calculated G_T/G matches the measured S excellently. The agreement is an important cross-check, confirming the results and interpretation above. Furthermore, this result implies that the thermopower is suppressed not solely by the presence of the chiral anomaly, as suggested previously[15], but rather by the presence of both the chiral and mixed axial–gravitational anomalies (Extended Data Fig. 11).

In conclusion, our measurements reveal a positive magneto-thermoelectric conductance in the Weyl semimetal NbP, a signature that is linked to the presence of the mixed axial–gravitational anomaly of chiral fermions in three spatial dimensions. In short, the thermally biased experiment confirms the predicted $B_{\|}^2$ dependence of G_T at low magnetic fields, its dependence on the relative orientation of the magnetic field and the thermal gradient, and the suppression of thermoelectric transport at high magnetic fields. These effects arise concurrently with the standard chiral anomaly, the signatures of which we observed in the field-induced correction to the standard electric conductance. Our results show that it is possible to detect the presence of the mixed axial–gravitational anomaly of Weyl fermions, particularly elusive in other contexts, in relatively simple transport experiments using a macroscopic condensed matter system in a flat space-time.

Online Content Methods, along with any additional Extended Data display items and Source Data, are available in the online version of the paper; references unique to these sections appear only in the online paper.

Received 29 October 2016; accepted 25 May 2017.

1. Bertlmann, R. A. *Anomalies in Quantum Field Theory* (Oxford Univ. Press, 2000).
2. Adler, S. L. Axial-vector vertex in spinor electrodynamics. *Phys. Rev.* **177,** 2426–2438 (1969).
3. Bell, J. S. & Jackiw, R. A PCAC puzzle: $\pi^0 \rightarrow \gamma\gamma$ in the σ-model. *Nuovo Cimento A* **60,** 47–61 (1969).
4. Nielsen, H. B. & Ninomiya, M. The Adler–Bell–Jackiw anomaly and Weyl fermions in a crystal. *Phys. Lett. B* **130,** 389–396 (1983).
5. Landsteiner, K., Megías, E. & Pena-Benitez, F. Gravitational anomaly and transport phenomena. *Phys. Rev. Lett.* **107,** 021601 (2011).
6. Lucas, A., Davison, R. A. & Sachdev, S. Hydrodynamic theory of thermoelectric transport and negative magnetoresistance in Weyl semimetals. *Proc. Natl Acad. Sci. USA* **113,** 9463–9468 (2016).
7. Xu, S.-Y. *et al.* Discovery of a Weyl Fermion semimetal and topological Fermi arcs. *Science* **349,** 613–617 (2015).
8. Xu, S.-Y. *et al.* Discovery of a Weyl fermion state with Fermi arcs in niobium arsenide. *Nat. Phys.* **11,** 748–754 (2015).
9. Huang, S.-M. *et al.* A Weyl fermion semimetal with surface Fermi arcs in the transition metal monopnictide TaAs class. *Nat. Commun.* **6,** 7373 (2015).
10. Nielsen, H. B. & Ninomiya, M. Absence of neutrinos on a lattice: (I). Proof by homotopy theory. *Nucl. Phys. B* **185,** 20–40 (1981).
11. Son, D. T. & Spivak, B. Z. Chiral anomaly and classical negative magnetoresistance of Weyl metals. *Phys. Rev. B* **88,** 104412 (2013).
12. Xiong, J. *et al.* Evidence for the chiral anomaly in the Dirac semimetal Na_3Bi. *Science* **350,** 413–416 (2015).
13. Huang, X. *et al.* Observation of the chiral-anomaly-induced negative magnetoresistance in 3D Weyl semimetal TaAs. *Phys. Rev. X* **5,** 031023 (2015).
14. Niemann, A. C. *et al.* Chiral magnetoresistance in the Weyl semimetal NbP. *Sci. Rep.* **7,** 43394 (2017).
15. Hirschberger, M. *et al.* The chiral anomaly and thermopower of Weyl fermions in the half-Heusler GdPtBi. *Nat. Mater.* **15,** 1161–1165 (2016).
16. Li, H. *et al.* Negative magnetoresistance in Dirac semimetal Cd_3As_2. *Nat. Commun.* **7,** 10301 (2016).
17. Arnold, F. *et al.* Negative magnetoresistance without well-defined chirality in the Weyl semimetal TaP. *Nat. Commun.* **7,** 11615 (2016).
18. Shekhar, C. *et al.* Observation of chiral magneto-transport in RPtBi topological Heusler compounds. Preprint at https://arxiv.org/abs/1604.01641 (2016).
19. Alvarez-Gaumé, L. & Witten, E. Gravitational anomalies. *Nucl. Phys. B* **234,** 269–330 (1984).
20. Eguchi, T. & Freund, P. G. O. Quantum gravity and world topology. *Phys. Rev. Lett.* **37,** 1251–1254 (1976).
21. Landsteiner, K., Megías, E. & Peña-Benitez, F. in *Strongly Interacting Matter in Magnetic Fields* (eds Kharzeev, D. *et al.*) 433–468 (Springer, 2013).
22. Kaminski, M., Uhlemann, C. F., Bleicher, M. & Schaffner-Bielich, J. Anomalous hydrodynamics kicks neutron stars. *Phys. Lett. B* **760,** 170–174 (2016).
23. Lundgren, R., Laurell, P. & Fiete, G. A. Thermoelectric properties of Weyl and Dirac semimetals. *Phys. Rev. B* **90,** 165115 (2014).
24. Kim, K.-S. Role of axion electrodynamics in a Weyl metal: violation of Wiedemann–Franz law. *Phys. Rev. B* **90,** 121108(R) (2014).
25. Sharma, G., Goswami, P. & Tewari, S. Nernst and magnetothermal conductivity in a lattice model of Weyl fermions. *Phys. Rev. B* **93,** 035116 (2016).
26. Spivak, B. Z. & Andreev, A. V. Magnetotransport phenomena related to the chiral anomaly in Weyl semimetals. *Phys. Rev. B* **93,** 085107 (2016).
27. Burkov, A. A. Chiral anomaly and diffusive magnetotransport in Weyl metals. *Phys. Rev. Lett.* **113,** 247203 (2014).
28. Shekhar, C. *et al.* Extremely large magnetoresistance and ultrahigh mobility in the topological Weyl semimetal candidate NbP. *Nat. Phys.* **11,** 645–649 (2015).
29. Sergelius, P. Berry phase and band structure analysis of the Weyl semimetal NbP. *Sci. Rep.* **6,** 33859 (2016).
30. Liang, T. *et al.* Evidence for massive bulk Dirac fermions in $Pb_{1-x}Sn_xSe$ from Nernst and thermopower experiments. *Nat. Commun.* **4,** 2696 (2013).

Acknowledgements This work was supported by the research grant DFG-RSF (NI616 22/1) 'Contribution of topological states to the thermoelectric properties of Weyl semimetals', Severo Ochoa SEV-2012-0249, FPA 2015-65480-P and SFB 1143, by the Helmholtz association through VI-521, and by the DFG (Emmy Noether programme) via grant ME 4844/1. We thank T. Sturm and A. Pöhl, for experimental support. We also acknowledge support by W. Riess, K. Moselund and H. Riel, and thank C. Bollinger for copy-editing.

Author Contributions J.G. conceived the experiment. M.S., C.S. and V.S. synthesized the single-crystal bulk samples. R.H. characterized the crystal structure. B.R. supervised the micro-ribbon definition and the compositional analysis. A.C.N. fabricated the samples. J.G. carried out the thermoelectric transport measurements with the help of A.C.N. J.G., A.C.N., F.M., B.G., T.M. and A.G.G. analysed the data. B.G., C.F., B.Y. and K.N. supervised the project. A.G.G., T.M. and K.L. provided the theoretical background for the work. All authors contributed to interpreting the data and writing the manuscript.

Author Information Reprints and permissions information is available at www.nature.com/reprints. The authors declare no competing financial interests. Readers are welcome to comment on the online version of the paper. Publisher's note: Springer Nature remains neutral with regard to jurisdictional claims in published maps and institutional affiliations. Correspondence and requests for materials should be addressed to J.G. (Johannes.gooth@outlook.com).

© 2017 Macmillan Publishers Limited, part of Springer Nature. All rights reserved.

III Experimental signatures of the mixed axial-gravitational anomaly in the Weyl semimetal NbP

-Supporting Information-

METHODS

Micro-ribbon fabrication. High-quality single bulk crystals of NbP are grown via a chemical vapour transport reaction using an iodine transport agent. A polycrystalline powder of NbP is synthesized by direct reaction of niobium (Chempur 99.9%) and red phosphorus (Heraeus 99.999%) within an evacuated fused silica tube for 48 h at 800 °C. The growth of bulk single crystals of NbP is then initialized from this powder by chemical vapour transport in a temperature gradient, starting from 850 °C (source) and increasing to 950 °C (sink), and in a transport agent with a concentration of 13.5 mg cm^{-3} iodine (Alfa Aesar 99.998%).

Subsequently, NbP micro-ribbons are cut out from the bulk crystals (Extended Data Fig. 1a,b) using gallium focused-ion beam etching (voltage, 30 kV; current, 65–80 pA). The samples are prepared such that their longitudinal direction coincides with the [100] crystal axis of NbP. Focused-ion beam etching caused *in situ* gallium doping of the ribbons. The final composition of the samples is analysed by scanning electron microscopy energy-dispersive X-ray spectroscopy (SEM-EDX), yielding 53% Nb, 45% P and 2% Ga (Extended Data Fig. 1c). We study ribbons 50 μm × 2.5 μm × 0.5 μm in size. The dimensions of the ribbons are obtained from SEM. The high aspect ratio of our samples ensures the suppression of jet currents during the transport measurements. The single-crystallinity of the ribbons is evident from the X-ray diffraction (XRD) pattern shown in Extended Data Fig. 1d.

Device fabrication. After cutting, the NbP micro-ribbons are directly transferred onto Si/SiO$_2$ chips in a solvent-less approach, using a micromanipulator. A soft mask for electrical contacts to the micro-ribbon is defined via laser-beam lithography (customized μPG system). A double layer of photoresist is spin-coated and baked (first photoresist: LOR 3B, spin-coated at 3,500 r.p.m. for 45 s, baked at 180 °C for 250 s; second photoresist: ma-P 1205, spin-coated at 3,500 r.p.m. for 30 s, baked at 100 °C for 30 s), before laser exposure and development for 40 s in ma-D 331 solution. Sputter deposition of Ti/Pt (10 nm/400 nm) is performed after 5 min of argon sputter cleaning. Titanium serves as the adhesion promoter and diffusion barrier for the platinum. Finally, a lift-off is performed, 1 h at 80 °C in Remover 1165. An optical micrograph of a final device is shown in Extended Data Fig. 2.

Thermoelectric measurements. Thermoelectric measurements are performed in a temperature-variable cryostat (Dynacool, Quantum Design) in vacuum. The cryostat is equipped with a ±9 T superconducting magnet. After fabrication, the micro-ribbon devices are wire bonded and mounted on a sample holder that allows rotation in angles from −10° to 370°. We specifically investigate three thermoelectric transport parameters of the NbP micro-ribbons: the electrical conductance $G = J/V$, the thermoelectric conductance $G_T = J/|\nabla T|$, and the thermopower $S = -V_{th}/|\nabla T|$, where J denotes the electrical current, V the voltage bias, ∇T a temperature gradient and V_{th} the voltage response to ∇T. All transport coefficients are measured in the linear response regime as a function of the cryostat base temperature T, magnetic field $\boldsymbol{B}$ and rotation angle φ, which is defined with respect to the transport direction along the longitudinal axis of the samples.

Electrical conductance measurements in a two-probe configuration are carried out under isothermal conditions with d.c. bias voltages of up to $V = 1$ mV applied with a Yokogawa voltage source and a 100-times voltage divider across the length of the ribbon. Our results are independent of contact iteration. The responding current signal J is enhanced using a current preamplifier (Stanford Research, model SR570) with an input impedance of 1 Ω. Contact lines across the full width of the sample ensure a homogeneous electric field distribution in the ribbon. Temperature-dependent J–V measurements (Extended Data Fig. 3) reveal ohmic contacts. The magneto-conductance is measured by sweeping the magnetic field with 5 mT s^{-1}.

Thermoelectric conductance measurements are performed with the same current recording set-up, but, crucially, without an electric field imposed at the sample. Instead, the on-chip Joule heater line near the end of the micro-ribbon is used to generate a temperature gradient ∇T along the length of the micro-ribbon. ∇T is measured by resistive thermometry, using two metal four-probe thermometer lines located at the ends of the micro-ribbons (Extended Data Fig. 2). The thermometers are driven by lock-in amplifiers (Stanford Research, model SR830) with a 500-nA a.c. bias current at distinct frequencies (<15 Hz) to prevent crosstalk. The thermometers are calibrated under isothermal conditions against the base temperature of the cryostat (Extended Data Fig. 4), from which $T(R)$ is determined, where R is the electrical resistance of the thermometers. The heating voltage V_H applied across a 2-kΩ shunt resistance at the heater line (Extended Data Fig. 5) is chosen to ensure a linear response of the current J to the temperature gradient ($J \propto |\nabla T|$; Extended Data Fig. 6). G_T is then obtained from linear fits of J versus the corresponding $|\nabla T|$ at fixed base temperatures; $|\nabla T|$ values of up to 350 mK are obtained. The magneto-thermoelectric conductance is measured at a fixed heating voltage of 12 V, sweeping the magnetic field with 5 mT s^{-1}. ∇T showed no dependence on the magnetic field. The field sweeping rate is chosen such that the results are independent of it.

To obtain S, the current measurement set-up is removed and replaced by a nanovoltmeter (Keithley, model 182A) to measure the open-circuit voltage V_{th} of the NbP micro-ribbons in response to ∇T. Choosing the same V_H as in the thermoelectric conductance measurements ensures a linear response of V_{th} to the temperature gradient ($V_{th} \propto |\nabla T|$; Extended Data Fig. 7). S is then extracted from linear fits of V_{th} versus $|\nabla T|$.

Temperature dependence of the transport coefficients at zero magnetic field. In the absence of an applied magnetic field, the electrical conductance exhibits a non-metallic $G(T)$ dependence with a negative temperature coefficient of resistance (Extended Data Fig. 8). Furthermore, without magnetic and electric fields applied along the sample, the measurement of thermoelectric conductance versus temperature reveal a change in sign at approximately 250 K (Extended Data Fig. 9). Below 250 K, the transport in the NbP micro-ribbons is dominated by conduction-band electrons, indicated by a negative sign of the thermoelectric conductance in the G_T–T plot. Because of the zero bandgap, holes are thermally excited in parallel, governing the transport at higher temperatures (positive G_T). The same generic features are observed in $S(T)$ (Extended Data Fig. 10).

Connection between the mixed axial–gravitational anomaly and thermal transport. *The mixed axial–gravitational anomaly.* For completeness, we present established quantum field theory and hydrodynamic theory results for chiral Weyl fermions that support the interpretation that the measurements presented here stem from a mixed axial–gravitational anomaly. We start by noting that, unlike pure gravitational anomalies, which are allowed only in space-time dimension $D = 4k - 2$, where k is an integer, mixed axial–gravitational anomalies are allowed in the $D = 3 + 1$ that is relevant for Weyl semimetals[19]. In particular, we are interested in the Abelian version of the mixed axial–gravitational anomaly, which is expressed via the non-conservation of axial current j^{μ}_{A} in a curved space-time that is characterized by the Riemann tensor $R^{\alpha}_{\beta\mu\nu}$. Following the notation of ref. 21, we write the conservation law for this current as

$$\partial_{\mu} j^{\mu}_{A} = \frac{d_{AVV}}{32\pi^2} \varepsilon^{\mu\nu\rho\sigma} F^{V}_{\mu\nu} F^{V}_{\rho\sigma} + \frac{b_A}{768\pi^2} \varepsilon^{\mu\nu\rho\sigma} R^{\alpha}_{\beta\mu\nu} R^{\beta}_{\alpha\rho\sigma} \quad (1)$$

where the labels ‘A’ and ‘V’ denote tensors built out of axial and vector fields, respectively, and d_{AVV} and b_A are numerical coefficients (defined below). The first term on the right-hand side of equation (1) represents the non-conservation of axial current due to the presence of external non-orthogonal electric and magnetic fields. It involves the electromagnetic (vector) field strength $F^{V}_{\mu\nu} = \partial_{\mu} A^{V}_{\nu} - \partial_{\nu} A^{V}_{\mu}$ through the U(1) vector gauge field A^{V}_{ν} where $\mu \in \{0, 1, 2, 3\}$. Its coefficient is set by the chiral anomaly coefficient d_{abc}, with $a, b, c \in \{A, V\}$; when $d_{abc} \neq 0$, the chiral anomaly is present. For the Abelian case, of interest here, it is simply determined by the difference between a triple product of charges q of right (‘r’) and left (‘l’) chirality:

$$d_{abc} = \sum_{r} \left(q^{r}_{a} q^{r}_{b} q^{r}_{c}\right) - \sum_{l} \left(q^{l}_{a} q^{l}_{b} q^{l}_{c}\right)$$

where $q^{r}_{V} = q^{r}_{A} = 1$ and $q^{l}_{V} = -q^{l}_{A} = 1$. Therefore, $d_{AVV} = 2$ for a pair of chiral fermions.

The second term on the right-hand side of equation (1) is the contribution of the mixed axial–gravitational anomaly to the non-conservation of chiral current. In the Abelian case, its coefficient is given by

$$b_a = \sum_{r} q^{r}_{a} - \sum_{l} q^{l}_{a}$$

with $a \in \{A, V\}$. If $b_a \neq 0$, then the mixed axial–gravitational anomaly is present[1,3,4] and $b_a = 2$ for each pair of chiral fermions.

Connection with thermal transport. Given the form of the gravitational term in equation (1), it is natural to ask how it is possible to detect its presence in a flat space-time in which $R^{\alpha}_{\beta\mu\nu} = 0$. The key but subtle observation is that the temperature dependence of linear transport coefficients for systems of Weyl fermions depends on a_g, even in flat space-time. This conclusion can be reached from the standard Kubo formalism[5], holography[31], hydrodynamic theory[8] or arguments based on a global version of the axial–gravitational anomaly[32].

Although hydrodynamic[6] and Kubo approaches lead to consistent predictions for the thermoelectric coefficient presented here, the former relies on interactions being the dominant scattering mechanism. Because the scattering in experimental samples seems to be mostly dominated by impurity scattering, we believe the Kubo approach to be more suitable for the description of our data.

In what follows we sketch a simple derivation that justifies the functional form of the positive magneto-thermoelectric conductance that we use. We consider a single Weyl cone, in which case the anomaly coefficients are $d_{\chi} = b_{\chi} = \pm 1$, and we define $a_{\chi} = d_{\chi}/(4\pi^2)$ and $a_g = b_{\chi}/24$. Our calculation relies on the Kubo formalism; although the low-field predictions obtained by this treatment are consistent with those from Boltzmann kinetic theory[23–26], key advantages of the Kubo formalism as compared to the Boltzmann approach are that it tracks the relationship to the

© 2017 Macmillan Publishers Limited, part of Springer Nature. All rights reserved.

mixed axial–gravitational anomaly in a transparent way and that it is directly applicable to large magnetic fields. We start with the equations that describe particle and energy conservation for a single Weyl fermion:

$$\dot{\rho}+\boldsymbol{\nabla}\boldsymbol{J}_{\rho}=a_{\chi}\boldsymbol{E}\cdot\boldsymbol{B} \tag{2}$$

$$\dot{\epsilon}+\boldsymbol{\nabla}\boldsymbol{J}_{\epsilon}=\boldsymbol{J}_{\rho}\cdot\boldsymbol{E} \tag{3}$$

where ρ is the electronic density and ϵ is the energy density. $\boldsymbol{J}_{\rho}$ and $\boldsymbol{J}_{\epsilon}$ are the electric and the energy current, respectively. Because the system lives in flat space-time, only the chiral anomaly enters these equations. We furthermore note that the energy conservation equation (3) includes a term that describes the work performed by the electric field.

We are interested in the magnetic-field-dependent contribution to the energy and charge current that will ultimately determine the positive magneto-thermoelectric conductance. As discussed in ref. 20, the standard Kubo formalism for Weyl fermions leads to

$$\boldsymbol{J}_{\rho}=a_{\chi}\mu\boldsymbol{B} \tag{4}$$

$$\boldsymbol{J}_{\epsilon}=\left(\frac{a_{\chi}}{2}\mu^{2}+a_{\mathrm{g}}T^{2}\right)\boldsymbol{B} \tag{5}$$

Equation (4) describes the chiral magnetic effect for a single Weyl fermion at chemical potential μ, which depends on the chiral anomaly coefficient a_{χ}. The energy current given in equation (5) is composed of two terms. The first term describes that the directed flow of particles in a system with a chiral anomaly leads to an energy current that is simply due to the energy associated with each electronic state. This term is normalized such that the energy current vanishes in the vacuum state, which corresponds to $\mu=0$. The second term, which describes the thermal contribution of interest, has recently been highlighted to be a consequence of the mixed axial–gravitational anomaly[5,31–35]. It is hence governed by the coefficient a_{g}, which establishes a link between the existence of a thermal contribution in $\boldsymbol{J}_{\epsilon}$ and the gravitational contribution to equation (1).

We now turn to the thermoelectric transport. To this end, we assume a finite magnetic field $\boldsymbol{B}$ and compute the anomalous response due to a gradient in temperature $\boldsymbol{\nabla}T$ and an electric field $\boldsymbol{E}$ (all of which are assumed to be spatially homogeneous) in the linear-response approximation. With these assumptions, we can insert equations (4) and (5) into equations (2) and (3) to obtain

$$\dot{\epsilon}=a_{\chi}\mu\boldsymbol{E}\cdot\boldsymbol{B}-2a_{\mathrm{g}}T\boldsymbol{\nabla}T\cdot\boldsymbol{B} \tag{6}$$

$$\dot{\rho}=a_{\chi}\boldsymbol{E}\cdot\boldsymbol{B} \tag{7}$$

The first term on the right-hand side of (6) is the work performed by the electric field on the background chiral-magnetic-effect current. If there are two nodes of opposite chirality, then this term encodes that each particle pumped between the Weyl nodes in parallel electric and magnetic fields also transfers its energy from one node to the other. The second term on the right-hand side of equation (6) shows that, in a completely analogous way, a temperature gradient parallel to the magnetic field leads to energy pumping between Weyl cones owing to the mixed axial–gravitational anomaly. In a Weyl semimetal, intervalley scattering will stop this pumping on a timescale τ, known as the intervalley scattering time. (In a strongly interacting electron fluid the energies of different Weyl cones could in principle equilibrate on a shorter timescale, owing to electron–electron interactions; however, this is not the case here.) The steady state is accounted for by the replacement $(\dot{\epsilon},\dot{\rho})\rightarrow(\delta\epsilon,\delta\rho)/\tau$.

At this point it is convenient to introduce the matrix

$$\Xi=\begin{pmatrix}\dfrac{\partial\epsilon}{\partial T} & \dfrac{\partial\epsilon}{\partial\mu}\\[2ex] \dfrac{\partial\rho}{\partial T} & \dfrac{\partial\rho}{\partial\mu}\end{pmatrix}$$

such that

$$\begin{pmatrix}\delta\epsilon\\ \delta\rho\end{pmatrix}=\Xi\begin{pmatrix}\delta T\\ \delta\mu\end{pmatrix}$$

and equations (6) and (7) can be written as

$$\Xi\begin{pmatrix}\delta T\\ \delta\mu\end{pmatrix}=\tau\begin{pmatrix}-2a_{\mathrm{g}}T & a_{\chi}\mu\\ 0 & a_{\chi}\end{pmatrix}\begin{pmatrix}\boldsymbol{\nabla}T\\ \boldsymbol{E}\end{pmatrix}\boldsymbol{B} \tag{8}$$

From equations (4) and (5), we obtain the ith components of the energy and particle currents,

$$\begin{pmatrix}\delta J_{\epsilon,i}\\ \delta J_{\rho,i}\end{pmatrix}=\tau\begin{pmatrix}2a_{\mathrm{g}}T & a_{\chi}\mu\\ 0 & a_{\chi}\end{pmatrix}\begin{pmatrix}\delta T\\ \delta\mu\end{pmatrix}B_{i}$$

which together with equation (8) define the response tensor κ_{ij} as

$$\kappa_{ij}=\begin{pmatrix}2a_{\mathrm{g}}T & a_{\chi}\mu\\ 0 & a_{\chi}\end{pmatrix}\Xi^{-1}\begin{pmatrix}-2a_{\mathrm{g}}T & a_{\chi}\mu\\ 0 & a_{\chi}\end{pmatrix}\tau B_{i}B_{j}$$

The anomaly-induced response in the current is thus given by

$$J_{i}=G_{\mathrm{T}}^{ij}\nabla_{j}T+G^{ij}E_{j}$$

where the conductance tensors have components

$$G^{ij}=\tau\frac{a_{\chi}^{2}}{\det(\Xi)}\left(\frac{\partial\epsilon}{\partial T}-\mu\frac{\partial\rho}{\partial T}\right)B_{i}B_{j} \tag{9}$$

$$G_{\mathrm{T}}^{ij}=\tau\frac{2a_{\chi}a_{\mathrm{g}}T}{\det(\Xi)}\frac{\partial\rho}{\partial T}B_{i}B_{j} \tag{10}$$

To explain our experimental measurements, we now consider the regimes of either low or high magnetic field, assuming a homogenous Fermi velocity of v_{F} (we use units such that the elementary charge $e=1$). In the first case, the system behaves as a gas of free Weyl fermions with an energy density of

$$\epsilon=\frac{1}{8\pi^{2}v_{\mathrm{F}}^{3}}\left(\mu^{4}+2\pi^{2}T^{2}\mu^{2}+\frac{7}{15}\pi^{4}T^{4}\right) \tag{11}$$

(see for instance ref. 36). In the second case, the system splits into degenerate one-dimensional systems, the number of which is set by the Landau level degeneracy, and the energy density is

$$\epsilon_{B}=\frac{|\boldsymbol{B}|}{v_{\mathrm{F}}}\left(\frac{\mu^{2}}{8\pi^{2}}+\frac{T^{2}}{24}\right) \tag{12}$$

For small and large magnetic fields, the particle densities are given respectively by

$$\rho=\frac{\mu^{3}+\pi^{2}T^{2}\mu}{6\pi^{2}v_{\mathrm{F}}^{3}} \tag{13}$$

and

$$\rho_{B}=\frac{|\boldsymbol{B}|}{4\pi^{2}v_{\mathrm{F}}}\mu \tag{14}$$

Combining the above allows us to obtain G^{ij} and G_{T}^{ij} in different magnetic-field regimes. For low magnetic fields, substituting equations (11) and (13) into equation (9) yields

$$G^{ij}=\frac{6a_{\chi}^{2}\pi^{2}v_{\mathrm{F}}^{3}(7\pi^{2}T^{2}+5\mu^{2})}{7\pi^{4}T^{4}+6\mu^{2}T^{2}\mu^{2}+15\mu^{4}}\tau B_{i}B_{j} \tag{15}$$

$$G_{\mathrm{T}}^{ij}=\frac{120a_{\chi}a_{\mathrm{g}}\pi^{2}T\mu v_{\mathrm{F}}^{3}}{7\pi^{4}T^{4}+6\mu^{2}T^{2}\mu^{2}+15\mu^{4}}\tau B_{i}B_{j} \tag{16}$$

whereas, for large magnetic fields, substituting equations (12) and (14) into equation (9) leads to

$$G^{ij}=4a_{\chi}^{2}\pi^{2}v_{\mathrm{F}}\tau\frac{B_{i}B_{j}}{|\boldsymbol{B}|}$$

$$G_{\mathrm{T}}^{ij}=0$$

By adding a Drude contribution and summing over the contributions from the different nodes, we obtain the functional form used in the main text.

Equations (10) and (16) establish a link between the presence of the chiral and mixed axial–gravitational anomalies, represented by $a_{\chi}\neq0$ and $a_{\mathrm{g}}\neq0$, respectively, and the enhancement of the thermoelectric response function of Weyl fermions in flat space-time due to a magnetic field applied parallel to a thermal gradient.

© 2017 Macmillan Publishers Limited, part of Springer Nature. All rights reserved.

In particular, if the axial–gravitational anomaly is absent, then there is no thermal transport. Because we probe the presence of the chiral anomaly ($a_\chi \neq 0$) independently by measuring a positive magneto-conductance, our results indicate that $a_g \neq 0$. This is the main finding of our work.

The physical effects can be summarized as follows. The thermal gradient increases (decreases) the energy density of left-moving (right-moving) charge carriers, which leads to an effective chiral imbalance that generates a current in the direction of the magnetic field via the chiral magnetic effect. Finally, as mentioned above and in the main text, the functional dependence used in here is consistent with more conventional semi-classical treatments based on the Boltzmann equation[23–26]; however, these do not track the origin of these anomalous transport features explicitly, and cannot access the high-magnetic-field limit directly.

Data availability. All data generated and analysed during this study are available within the paper and its Extended Data. Further data are available from the corresponding author on reasonable request.

31. Landsteiner, K., Megias, E., Melgar, L. & Pena-Benitez, F. Holographic gravitational anomaly and chiral vortical effect. *J. High Energy Phys.* **9,** 121 (2011).
32. Golkar, S. & Sethi, S. Global anomalies and effective field theory. *J. High Energy Phys.* **5,** 105 (2016).
33. Delbourgo, R. & Salam, A. The gravitational correction to PCAC. *Phys. Lett. B* **40,** 381–382 (1972).
34. Landsteiner, K. Notes on anomaly induced transport. *Acta Phys. Pol. B* **47,** 2617–2673 (2016).
35. Jensen, K., Loganayagam, R. & Yarom, A. Thermodynamics, gravitational anomalies and cones. *J. High Energy Phys.* **2,** 88 (2013).
36. LeBellac, M. *Thermal Field Theory* (Cambridge Univ. Press, 2000).

© 2017 Macmillan Publishers Limited, part of Springer Nature. All rights reserved.

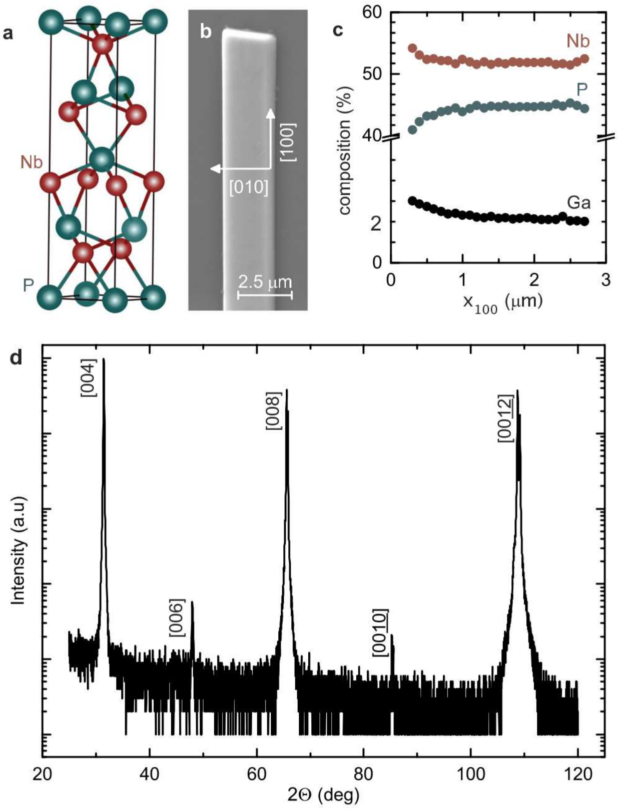

Extended Data Figure 1 | Material analysis of the NbP micro-ribbon. **a**, Sketch of the structure of the NbP crystal. **b**, SEM image of a NbP micro-ribbon before device processing. The longitudinal direction of the ribbon corresponds to the [100] axis of the crystal. **c**, Spatial composition of an exemplary NbP micro-ribbon, measured from the top along [100] using SEM-EDX, reveals an average of 53% Nb, 45% P and 2% Ga. x_{100} is the distance from the end of the sample along [100]. **d**, XRD spectrum of the NbP at room temperature (Cu K_α radiation). a.u., arbitrary units.

© 2017 Macmillan Publishers Limited, part of Springer Nature. All rights reserved.

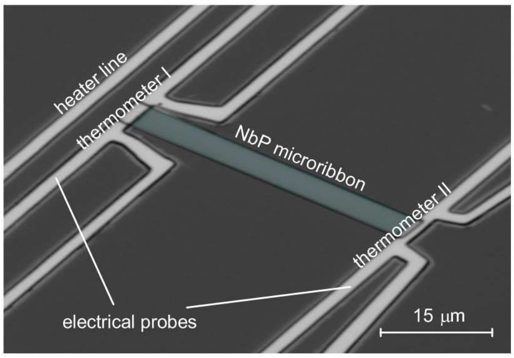
heater line
thermometer I
NbP microribbon
thermometer II
electrical probes
15 μm

Extended Data Figure 2 | Optical micrograph of a measurement device. The NbP micro-ribbon (green) is placed between two four-probe thermometers (grey), which also serve as electrical probes. The electrically insulated heater line (grey) close to one end of the sample creates a temperature gradient along the length of the sample.

© 2017 Macmillan Publishers Limited, part of Springer Nature. All rights reserved.

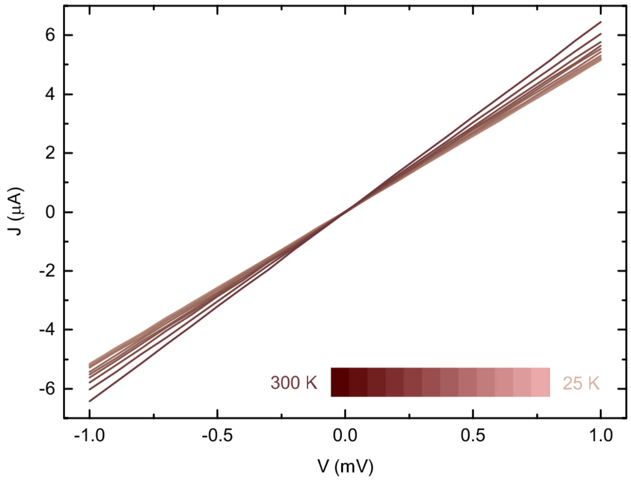

Extended Data Figure 3 | Isothermal ($\nabla T = 0$ K) current–voltage ($J-V$) characteristic of the NbP micro-ribbon at selected temperatures and zero magnetic field ($B = 0$ T). The linearity of the curves reveals ohmic electrical contacts.

© 2017 Macmillan Publishers Limited, part of Springer Nature. All rights reserved.

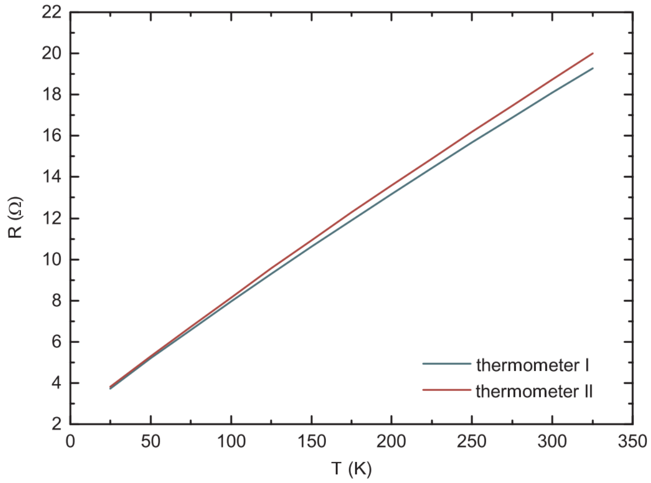

Extended Data Figure 4 | Thermometer calibration. Resistance *R* versus base temperature *T* of the cryostat, measured at isothermal conditions.

© 2017 Macmillan Publishers Limited, part of Springer Nature. All rights reserved.

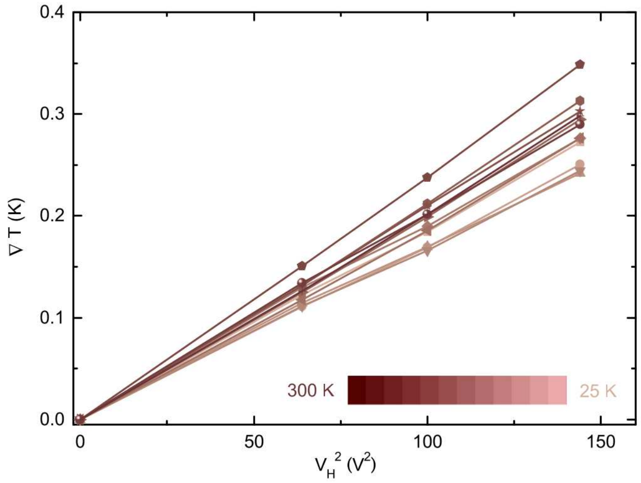

Extended Data Figure 5 | Temperature gradient ∇T along the sample as a function of the square of the heating voltage V_H at different base temperatures, which is proportional to the heating power.

© 2017 Macmillan Publishers Limited, part of Springer Nature. All rights reserved.

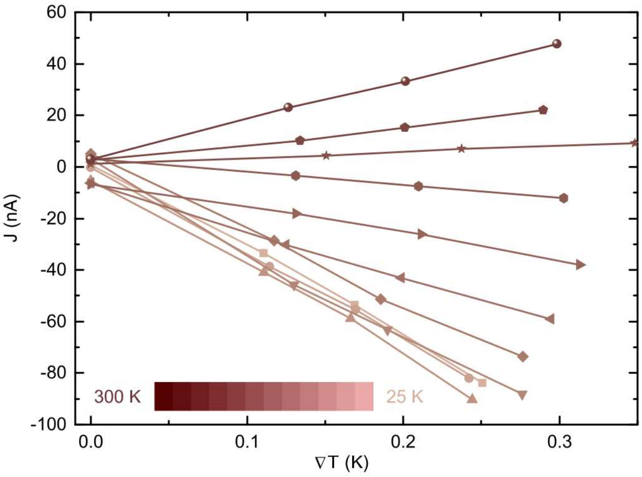

Extended Data Figure 6 | Linear response of the thermoelectric current *J* to the temperature gradient ∇*T*. We determine the thermoconductance $G_T = J/|\nabla T|$ from the slope of the linear fits. The error bars in Extended Data Fig. 8b are the uncertainties obtained from these fits.

© 2017 Macmillan Publishers Limited, part of Springer Nature. All rights reserved.

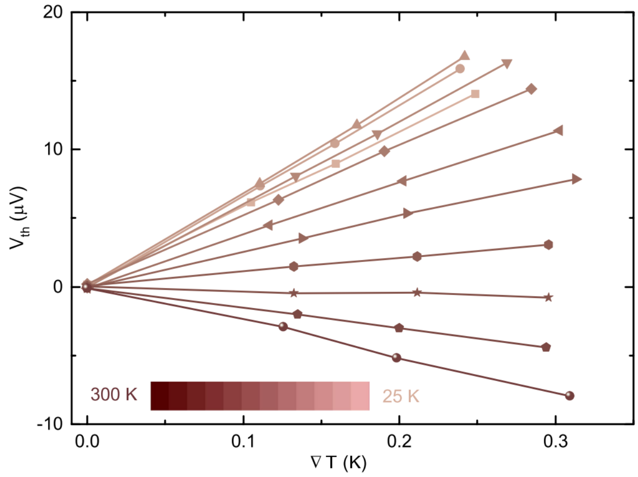

Extended Data Figure 7 | Linear response of the thermovoltage V_{th} to the temperature gradient ∇T. The thermopower $S = -V_{th}/|\nabla T|$ is determined from linear fits of the data.

© 2017 Macmillan Publishers Limited, part of Springer Nature. All rights reserved.

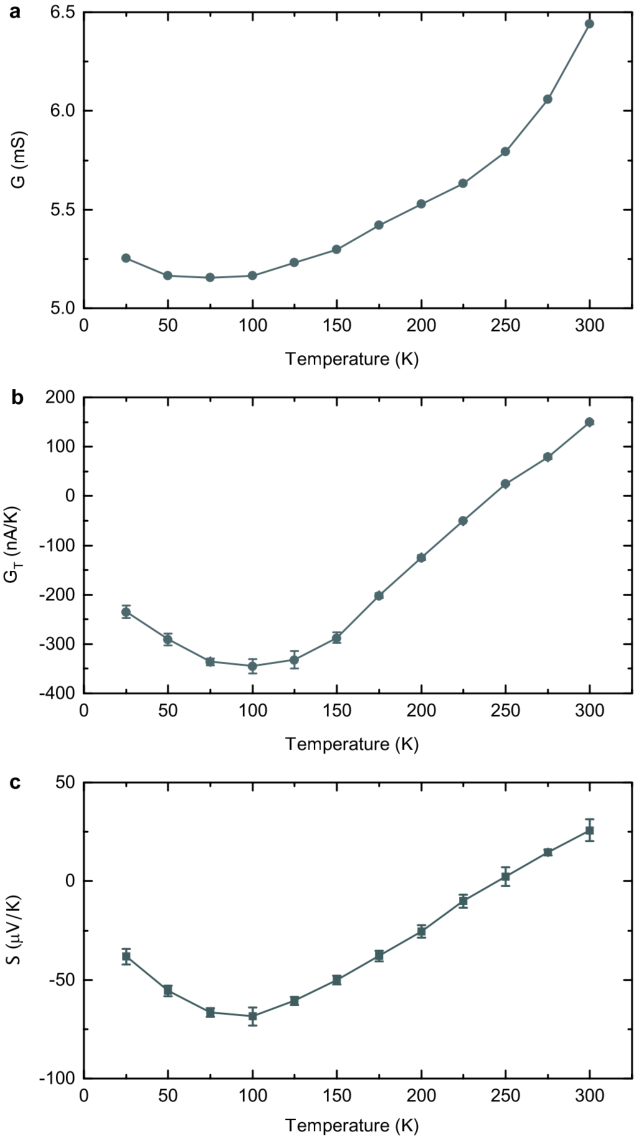

Extended Data Figure 8 | Zero-field transport. a, Electrical conductance G at zero magnetic field ($\boldsymbol{B} = \mathbf{0}$ T) in isothermal conditions ($\boldsymbol{\nabla} T = \mathbf{0}$ K) as a function of the base temperature. Values of G are obtained from the slope of the linear fits of the data given in Extended Data Fig. 3. **b**, Thermoelectric conductance G_T at zero magnetic field ($\boldsymbol{B} = \mathbf{0}$ T) and with no electric field imposed ($\boldsymbol{E} = \mathbf{0}$) as a function of the base temperature. Values of G_T are obtained from the slope of the linear fits of the data shown in Extended Data Fig. 6. Error bars, fit uncertainty of the slope. **c**, Themopower S at zero magnetic field ($\boldsymbol{B} = \mathbf{0}$ T) as a function of the base temperature. Values of S are obtained from the slope of the linear fits of the data shown in Extended Data Fig. 7. Error bars, fit uncertainty of the slope.

© 2017 Macmillan Publishers Limited, part of Springer Nature. All rights reserved.

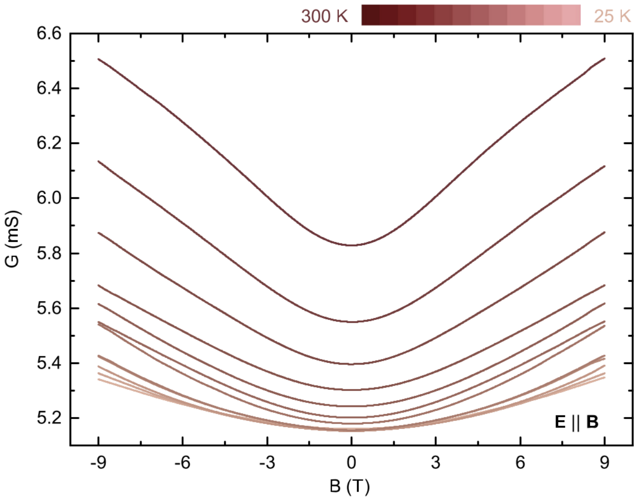

Extended Data Figure 9 | Magneto-conductance $G(E \parallel B)$ as a function of magnetic field B at selected base temperatures (colour scale).

© 2017 Macmillan Publishers Limited, part of Springer Nature. All rights reserved.

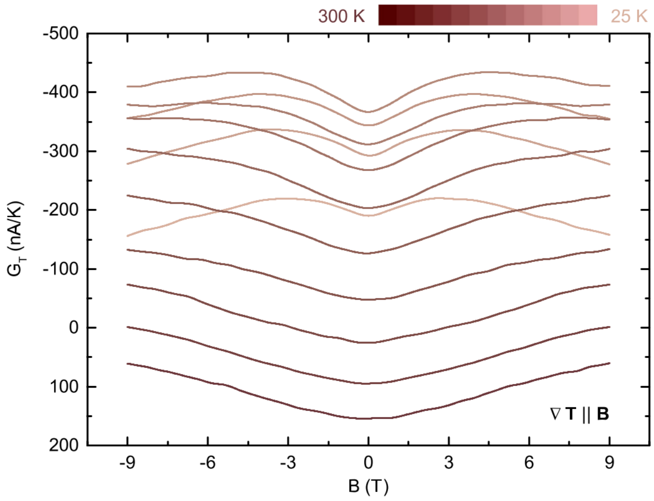

Extended Data Figure 10 | Magneto-thermoelectric conductance $G_T(\nabla T \parallel B)$ as a function of magnetic field B at selected base temperatures (colour scale).

© 2017 Macmillan Publishers Limited, part of Springer Nature. All rights reserved.

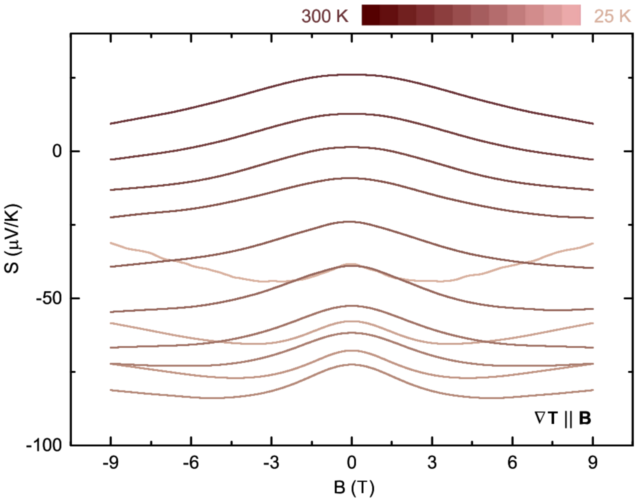

Extended Data Figure 11 | Magneto-thermopower *S*(∇*T* || *B*) as a function of magnetic field *B* at selected base temperatures (colour scale).

© 2017 Macmillan Publishers Limited, part of Springer Nature. All rights reserved.

VIII

Das Universum in einem Kristall

Anna C. Niemann, Johannes Gooth, Claudia Felser, & Kornelius Nielsch

Reprinted with permission from *Physik in unserer Zeit* **49**, 4 (2018)

Copyright 2018 WILEY-VCH Verlag GmbH & Co. KGaA, Weinheim.

Author Contributions: A.C.N. and J.G. wrote the manuscript. C.F. and K.N. supervised the project.

DOI: 10.1002/piuz.201801511

Quantenanomalien in Weyl-Halbmetallen

Universum im Kristall

Anna C. Niemann | Johannes Gooth | Claudia Felser | Kornelius Nielsch

Erhaltungsgrößen spielen in der Physik eine zentrale Rolle. Durch Quantisierungseffekte müssen diese allerdings in bestimmten Extremsituationen nicht mehr zwangsläufig erhalten sein. In Weyl-Halbmetallen gelang es uns nun, den Bruch einer Erhaltungsgröße nachzuweisen – eine sogenannte Quantenanomalie. Dies konnte einen schwer zugänglichen Effekt aus der Hochenergiephysik bestätigen.

Im Alltag spielen Erhaltungssätze eine zentrale Rolle, denn sie bestimmen letztendlich, welche physikalischen Prozesse in unserer Welt möglich sind und welche nicht. Ihre zentrale Aussage ist, dass sich bestimmte physikalische Größen, die Erhaltungsgrößen, im Lauf der Zeit innerhalb eines isolierten physikalischen Systems nicht ändern. Erhaltungsgrößen aus der klassischen Physik sind beispielsweise Energie, Impuls, Drehimpuls und elektrische Ladung.

Der bekannteste Erhaltungssatz ist wohl die Energieerhaltung, die besagt, dass Energie weder erzeugt noch vernichtet werden kann; sie kann lediglich von einer Erscheinungsform in eine andere umgewandelt werden. In einem isolierten System bleibt somit die Summe aller Energien konstant, egal in wie vielen und welchen Formen diese vorliegen. Eine wichtige Funktion der Erhaltungssätze besteht darin, das makroskopische Verhalten eines Systems vorherzusagen, ohne die mikroskopischen Details eines physikalischen Prozesses oder einer chemischen Reaktion berücksichtigen zu müssen.

Es zeigt sich, dass jede Erhaltungsgröße Folge einer fundamentalen Symmetrie ist. Dabei versteht man unter einer Symmetrie eine Eigenschaft des Systems, die nach einer bestimmten Änderung, einer Transformation, unverändert bleibt. Dieser als Noether-Theoreme [1] bekannte Zusammenhang wurde 1918 von Emmy Noether formuliert (s. „Hundert Jahre Noether-Theoreme“ in diesem Heft auf S. 176).

Ein Beispiel dafür, dass eine Erhaltungsgröße direkt aus Symmetrieüberlegungen abgeleitet werden kann, ist ein einkristalliner Festkörper. Dieser hat eine periodische Atomstruktur, die auch eine Symmetrie darstellt. Verschiebt man ein System von Leitungselektronen im Inneren des Kristalls über eine ganzzahlige Anzahl von Perioden der Atomstruktur, macht dies für die Leitungselektronen keinen Unterschied. Das führt zu einer erhaltenen Größe namens Quasi-Impuls und ist die Basis von unserer heutigen Elektronik [2]. Andersherum sind für Leitungselektronen in amorphen Festkörpern eben nicht alle Orte im Festkörper gleich, da es keine kristalline, periodische Struktur gibt. Es gibt daher keinen Quasi-Impuls, und die Ladung kann nur noch sehr schlecht durch den Festkörper fließen.

Quantenanomalien versus Erhaltungsgrößen

Lange Zeit wurde angenommen, dass unsere Welt mit den unumstößlichen Erhaltungssätzen der klassischen Physik komplett beschrieben ist. Dies änderte sich jedoch 1927 mit der Einführung der Quantenfeldtheorie, die eine Kombination klassischer Feldtheorien, etwa der Elektrodynamik, mit der Quantenmechanik darstellt. Beim Übergang von der klassischen Physik zu einer quantenmechanischen Betrachtung sind die Erhaltungsgrößen der klassischen Physik nicht mehr zwangsläufig erhalten. Man spricht dann von Quantenanomalien – oder in Bezug auf die Noether-Theoreme von Symmetriebrechungen durch Quantenfluktuationen [3].

Solche Symmetriebrechungen spielen unter anderem eine wichtige Rolle in der Entwicklung unseres Universums, das heute vorwiegend aus Materie besteht. Man geht davon aus, dass kurz nach dem Urknall vor rund 13,8 Milliarden Jahren Materie und Antimaterie zunächst aufgrund von Symmetrien, also Erhaltungssätzen, zu gleichen Anteilen entstanden sind. Die Existenz von Antimaterie ist heute

Online-Ausgabe unter:
wileyonlinelibrary.com

© 2018 Wiley-VCH Verlag GmbH & Co. KGaA, Weinheim

Das Universum im Kristall: Die Festkörperphysik erlaubt es, mit neu entdeckten Materialien manche ungelöste Fragestellung aus der Hochenergiephysik zu erforschen *(Bild: R. Strasser, K. Scherer; Komposition: M. Büker)*.

experimentell bewiesen. Ihre mathematische Beschreibung findet die Antimaterie als negative Energielösungen in der Dirac-Gleichung, die das Verhalten von relativistischen Fermionen beschreibt. Dabei versteht man unter Fermionen Teilchen wie Elektronen, die einen halbzahligen Eigendrehimpuls haben, also einen Spin von +1/2 oder −1/2.

Treffen Teilchen und Antiteilchen aufeinander, vernichten sie sich gegenseitig. Übrig bleibt nur ihre Energie in Form von Strahlung. Somit hätten sich Materie und Antimaterie kurz nach dem Urknall gegenseitig komplett vernichten sollen. Wie kommt es also, dass die Materie nicht restlos verschwunden ist? Symmetriebrechende Quantenanomalien in der kosmologischen Evolution gelten heute als wahrscheinlichste Erklärung dafür, dass unser Universum hauptsächlich aus Materie besteht und Antimaterie verschwunden zu sein scheint [3].

Nun ist es hier aber mitnichten so, dass Energie, Impuls oder Ladung in der Quantenmechanik völlig freie Größen sind, die keinerlei Erhaltungssätzen unterworfen sind. Die Quantenmechanik kann klassische Erhaltungssätze nur unter extremen Bedingungen, etwa auf ultrakurzen Zeitskalen oder in sehr starken Kraftfeldern aushebeln. Während des Abbremsens der kosmologischen Expansion nach dem Urknall und der damit verbundenen Abkühlung des Universums wurden zum Beispiel schrittweise kritische Temperaturen erreicht, bei denen neue Kräfte und neue Teilchen auftreten, die jeweils zu Symmetriebrechungen führen [3].

Die Quantenanomalien, mit denen wir uns hier beschäftigen, treten für eine Art von Teilchen auf, die *Weyl-Fermionen* genannt wird. Benannt sind sie nach dem deutschen Mathematiker Hermann Weyl. Um ihren Namen nachzuvollziehen, muss man einen Schritt zurückgehen und sich mit Paul Dirac beschäftigen. Dieser hat in den 1920er-Jahren mit seiner Dirac-Gleichung [3] eine quantenmechanische Beschreibung für das Verhalten von Fermionen geliefert, die den Anforderungen der speziellen Relativitätstheorie genügt. Hermann Weyl hat diese dann weiter verfeinert und eine Beschreibung für relativistische und gleichzeitig masselose Fermionen entwickelt. Seine Formel wird ihm zu Ehren heute Weyl-Gleichung [4] genannt; und die Teilchen, die dieser mathematischen Beschreibung folgen, heißen Weyl-Fermionen.

Weyl-Fermionen haben eine streng erhaltene physikalische Eigenschaft, die Chiralität genannt wird. Diese beschreibt die Händigkeit ihres Spins relativ zu ihrer Bewegungsrichtung. Der Spin-Vektor kann entweder entlang oder entgegengesetzt der Bewegungsrichtung zeigen, was einem positiven oder negativen Wert der Chiralität entspricht (Abbildung 1). Die Chiralitätserhaltung kann als Folge der chiralen Symmetrie der Dirac-Gleichung für masselose Teilchen angesehen werden: Sie hat keine Vorliebe für eine bestimmte Chiralität und vermischt die beiden Chiralitäten nicht. Wenn man jedoch von der freien Dirac-Gleichung zur entsprechenden Quantisierung übergeht, stellt man fest, dass die scheinbar offensichtliche chirale Symmetrie gebrochen ist, sobald die Fermionen in ein elektromagnetisches Feld mit parallelen elektrischen und magnetischen Komponenten gebracht werden. Man spricht von einer *chiralen Anomalie*.

Im Standardmodell der Teilchenphysik werden bestimmte Anteile der Teilchen-Antiteilchen-Asymmetrie auf eben diese chirale Anomalie zurückgeführt. Darüber hinaus ist vorhergesagt, dass eine zugrundeliegende gekrümmte Raumzeit einen deutlichen Beitrag zum chiralen Ungleichgewicht liefert. Dieser Effekt ist als *axial-gravitative Anomalie* bekannt. In extremen Gravitationsfeldern, die einer stark gekrümmten Raumzeit entsprechen, trägt die axial-gravitative Anomalie somit auch zur Teilchen-Antiteilchen-Asymmetrie bei [3].

Zugegeben, die Voraussetzungen für Quantenanomalien klingen erst einmal recht konstruiert. Und gerade das natürliche Auftreten von ausreichend großen Kraftfeldern auf der Erde ist extrem unwahrscheinlich. Daher sind wir normalerweise auf Experimente angewiesen, welche die hochenergetischen Bedingungen des frühen Universums nachbilden, zum Beispiel in Teilchenbeschleunigern. In diesen Großanlagen der Hochenergiephysik werden elektrisch geladene Teilchen durch elektrische und magnetische Felder annähernd auf Lichtgeschwindigkeit beschleunigt. Sie erreichen damit riesige kinetische Energien. Durch Kollision der hochenergetischen Teilchen lässt sich dann der fundamentale Aufbau von subatomaren Teilchen und deren Wechselwirkungen untersuchen, was die zentrale Fragestellung der Hochenergiephysik darstellt.

Die chirale Anomalie wurde so im Kontext eines Beschleunigerexperimentes entdeckt. 1969 versuchten die

ABB. 1 | CHIRALITÄT

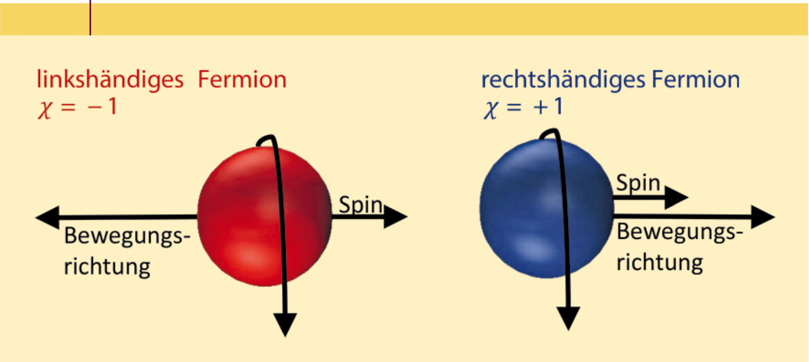

Die Chiralität gibt für masselose Fermionen die Spinrichtung in Bezug auf die Bewegungsrichtung an. Je nach Ausrichtung dieser beiden Größen unterscheidet man zwischen linkshändigen (rot) und rechtshändigen (blau) Fermionen, denen jeweils die Variablen $\chi = -1$ und $\chi = +1$ zugeordnet sind.

Theoretiker Stephen Adler sowie John Stewart Bell und Roman Jackiw unabhängig voneinander, den beobachteten Zerfall eines neutralen Pions in zwei Photonen zu erklären [4, 5]. Auch wenn es sich in diesem Fall nicht um masselose Fermionen, sondern um Bosonen handelt, ist die Chiralität definiert – allerdings lässt sie sich nicht mehr wie für masselose Fermionen mit der Händigkeit der Teilchen (Abbildung 1) gleichsetzen. Der beobachtete Zerfall des Pions sollte eigentlich durch die chirale Symmetrieerhaltung verboten sein, doch es zeigte sich, dass dies nicht der Fall ist. Heute heißt die chirale Anomalie daher auch Adler-Bell-Jackiw-Anomalie.

Die Bedingungen, unter denen eine axial-gravitative Anomalie nachweisbar sein könnte, sind jedoch auch in der Großforschung nicht erreichbar. Die benötigten Gravitationsfelder sind zu stark. Zwar wurde die axial-gravitative Anomalie als relevant für die hydrodynamische Beschreibung von Neutronensternen [6] und den chiralen Effekt im Zusammenhang mit Quark-Gluon-Plasmen vorgeschlagen [7], aber Hochenergieexperimente fanden bislang keine Signatur hierfür. Ein relevanter zu beobachtender Prozess wäre der Zerfall eines neutralen Pions in zwei – hypothetische – Gravitonen [8]. Das allerdings liegt weit jenseits der heutigen Detektortechnik.

Unlängst gelang es jedoch in der Festkörperphysik, gleich zwei Arten von Quantenanomalien zu beobachten, die sich als ungewöhnliche Magnetfeldabhängigkeiten von unterschiedlich getriebenen elektrischen Strömen manifestieren. Es handelt sich dabei um die chirale Anomalie [9, 10] und die gemischte axial-gravitative Anomalie [11]. Zum Nachweis der Letzteren sind thermoelektrische Experimente in magnetischen Feldern notwendig – vor allem aber geeignete Materialsysteme: Weyl- oder Dirac-Halbmetalle. Unsere Gruppen am Leibnitz-Institut für Festkörper- und Werkstoffforschung und am Max-Planck-Institut für die chemische Physik fester Stoffe in Dresden forschen schon seit einigen Jahren mit solchen Systemen.

Weyl- und Dirac-Halbmetalle

Um ein anschauliches Bild vom Elektronentransport in Festkörpern zu erlangen, nutzt die Festköperphysik das Modell der elektronischen Struktur. Darin wird beschrieben, welche Energie (*E*) und welchen Impulsvektor (*k*) die Elektronen in einem Kristall einnehmen können. Dieser Zusammenhang entsteht aus der Wechselwirkung von freien Elektronen mit den Atomrümpfen, aus denen der Kristall aufgebaut ist. Man könnte sagen, die Elektronen in einem Festkörper spüren das Potential der umliegenden Ionenrümpfe und haben dadurch teilweise andere Eigenschaften als Elektronen, die sich im freien Raum bewegen.

Das Diagramm, das den Zusammenhang zwischen Energie und Impuls zeigt, wird Bandstruktur genannt. In seiner einfachsten Darstellung besteht so eine Bandstruktur aus einem mit Elektronen besetzten Valenzband und einem unbesetzten Leitungsband (Abbildung 2a). Mit Erfahrung kann man aus solchen Bandstrukturen allerhand Eigenschaften der Elektronen ablesen, zum Beispiel ob der Festkörper ein Isolator, Halbleiter oder Metall ist. Bei einem Metall zum Beispiel ist das Leitungsband teilweise mit Elektronen gefüllt, was es elektrisch leitfähig macht. Darüber hinaus kann man aus der Bandstruktur die Masse der Ladungsträger und deren Geschwindigkeit im Festkörper bestimmen. Elektronen in einem Festkörper müssen zum Beispiel keineswegs die Masse von Elektronen im freien Raum haben, sondern können effektiv auch erheblich leichter oder schwerer als diese sein.

Abbildung 2a zeigt die Bandstruktur eines gewöhnlichen Halbmetalls. Alle Halbmetalle, also auch Dirac- und Weyl-Halbmetalle, haben gemeinsam, dass sich Leitungs- und Valenzband berühren. Bei gewöhnlichen Halbmetallen

ABB. 2 | **HALBMETALL-BANDSTRUKTUREN**

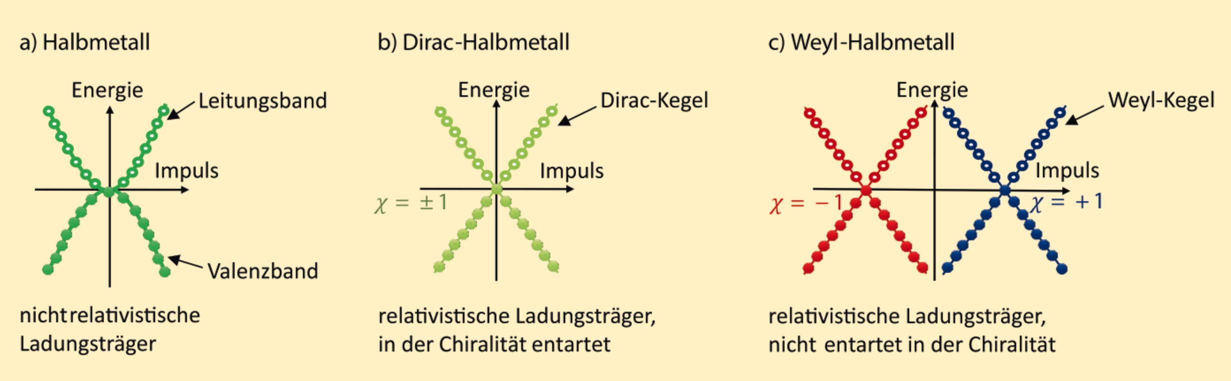
a) Halbmetall
Energie
Leitungsband
Impuls
Valenzband
nichtrelativistische Ladungsträger
b) Dirac-Halbmetall
Energie
Dirac-Kegel
Impuls
χ = ±1
relativistische Ladungsträger, in der Chiralität entartet
c) Weyl-Halbmetall
Energie
Weyl-Kegel
Impuls
χ = −1
χ = +1
relativistische Ladungsträger, nicht entartet in der Chiralität

Bandstrukturen beschreiben den Zusammenhang zwischen Energie und Impuls von Ladungsträgern in einem Festkörper. Ausgefüllte Kreise stellen hier besetzte Zustände im Valenzband dar, unausgefüllte Kreise unbesetzte Zustände im Leitungsband. a) Halbmetalle mit nichtrelativistischen Ladungsträgern besitzen zwei sich berührende, gekrümmte Bänder. b) Dirac-Halbmetalle haben lineare Bandstrukturen, die relativistische Ladungsträger beherbergen und bezüglich der Chiralität entartet sind. c) Weyl-Halbmetalle haben ebenfalls lineare Energie-Impuls-Beziehungen, die beiden Weyl-Kegel beherbergen jeweils eine Chiralität.

© 2018 Wiley-VCH Verlag GmbH & Co. KGaA, Weinheim

ist außerdem immer ein gekrümmter – zumeist parabelförmiger – Zusammenhang zwischen Energie und Impuls zu beobachten. Dieser wird von der Schrödinger-Gleichung beschrieben. Er verdeutlicht damit, dass in diesen gewöhnlichen Halbmetallen nichtrelativistische Ladungsträger vorliegen, die eine endliche Ruhemasse haben.

Im Gegensatz dazu besitzen spezielle Festkörper, die lange Zeit wenig beachtet wurden, eine relativistische Bandstruktur. Sie wird von der Dirac-Gleichung beschrieben. In solchen Dirac-Halbmetallen ist die Beziehung zwischen Energie und Impuls linear (Abbildung 2b). Man beschreibt diese lineare elektronische Struktur auch als zwei kegelförmige Bänder, Dirac-Kegel, die sich umgekehrt übereinanderliegend an einer Spitze berühren.

Ein genauerer Blick auf das in Abbildung 2b gezeigte Beispiel offenbart, dass es für die negativen Energielösungen der Hochenergiephysik in der Festkörperphysik eine direkte und einfache Analogie gibt: gefüllte Valenzbänder in der elektronischen Struktur von Dirac- oder Weyl-Halbmetallen. Der obere Dirac-Kegel ist das Leitungsband und repräsentiert das Analogon zur Materie, der untere ist das Valenzband und repräsentiert das Antimaterie-Analogon. Die Ladungsträger auf diesen Dirac-Kegeln verhalten sich wie Teilchen ohne Ruhemasse, die sich mit einer effektiven „Lichtgeschwindigkeit“ von $c^* \approx 10^6$ m/s durch den Kristall bewegen.

Hochenergiephysik-Analogon im Festkörper

Der erste Festkörper mit relativistischen Ladungsträgern wurde 2005 entdeckt, mit der Untersuchung des Elektronentransports in Graphen [12]. Es besitzt eine lineare Bandstruktur, die durch die Dirac-Gleichung bestimmt wird. Die Elektronen ahmen relativistische Teilchen ohne Ruhemasse mit einer effektiven „Lichtgeschwindigkeit“ von $c^* \approx 10^6$ m/s nach. Diese Ladungsträger mit Energie E und Masse m sind durch $E = mc^{*2}$ beschreibbar, also einer an c^* angepassten Form von Einsteins berühmter Gleichung. In der Festkörperphysik ist dies eine höchstspannende Angelegenheit, da Elektronen mit solchen Eigenschaften bis dahin nur in Teilchenbeschleunigern erzeugt werden konnten.

2015 wurde dann erstmals ein dreidimensionales Gegenstück mit diesem ungewöhnlichen Elektronenverhalten gefunden: Das Dirac-Halbmetall $NaBiO_3$ beherbergt relativistische Fermionen in drei Dimensionen [9]. Solche dreidimensionalen Dirac-Halbmetalle sind bezüglich der Chiralität entartet. Das bedeutet, dass jede Position auf den Leitungsbändern nicht nur von einem Elektron besetzt wird, sondern von zwei Elektronen unterschiedlicher Chiralität.

Und tatsächlich brachten die Materialwissenschaften 2015 schließlich die Weyl-Gleichung in die experimentelle Festkörperphysik ein. Vom Konzept der Dirac-Halbmetalle geleitet wurde ein Einkristall entdeckt, der zusätzlich zur Voraussetzung einer linearen Bandstruktur eine unsymmetrische Kristallstruktur aufweist. Dieser Bruch der sogenannten Inversionssymmetrie führt zu einer klaren Trennung der Elektronen unterschiedlicher Chiralität in der elektronischen Struktur. Anstelle eines Dirac-Kegels, der sowohl linkshändige als auch rechtshändige Ladungsträger beherbergt, besitzen Weyl-Halbmetalle zwei Weyl-Kegel an unterschiedlichen Positionen entlang der Impulsachse (Abbildung 2c), die jeweils entweder rein links- oder rein rechtshändige Ladungsträger beherbergen.

Die Abbildung dieser Weyl-Bandstruktur mit winkelaufgelöster Photoemissions-Spektroskopie in Tantalarsenid (TaAs) stellt die erste experimentelle Beobachtung von Weyl-Fermionen überhaupt dar [13]. Die Teilchenphysik hatte jahrzehntelang vergebens danach gesucht. Man weiß heute, dass Weyl-Kegel sogar viel häufiger in Materialien auftreten als Dirac-Kegel. Zudem kann man faktisch jedes Dirac-Halbmetall durch Anlegen eines ausreichend starken Magnetfeldes in ein Weyl-Halbmetall transformieren – zur großen Freude der Experimentalphysikerinnen und -physiker. Mit diesem Wissen können wir uns nun den Experimenten zu Quantenanomalien in Festkörpern zuwenden.

Quantenanomalien in Weyl-Halbmetallen

Der Nachweis der chiralen Anomalie und der gemischten, axial-gravitativen Anomalie in Weyl-Halbmetallen basiert auf Messungen des elektrischen Stroms unter dem Einfluss von Magnetfeldern. Im Bild der Bandstruktur lässt sich schön verdeutlichen, was der Transport eines elektrischen Stroms durch einen Festkörper bedeutet. Ein elektrischer

ABB. 3 | STROMTRANSPORT

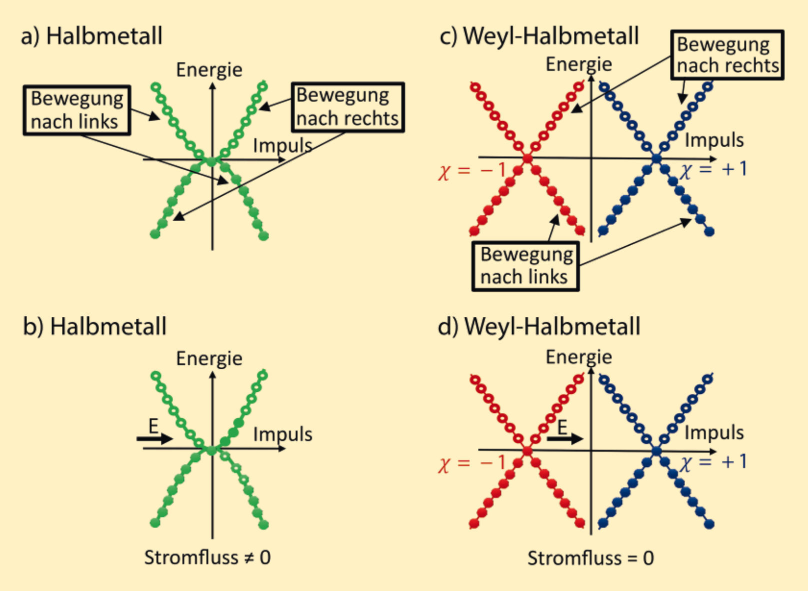

a) In der Bandstruktur von Halbmetallen hängt die Neigung der Bänder mit der Bewegungsrichtung der Elektronen zusammen. Elektronen auf nach links geneigten Bändern bewegen sich nach links, auf nach rechts geneigten Bändern entgegengesetzt. b) Legt man ein elektrisches Feld E an das Halbmetall an, ändert sich die Besetzung von nach links und nach rechts geneigten Bändern. Es fließt ein elektrischer Strom. c) Auch in einem Weyl-Halbmetall beherbergen nach links geneigte Bänder und nach rechts geneigte Bänder Elektronen mit entgegengesetzten Bewegungsrichtungen. d) Durch die Chiralitätserhaltung fließt hier jedoch trotz einem angelegten elektrischen Feld kein oder nur ein stark unterdrückter Strom.

© 2018 Wiley-VCH Verlag GmbH & Co. KGaA, Weinheim

Strom fließt durch ein Metall oder Halbmetall, wenn sich mehr Elektronen in eine Richtung der Probe bewegen als in die andere.

In der Bandstruktur lässt sich die Elektronenbewegung direkt ablesen: Nach rechts „geneigte“ Bänder stellen nach rechts wandernde Elektronen dar, entgegengesetzt ist es bei nach links geneigten Bänder. Die Anzahl der Elektronen in den jeweiligen Bändern ist in Abbildung 3 durch gefüllte Punkte dargestellt, die leeren Plätze (Zustände) durch nichtgefüllte Punkte. Wenn kein elektrischer Strom durch die Probe getrieben wird, wie in Abbildung 3a gezeigt, bewegen sich gleich viele Elektronen in entgegengesetzte Richtungen, alle Bänder sind also gleich gefüllt. Legt man nun zum Beispiel ein elektrisches Feld zwischen dem linken und rechten Ende der Probe an, dann fließt ein Strom von links nach rechts (Abbildung 3b). In der Bilanz bewegen sich also mehr Elektronen nach rechts als nach links, was in der Bandstruktur einer Verschiebung von besetzten Zuständen aus den nach links geneigten Bändern zu den nach rechts geneigten Bändern gleichkommt.

Wenn wir dieses Bild nun auf die Bandstruktur in Weyl-Halbmetallen (Abbildung 3c) übertragen, würden wir auch hier erwarten, einen elektrischen Strom treiben zu können. Es stellt sich allerdings heraus, dass das in Weyl-Halbmetallen ein Problem darstellt. Aber warum ist der Stromfluss in diesen Materialien unterdrückt? Das Geheimnis liegt darin, dass in Weyl-Halbmetallen eine weitere Eigenschaft der Elektronen mit ins Spiel kommt: die Chiralität, die zusammen mit der „Neigung“ der Bänder daraus entsteht, dass jedes der Bänder nur Elektronen eines bestimmten Spins trägt. Die Chiralitätserhaltung verbietet es in diesen Materialien, dass links und rechts geneigte Bänder mit unterschiedlich vielen Elektronen besetzt sind. Folglich kann kein Strom fließen (Abbildung 3d).

Zusammengefasst lässt sich also sagen, dass die Teilchenzahl auf den beiden Weyl-Kegeln unterschiedlicher Chiralität eine strikt erhaltene Größe ist. Dies hat zur Folge, dass elektrische Ströme, die durch Landungsträger auf den Weyl-Kegeln getragen werden, stark unterdrückt sind. Trotzdem haben reale Weyl-Materialien einen metallischen Charakter, denn neben Elektronen auf den Weyl-Kegeln tragen auch noch weitere Ladungsträger zum elektronischen Transport bei. Die dennoch starke Unterdrückung des Ladungstransports auf den Weyl-Bändern liefert aber die Basis zum Vermessen von Quantenanomalien in Festkörpern.

Chirale Anomalie

Zum Nachweis der chiralen Anomalie haben wir an einem Weyl-Halbmetall eine elektrische Leitwertmessung erst ohne und dann mit einem zum elektrischen Feld parallelen Magnetfeld durchgeführt. Im Magnetfeld ändert sich zunächst die Bandstruktur der Weyl-Halbmetalle. Abbildung 4a zeigt diese ohne Magnetfeld, 4b in einem Magnetfeld, das hinreichend groß ist. Statt der anfänglich vier linearen Bänder um die Impulsachse, welche die beiden Weyl-Kegel gebildet haben, sind in dem Magnetfeld lediglich zwei linear verlaufende Bänder verschiedener Neigung, aber mit demselben Spin übrig. Da die entgegengesetzten Neigungen entgegengesetzte Bewegungsrichtungen der Elektronen repräsentieren, verkörpern die beiden Bänder folglich unterschiedliche Chiralitäten.

Weit unter- und oberhalb der Impulsachse sind parabolisch verlaufende Bänder zu sehen. Man spricht bei dieser Aufspaltung der Bandstruktur von einer Landau-Quantisierung. Ursache sind die quantisierten Kreisbahnen, auf welche das Magnetfeld die Elektronen während ihrer Bewegung durch den Festköper lenkt. Wichtig ist, dass auf der

ABB. 4 | LANDAU-QUANTISIERUNG

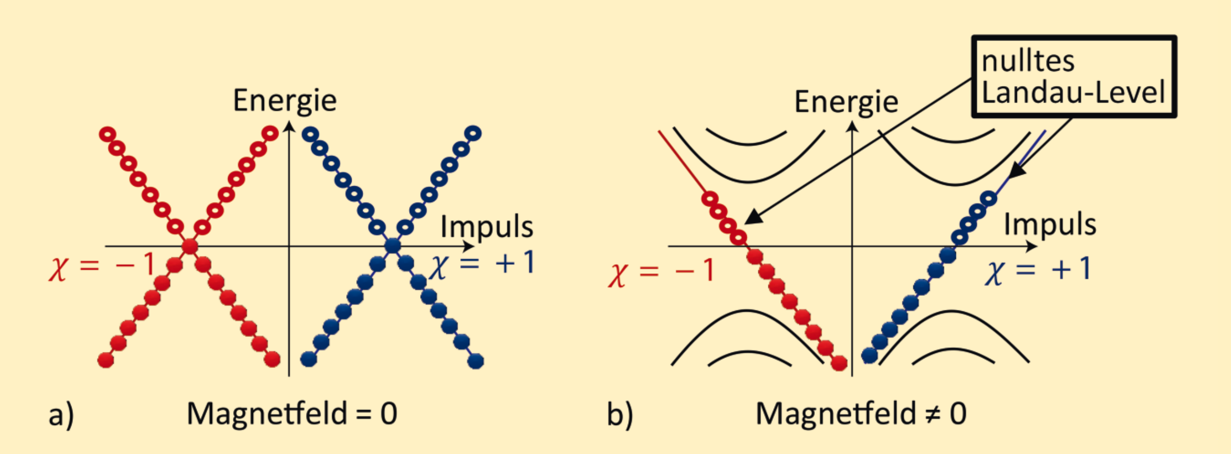

Die Bandstruktur der Weyl-Halbmetalle a) unterliegt einer Landau-Quantisierung b), wenn es sich in einem homogenen Magnetfeld befindet. Das sogenannte nullte Landau-Niveau verläuft immer noch linear und beherbergt relativistische Elektronen, für welche die Chiralität eine Erhaltungsgröße ist. Alle höheren Landau-Niveaus haben hingegen einen gekrümmten Verlauf und beherbergen nichtrelativistische Elektronen. Für diese ist die Chiralität keine Erhaltungsgröße.

neu entstandenen Bandstruktur nur noch die Elektronen der linearen Bänder, dem sogenannten nullten Landau-Niveau, Weyl-Fermionen sind. Nur für diese Elektronen ist die Chiralität auch weiterhin eine Erhaltungsgröße.

Liegt das Magnetfeld senkrecht zum elektrischen Feld an, bleibt der elektrische Strom, der von den Weyl-Bändern getragen wird, unterdrückt. Man misst lediglich einen geringen elektrischen Leitwert durch die gekrümmten Bänder der höheren Landau-Niveaus, denn ihr Beitrag lässt sich in realen Weyl-Halbmetallen nicht ausschalten. Außerdem können – sowohl ohne als auch mit angelegtem Magnetfeld – weitere parabolische, nichtrelativistische Bänder einen geringen Beitrag zur Leitfähigkeit des Materials liefern. Die Situation ändert sich bei einem parallel zum elektrischen Feld ausgerichteten Magnetfeld. Abbildung 5a zeigt einen solchen Versuchsaufbau mit dem Weyl-Halbmetall Niobphosphid (NbP). Nun misst man einen Anstieg des elektrischen Stroms und des elektrischen Leitwerts (Abbildung 5b).

Diese Beobachtung wird durch einen Bruch der chiralen Erhaltungsgröße erklärt. Er erlaubt es, in parallelen elektrischen und magnetischen Feldern mehr links- als rechtshändige Elektronen zu erzeugen (Abbildung 6a). Die Stärke dieser Erhaltungssatz-Verletzung hängt von der Stärke des Magnetfeldes ab. Für eine parallele Ausrichtung in einem elektrischen und magnetischen Feld wird in Abbildung 6b folglich ein kontinuierlich ansteigender Leitwert beobachtet. Für nicht parallele Ausrichtungen, also einem Winkel zwischen $\boldsymbol{E}$ und $\boldsymbol{B}$ oberhalb null, beobachten wir hingegen nur eine sehr geringe Erhöhung oder sogar negative Änderung des Leitwerts.

Diese chirale Anomalie wurde in den letzten drei Jahren weltweit nachgewiesen [9, 10], sowohl in Weyl- als auch Dirac-Halbmetallen, die sich im Magnetfeld ganz ähnlich verhalten. Spannend ist daran, dass Effekte aus der Hochenergiephysik nun in Festkörperlaboratorien nachempfunden werden können – wie die chirale Anomalie als Mechanismus im schon erwähnten Zerfall eines neutralen Pions in zwei Photonen [4, 5]. Weyl-Materialien bilden damit eine Brücke zwischen zwei Forschungsfeldern, die auf der Energieskala nicht weiter voneinander entfernt sein könnten.

Für die Festkörperphysik ist das auch deshalb eine aufregende Entdeckung, weil interessante Effekte aus der Hochenergiephysik sich vielleicht sogar in neue Technologie umsetzen lassen. Andersherum könnte die Festkörperphysik helfen, Effekte, die zuvor nur für die Hochenergiephysik relevant schienen aber nicht nachweisbar waren, experimentell zugänglich zu machen. Ein solches, kürzlich veröffentlichtes Beispiel bietet die axial-gravitative Anomalie [11].

ABB. 5 | CHIRALE ANOMALIE 1

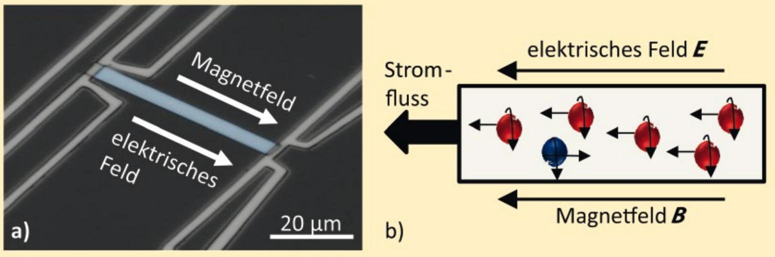

Nachweis der chiralen Anomalie im Weyl-Halbmetall Niobphosphid (NbP). a) Vergrößerte Abbildung der NbP-Probe (blau eingefärbt) in der elektrischen Kontaktstruktur (weiß). b) Bei der Messung des elektrischen Leitwerts kommt es in parallelen elektrischen und magnetischen Feldern zu einem Bruch der chiralen Symmetrie. Infolgedessen fließt ein makroskopisch messbarer Strom.

ABB. 6 | CHIRALE ANOMALIE 2

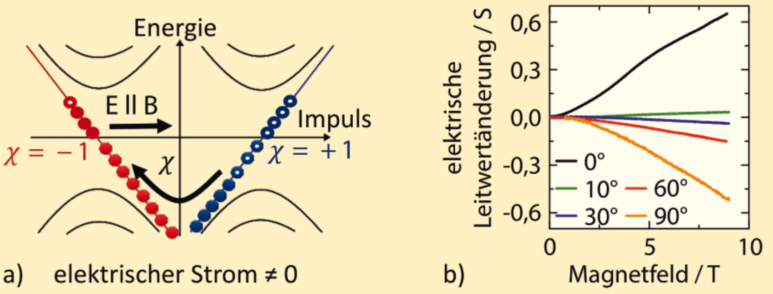

a) In der Bandstruktur kommt es in parallelen elektrischen und magnetischen Feldern zu einer Umbesetzung des nach links und nach rechts geneigten chiralen Bands. b) In der elektrischen Leitwertmessung misst man einzig für parallele elektrische und magnetische Felder eine starke Zunahme des Stromflusses bei ansteigendem Magnetfeld. Dies wird als Signatur der chiralen Anomalie interpretiert. Die Winkelangaben geben die relative Ausrichtung von magnetischem und elektrischem Feld zueinander an. 0° steht für parallel, 90° für senkrecht verlaufende Felder.

Axial-gravitative Anomalie

Die axial-gravitative Anomalie beschreibt den Bruch der chiralen Symmetrie in Gravitationsfeldern in Kombination mit einigen anderen Feldern, zum Beispiel einem Magnetfeld. Wie schon diskutiert, sind auf der Erde bei Weitem nicht die Gravitationsfelder erreichbar, die zum Nachweis der axial-gravitativen Anomalie nötig wären. Dieses Problem konnten wir nun lösen.

Dazu nutzten wir die Erkenntnis, dass für die relativistischen Weyl-Fermionen ein Gravitationsfeld durch einen Temperaturgradienten simuliert werden kann. Sie geht auf den amerikanischen Theoretiker Joaquin Mazdak Luttinger zurück. Als dieser 1964 statistische Größen wie Entropie und Temperatur quantenfeldtheoretisch beschreiben wollte, fand er heraus, dass in relativistischen Systemen Temperaturgradienten Analoga für Gravitationsfelder darstellen [14]. Dies lässt sich mit $E = mc^2$ verstehen. Massen werden bekanntlich in Gravitationsfeldern bewegt und Energie als Wärme in Temperaturgradienten. Folglich können Temperaturgradienten in relativistischen Systemen als Stellvertreter für Gravitationsfelder angesehen werden.

Diesen Zusammenhang konnten wir nun nutzen, um die axial-gravitative Anomalie in einem Weyl-Halbmetall nach-

© 2018 Wiley-VCH Verlag GmbH & Co. KGaA, Weinheim

zuweisen. Dazu bedienten wir uns der Thermoelektrik. Erhitzt man eine Probe an einer Seite, dann entsteht ein Temperaturgradient zwischen der warmen und der kalten Seite. In einem Metall haben die Elektronen auf der heißen Seite eine höhere kinetische Energie als auf der kalten Seite. Das hat zur Folge, dass sich die Ladungsträger auf der heißen Seite im Mittel stärker bewegen als diejenigen auf der kalten Seite, was zu einem elektrischen Stromfluss führt. Die Größe, die das Verhältnis von erzeugtem elektrischem Strom zum angelegten Temperaturgradienten darstellt, wird thermoelektrischer Leitwert genannt.

Im Experiment setzten wir nun das Weyl-Halbmetall NbP einem Temperaturgradienten und einem Magnetfeld aus. Wir erinnern uns: Durch den Erhaltungssatz der Chiralität ist ein Stromfluss in Weyl-Habmetallen ohne Magnetfeld verboten. Liegt das Magnetfeld senkrecht zum Temperaturgradienten an, zeigt sich, dass der elektrische Stromfluss unterdrückt ist, was zu einem geringen thermoelektrischen Leitwert führt. Schaltet man nun das Magnetfeld parallel zum Temperaturgradienten ein (Abbildung 7a), beobachtet man einen Anstieg des elektrischen Stroms und einen damit verbundenen Anstieg des thermoelektrischen Leitwerts (Abbildung 7b). Die Erklärung ist ein Bruch der chiralen Erhaltungsgröße aufgrund der axial-gravitativen Anomalie.

ABB. 7 | AXIAL-GRAVITATIVE ANOMALIE 1

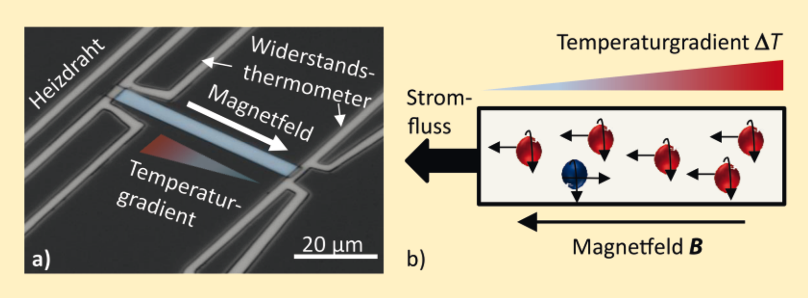

Nachweis der axial-gravitativen Anomalie im Weyl-Halbmetall Niobphosphid (NbP). a) Vergrößerte Abbildung der NbP-Probe (blau eingefärbt) in der elektrischen Kontaktstruktur (weiß). b) Bei der Messung des thermoelektrischen Leitwerts kommt es im parallelen magnetischen Feld und Temperaturgradienten zu einem Bruch der chiralen Symmetrie: Es fließt ein makroskopisch messbarer Strom.

ABB. 8 | AXIAL-GRAVITATIVE ANOMALIE 2

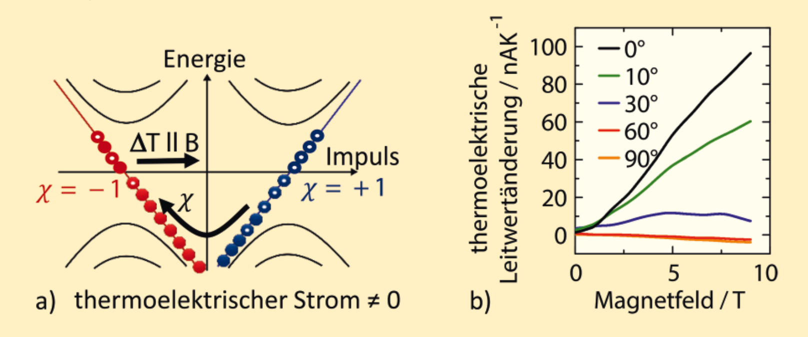

a) Sobald Temperaturgradient und magnetisches Feld parallel verlaufen, kommt es in der Bandstruktur zu einer Umbesetzung des nach links und nach rechts geneigten chiralen Bands. b) In der thermoelektrischen Leitwertmessung misst man für parallele magnetische Felder und Temperaturgradienten die stärkste Zunahme des Stromflusses bei ansteigendem Magnetfeld. Dies wird als Signatur der axial-gravitativen Anomalie interpretiert. Die Winkelangaben geben die Ausrichtung von magnetischem Feld und Temperaturgradienten an. 0° steht für parallel, 90° für senkrecht verlaufende Felder.

In der Bandstruktur des Weyl-Halbmetalls wird dieser Bruch der Chiralitätserhaltung durch eine ungleiche Besetzung der beiden chiralen Bänder deutlich (Abbildung 8a). In der thermoelektrischen Leitwertmessung (Abbildung 8b) finden wir für parallele magnetische Felder und Temperaturgradienten die stärkste Zunahme des Stromflusses bei ansteigendem Magnetfeld. Bei nichtparallelen Ausrichtungen von Magnetfeld und Temperaturgradienten beobachten wir hingegen eine deutlich geringere Zunahme des thermoelektrischen Leitwerts. Dies wertet die Forschung als ersten experimentellen Nachweis der gemischten, axial-gravitativen Anomalie. Der Begriff „Gravitation“ hat hier eine rein historische Bedeutung, da die Quantenanomalie nur durch den Temperaturgradienten und das Magnetfeld entsteht – in Analogie zum Gravitationsfeld.

Mit der axial-gravitativen Anomalie konnte also die Festkörperphysik einen Effekt nachweisen, der in der Hochenergiephysik zwar vorausgesagt wurde, dort aber experimentell nicht zugänglich ist. Angesichts dieser jüngsten Entwicklungen in der Festkörperphysik sollte die Entdeckung neuartiger Quantenanomalien wie etwa die quantenmechanische Brechung der Spiegelsymmetrie unserer Welt nur noch eine Frage der Zeit sein.

Zusammenfassung

In der klassischen Physik spielen Erhaltungsgrößen wie Energie oder Impuls eine zentrale Rolle. Durch Quantisierungseffekte sind solche Größen in bestimmten Extremsituationen allerdings nicht mehr zwangsläufig erhalten. Die Untersuchung solcher Quantenanomalien ist nun der Festkörperphysik dank neuer Materialsysteme zugänglich geworden. In Weyl-Halbmetallen konnten so Quantenanomalien als Bruch der Erhaltungsgröße Chiralität in Form der chiralen Anomalie und der axial-gravitativen Anomalie nachgewiesen werden. Bei letzterer gelang dies mit Hilfe von thermoelektrischen Messungen. Damit konnte die Festkörperphysik einen als nicht nachweisbar geglaubten Effekt der Hochenergiephysik dem Experiment zugänglich machen.

Stichwörter

Erhaltungsgröße, Quantenanomalie, chirale Anomalie, axial-gravitative Anomalie, Weyl-Halbmetall, Thermoelektrik.

© 2018 Wiley-VCH Verlag GmbH & Co. KGaA, Weinheim

Literatur

[1] E. Noether, Nachr. D. König. Gesellsch. D. Wiss. Zu Göttingen, Math-phys. Klasse. **1918**, 235.
[2] N. W. Ashcroft, D. N. Merim, Festkörperphysik, 3. Aufl., Oldenbourg Verlag, München 2007.
[3] G. E. Volovik, The Universe in a Helium Droplet. Oxford University Press, New York 2003.
[4] S. L. Adler, Phys. Rev. **1969**, *177*, 5.
[5] J. S. Bell, R. Jackiw, Nuovo Cim. **1969**, *A60*, 4.
[6] M. Kaminski et al., Phys. Lett. B **2016**, *760*, 170.
[7] K. Landsteiner et al, *Phys. Rev. Lett.* **2011**, *107*, 021601.
[8] T.A. Larsson, ArXiv Prepr. hep-th/0404033, 2004.
[9] J. Xiong et al., Science **2015**, *350*, 6259.
[10] A. C. Niemann et al., Sci. Rep. **2017**, *7*, 43394.
[11] J. Gooth et al., Nature **2017**, *547*, 7663.
[12] K. S. Novoselov et al., Nature **2005**, *438*, 7065.
[13] S.-Y. Xu et al., Science **2015**, *349*, 6248.
[14] J. M. Luttinger, Phys. Rev. **1964**, *135*, 6A.

Anschriften
Prof. Dr. Kornelius Nielsch, IFW Dresden,
Helmholtzstraße 20, D-01069 Dresden.
A.Niemann@ifw-dresden.de,
K.Nielsch@ifw-dresden.de

Prof. Dr. Claudia Felser, MPI CPfS Dresden,
Nöthnitzer Straße 40, D-01187 Dresden.
Johannes.Gooth@cpfs.mpg.de,
Claudia.Felser@cpfs.mpg.de

Die Autoren

*V. l. n. r.: **Anna C. Niemann** studierte Physik an der Universität Hamburg. Momentan promoviert sie an der Universität Hamburg über Transportmessungen an topologischen Materialien und arbeitet am Leibniz-Institut für Festkörper- und Werkstoffwissenschaften Dresden. **Johannes Gooth** ist Gruppenleiter am Max-Planck-Institut für Chemische Physik fester Stoffe in Dresden. Er studierte Physik an den Universitäten Hamburg und Lund in Schweden. 2014 promovierte er an der Universität Hamburg. Als Postdoc ging er 2015 zu IBM Research Zurich und wechselte 2017 zu Amir Yacoby an die Harvard University, USA. **Claudia Felser** studierte Chemie und Physik an der Universität zu Köln und promovierte dort 1994 in Physikalischer Chemie. Nach Postdoc-Stipendien am MPI für Festkörperforschung in Stuttgart und am CNRS in Nantes, Frankreich, wurde sie 2003 ordentliche Professorin an der Universität Mainz. Seit Dezember 2011 ist sie Direktorin am MPI für Chemische Physik fester Stoffe in Dresden. **Kornelius Nielsch** ist derzeit Direktor am Leibniz-Institut für Festköper und Werkstoffforschung (IFW) in Dresden und war von 2007 bis 2015 als Professor für Experimentalphysik an der Universität Hamburg tätig. Er studierte Physik in Duisburg, promovierte am Max-Planck-Institut für Mikrostrukturphysik in Halle, wo er nach einem Auslandsaufenthalt am MIT in Cambridge, Massachusetts (USA), eine BMBF-Nachwuchsgruppe leitete.*

© 2018 Wiley-VCH Verlag GmbH & Co. KGaA, Weinheim